4

MCEER MONOGRAPH

Seismic Design of Buried and Offshore Pipelines

Michael J. O'Rourke
(Jack) X. Liu

MCEER-12-MN04

MCEER
EARTHQUAKE ENGINEERING TO EXTREME EVENTS

MCEER
EARTHQUAKE ENGINEERING TO EXTREME EVENTS

MCEER is a national center of excellence dedicated to the discovery and development of new knowledge, tools and technologies that equip communities to become more disaster resilient in the face of earthquakes and other extreme events. MCEER accomplishes this through a system of multidisciplinary, multi-hazard research, in tandem with complimentary education and outreach initiatives.

Headquartered at the University at Buffalo, The State University of New York, MCEER was originally established by the National Science Foundation in 1986, as the first National Center for Earthquake Engineering Research (NCEER). In 1998, it became known as the Multidisciplinary Center for Earthquake Engineering Research (MCEER), from which the current name, MCEER, evolved.

Comprising a consortium of researchers and industry partners from numerous disciplines and institutions throughout the United States, MCEER's mission has expanded from its original focus on earthquake engineering to one which addresses the technical and socio-economic impacts of a variety of hazards, both natural and man-made, on critical infrastructure, facilities, and society.

The Center derives support from several Federal agencies, including the National Science Foundation, Federal Highway Administration, and the Department of Homeland Security/Federal Emergency Management Agency, and the State of New York, other state governments, academic institutions, foreign governments and private industry.

Seismic Design of Buried and Offshore Pipelines

by Michael J. O'Rourke[1] and
(Jack) X. Liu[2]

November 28, 2012

Monograph MCEER-12-MN04

1 Professor, Department of Civil and Environmental Engineering, Rensselaer Polytechnic Institute
2 Principal Consultant, Liu Advanced Engineering, LLC

Published by:
MCEER
University at Buffalo, State University of New York
133A Ketter Hall
Buffalo, NY 14260
Phone: (716) 645-3391
Fax: (716) 645-3399
email: mceer@buffalo.edu
http://mceer.buffalo.edu

ISBN 978-0-9656682-4-8

Jane Stoyle Welch, Managing Editor
David Pierro, Illustration and Cover Design
Sarah D'Iorio, Layout and Composition
Anna J. Kolberg, Page Design
Cover photographs provided by M. O'Rourke

MCEER Monograph No. 4

Preface

BY MICHAEL O'ROURKE

Buried pipeline systems are commonly used to transport water, sewage, oil, natural gas and other materials. In the conterminous United States, there are about 172,000 miles of crude oil pipelines and 1,540,000 miles of gas pipelines (USDoT, 2011). The total length of water and sewage pipelines is not readily available. These pipelines are often referred to as "lifelines" since they carry materials essential to the support of life and maintenance of property. Pipelines can be categorized as either continuous or segmented. Steel pipelines with welded joints are considered to be continuous while segmented pipelines include cast iron pipe with caulked or rubber gasket joints, ductile iron pipe with rubber gasket joints, concrete pipe, and asbestos cement pipe, etc.

The earthquake safety of buried pipelines continues to attract the attention of both researchers and practitioners. Important characteristics of buried pipelines are that they generally cover large areas and are subject to a variety of geotectonic hazards. Another characteristic of buried pipelines, which distinguishes them from above-ground structures and facilities, is that the inertia forces due to the weight of the pipeline and its contents are relatively unimportant. Buried pipelines can be damaged either by permanent movements of ground (i.e., PGD) or by transient seismic wave propagation.

Permanent ground movements include surface faulting, lateral spreading due to liquefaction, and landsliding. Although PGD hazards are usually limited to small regions within the pipeline network, their potential for damage is very high since they impose large deformation on pipelines. On the other hand, the wave propagation hazards typically affect the whole pipeline network, but with lower damage rates (i.e., lower pipe breaks and leaks per unit length of pipe). For example, during the 1906 San Francisco earthquake, the zones of lateral spreading accounted for only 5% of the built-up area affected by strong ground shaking. However, approximately 52% of all pipeline breaks occurred within one city block of these zones, according to T. O'Rourke et al. (1985). Presumably, the remaining 48% of pipeline damage can be attributed to wave propagation. Hence, although the total amount of damage due to PGD and wave propagation was roughly equal, the damage rate in the small isolated areas subject to PGD was about 20 times higher than that due to wave propagation.

Continuous pipelines may rupture in tension or buckle in compression. Observed seismic failure for segmented pipelines, particularly those with large diameters and relatively thick walls, is mainly due to distress at the pipeline joints (axial pull-out in tension, crushing of bell and spigot in compression). For smaller diameter segmented pipes, circumferential flexural failures (round cracks) have also been observed in areas of ground curvature.

This monograph reviews the behavior of buried pipeline components subject to permanent ground deformation and wave propagation hazards, as well as existing methods to quantify the response. To the extent possible and where appropriate, the review focuses on simplified procedures that can be directly used in the seismic analysis and design of buried pipeline components. System behavior of a buried pipeline network is not discussed in any great detail. Similarily, topics that are a concern for ordinary pipe in non-seismic environments but do not significantly influence seismic behavior (trench bracing requirements, backfill compaction, acceptance testing and the like) are not discussed. Where alternate approaches for analysis or design are available, attempts are made to compare the results from the different procedures. In addition, we attempt to benchmark the usefulness and relative accuracy of various approaches through comparison with available case histories. Finally, the use of the relations presented herein is illustrated with design examples.

This monograph is divided into 14 chapters. Chapter 1 is a review of basic concepts and terminology for both earthquakes and pipelines. Chapter 2 describes the different forms of permanent ground deformation (surface faulting, lateral spreading, landsliding), and presents procedures to quantify and model both the amount of PGD as well as the spatial extent of the PGD zone. Chapter 3 reviews seismic wave propagation and presents procedures for estimating ground strain due to travelling wave effects. Chapter 4 presents the failure modes and corresponding failure criteria for buried pipelines subject to seismic effects. Chapter 5 reviews commonly used techniques to model the soil-pipe interaction in both the longitudinal and transverse directions. Chapters 6 and 7 present the response of continuous pipelines subject to longitudinal PGD and transverse PGD, respectively, while Chapter 8 discusses continuous pipe response due to faulting. Chapter 9 presents the response of segmented pipelines subject to permanent ground deformation. Chapters 10 and 11 discuss the behavior of continuous and segmented pipeline components subject to seismic wave propagation, respectively. Chapter 12 presents seismic fragility relations for both wave propagation and PGD hazards. Chapter 13 presents current countermeasures to reduce damage to pipelines during earthquakes. Finally, Chapter 14 presents three design examples that illustrate the application of relations and procedures introduced in earlier chapters.

Acknowledgments

This monograph is a revision of a previous monograph by the authors entitled *Response to Buried Pipelines Subject to Earthquake Effects*, published by the Multidisciplinary Center for Earthquake Engineering Research (MCEER) in 1999.

A number of key results in this and the prior monograph come from Japan. Much of this Japanese research was presented at a series of U.S.-Japan workshops, originally organized by Professor M. Shinozuka of the U.S. and the late Professor K. Kubo of Japan. Subsequently, the workshop series was organized and led by Professors M. Hamada (Japan) and T. O'Rourke (U.S.). Hence, in addition to their significant individual technical contributions, the authors would like to acknowledge the admirable international cooperation and professional leadership of Professors M. Hamada, K. Kubo, T. O'Rourke and M. Shinozuka.

The understanding of earthquake behavior of buried pipelines has progressed to the point where detailed guideline documents were warranted. The authors would like to acknowledge the investment of the America Lifeline Alliance (ALA) and the leadership of J. Eidinger on seismic guidelines for water and wastewater lifelines. Similarly, the authors would like to acknowledge the investment of the Pipeline Research Council International (PRCI) and the work of D. Honegger and D. Nyman on seismic guidelines for gas and liquid fuel lifelines.

This monograph contains new content from a number of sources. In this regard, the authors would like to acknowledge the editors of Earthquake Spectra and the ASCE journal series, as well as the organizers of the Technical Council for Lifeline Earthquake Engineering (TCLEE) conference series and the Offshore Technology Conference (OTC) series. A substantial portion of the new content is based on research first presented in these forums.

Finally, the authors would like to acknowledge the many useful suggestions provided by the monograph reviewers.

Contents

1 Earthquake and Pipeline Fundamentals 1
1.1 Earthquake Fundamentals 1
1.2 Pipeline Fundamentals 5
1.3 Chapter Summary 6

2 Permanent Ground Deformation Hazards 11
2.1 Fault 11
2.2 Landslides 16
2.2.1 Onshore Landslides 16
2.2.2 Offshore Landslides 20
2.3 Lateral Spreading 24
2.3.1 Amount of PGD 29
2.3.2 Spatial Extent of Lateral Spread Zone 32
2.3.3 PGD Pattern 34
2.4 Seismic Settlement 37

3 Wave Propagation Hazard 39
3.1 Wave Propagation Fundamentals 39
3.2 Ground Motion Parameters 41
3.3 Wave Propagation Velocity 44
3.3.1 Body Waves 44
3.3.2 Surface Waves 46
3.4 Wavelength 49
3.5 Ground Strain and Curvature Due to Wave Propagation 50
3.6 Observed Ground Strain and Effective Propagation Velocities 54
3.7 Transient Ground Strain Due to Variable Subsurface Conditions 58
3.7.1 Laboratory Results and Numerical Models 58
3.7.2 Simplified Model 65
3.7.3 Comparison 66

4 Pipe Limit States and Failure Criterion 69
4.1 Continuous Pipeline with Butt Welds 70
4.1.1 Tensile Rupture - PGD Hazard 70

4.1.2 Local Buckling - PGD Hazard 72
4.1.2.1 Stress Limit 74
4.1.2.2 Strain Limit 76
4.1.3 Wave Propagation Hazard 81
4.1.4 Beam Buckling 83
4.1.4.1 Onshore Pipelines 83
4.1.4.2 Offshore Pipelines 84
4.2 Continuous Pipeline with Welded Slip Joints 86
4.2.1 Axial Tension 87
4.2.1.1 Analytical Models 87
4.2.1.2 Experimental Results 87
4.2.2 Axial Compression 89
4.2.2.1 Analytical Models 89
4.2.2.2 Experimental Results 92
4.2.3 Recommended Limit States 95
4.2.4 Comparison with Butt Welds 95
4.3 Segmented Pipeline 96
4.3.1 Axial Pull-out 98
4.3.2 Crushing of Bell and Spigot Joints 99
4.3.3 Circumferential Flexural Failure and Joint Rotation 103

5 Soil-Pipe Interaction 107
5.1 Onshore Pipelines in Competent Non-Liquefied Soil 108
5.1.1 Longitudinal Movement 109
5.1.2 Transverse-Horizontal Movement 111
5.1.3 Transverse Vertical Movement, Upward Direction 120
5.1.4 Transverse-Vertical Movement, Downward Direction 123
5.2 Onshore Pipelines in Liquefied Soil 124
5.3 Offshore Pipelines 126
5.3.1 Pipe Embedment 126
5.3.2 Longitudinal Movement 128
5.3.3 Horizontal Transverse Movement 129
5.3.4 Vertical Transverse Movement, Upward Direction 131
5.3.5 Vertical Transverse Movement, Downward Direction 131
5.3.6 Variable Properties for Normal/ Reverse Fault 132

6 Response of Buried Continuous Pipelines to Longitudinal PGD 133

6.1 Elastic Pipe Model 134
6.2 Inelastic Pipe Model 139
6.2.1 Wrinkling 142
6.2.2 Tensile Failure 144
6.3 Influence of Expansion Joints 145
6.4 Influence of an Elbow or Bend 148

7 Response of Buried Continuous Pipelines to Transverse PGD 155
7.1 Idealization of PGD Patterns 157
7.2 Onshore Pipe Subjected to Spatially Distributed PGD 159
7.2.1 Finite Element Methods 159
7.2.2 Analytical Methods 172
7.2.3 Comparison Among Approaches 178
7.2.4 Expected Response 180
7.2.5 Comparison with Onshore Case Histories 182
7.3 Onshore Pipelines in Liquefied Soil 183
7.3.1 Horizontal Movement 183
7.3.2 Vertical Movement 184
7.4 Onshore Pipe Subject to Abrupt PGD 189
7.5 Offshore Pipelines 191

8 Response of Buried Continuous Pipelines to Faulting 195
8.1 Pipe Damage Observations 196
8.2 Strike Slip Fault – Nominal Tension 199
8.2.1 Centrifuge Tests – Nominal Tension 199
8.2.2 Analytical Models – Nominal Tension 201
8.2.3 Finite Element Models 209
8.2.4 Comparison Among Approaches 211
8.3 Strike-Slip Fault – Nominal Compression 213
8.4 Normal and Reverse Faults 216
8.5 Comparison with Case Histories 217

9 Response of Segmented Pipelines to PGD 221
9.1 Longitudinal PGD 222
9.1.1 Distributed Deformation 222
9.1.2 Abrupt Deformation 224
9.2 Transverse PGD 226
9.2.1 Spatially Distributed PGD 226
9.3 Fault Offsets 229

10 Response of Buried Continuous Pipelines to Wave Propagation **239**
10.1 Straight Continuous Pipelines 239
10.1.1 Newmark's Approach 240
10.1.2 Sakurai and Takahashi Approach 241
10.1.3 Shinozuka and Koike Approach 242
10.1.4 M. O'Rourke and El Hmadi Approach 243
10.1.5 Comparison Among Approaches 248
10.1.6 Case Histories of Wave Propagation Damage to Continuous Pipe 249
10.1.6.1 1985 Michoacan Earthquake 249
10.1.6.2 1994 Northridge Earthquake 251
10.2 Behavior at Treatment Plants 254
10.3 Bends and Tees 257
10.3.1 Shah and Chu's Approach 257
10.3.2 Shinozuka and Koike's Approach 260
10.3.3 Finite Element Approach 261
10.3.4 Comparison Among Approaches 262
10.3.5 Generalized Behavior at an Elbow 263

11 Response of Segmented Pipelines to Wave Propagation **265**
11.1 Straight Pipelines/Tension 265
11.2 Straight Pipelines/Compression 272
11.3 Elbows and Connections 276
11.4 Comparison Among Approaches 279

12 Seismic Fragility Relations for Buried Pipe **281**
12.1 Wave Propagation Relations 282
12.2 PGD Relations 285
12.3 Ground Strain Relation 286
12.4 Influence of Modifying Factors 292
12.5 System Performance 294

13 Countermeasures to Mitigate Seismic Damage **297**
13.1 Routing and Rerouting 297
13.2 Optimal Orientation in the Horizontal Plane 298
13.3 Optimal Location in the Vertical Direction 301
13.4 Ground Remediation 302
13.5 Stronger Pipe 303
13.6 Load Reduction 304

13.7 Flexible Material, Slip and Ball Joints........ 305
13.8 Anchor Points and Soft Joint Springs........ 309

14 Design Examples........ 315
14.1 Retrofit: Water Pipeline Crossing Lateral Spread Zone........ 315
14.2 Risk Assessment: Water Supply Network Subject to Wave Propagation........ 321
14.3 Orientation for Offshore Pipeline in Mississippi River Delta........ 327

References........ 333
Author Index........ 349
Contributors........ 355

Abbreviations

AC	Asbestos Cement
ALA	American Lifeline Alliance
API	American Petroleum Institute
ASCE	American Society of Civil Engineers
ATC	Applied Technology Council
AWSS	Auxiliary Water Supply System
AWWA	American Water Works Association
BEF	Beam on Elastic Foundation model
CC	Concrete Cylinder pipe
CI	Cast Iron pipe
Conc	Concrete pipe
CPT	Cone Penetration Test
CSA	Canadian Standards Association
DI	Ductile Iron pipe
EBMUD	East Bay Municipal Utility District
ECP	Prestressed Embedded Cylinder pipe
EP	Expanded Polystyrene
FE	Finite Element
FF	Free Face
FS	Factor of Safety
GS	Ground Slope
HAZ	Heat Affected Zone
HDPE	High-Density Polyethylene pipe
L-waves	Love waves
LADWP	Los Angeles Department of Water and Power
LCP	Prestressed Lined Cylinder pipe
LSI	Liquefaction Severity Index

MMI	Modified Mercalli Intensity
MRD	Mississippi River Delta
NGA	Next Generation of Ground Motion Attenuation Models
NIBS	National Institute of Building Sciences
OTC	Offshore Technology Conference
P-waves	Compressional waves
PE	Polyethylene pipe
PGA	Peak Ground Acceleration
PGD	Permanent Ground Deformation
PGV	Peak Ground Velocity
PRCI	Pipeline Research Council International
PSHA	Probabilistic Seismic Hazard Analysis
PVC	Polyvinyl Chloride pipe
R-waves	Rayleigh waves
RCC	Reinforced Concrete Cylinder Pipe
R.O.	Ramberg-Osgood
RR	Repair Rate
S-waves	Shear waves
SCWD	Seismic City Water District
SPT	Standard Penetration Test
TCLEE	Technical Council on Lifeline Earthquake Engineering
USGS	United States Geological Survey
USDoT	United States Department of Transportation
WS	Welded Steel
WSAWJ	Welded Steel Arc-Welded Joint
WSCJ	Welded Steel Caulked Joint
WSJ	Welded Slip Joint
WSGWJ	Welded Steel Gas-Welded Joint

Notations

A	cross-section area of pipe
$a(t)$	ground acceleration as a function of time
a_c	critical acceleration (gal)
A_{core}	area of concrete core
A_{max}	maximum ground acceleration
a_{max}	maximum ground acceleration (gal)
a	plasticity reduction factor
B	contact width of offshore pipe with seabed
b_{eff}	effective ligament length (mm)
C	phase velocity of seismic wave
C_a	adhesive strength at lead-caulked joint
C_{eff}	effective phase velocity
C_H	shear wave velocity of a half space
C_L	shear wave velocity of uniform soil layer
C_{max}	maximum compression force in pipe
C_{ph}	phase velocity of R-wave
C_R	propagation velocity of R-wave
C_s	apparent propagation velocity of S-wave with respect to ground surface or shear wave velocity of soil
C_1, C_2, C_3	shear wave velocity of layer or half space
c	local buckling imperfection factor
D	pipe diameter
$D_{A'}, D_B$	peak ground displacements
$D50_{15}$	mean grain size in T_{15} (mm)
d_l	depth of lead caulking
D_{max}	permanent ground displacement (cm)
D_N	Newmark displacement (cm)
d_p	embedment depth for bell and spigot joint
D_r	relative density of soil
d_w	depth to water table (ft)
E	modulus of elasticity
E_s	secant modulus of elasticity
E_t	tangent modulus of elasticity

e_c	eccentricity at welded slip joint
E_i	initial Young's modulus
E_p	modulus of pipe after yield
F_a	axial force in pipe due to restrained joints
F	axial force in pipe, or transverse force on pipe per unit length
f	frequency in Hz
F_i	axial force at the ith joint
F_c	axial force in pipe at toe of PGD zone
F_{cr}	compressive failure force at joint
F_L	liquefaction intensity factor
F_{15}	average fines contents in T_{15} (%)
F_R	axial force at joint R
F_S	axial force at joint S
F_P	force at pin connection
F_{exx}	weld metal strength
F_{max}	maximum force per unit length at soil-pipe interface
F_s	joint slippage force
F_u	joint ultimate axial force
F_y	pipe yield stress
g	acceleration due to Earth's gravity
g_p	gap at welded slip joint
G, G_s	shear modulus of soil
H_A, H_B	thickness of layer
H	depth to center-line of pipeline
H_1	thickness of saturated sand layer (m) or thickness of layer
H_2	height of embankment (m), or thickness of layer
H_c	depth to top of pipe
H_{cr}	critical depth of cover
H_s	thickness of uniform soil layer
I_a	Arias intensity (m/sec)
I_p, I	moment of inertia
k	friction reduction factor, ratio of joint eccentricity to wall thickness
k_o	coefficient of lateral soil pressure at rest
K	spring stiffness
K_1	equivalent soil spring stiffness for PGD zone
K_2	equivalent soil spring stiffness beyond the PGD zone
K_c	bearing capacity factor for undrained soil
K_g	soil stiffness per unit length
K_j	axial stiffness at a joint
K_{post}	joint stiffness after slippage
K_{pre}	joint stiffness prior to slippage
K_m	correction factor for moment magnitude

K_w	correction factor for water table depth
k_p	soil lateral pressure coefficient for passive condition
k_a	soil lateral pressure coefficient for active condition
L	length of PGD zone in direction of ground movement
L'	effective slippage length at bend
L_O	pipe segment length, or distance from elbow to margin of PGD zone
L_a	effective unanchored length
L_{AB}	horizontal projection of inclined rock surface
L_c	horizontal projection of curved portion of pipe
L_{cr}	critical length of PGD zone
L_e	pipe length in which elastic strain develops
L_{em}	embedment length needed to develop equivalent ground strain α
L_l	length of pipe leg
L_p	pipe length in which plastic strain develops, or length along pipe
L_s	separation distance between two stations
l_t, l_c	lengths along pipe
L_d	pipe development length
l	length of curved portion of bell joint
L_1	distance from compression margin of PGD zone to point of zero pipe axial stress
L_A	distance from margin of transverse PGD zone to pipeline anchor point
L_3	distance along pipe
L_1, L_2	distance from head or toe of PGD zone to location of expansion joint
l_1, l_2	distance along pipe segment
M	bending moment, or earthquake magnitude
M_{max}	maximum bending moment
M_w	earthquake moment magnitude
n	number of restrained joints, Ramberg-Osgood parameter, or parameter of transverse PGD distribution
N	standard penetration test value
N_c	bearing capacity factor for horizontal strip footings for clay
N_{ch}	horizontal bearing capacity factor for clay
N_{cv}	vertical uplift factor for clay
$(N_l)_{60}$	corrected SPT N-value

N_q	bearing capacity factor for horizontal strip footings on sand
N_{qh}	horizontal bearing capacity factor for sand
N_{qv}	vertical uplift factor for sand
N_y	bearing capacity factor for downward loading sand
P, P_i, p	internal pressure (operating pressure) in pipe
p_u	maximum soil resistance in horizontal transverse direction
P_{uplift}	uplift (buoyancy) force per unit length on pipe in liquefied zone
P_{ml}	map unit reduction factor
P_e	external pressure on pipe
p_y	internal pressure for hoop stress equal σ_y
P_s	tensile force in joint at slippage
P_u	ultimate tensile force in joint
P_{u1}	lateral force per unit length in PGD zone
P_{u2}	lateral force per unit length beyond PGD zone
PGV	peak ground velocity
PGA	peak ground acceleration
PGD	permanent ground deformation
q	factor quantifying degree of slippage
q_u	maximum resistance in vertical transverse direction
Q	$\frac{3}{16}\ \frac{\lambda K_g}{AE\zeta}$
R	source distance (km), pipe radius, or run-out distance
r	Ramberg-Osgood parameter
r'	parameter of PGD distribution
R_c	radius of curvature of pipe
R_f	reduction factor
R^*	adjusted distance parameter (km)
R_o	distance parameter (km), or pipe radius
R_f	reduction factor for pipe displacement
R_e	Reynolds number ($\gamma VD/\eta$)
R_s	closest distance to seismogenic rupture, or hypocentral distance
RR	repair rate (repairs/km)
RR_R	repair rate for R-waves (repairs/km)
RR_s	repair rate for S-waves (repairs/km)
s	normalized distance across transverse PGD zone
S	ground slopes (%), or shear in pipe

S_1	axial force acted on bent for Leg 1
s_m	normalized distance from margin of PGD zone to location of peak transverse ground displacement
S_u	undrained shear strength of soil
t	pipe wall thickness
T	shaking period, or axial tension in pipe
T_{max}	maximum tension force in pipe
T_{15}	thickness of saturated cohesionless soils with corrected SPT value less than 15 (m)
t_u	maximum longitudinal force per unit length at soil-pipe interface
t_w	nominal fillet weld size
T_o	peak axial force in pipe subject to transverse PGD
u	ground motion
u^u_j	joint displacement leakage threshold
u_g	ground displacement in longitudinal direction
u_p	displacement of pipeline in longitudinal direction
V	velocity for pipe moving in liquefied soil
V_{max}	peak horizontal ground velocity, peak particle velocity in radial direction
V_s	shear wave velocity
W	width of PGD zone perpendicular to direction of ground movement
w_s	submerged pipe weight per unit length
W_2	distance beyond margin of transverse PGD zone where pipe transverse displacement is non-zero
W_1	half width of PGD zone perpendicular to direction of ground movement
W_{cr}	critical width of liquefied zone
W_s	distance between pipe supports
x	non-normalized distance from the margin of the PGD zone
x_u	maximum elastic relative displacement in longitudinal direction
Y	free face ratio (%)
y	lateral displacement of soil
y_1	transverse pipe displacement in PGD zone
y_2	transverse pipe displacement outside PGD zone
y_u	maximum elastic relative displacement in horizontal transverse direction
z	pipe embedment into seabed

z_u maximum elastic relative displacement in vertical transverse direction

α inclined angle of slope, adhesion coefficient for clay, equivalent ground strain, or relative rotation at a joint

α_{gw} girth weld factor

α_h ratio of yield to tensile strength

α_n ratio of hoop stress to yield stress

χ $\frac{n}{1+r}\left(\frac{T_o}{A\sigma_y}\right)$

β intersection angle between pipe and fault trace, ratio of pipe to spring stiffness, or wedge angle

β_c, β_o conversion factors

$\beta_{optimal}$ optimal orientation of pipeline

β_p pipe burial parameter

β^2 $\sqrt{K_g/AE}$

γ total unit weight, angle of attack, or density of liquefied soil

γ_{cr} critical shear strain

γ_o maximum shear strain at pipe-soil interface

$\gamma_{contents}$ unit weight of pipe content

γ_{pipe} unit weight of pipe

γ_{soil} unit weight of soil

$\bar{\gamma}$ effective unit weight of soil

γ_s incidence angle of S-wave with respect to vertical

δ permanent displacement of ground or pipe

δ_c pipe displacement at toe of PGD zone

δ_{cr} critical displacement of ground or pipe

$\delta_{cr\text{-}axial}$ critical displacement-axial

$\delta_{cr\text{-}bending}$ critical displacement-bending

δ_a axial component of fault displacement, or pullout capacity

δ_l transverse component of fault displacement, or lateral capacity

δ_f average fault displacement (cm)

δ_{gs} ground settlement (cm)

δ_h horizontal fault displacement

δ_p peak pipe displacement

δ_T total transverse displacement

δ' imposed pipe displacement

δ_1 maximum transverse pipe displacement within margin of PGD zone, pipe displacement between Point A and elbow

δ_2 transverse pipe displacement at margin of PGD zone

δ_v vertical fault displacement

δ_{max} peak pipe displacement, maximum uplift displacement

Δ radial offset fabrication tolerance

Δ' relative joint displacement for restraint

Δ_1 lateral displacement of Leg 2

Δ_2 axial deformation of Leg 1

$\Delta\epsilon_{cr}$ change in critical buckling strain

Δ_g ground deformation

Δ_{inward} inward movement of pipe at margin of transverse PGD zone

ΔL total elongation of pipe

ΔL_1, ΔL_2 change in arc length

Δ_p displacement parallel to pipe

Δ_s relative joint displacement at slippage

Δ_u ultimate relative joint displacement

Δ_w pipe movement of tank wall

Δu relative displacement at joint

Δu_{avg} average relative displacement at joint

ΔU_R relative displacement at joint R

Δu_{ult} relative displacement for joint closure

Δx_r joint opening due to joint rotation

Δx_t joint opening due to joint extension

Δx total maximum opening at one side of a joint due to transverse PGD

$\Delta \bar{x}$ mean joint displacement

$\Delta\theta$ relative rotation at pipe joint

$\epsilon_{elastic}$ total (axial plus flexural) strain in pipe

ϵ_{cr} critical local buckling strain

ϵ_{rr} peak ground strain

ε engineering strain

$\bar{\varepsilon}$ average pipe strain

ε_a maximum pipe axial strain

ε_{allow} allowable pipe strain

ε_b pipe bending strain

ε_b^{I} bending strain due to moment

ε_b^{II} bending strain due to "curvature"

ε_g ground strain

ε_p pipe axial strain

ε_s slip strain

ε_{peak} peak pipe strain

ε_{body} ground strain due to body waves

$\varepsilon_{surface}$	ground strain due to surface waves
ε_y	yield strain
ε_{max}	maximum ground strain, peak pipe strain
ζ,ξ	$\sqrt[4]{(K_g/4EI)}$
η	coefficient of viscosity of liquefied soil
κ_g	maximum ground curvature
λ	wavelength
μ	friction coefficient, or coefficient of variation
ν_H	Poisson's ratio of half space
ν_L	Poisson's ratio of layer
ρ	density of pipe material
σ	axial tensile stress
σ_{comp}	compressive strength of concrete
σ_{cr}	critical compressive stress for local buckling
σ_v	total overburden pressure
σ'_v	effective overburden pressure
σ_y	apparent yield stress
σ_h	hoop stress
$\sigma_{0.7}$	actual stress for $E_s = 0.7E$
$\sigma_{initial}$	initial compressive stress in pipe
τ	parameter of PGD distribution
τ_s	shear force at pipe-soil interface
ϕ	angle of shear resistance of sand
θ	$\cos^{-1}(1-\frac{2z}{D})$

1

Earthquake and Pipeline Fundamentals

As the title suggests, this monograph concerns itself with the behavior and design of buried onshore and offshore pipelines subject to earthquakes. In this first chapter, basic concepts and terminology related to both earthquakes and pipelines are introduced. This is followed by a brief overview of the content in each of the following chapters.

1.1 Earthquake Fundamentals

Earthquakes have been with us for a very long time. Ancient peoples developed various theories to explain these large ground movements. For example, the ancient Japanese thought that earthquakes were caused by the thrashing of a giant catfish that lived in mud beneath the earth. The modern explanation for seismic activity is the Plate Tectonics theory. It postulates that the earth's surface is composed of seven or eight major plates and a larger number of minor plates. Earthquake faults are the boundaries between the individual plates. For instance, the San Andreas Fault system separates the North American Plate to the East from the Pacific Plate to the West. Earthquakes result from the relative movement of one plate with respect to its neighbor. Along the San Andreas Fault, the North American Plate moves towards the South, while the Pacific Plate moves to the North. As will be mentioned shortly, this corresponds to a Transform Plate Boundary.

Plate movement is apparently due to a heat transfer process below the earth's surface. In a simple model of the earth's interior, there is a relatively thin, cool Lithosphere at the surface, a warmer mantle below and a very hot core at the center. The molten mantle material circulates, picking up heat near the core, rises towards the Lithosphere where the heat is released with the mantle material, then descends downward towards the core where the cycle repeats itself. When the rising molten material reaches the Lithosphere and diverges (goes in two opposite horizontal directions), the plates tend to pull apart. Such Divergent Plate Boundaries lead to relatively small "ridge" earthquakes. When two mantle material streams moving in horizontally opposite directions below the Lithosphere converge and head downward, one plate tends to move beneath the other. These Convergent Plate Boundaries lead to relatively large "subduction" earthquakes. The third type is a Transform Plate Boundary, such as the San Andreas, where one plate moves laterally with respect to its neighbor. One expects moderate to large strike-slip earthquakes at such Transform Plate Boundaries.

Movement at the plate boundaries is sporadic, typically with at least decades between significant movements. Forces build over time, eventually fracturing the brittle Lithospheric rock. The sudden fracture and relative movement across the fault rupture surface releases built-up energy and generates seismic waves which propagate away from the fault rupture zone. The passage of these seismic waves causes the ground to shake back and forth. However, the ground shaking is transient: the shaking starts when seismic waves arrive at the site and ends when the waves have passed.

The ground shaking may trigger landslides of marginally stable slopes, liquefaction and lateral spreading of saturated sandy soil, and settlement of the ground surface. However, unlike the ground shaking that triggers these ground movements, these deformations are permanent (i.e., they remain after the seismic shaking has stopped).

There are a number of different measures of earthquake size. Prior to the widespread deployment of instruments, the Modified Mercalli Intensity (MMI) scale was used to characterize earthquake size. The intensity was based upon the earthquake's effects on people, natural features and man-made facilities. As such, it varied from high intensity values close to the earthquake's epicenter to lower values at more distant locations. For example, MMI VIII corresponds to people generally being frightened, and trees being shaken strongly with considerable damage to ordinary substantial buildings. MMI V corresponds to many people awakened with some broken glassware and dishes.

The first instrument-based measure of earthquake size was the Richter Magnitude, now called the Local Magnitude. The Richter

Magnitude is based on the response of a specific instrument located at a specific distance from the event. Although it is widely recognized by the public, the Richter Magnitude has a problem correctly measuring large events. Specifically, the Richter scale has a saturation level at roughly 6.8. That is, irrespective of the actual earthquake size, the Richter Magnitude does not exceed 6.8. In scientific circles, the Moment Magnitude is the most commonly used measure. It is a function of the seismic moment M_o, which in turn is the product of the below grade area that ruptured, the average rupture displacement, and strength of rock that ruptured. As such, it is directly related to the amount of fault movement, the length of the fault rupture and the energy released. For Moment Magnitudes less than about 6.8, the Richter and Moment Magnitudes are the same number.

There are also more specialized engineering measures of earthquake size. These include peak ground acceleration (PGA) and peak ground velocity (PGV). PGA and PGV are usually site specific values. Empirical attenuation relations allow one to estimate the expected PGA and PGV values given earthquake size and source-to-site distance.

The amount of offset at the surface expression of a fault is also of interest for engineering purposes. Fault offsets are typically quantified by either the average or the maximum offset, and are estimated by empirical relations based upon the earthquake Moment Magnitude. The amount of permanent movement due to landslides and lateral spreads is largely controlled by earthquake size, source-to-site distance, ground slope and various detailed soil properties.

In terms of their effects on buried pipelines, the two general classes of seismic hazards are the wave propagation hazard and the permanent ground deformation (PGD) hazard. The wave propagation hazard is transient and corresponds to ground shaking. It results in transient strains in buried pipelines, strains that disappear when the shaking has stopped. The wave propagation hazard occurs in every event and generally leads to low to moderate damage rates for buried pipe (repairs per kilometer of pipe) over wide areas.

The PGD hazard corresponds to permanent offset at a fault, permanent amounts of landslide movement and the like. It results in permanent strains in buried pipe, strains that remain after the shaking has stopped. The PGD hazard does not necessarily occur in every event, but when it does it generally results in moderate to high damage rates for buried pipe (again per kilometer of pipe) in the limited areas where it occurs. Table 1.1 contains brief definitions of seismic terminology used in this monograph.

Table 1.1 Earthquake Terminology

Term	Definition
Apparent Propagation Velocity	Speed of traveling wave with respect to a particular direction different from the wave's actual direction of travel. Alternatively, propagation velocity back calculated from ground strain measurements for waves with incoherence.
Attenuation Relation	Equations for estimating engineering parameters (i.e., PGA and PGV) as functions of earthquake size and site-to-source distance.
Cap Layer	A non-liquefied layer close to the ground surface with liquefied soil below.
Drag Length	In the offshore environment, the plan dimension parallel to the direction of movement of the soil block experiencing a landslide.
Epicenter	Point on earth surface directly above location of initial earthquake rupture.
Epicentral Distance	Horizontal distance along earth surface between earthquake epicenter and site of interest.
Fault	Boundary between plates, and place where earthquakes typically originate.
Focal Depth	Vertical distance from epicenter to below ground point of initial earthquake rupture.
Fault Offset	Relative horizontal and/or vertical movement of one side of the fault with respect to the other side.
Lateral Spread	Nominally horizontal landslide-like movement of the ground, the result of liquefaction of the underlying soil.
Liquefaction	Complex process whereby saturated cohesionless soil loses its shear strength due to increased pore water pressure from ground shaking.
Longitudinal PGD	Permanent Ground Deformation in which the ground movement is parallel to the pipe's longitudinal axis.
Magnitude	A dimensionless number which characterizes the size of an earthquake.
Moment Magnitude	A magnitude based upon the seismic moment.
Normal Fault	Vertical movement along a vertically inclined fault in which the overhanging side (side above the incline) moves downward with respect to the other side.
PGA (Peak Ground Acceleration)	Engineering measure of the amount of shaking (maximum acceleration of ground) at a particular site.
PGV (Peak Ground Velocity)	Engineering measure of the ground shaking (maximum ground velocity) at a particular site.

■ **Table 1.1 Earthquake Terminology (Continued)**

Term	Definition
Particle Velocity	Velocity of a point on the ground surface, its largest value is PGV.
Propagation Velocity	Speed at which a disturbance, such as an earthquake wave, travels through the earth or along the earth surface.
Reverse Fault	Vertical movement along a vertically inclined fault in which the overhanging side (above the incline) moves upward with respect to the other side.
Runout Distance	In the offshore environment, total distance that the sliding block of soil moves from initial location of the head to the final location of the toe.
Strike-Slip Fault	A fault where one side moves horizontally with respect to the other side. Left lateral if other side appears to have moved to the left.
Surface Rupture	Earthquake rupture at depth which reaches the ground surface.
Transverse PGD	Permanent Ground Deformation in which the ground movement is perpendicular to the pipe longitudinal axis.
Transient Ground Strain	Ground shaking induced ground strain; alternatively, local ground strain due to local differences in soil properties.

1.2 Pipeline Fundamentals

Pipelines differ in relation to the fluids they transport: gas, liquid fuels, potable water, sewage, etc. They differ in relation to their material: steel, cast iron, concrete, etc. They also differ in relation to their physical characteristics: diameter, wall thickness, burial depth, etc. However, in terms of seismic behavior and design, the most important difference is in relation to the manner in which they are connected. If the axial and rotational stiffness of the pipeline joint is comparable to that for the pipe section away from the joint, the pipeline is considered to be continuous. Steel pipe with butt-welded girth joints, steel pipe with fillet-welded slip joints (WSJ), steel pipe with bolted flanges, and HDPE pipe with fused joints are examples of continuous pipeline. Although there are differences in the strength of butt-welded, bolted flange and WSJ pipe, they all generally perform better than segmented pipeline when subject to earthquake hazards. Specifically, it is not unusual for continuous pipelines to be damaged by the PGD hazard, but it is unusual when they are damaged by the wave propagation hazard.

The other group is segmented pipelines. For segmented pipeline, the stiffness of the joints is significantly lower than that for the portion away from the joint. Cast iron pipe with lead-caulked joints, ductile iron pipe with push-on rubber gasketed joints, concrete cylinder pipe with rubber gasketed joints covered with exterior cement grout are examples of segmented pipelines. Due to their comparatively low stiffness, segmented pipelines subject, for example, to axial tension will pull-apart at the joints before experiencing a material failure in the pipe section between the joints. As noted above, the seismic performance of segmented pipeline is not as good as that for continuous pipelines. Specifically, it is common that segmented pipelines are damaged by the wave propagation as well as the PGD hazards. Table 1.2 contains brief definitions of pipeline terminology used in this monograph.

Table 1.2 Pipeline Terminology

Term	Definition
Continuous Pipeline	Pipeline having joints with axial and rotational stiffness comparable to that away from the joint.
Segmented Pipeline	Pipeline having joints with axial and rotational stiffness much lower than that away from the joints.
Welded Slip Joints (WSJ)	Joints with interior or exterior fillet welds, connecting the bell end of one segment to the spigot end of another.
Riser	Vertical pipeline in which product travels upward or downward.

1.3 Chapter Summary

Chapters 2 and 3 cover seismic hazards. Specifically, PGD hazards including fault offsets, landslides, lateral spreading and seismic settlements are discussed in Chapter 2. Available empirical and analytical relations for estimating the amount of movement are provided. Finally, limited information on the spatial extent of the lateral spread zone, which is particularly important for buried pipes, is provided.

The wave propagation hazard is covered in Chapter 3. The different types of seismic waves and simplified analytical relations for the resulting ground strains are presented. The importance of incoherence for traveling waves (changes in wave shape along the propagation path) and the resulting effective propagation velocities are introduced. Finally, transient ground strains resulting from local differences in subsurface properties are presented.

Pipe limit states and failure criteria are discussed in Chapter 4. For continuous pipelines, the design tensile and compressive strains recommended by various groups are presented for butt-welded and welded slip joint pipe, as well as for both the PGD and wave propagation hazards. Corresponding limit state recommendations for segmented pipelines, although limited, are also discussed.

Chapter 5 presents current information on the interaction forces at the soil-pipe interface for both onshore and offshore pipelines. Current recommendations are largely empirical as they are based upon laboratory tests. However, as much of the underlying mechanics are provided as possible so that readers have a basis for evaluating empirical results.

The response of continuous pipelines to various types of PGD is covered in Chapters 6 through 8, while Chapter 9 covers segmented pipeline response to the same hazard. Specifically, the response of continuous pipelines to longitudinal PGD is presented in Chapter 6. This is a particularly important problem since even butt-welded pipe is susceptible to damage from longitudinal PGD. The influences of expansion/contraction joints are covered, as well as the fact that the use of such special joints can be beneficial or detrimental depending on circumstances.

Chapter 7 covers the response of continuous pipelines to Transverse PGD. For onshore pipe, the behavior is quite different depending upon whether the PGD is abrupt (ground movement at margins of slide comparable to that near center) or distributed (ground movement at margins of slide much less than that near center). For onshore pipe subject to distributed transverse PGD, the typical displacements are small enough and the widths of the zones are wide enough that resulting pipe strains are relatively small. In the offshore environment, ground movement and the spatial extent of the PGD zone can be quite large, and applicable analytical relations for pipe strain are provided.

The response of continuous pipelines to fault offsets is covered in Chapter 8. Closed form analytical as well as finite element results are presented for the preferred case where the pipe is placed in nominal tension. Centrifuge results are presented, which indicate that strike-slip offsets resulting in nominal tension are preferred to strike-slip offsets resulting in nominal compression. Similarly, the centrifuge results show that normal faulting is preferred over reverse faulting.

Chapter 9 covers the response of segmented pipeline to longitudinal PGD, transverse PGD and fault offsets. It is shown that segmented pipelines would likely survive distributed transverse PGD, but would not be expected to survive abrupt transverse PGD, longitudinal PGD, nor surface faulting.

The responses of continuous and segmented pipelines to the wave propagation hazard are addressed in Chapters 10 and 11, respectively. Specifically, in Chapter 10, simple relations for pipe strain induced in continuous pipelines by wave propagation are presented and explained. Furthermore, two case histories are presented which demonstrate that wave propagation damage to continuous pipelines is possible but not common. Similarly, simple relations for pipe strain when the pipe enters a tank or building are provided. Finally, it is shown, at least for ground strain levels less than 0.1%, that the total strain at an elbow (bending plus some axial) is usually less than that away from the elbow (primarily all axial).

The response of segmented pipelines to the wave propagation hazard is presented in Chapter 11. Simple relations for the expected response at the **average** joint are presented. However, it is shown that the response at a particularly weak or flexible joint (joint most likely to be damaged) is complicated and requires information on the **variation** of joint properties from joint to joint. Computer simulations and experimental observations are presented which provide confirmation of these views.

Chapter 12 presents fragility relations for segmented pipelines. Relations based upon ground strain are shown to provide a much better fit to both wave propagation and PGD-related damage than either the wave propagation alone relations (based upon PGV) or the PGD alone relations (based upon the amount of movement). Finally, recommendations for "acceptable" amounts of damage are converted into acceptable amounts of ground strain for various classes of pipe.

Possible mitigation measures are addressed in Chapter 13. These include routing and rerouting techniques, preferred orientation techniques, hazard reduction through ground remediation, and improved performance through the use of anchor points or soft-springs.

The monograph concludes with three example problems in Chapter 14. The first example is a WSJ pipeline crossing a longitudinal PGD zone for which four retrofit approaches are investigated. The second example involves an estimate of wave propagation damage to a segmented cast iron water pipeline. The preferred orientation for an offshore pipeline crossing a large potential mudslide is covered in the third example.

2

Permanent Ground Deformation Hazards

The principal forms of permanent ground deformation (PGD) are surface faulting, landsliding, seismic settlement and lateral spreading due to soil liquefaction. Pipeline performance, when subjected to PGD, depends in large part on the amount of PGD and the spatial extent of the PGD zone, which will be discussed in detail in this chapter. The aim is to provide a general overview of each of the four forms of permanent ground deformation. Empirical or analytical relations for the amount of PGD are presented, as well as observations of the spatial extent of the PGD zone. When available, values recommended for design are provided.

2.1 Fault

As noted in Chapter 1, earthquakes originate well below the earth surface, along faults in the earth's crust. If the earthquake magnitude is large enough, the offset will propagate all the way to the surface, resulting in a surface rupture or surface expression of the fault offset. Youngs et al. (2003) presents a number of relations for the probability of surface rupture as a function of earthquake magnitude. As shown in Figure 2.1, there is less than a 10% chance of surface rupture for a magnitude 5 event, about a 50% chance for events with magnitudes in the 6 to 6.5 range, and more than a 90% chance for a magnitude 7.5 event.

Often there is some uncertainty as to the exact location of a surface fault, as well as the distribution of the fault offset across the fault zone. For example, in a project involving the Hetch-Hetchy Aqueducts crossing the Hayward Fault in Fremont, California, 85% of the offset was expected to occur in a 10-foot-wide "active creep zone" with the remaining 15% occurring in "subsidiary faulting zones" on either side. The American Lifeline Alliance (ALA) *Design Guidelines for Seismic Resistant Water Pipe-*

line Installations (2005), recommends four separate scenarios in relation to fault offset distribution. They envision a main offset zone (Zone A) and two secondary zones (Zone B), with the width of the zones being established by an engineering geologist. In three of the ALA scenarios, 85% of the total movement occurs as a knife edge at the left-hand edge, right-hand edge or the middle of Zone A. These distinctions are important only if the soil properties, pipe properties or burial depths on one side of the fault are significantly different from those on the other side. In that case, as will be shown later, the worst case location for the fault offset would be closer to the stiff soil, deep burial side.

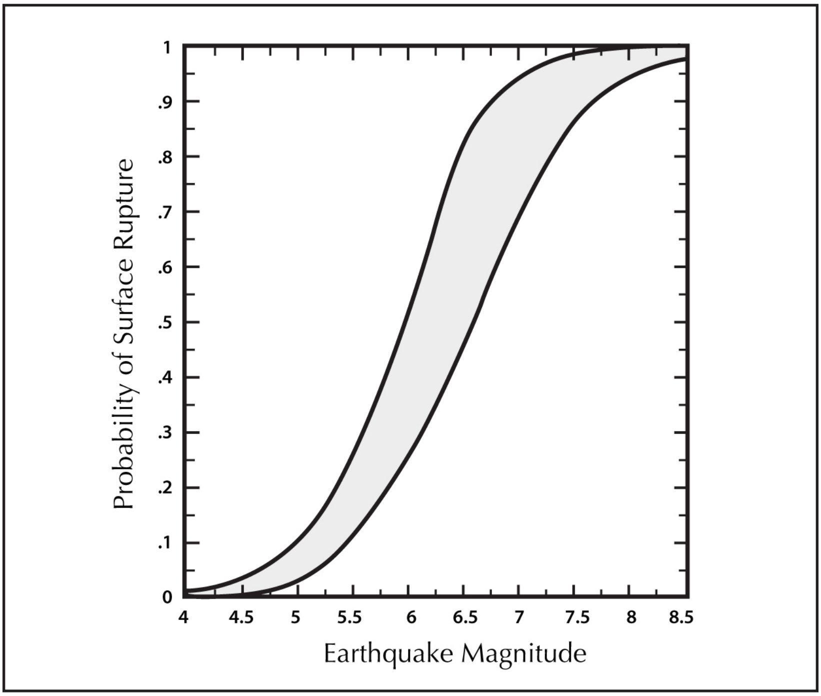

After Youngs et al., 2003

■ **Figure 2.1 Probability of Surface Rupture as a Function of Earthquake Magnitude**

Principal types of fault movement include strike-slip, normal-slip and reverse slip, as shown in Figure 2.2. In a strike-slip fault, the offset is in a horizontal plane, which deforms a continuous pipe primarily in axial tension and bending or axial compression and bending depending on the pipe-fault intersection angle. In normal and reverse faults, the predominant ground displacement is vertical. When the overhanging side of the fault moves downwards, the fault is normal, which deforms a horizontal pipe in axial tension and bending. When the overhanging side of the fault moves upwards, the fault is reverse, which deforms a horizontal pipe in axial compression and bending.

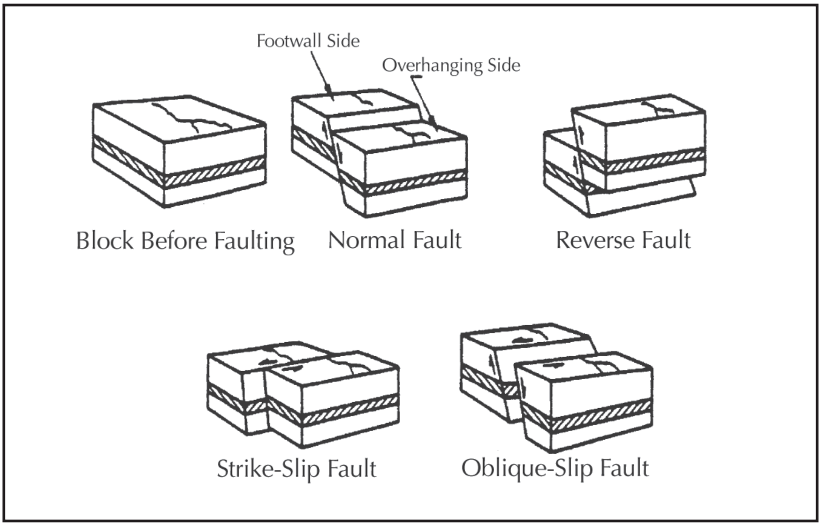

After Meyersohn, 1991

■ **Figure 2.2 Block Diagrams of Surface Faulting**

Various empirical relations between fault displacement and earthquake size have been proposed. The Wells and Coppersmith relations are arguably the most widely recognized and seem to be the relations used most frequently in practice. Wells and Coppersmith (1994) selected 244 earthquakes for analysis from a worldwide database of 421 historical earthquakes. They establish empirical relations between surface rupture length, maximum rupture displacement and average rupture displacement as a function of the earthquake moment magnitude. The relations for the average displacement are:

$$\log \delta_f = -6.32 + 0.90M \textit{ for Strike-Slip Fault} \tag{2.1}$$

$$\log \delta_f = -4.45 + 0.63M \textit{ for Normal Fault} \tag{2.2}$$

$$\log \delta_f = -0.74 + 0.08M \textit{ for Reverse Fault} \tag{2.3}$$

where δ_f is the average fault displacement, in meters, and M is the moment magnitude. The observed fault displacement in the Wells and Coppersmith's database (i.e., moment magnitude ranges from 5.6 to 8.1) varies from 0.05 to 8.0 m for strike-slip faults, 0.08 to 2.1 m for normal faults, and 0.06 to 1.5 m for reverse faults, as shown in Figure 2.3. Note that the single curve (i.e., solid lines) in Figure 2.3(a) is for a combined "all-slip type" model, while the three curves in Figure 2.3(b) are for strike slip, reverse and normal faults, respectively.

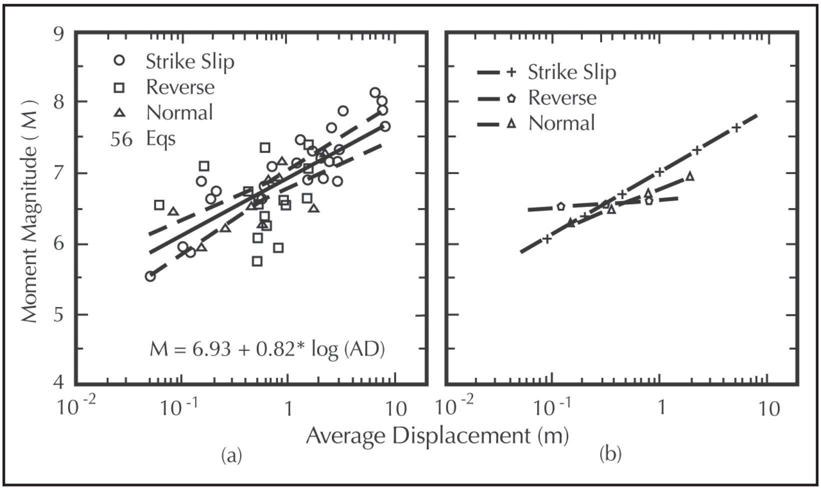

After Wells and Coppersmith, 1994

Figure 2.3 Regression of Average Surface Displacement on Magnitude

If a fault is poorly known or blind (i.e., lack of clear surface expression to judge fault type), the all-slip type regression provided by Wells and Coppersmith can be used to evaluate the expected fault displacement.

$$\log \delta_f = -4.80 + 0.69M \textit{ for all} \quad (2.4)$$

As one might imagine, there is a lot of variability in the offset displacement along the surface rupture length. However, the largest displacement often occurs towards the middle of the surface rupture length and the smallest towards the ends.

For the data analyzed by Wells and Coopersmith (1994), the ratio of the average displacement to the maximum displacement (both along an individual surface rupture) ranged from 0.2 to 0.8. Considering all events, the average displacement was about half the maximum displacement.

In the ALA Guideline (2005), the return period for various pipeline design parameters are given in terms of the so-called Pipe Function Classification. This classification system ranks pipelines in terms of seismic importance, with Class I being pipe with very low seismic importance, Class II being ordinary pipe, Class III being critical pipe that provides service to a large number of customers and Class IV being essential pipe that is intended to remain operational after the event. As noted in the Guideline Commentary, for a community with about 1,000 miles of water pipeline, it is expected that perhaps 5% of the pipe, by mileage, would be Function Class I, 75 to 85% would be Function Class II, 10% or 20% would be Function Class III and only 1 to 5% would be Function Class IV. In general, seismic events with return periods of 475, 975 and 2,475 years are recommended for Pipe Function Classes II, III and IV, respectively. In relation to fault offsets, the ALA Guidelines recommend using the average displacement given in Equations 2.1 through 2.4 for Function Class II and 1.5 and 2 times the average for Classes III and IV, respectively, as shown in Table 2.1. Although not stated explicitly, the average displacement (Class II, ordinary pipe) is presumably calculated with the moment magnitude having a 475-year return period. Because of the ratio of average to maximum fault displacements, the recommended design offset for essential pipe (Class IV) is the maximum displacement for the 475-year event.

In the 2004 *PRCI Guidelines for the Seismic Design and Assessment of Natural Gas and Liquid Hydrocarbon Pipelines* (Honegger and Nyman, 2004) the fault displacement recommended for design is a function of the site location (e.g., environmentally

Table 2.1 2005 ALA Guidelines Recommended PGD Hazards

Pipe Function Classification	Fault Offset	Landslide	Lateral Spread Displacements	Lateral Spread Width, *W*	Lateral Spread Length, *L*
Class II Ordinary	Equation 2.1 through 2.4 (depending on fault type) for 475-Year Event	Equation 2.6 for 475-Year Event	Equation 2.16 for 475-Year Event	900 ft	300 ft
Class III Critical	1.5 × Class II	1.75 × Class II	1.5 × Class II	700 ft	500 ft
Class IV Essential	2.0 × Class II	2.5 × Class II	2.0 × Class II	500 ft	700 ft

sensitive areas) and potential consequences of loss of pressure integrity (e.g., explosion and fire). The recommended fault displacements range from the average value (Equations 2.1 through 2.4) to the maximum value (nominally twice the value in Equations 2.1 through 2.4) for a return period presumably selected by the owner and/or regulators.

2.2 Landslides

Landslides are mass ground movements. Onshore landslides can be triggered by seismic shaking which increases the lateral driving forces, or by wet weather which reduces the soil masses resistance to downslope movements. Offshore landslides can be caused mainly by seismic shaking or by storm waves. Each type is discussed separately below.

2.2.1 Onshore Landslides

A large number of classification systems have been developed for onshore landslides. The most widely used classification system in the United States was devised by Varnes (1978). Varnes identified five principal categories based on soil movements, geometry of the slide and the types of material involved. Varnes's categories are: falls, topples, slides, spreads and flows. Herein, lateral spreading is considered to be a liquefaction-induced phenomenon and is discussed in Section 2.3.

Based on their effects on pipelines, Meyersohn (1991) established three types of landslides, as shown in Figure 2.4. Type I includes rock fall and rock topple, which can cause damage to above-ground pipelines by direct impact of falling rocks. This type of landslide has relatively little effect on buried pipelines and is not discussed in detail herein. Type II includes earth flow and debris flow, in which the transported material behaves as a viscous fluid. Large movements (several meters or more) are often associated with this type of landslide but the expected amount of movement is difficult to predict. Type II landslides are not discussed herein. Type III includes earth slump and earth slide, in which the earth moves more or less as a block. They usually develop along natural slopes, river channels, and embankments. Because

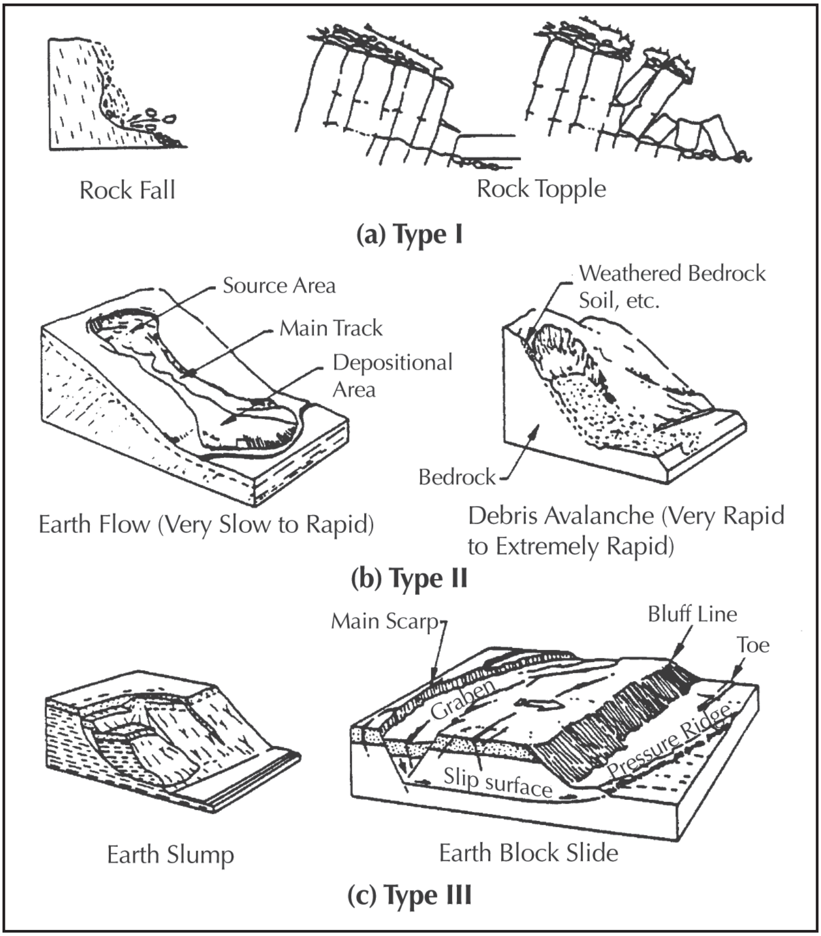

After Meyersohn, 1991

■ **Figure 2.4 Selected Ground Failure Associated with Landsliding**

pipelines often cross such zones, the following will focus on this type of landslide.

Intuitively, the potential for an earthquake-induced onshore landslide is an increasing function of the earthquake size and the slope angle. According to a recent summary by Miles and Keefer (2009), the **minimum** slope angle for "soil slumps and soil block sides" is 5 to 15 degrees. Empirical methods have also been used to determine upper bounds for the occurrence of onshore landslides. Figure 2.5 shows one such relation (Applied Technology Council, 1985), in which the maximum distance of observed landslides to the fault rupture zone is plotted as a function of earthquake magnitude.

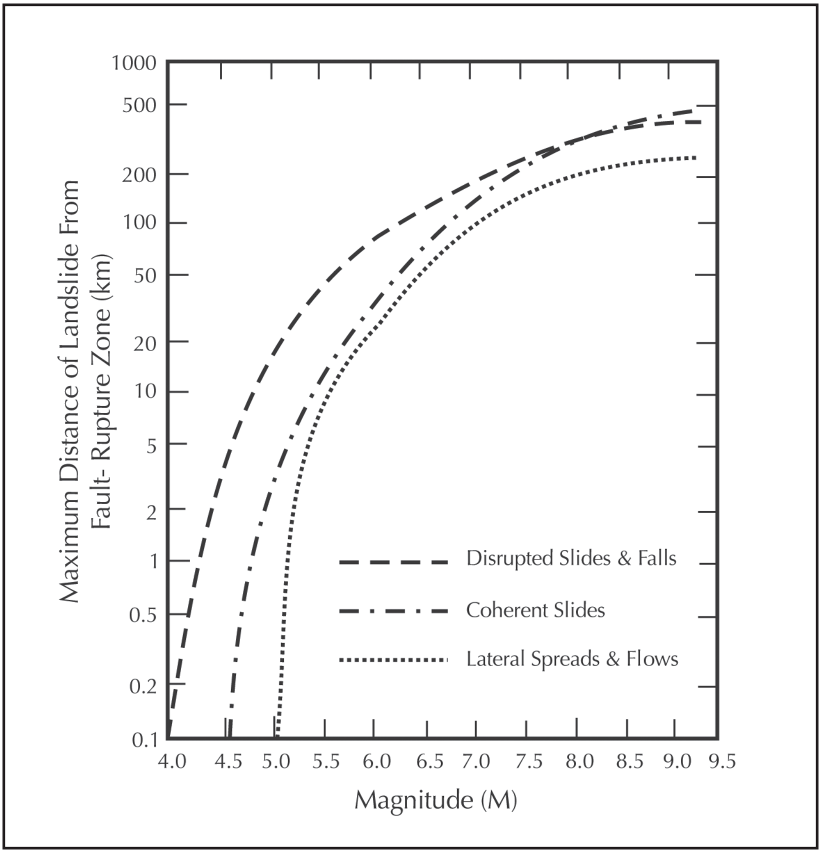

After ATC-13, 1985

■ **Figure 2.5 Occurrence of Landslide vs. Magnitude of Earthquake**

Work by Jibson and Keefer (1993) resulted in analytical estimates of the expected amount of landslide movement. They used the computer program STABL (Siegel, 1978) to search for the critical failure surface by randomly generating slip surfaces and calculating the factor of safety (*FS*). As used herein, the factor of safety is the ratio of the sum of the resisting forces and the sum of the driving forces that tend to cause movement. That is, the critical failure surface is the slip surface with the lowest factor of safety.

Based on Newmark's Block model (Newmark, 1965), the critical acceleration, a_c, can then be defined as:

$$a_c = g\,(FS - 1)\sin\alpha \qquad (2.5)$$

where g is the acceleration due to gravity, α is the inclined angle of the slope and *FS* is the factor of safety. The critical acceleration is a threshold, above which movement of the block is possible. The displacement of the block is then calculated by double integration of the ground accelerations larger than the critical acceleration a_c.

Jibson and Keefer selected 11 strong-motion records to estimate the Newmark displacement. For each of the strong-motion records, they calculated the Newmark displacement for several critical accelerations between 0.02 and 0.4 g, which is considered to be the practical range of interest for most earthquake-induced landslides. The resulting data are plotted in Figure 2.6, for which the best regression function is:

$$\log D_N = 1.460 \log I_a - 6.642\, a_c + 1.546 \tag{2.6}$$

where D_N is the Newmark displacement in centimeters, a_c is the critical acceleration in g's and I_a is the Arias Intensity in *m*/s, defined as:

$$I_a = \frac{\pi}{2g} \int [a(t)]^2 dt \tag{2.7}$$

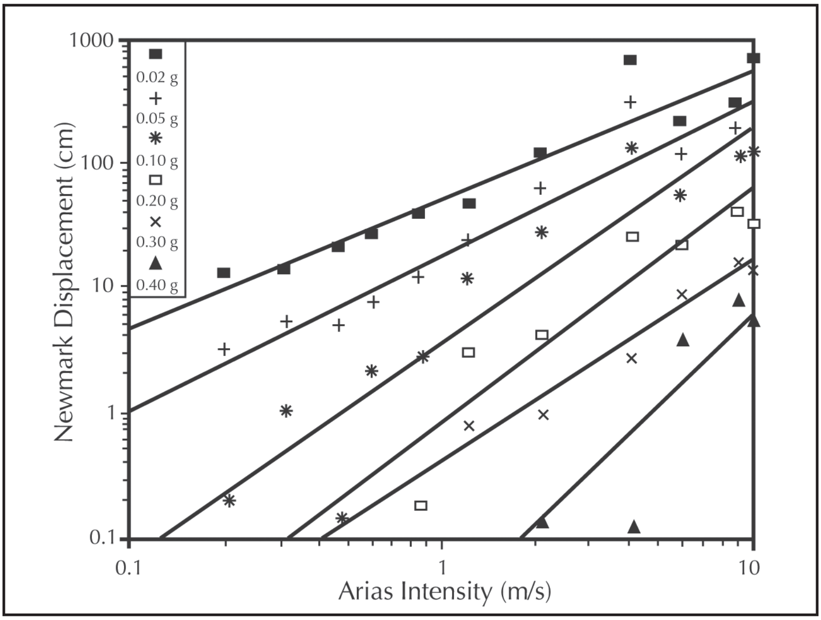

After Jibson and Keefer, 1993

Figure 2.6 Newmark Displacement vs. Arias Intensity for Critical Accelerations of 0.02-0.40 g

where *a(t)* is the ground acceleration time history. As expected, the Newmark displacement is an increasing function of I_a and a decreasing function of threshold critical acceleration.

In this regard, Wilson and Keefer (1983) developed a simple relationship between Arias Intensity, earthquake magnitude, *M*, and source distance, *R*, in kilometers:

$$\log I_a = M - 2\log R - 4.1 \tag{2.8}$$

Note that Equation 2.8 is developed from California earthquakes and may slightly underestimate shaking intensity in the central United States.

In the ALA Guidelines (2005), the landslide displacements recommended for design are given a D_N, 1.75 D_N and 2.5 D_N, respectively, for Pipe Function Class II, III and IV. The displacement D_N is that given in Equation 2.6, presumably for an event with a return period of 475 years. The factors of 1.75 and 2.5 apparently result in design displacements with return periods of 975 and 2,175 years, respectively. The spatial extent of the design landslide is not specified.

2.2.2 Offshore Landslides

As noted above, offshore landslides are caused mainly by earthquake shaking or storm waves, although underwater mud volcanoes and seafloor erosion are occasionally the cause. As one would expect, the locations for seismically induced offshore landslides are in earthquake prone areas. For storm wave-induced landslides, the locations are coastal regions, specifically downstream of river deltas with high sediment loads. Rapid sedimentation in these areas result in very weak seafloor and near seafloor soils. Finally, the permeability of seafloor soils influence the likelihood of landslides. Both seismic waves and storm waves induce dynamic or cyclic loading, which for fine soils can lead to excess pore water pressures and loss of shear strength.

The loading mechanism for earthquake shaking induced offshore slides is essentially the same as for onshore slides, lateral inertia force. The mechanism for storm wave landslides is different. Vertical pressure on the ocean floor is larger under the storm wave crest and lower under the wave trough. When the wave crest is over the head of a potential slide area, and the trough is over the toe, a net moment due to the difference in vertical water pressure exists about the center of the potential slide tending to rotate the slide (both the head and toe moving downslope). Of the two types, storm wave offshore landslides are less common than earthquake-induced offshore landslides based on the 366 slope failures for which the trigger mechanism was reported (Hance, 2003). Given the scope of this monograph, we will concentrate on the later.

Like their onshore counterparts, the ground movement for offshore landslides is downslope. However, the slope for submarine slides is typically much smaller and the run-out distance is typically much larger than that for onshore slides. For example, Hance (2003) studied 534 submarine landslides, of which about 40% were induced by earthquakes and about 30% where induced by rapid sedimentation and storm waves. Figure 2.7 shows the distribution of slope angle for 339 of these events. Note that slope angles between 3 and 4 degrees are the most common. The mean was 5.8 degrees, while the median slope was 4.0 degrees. The minimum slope was just 0.5 degrees. However, it is thought that because of soil liquefaction caused by a strong earthquake, the soil lost essentially all its shear strength in that extreme case.

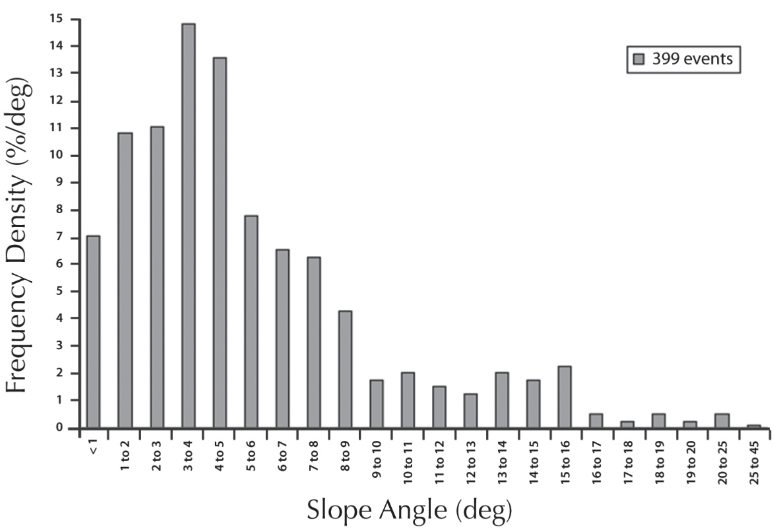

After Hance and Wright, 2003

■ **Figure 2.7 Frequency Distribution for the Average Slope Angle for Submarine Landslides**

The simplified geometry of a submarine slide is sketched in Figure 2.8 showing a volume of soil sliding downslope. The total amount of movement (limit of disturbed seafloor downslope of headscarp) is the run-out distance, *R*. According to Hance, the median run-out distance is 8 km, while the mean is 41 km. As with all the offshore landslide parameters, the mean is substantially larger than the median. This indicates that the distribution is skewed, with a "highside" tail. Figure 2.9 presents the run-out distance as a function of the slope angle, again from Hance (2003). Except for one data point, all the run-out distances are more than 300 m. It is possible that some smaller landslides, with run-out distances less than 300 m, were simply unnoticed. Finally, note that the largest run-out distances are associated with slopes less than 10 degrees. It is possible that a thin layer of water may be trapped under the slide. This may explain the extraordinary large run-out distances for some of the gentle slope conditions.

The median and mean for the slide thickness are 50 m and 141 m, respectively. The two other geometric parameters are the slide area (median = 200 km^2, mean = 3,600 km^2) and slide volume (median = 3.5 km^3, mean = 354 km^3). As will be demonstrated in subsequent chapters, pipeline response is strongly influenced by the length *L* (downslope plan dimension as shown in Figure 2.8) and the width *W* (cross-slope plan dimension). The width can be estimated by dividing the total plan area by the run-out distance, while the length can be estimated by dividing the volume by the product of the thickness and width. Using median values, the estimated median width is 25 km, while the estimated median length is 2.8 km. This estimated median length seems reasonable since it is less than the median run-out distance of 8 km.

As will be explained in more detail in Chapters 6 and 7, the response of a pipeline to a landslide is a function of the orientation of a pipeline to the direction of ground movement. However, irrespective of the orientation, the response is controlled by the smaller of the imposed displacement or the maximum force available at the soil-pipe interface. The imposed displacements for submarine slides are so large that pipeline response is likely controlled by the maximum force available at the soil-pipe interface. Fortunately, as will be disclosed in more detail in Chapter 5, the maximum soil forces for submarine pipeline are substantially lower than those for on-slope pipelines with typical burial depths.

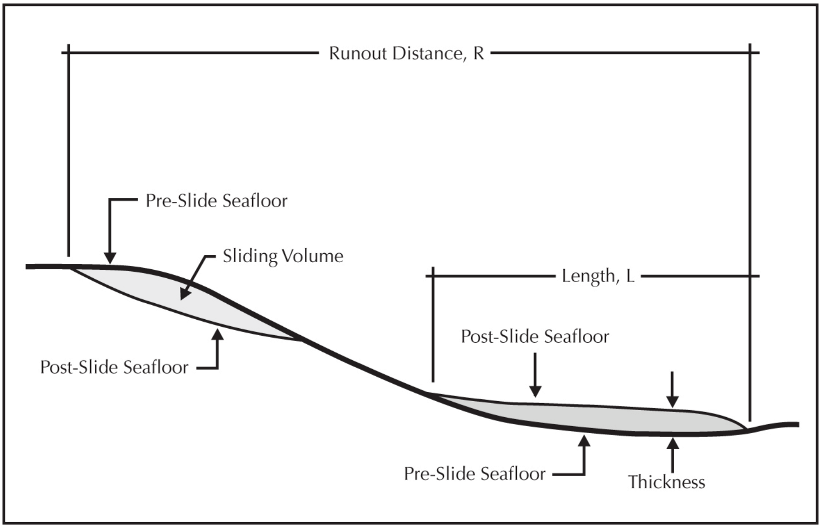

■ Figure 2.8 Simplified Geometry of Submarine Landslide

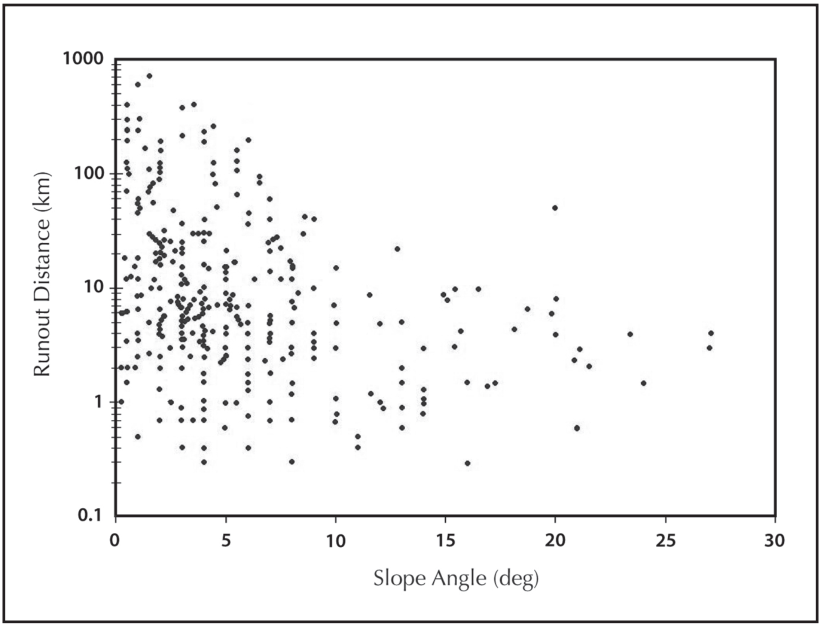

After Hance and Wright, 2003

■ Figure 2.9 Run-out Distance for Submarine Landslides

2.3 Lateral Spreading

Lateral spreads develop when a loose saturated sandy soil deposit liquefies due to seismic shaking. The increase in pore water pressure resulting from the liquefaction process causes non-cohesive soil to lose its shear strength, which in turn results in the flow or lateral movement of soil. Although the ground movement is primarily horizontal, Towhata et al. (1991) observed that vertical soil movement often accompanies liquefaction-induced lateral spreading. However, the vertical component is typically small and will be disregarded herein.

Liquefaction is a complex topic which has been the subject of separate monographs and numerous professional journal papers. For larger projects, a geotechnical engineer will often provide an assessment of the potential for liquefaction and associated movements. There are a number of methodologies for performing such an analysis. For example, based on a 1997 NCEER workshop recommendation, Honegger and Nyman (2004) present procedures that require either SPT (Standard Penetration Test) or CPT (Cone Penetration Test) information.

Along the same lines, the HAZUS Technical Manual (NIBS, 1996) presents a procedure for estimating the probability of liquefaction. In the HAZUS methodology, the potential for liquefaction is a function of the soil liquefaction susceptibility, the peak acceleration at the site and correction factors. As shown in Table 2.2, liquefaction susceptibility category (high, moderate, etc.) is a function of the type of deposit (delta, flood plain, etc.) and the deposit age (Modern, Holocene, etc.). For a given susceptibility category, the probability of liquefaction is a function of the sites' peak horizontal ground acceleration, PGA, the earthquake moment magnitude, M, and the depth to the water table, d_w (ft). For M = 7.5 and d_w = 5 ft, Figure 2.10 presents the probability of liquefaction for various susceptibility groups as a function of PGA. Note there is a 50-50 chance of liquefaction of a high susceptibility category deposit for PGA of about 0.18 g, again for M = 7.5 and d_w = 5 ft. The general relation including correction factors for moment magnitudes other than 7.5, K_m, and depths to the water table other than 5 ft, K_w, is:

$$\text{Prob (liq)} = \frac{\text{Prob (liq for } M = 7.5\ d_w = 5)}{K_m \cdot K_w}\ P_{ml} \qquad (2.9)$$

■ **Table 2.2 Liquefaction Susceptibility Category Utilized in HAZUS**

Type of Deposit	General Distribution of Cohesionless Sediments in Deposits	Likelihood that Cohesionless Sediments when Saturated would be Susceptible to Liquefaction (by Age of Deposit)			
		< 500 yr Modern	Holocene < 11 ka	Pleistocene 11 ka - 2 Ma	Pre-Pleistocene > 2 Ma
(a) Continental Deposits					
River channel	Locally variable	Very High	High	Low	Very Low
Flood plain	Locally variable	High	Moderate	Low	Very Low
Alluvial fan and plain	Widespread	Moderate	Low	Low	Very Low
Marine terraces and plains	Widespread	------	Low	Very Low	Very Low
Delta and fan-delta	Widespread	High	Moderate	Low	Very Low
Lacustrine and playa	Variable	High	Moderate	Low	Very Low
Colluvium	Variable	High	Moderate	Low	Very Low
Talus	Widespread	Low	Low	Very Low	Very Low
Dunes	Widespread	High	Moderate	Low	Very Low
Loess	Variable	High	High	High	Unknown
Glacial till	Variable	Low	Low	Very Low	Very Low
Tuff	Rare	Low	Low	Very Low	Very Low
Tephra	Widespread	High	High	?	?
Residual soils	Rare	Low	Low	Very Low	Very Low
Sebka	Locally variable	High	Moderate	Low	Very Low
(b) Coastal Zone					
Delta	Widespread	Very High	High	Low	Very Low
Esturine	Locally variable	High	Moderate	Low	Very Low
Beach					
High Wave Energy	Widespread	Moderate	Low	Very Low	Very Low
Low Wave Energy	Widespread	High	Moderate	Low	Very Low
Lagoonal	Locally variable	High	Moderate	Low	Very Low
Fore shore	Locally variable	High	Moderate	Low	Very Low
(c) Artificial					
Uncompacted Fill	Variable	Very High	------	------	------
Compacted Fill	Variable	Low	------	------	------

where

$$K_m = 0.0027M^3 - 0.0267M^2 - 0.2055M + 2.9188 \quad (2.10)$$

and

$$K_w = 0.022d_w + 0.93 \quad (2.11)$$

The magnitude correction factor K_m varies from 1.7 for a $M = 4.5$ event down to 0.90 for a $M = 8.5$ event. It accounts for the influence of ground shaking duration—increased potential for liquefaction for increased duration, longer duration for larger magnitude events.

The water table correction factor K_w varies from 1.0 for $d_w = 5$ ft up to 1.6 for $d_w = 30$ ft. It accounts for a decrease in liquefaction potential with an increase in the depth to the water table.

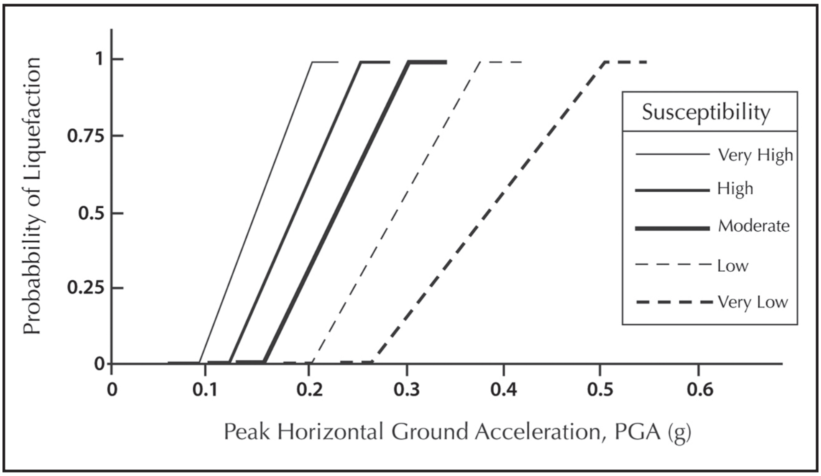

Figure 2.10 Conditional Probability of Liquefaction Used in HAZUS

The final factor in Equation 2.9 is P_{ml}, the map unit factor. As shown in Table 2.3, it varies from 0.25 for deposits in the very high susceptibility category down to 0.02 for deposits in the very low category. It accounts for the fact that liquefaction is taken as having occurred when any portion of a given deposit liquefies. That is, due to variations in relative density and grain size distributions, when "liquefaction occurs" only a comparatively small fraction of soil (same susceptibility category) actually liquefies. The map unit values used in HAZUS (Table 2.3) relied heavily on the judgment of Geomatrix geotechnical engineers. As reported by Wijewickreme et al. (2005), the Terasen (now Fortis BC) Gas project in British Columbia utilized a similar concept. In that case, the map unit factor—percent of mapped susceptible area expected to liquefy—was taken to be 34% for areas within 1 km of the coast or major river channels, and 17% elsewhere.

Table 2.3 Map Unit Reduction Factor, P_{ml} Used in HAZUS

Liquefaction Susceptibility Category	Percentage of Plan Area Expected to Liquefy
Very High	25%
High	20%
Moderate	10%
Low	5%
Very Low	2%

In terms of pipeline response, two situations are possible. In the first case, such as at the Ogata Primary School site during the 1964 Niigata event, the top surface of the liquefied layer is essentially at the ground surface. For this case, a pipeline is subject to horizontal force due to liquefied soil flow over and around the pipeline, as well as uplift or buoyancy forces. In the second case, such as at the Mission Creek site during the 1906 San Francisco event, the top surface of the liquefied layer is located below the bottom of the pipeline. That is, the pipeline is contained in a non-liquefied surface soil layer (Cap Layer) which rides over the liquefied layer. For this second case, the pipeline is subject to horizontal forces due to non-liquefied soil-structure interaction but not subject to buoyancy effects. Pipeline response to such horizontal loading is discussed in Chapters 6 and 7. Pipeline response to buoyancy forces is discussed in Chapter 7.

The direction of movement for the lateral spread is controlled by geometry. When the lateral spread occurs at or near a free face, the movement is generally towards the free face. According to Barlett and Youd (1992), these free face lateral spreads have occurred within 300 m (984 ft) of the free face, with the average distance from the free face being about 100 m (328 ft). When the lateral spread occurs away from a free face, the movement is down the slope of the ground surface or down the slope of the bottom of the liquefied layer, whichever is larger. According to data presented by Bardet et al. (2002), the ground slopes associated with these "away from free face" lateral spreads are typically less than about 1.5%.

The ALA Guidelines (2005) recommend that, for locations within 1,000 ft of a water boundary or on land with an average slope larger than 1%, the ground movement be taken as downslope or towards the water for design purposes. For other locations, ground movement in any direction should be considered.

There are four geometric characteristics of a lateral spread which influence pipeline response in a horizontal plane. With reference to Figure 2.11, these are the amount of PGD movement δ, the transverse width of the PGD zone *W*, the longitudinal length of the PGD zone *L*, and the pattern or distribution of ground movement within the zone.

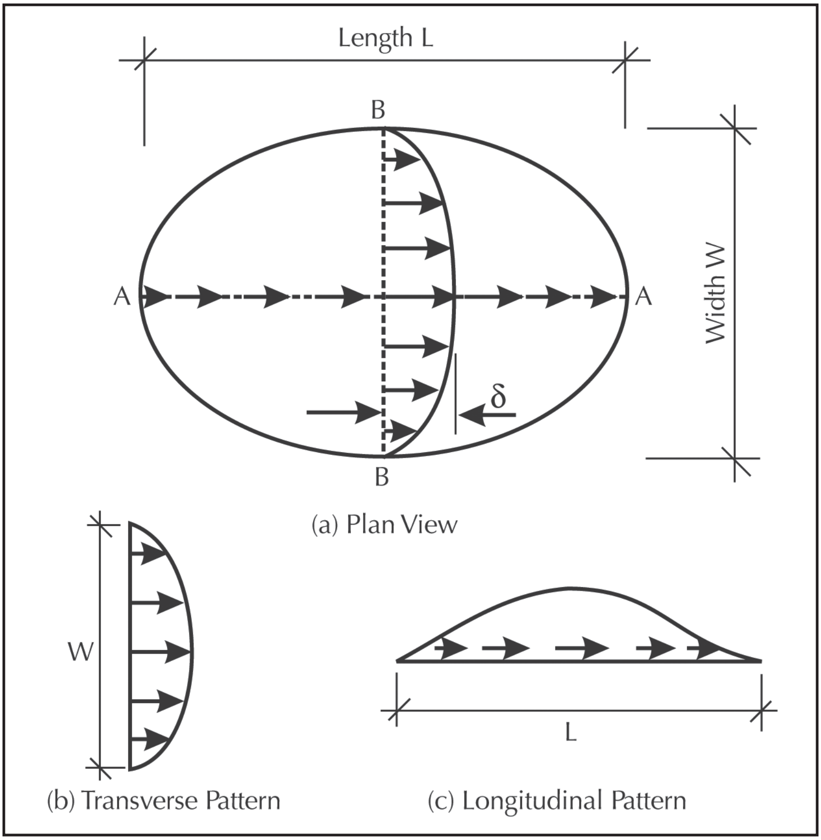

■ **Figure 2.11 Characteristics of Lateral Spreading**

2.3.1 Amount of PGD

The amount of lateral spread movement is one of the parameters that influences pipeline performance. These PGD movements tend to be large. According to data presented by Bardet et al. (2002), the most common displacement for both ground slope (GS) and free face (FF) lateral spreads are typically in the 1 to 2 m range, with the largest observed GS and FF displacements being about 4 m and 10 m, respectively. Predicting the amount of ground displacement due to soil liquefaction is a challenging problem. Nevertheless, there have been a number of studies, both analytical and empirical, which have addressed this issue. These studies are reviewed below.

Analytical and Numerical Models

Dobry and Baziar (1990), and Mabey (1992) estimate liquefaction-induced displacement using a Newmark sliding block analysis. In this analysis, a 1-D rigid soil block model is allowed to displace along a planar failure surface during time intervals when the sum of the inertial (i.e., earthquake) and gravity (i.e., self weight) components along the slide surface exceeds the shear resistance of the soil. Hamada et al. (1987), Towhata et al. (1991), and Yasuda et al. (1991) used 2-D, static elastic models to estimate the amount of lateral spreading displacement. Finally, Orense and Towhata (1992) used a variational principle to develop a 3-D analytical relation for the amount of liquefaction-induced ground displacement. The method is based on the principle of minimum potential energy.

However, as pointed out by Bartlett and Youd (1992), these analytical and numerical models have not been applied to a wide range of earthquake and site conditions. In practice, the empirical relations to be discussed next are more commonly used.

Empirical Models

Several empirical models have been proposed to predict lateral spread displacements. Bardet et al. (2002) presents a summary of the previous work. This includes the Hamada et al. (1986) relation in which the horizontal displacements are given as a function of the thickness of the liquefied layer, and the larger of the ground slope or the slope of the bottom of the liquefied layer. Also included in the Bardet et al. summary is the Youd and Perkins (1987)

Liquefaction Severity Index, in which the displacement is given as a function of epicentral distance and earthquake magnitude.

However, a series of empirical relations developed by Youd and colleagues at Brigham Young University are arguably the most widely recognized and commonly used in practice. The most recent of the Youd relations, Youd et al. (2002), will be presented herein.

Using data from a number of events, Youd et al. (2002) developed two empirical relations for the expected amount of PGD due to liquefaction. The first is for lateral spreads down gentle ground slopes (*GS*) and the other is for lateral spreads at a free face (*FF*).

For gently sloping ground (*GS*) conditions, the relation is:

$$\log \delta = -16.213 + 1.532M - 1.406 \log R^* - 0.012R \\ + 0.338 \log S + 0.540 \log T_{15} + 3.413 \log(100 - F_{15}) \\ - 0.795 \log(D50_{15} + 0.1) \qquad (2.12)$$

For PGD at a free face (*FF*):

$$\log \delta = -16.71 + 1.532M - 1.406 \log R^* - 0.012R \\ + 0.592 \log Y + 0.540 \log T_{15} + 3.413 \log(100 - F_{15}) \\ - 0.795 \log(D50_{15} + 0.1) \qquad (2.13)$$

where δ is the permanent horizontal displacement of ground (m), M is the earthquake magnitude, S is the ground slope (in percent, shown in Figure 2.12(a)), Y is the free face ratio (in percent, shown in Figure 2.12(b)), F_{15} is the average fines contents in T_{15} (%), $D50_{15}$ is the mean grain size in T_{15} (mm) and T_{15} is the thickness (m) of saturated cohesionless soils with a corrected SPT value less than 15. In this most recent Youd relation, R^* is an adjusted distance parameter (km):

$$R^* = R + R_o \qquad (2.14)$$

and

$$R_o = 10 \exp (0.89M - 5.64) \qquad (2.15)$$

where R is the horizontal or mapped distance (km) from the site to the nearest bound of the seismic energy source. For locations with $R < 0.5$ km, Youd recommends a value of 0.5 km.

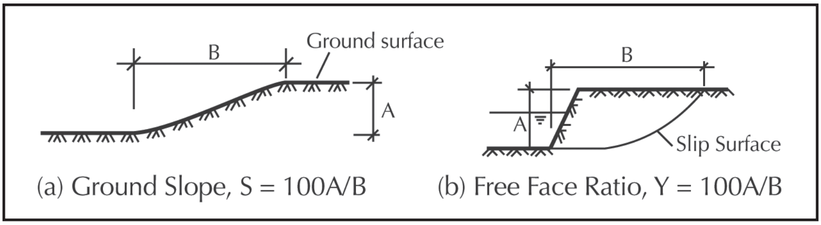

Figure 2.12 Elevation View Showing Ground Slope and Free Face Ratio

In a sense, the Youd relations combine the Hamada relation, in which displacement is a function of the layer thickness and site geometry, with the LSI, in which displacement is a function of earthquake size and distance. Unique aspects of the new Youd relationships are the inclusion of soil characteristics, F_{15} and $D50_{15}$ as well as the distinction between free face and ground slope cases. The overall accuracy of Equations 2.12 and 2.13 is relatively good, in that predicted values are typically within a factor of two of the observed values.

Finally, Bardet et al. (2002) have developed a so-called four parameter empirical relation for lateral spread displacements. Like Youd, the Bardet et al. relations apply to either ground slope or free face conditions. In point of fact, Bardet uses the same parameters as Youd to quantify site geometry. Unlike Youd, the Bardet relations do not consider the soil parameters F_{15} and $D50_{15}$, and as one might expect, the predictive capability of the Bardet relations are not quite as good as that of the Youd relations. However, an advantage of the Bardet relations is that the probability of exceedance and associated confidence intervals can be determined.

Bardet has two relations, one (Data Set A) that considers 467 data points and a second that only considers the 213 data points with displacements less than 2.0 m. The Data Set A relation is:

$$\log(\delta + 0.01) = -7.280 + 1.017\,M - 0.278\log(R) - 0.026\,R + 0.497\log(Y) + 0.454\log(S) + 0.558\cdot\log(T_{15}) \qquad (2.16)$$

where all the parameters are the same as in Equations 2.12 and 2.13 except that R is now simply the epicentral distance.

Since it does not require soil properties, the Bardet relation is easier to apply than the Youd relation. It is possible that this advantage is the reason for it being recommended for estimation of lateral spread displacement in the 2005 ALA Guideline. Specifically, as shown in Table 2.1, the value from Equation 2.16 is to be used for design of ordinary (Function Class II) pipe, while 1.5 and 2.0 times the Bardet value is to be used for critical (Function Class III) and essential (Function Class IV) pipe, respectively.

An alternate for cases where the soil parameters F_{15} and $D50_{15}$ are unknown or difficult to obtain, presumably would be to use representative values in the Youd relations. Based upon figures in Youd et al. (2002), the median for $D50_{15}$ is about 4 mm while the median for F_{15} is about 15%.

2.3.2 Spatial Extent of Lateral Spread Zone

As will be seen later, the width and the length of the PGD zone have a strong influence on pipe response to PGD. Unfortunately, the currently available information on the spatial extent of the lateral spread zone is somewhat limited and largely empirical. One expects that the spatial extent of the lateral spread zone strongly correlates with the plan dimensions of the area that liquefies. However, even if true, this would require information from a number of bore holes to establish the boundary between the liquefied (or likely to liquefy) and non-liquefied (unlikely to liquefy) regions. In the following, both the width W and length L as shown in Figure 2.11 will be discussed.

Information on observed values for the spatial extent of the lateral spread zone has been developed by Suzuki and Masuda (1991). Using data from the 1964 Niigata and 1983 Nihonkai-Chubu earthquakes, they presented scattergrams in Figure 2.13 of the amount of ground movement and spatial extent of the lateral spread zone for PGD apparently away from a free face. Note that most all the observed widths are distributed in the range of about 80 to 600 m (262 to 1,968 ft) and the lateral displacement tends to increase with increasing width. For example, as observed in the 2005 ALA Guidelines, the average amount of displacement is about 0.3% of the width of the zone. The widths of the lateral spread zone recommended for design purposes in the ALA Guideline are functions of the pipe's function class. They also recognize that for a given amount of displacement, smaller values of W result in larger pipe strain. Specifically, the ALA Guidelines recommend a width of 900 ft for Function Class II pipe. This roughly corresponds to the average value in Figure 2.13. Values of 700 and 500 ft, respectively, are recommended for Classes III and IV, as shown in Table 2.1.

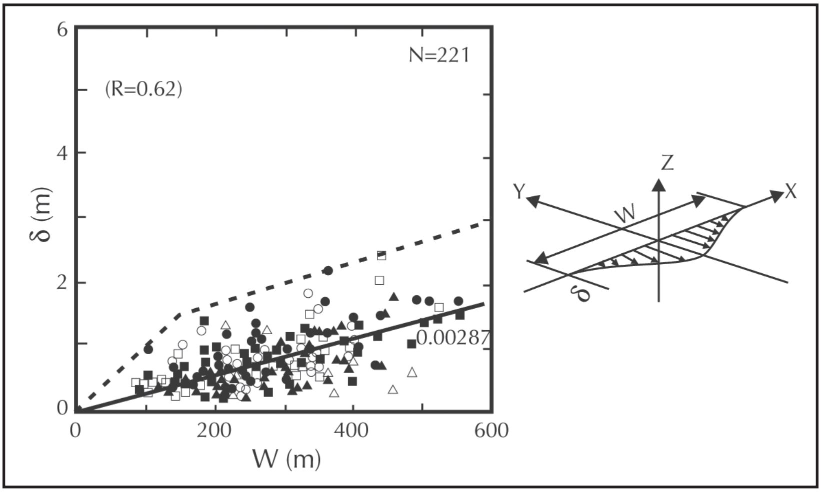

After Suzuki and Masuda, 1991

■ **Figure 2.13 Observed Data on the Amount of PGD and the Width of the Lateral Spread Zone Away From a Free Face**

In terms of the length of the lateral spread zone at a free face, the study by Bartlett and Youd (1992) provides useful information. Figure 2.14 shows observed data on the amount of PGD and the length of the lateral spread zone at a free face. In comparison to the ground slope cases in Figure 2.13, the displacements for the free face cases in Figure 2.14 are larger. On the other hand, the

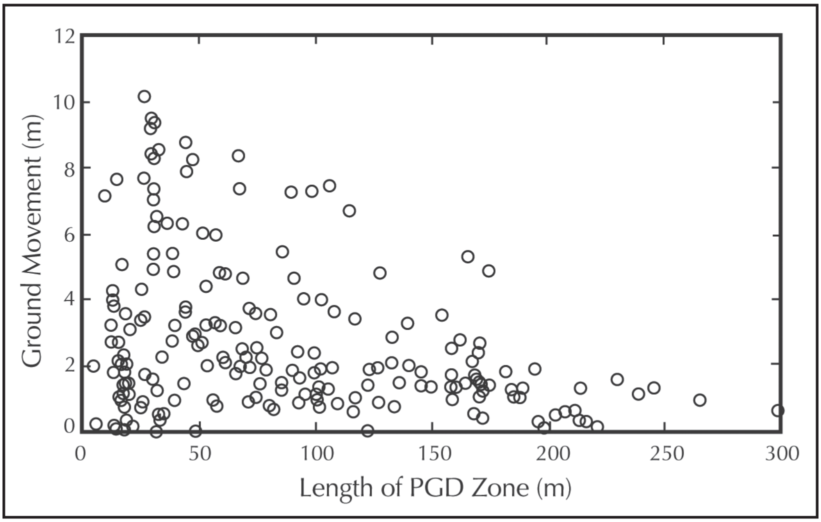

After Bartlett and Youd, 1992

■ **Figure 2.14 Observed Data on the Amount of PGD and the Length of the Lateral Spread Zone at a Free Face** length of the PGD zone, at least for the free face cases in Figure 2.14, are smaller than the widths in Figure 2.13. Although there is a large amount of scatter, the ground displacement appears to be a decreasing function of the length of the lateral spread zone for this free face situation. Using data from Hamada and O'Rourke (1992), Honegger (1994) developed an empirical cumulative distribution function for the length of the lateral spread zone. As shown in Figure 2.15, more than 50% are below 100 m and 95% are below 300 m. For design purposes, the 2005 ALA Guidelines recommend a length of 300 ft for Function Class II pipe. This is close to the median value in Figure 2.15 and appears to be a bit above the average value in Figure 2.14. Recognizing that larger lengths tend to result in higher pipe strain, the ALA Guidelines recommended lengths of 500 ft and 700 ft for pipe Function Classes III and IV, respectively.

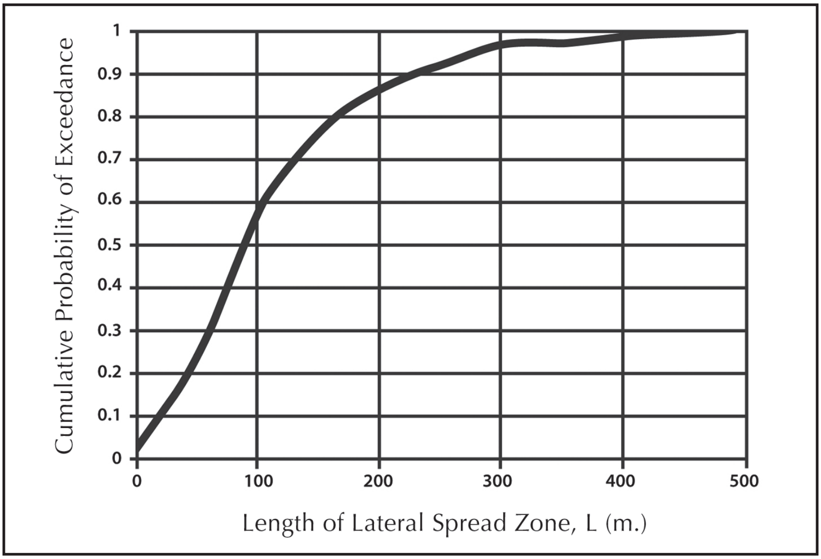

After Honegger, 1994

■ **Figure 2.15 Probability of Exceedance for Length of Lateral Spread Zone**

2.3.3 PGD Pattern

As noted previously, the response of buried pipelines to PGD is influenced by the pattern of deformation; that is, the variation of permanent ground displacement across the width (Figure 2.11(b)) or along the length (Figure 2.11(c)) of the lateral spread zone. The study by Hamada et al. (1986) of liquefaction in the 1964 Niigata earthquake and 1983 Nihonkai-Chubu earthquake provides a wealth of information on observed longitudinal PGD patterns. Figure 2.16 shows longitudinal PGD observed along five of 27 lines in Noshiro City resulting from the 1983 Nihonkai-Chubu earthquake. In this figure, the height of the vertical line is proportional to the observed horizontal PGD at the point.

Note that about 20% of the observed patterns (six out of 27) have the same general shape as Figure 2.16(a). That is, they

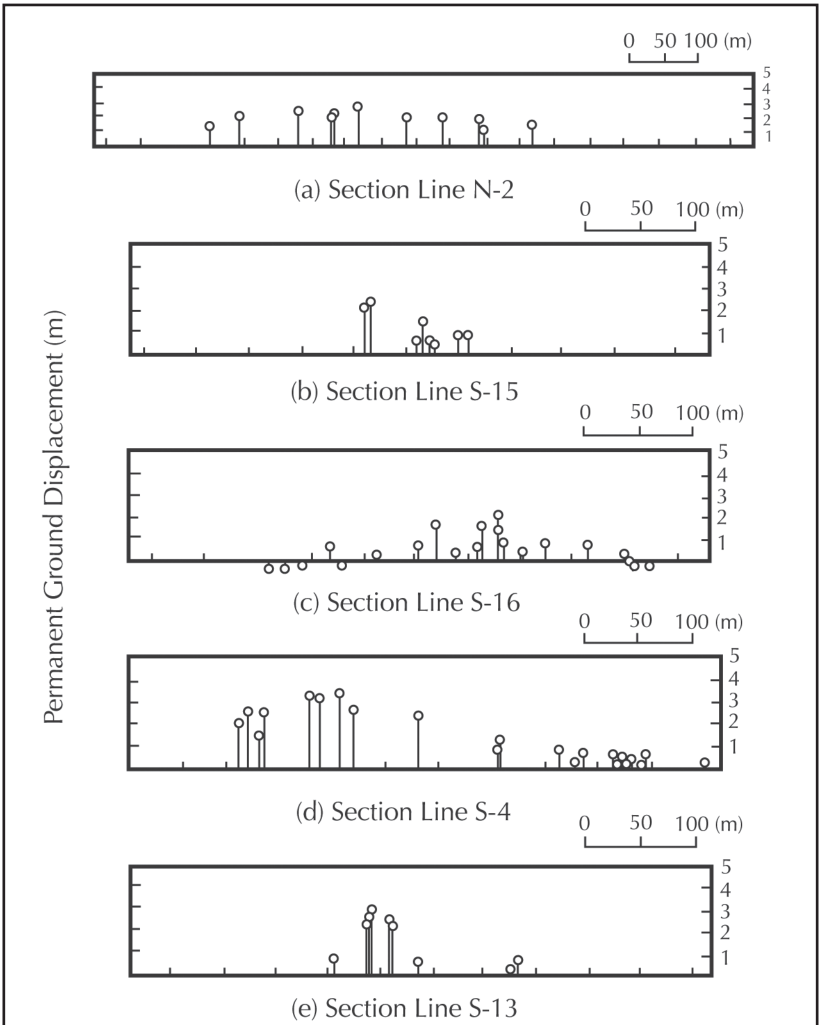

After Hamada et al., 1986

■ **Figure 2.16 Observed Longitudinal Permanent Ground Deformation Patterns** show relatively uniform PGD movement over the whole length of the lateral spread zone. The response of continuous buried pipeline to idealizations of these longitudinal patterns of PGD is discussed in Chapter 6.

Information on transverse patterns of PGD as shown in Figure 2.1(b) is more limited. Figure 2.17 shows four transverse PGD patterns observed in the 1971 San Fernando earthquake. The general lack of information on transverse patterns is unfortunate since the behavior of pipe subject to an abrupt offset at the margins of the PGD zone, such as near Pipeline 4 in Figure 2.17, is substantially different than that when there is little or no offset at the margin, such as near Pipeline 2 in Figure 2.17.

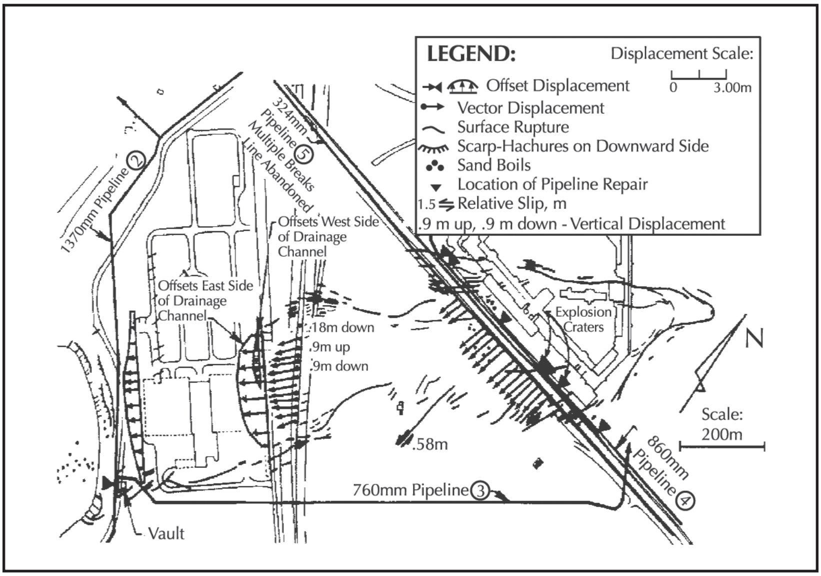

After T. O'Rourke and Tawfik, 1983

■ **Figure 2.17 Observed Transverse PGD Patterns from the 1971 San Fernando Earthquake**

2.4 Seismic Settlement

Earthquake-induced subsidence may be caused by densification of dry sand, consolidation of clay or consolidation of liquefied soil. Among these three types, the liquefaction-induced ground settlement is somewhat more important in that it can lead to larger ground movement and, hence, higher potential for damage to a buried pipeline system. Ground settlement induced by soil liquefaction is discussed briefly below.

According to Honegger et al. (2006), ground settlements from volumetric contraction of liquefied soil may be as much as 10% of the liquefied layer thickness for loose sand, as much as 5% for moderately dense sands and as much as 1% for dense sands. These should be viewed as upper bounds.

An example of observed seismic settlement due to liquefaction is shown in Figure 2.18. This figure presents contours of ground settlement in the Marina District occasioned by the 1989 Loma Prieta earthquake (T. O'Rourke et al., 1991). Note that the maximum ground settlement is about 140 mm (5.5 in). This movement is quite small in comparison to the expected amount of lateral spread deformation discussed previously. Also, the rate of change of displacement is quite small. The largest gradient is along Fillmore, South of Beach. The settlement increases from 20 to 100 mm over a distance of roughly 65 m. This corresponds to a gradient of 0.12%, less than that for the lateral spread data in Figure 2.16. Hence, settlements tend to be small. As observed by Honegger et al. (2006), these relatively small displacements are unlikely to cause damage, particularly to well-constructed welded steel pipe.

There are, however, fairly well established procedures for estimating settlements. For saturated sands without lateral spread movement, Tokimatsu and Seed (1987) developed an analytical procedure to evaluate ground settlement. The volumetric strain for each saturated sandy soil layer, multiplied by the layer thickness, is added up.

T. O'Rourke et al. (1991) used a similar approach to estimate liquefaction-induced settlement in the Marina District. As noted by T. O'Rourke et al., there is good agreement between the esti-

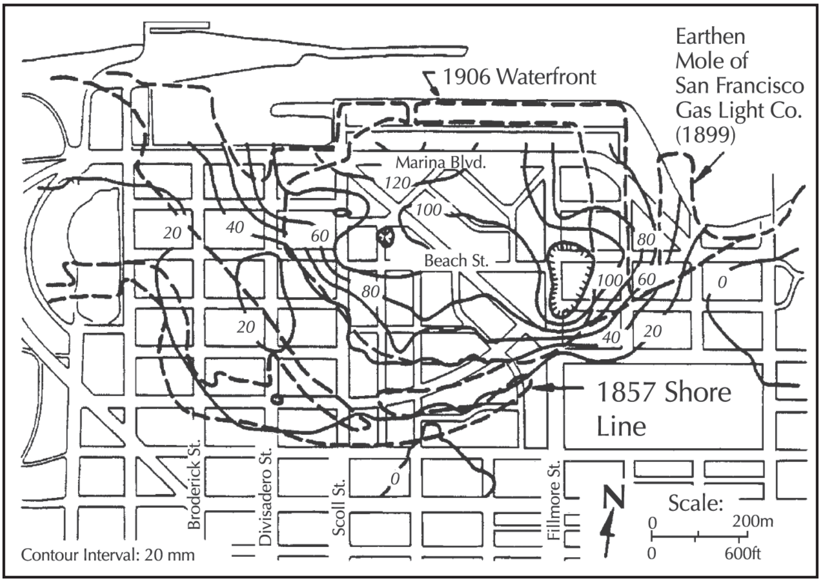

After T. O'Rourke et al., 1991

■ **Figure 2.18 Contour of Ground Settlement in Marina District**

mated and measured settlements for the natural soils and land-tipped fill, but the estimated settlements of the hydraulic fill are almost twice as much as those observed in the field.

Takada and Tanabe (1988) developed two empirical regression equations for liquefaction-induced ground settlement at embankments and plain (level) sites based on 404 observations during five Japanese earthquakes.

For embankments:

$$\delta_{gs} = 0.11H_1H_2a_{max}/N + 20.0 \tag{2.17}$$

For plain sites:

$$\delta_{gs} = 0.30H_1a_{max}/N + 2.0 \tag{2.18}$$

where δ_{gs} is the ground settlement in centimeters, H_1 is the thickness of saturated sand layer (in meters), H_2 is the height of embankment (in meters), N is the SPT N-value in the sandy layer, and a_{max} is the ground acceleration in gals.

3

Wave Propagation Hazard

Transient ground strains due to either wave propagation effects or variable subsurface effects are discussed in this chapter. Wave propagation or traveling wave effects are always present during earthquakes. The wave propagation hazard for a particular site is characterized by the peak ground motion parameters (acceleration and velocity), as well as the appropriate propagation velocity and wavelength. As the name suggests, variable subsurface effects only occur when there are significant differences in the soil profile for two "nearby" sites, such as at the edge of a valley. That is, variable subsurface effects do not occur if the soil profiles are the same along a particular pipeline route.

This chapter briefly reviews attenuation relations for peak ground motion parameters, as well as simplified procedures for determining the apparent propagation velocities and wavelengths for both body and surface waves. The ground strain and curvature due to wave propagation and the resulting upper bound pipe strains are then presented. Finally, transient ground strains due to variable subsurface conditions are discussed. These are transient effects in that they die out when the ground shaking stops. However, they are not due to traveling waves. Rather, they are due to local differences in site response or site amplification. That is, they can be due to differences in ground displacement at "nearby" sites caused by vertically incident waves.

3.1 Wave Propagation Fundamentals

There are two types of seismic waves: body waves and surface waves. The body waves propagate through earth, while the surface waves travel along the ground surface. Body waves are generated by seismic faulting while, for the simplest case, surface waves are generated by the reflection and refraction of body waves at the ground surface. Body waves include pressure waves (P-waves) and shear waves (S-waves). As sketched in Figure 3.1, for pressure waves, the ground or particle motions are parallel to the direction of propagation, which generates alternating compressional and tensile strain. For S-waves, the ground moves perpendicular to the direction of propagation. This results in shear and bending in the plane of wave propagation.

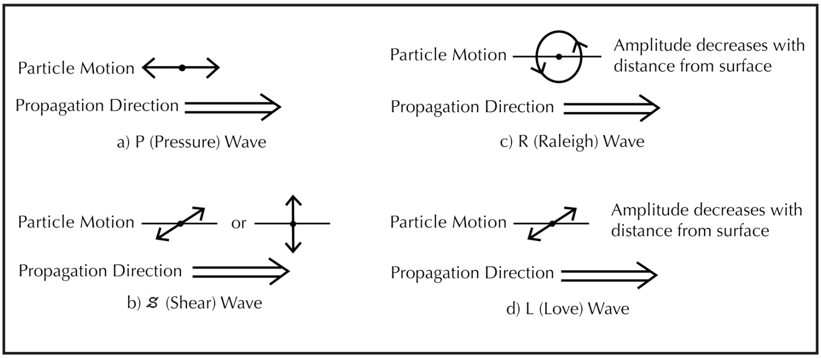

■ **Figure 3.1 Particle Motion for Various Seismic Waves Propagating Left to Right**

The situation for surface waves is somewhat more complex. Rayleigh and Love waves are the two main types of surface waves generated by earthquakes. For Love waves (L-waves), the particle motion is along a horizontal line perpendicular to the direction of propagation, while for R-waves the particle motion traces a retrograde ellipse in a vertical plane with the horizontal component of motion being parallel to the direction of propagation. Hence, L-waves, like S-waves, produce shear and bending in a horizontal plane along the direction of wave propagation. R-waves produce alternating tension and compression in the horizontal direction of propagation, as well as shear and bending in the vertical plane parallel to the direction of propagation. For both L- and R-waves, the amplitude of motions decreases with depth below the ground surface.

Figure 3.2 shows the east-west ground velocity time histories in the hill and lake zones of Mexico City during the 1985 Michoacan earthquake. Notice that in the hill zone record, the peak ground velocity is about 10 cm/sec (Figure 3.2(a)) and the ground motion dies out about 60 sec after initial triggering. In the lake zone record (Figure 3.2(b)), the ground velocity during the first 30 to 40 sec after initial triggering is roughly about 10 cm/sec, similar to the hill zone record. However, the peak ground velocity of 30 or 40 cm/sec occurs roughly a minute or two after initial triggering. This suggests that Rayleigh waves could well have been present in the lake zone record. Note that if R-waves are present, they arrive after the arrival of the direct body waves. That is, P-waves travel fastest and arrive at a site first, followed by S-waves. If surface waves are present, they travel slower and typically arrive after the body waves.

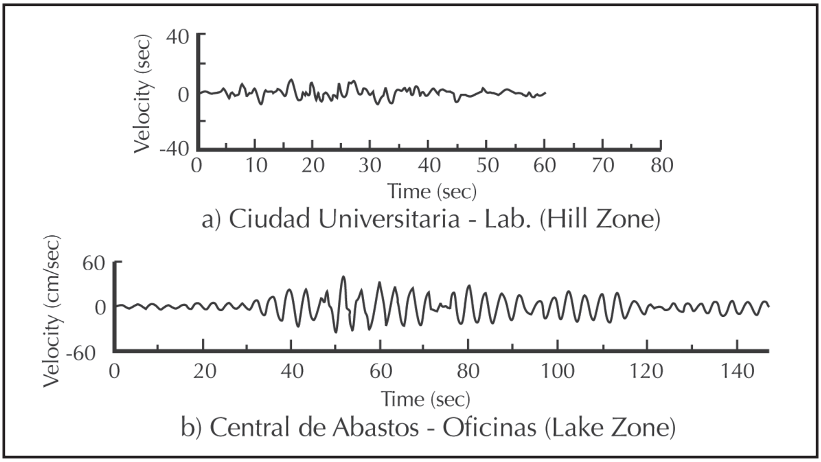

After M. O'Rourke and Ayala, 1990

Figure 3.2 Ground Velocity Time History in Hill and Lake Zones During the 1985 Michoacan Earthquake

3.2 Ground Motion Parameters

There are a number of ground motion parameters of interest to earthquake engineers. These include peak ground acceleration, peak ground velocity, and response spectra acceleration for various building periods. For buried pipelines, the most important are peak ground velocity and, to a lesser extent, peak ground acceleration. As will be shown herein, ground strains and pipe strains due to wave propagation are directly related to peak ground velocity. In terms of the PGD hazard, ground acceleration clearly influences the amounts of landslide and lateral spread movement as well as seismic settlements. However, for the estimation procedures identified in Chapter 2, only the relations for seismic settlement directly use peak ground acceleration.

Ground motion parameters are typically characterized by attenuation relations. A ground motion parameter is presented as a function of earthquake size (typically moment magnitude) and distance from source to site. Depending on the specific relation, other parameters, such as fault type and/or the thickness and stiffness of the soil layer, may be included. Unfortunately, from a user standpoint, there are a large number of attenuation relations, and there appears to be little consensus as to which is the best. Furthermore, there seems to be a fair amount of scatter of observed values compared to the ones predicted by the attenuation relations, with the outliers typically being larger or smaller than the mean or expected value by a factor of two. Quite recently, results from the Next Generation of Ground Motion Attenuation Models (NGA) project were published in a special issue (Vol. 24, No. 1, February 2008) of *Earthquake Spectra*. For example, Figures 3.3 and 3.4 show attenuation relations developed by Campbell and Bozorgnia (2008) for peak ground acceleration and peak ground velocity as a function of the closest distance to the rupture for various moment magnitudes. Both figures are for strike-slip faults with the average shear wave velocity for the top 30 m being 760 m/sec and the depth to basement rock of 2.5 km. Note that the peak ground velocities close to the rupture are about 90 cm/sec and 10 cm/sec for moment magnitudes of 8 and 5, respectively. At 100 km from the rupture, the peak ground velocities are 10 cm/sec and 0.3 cm/sec, again for moment magnitudes of 8 and 5.

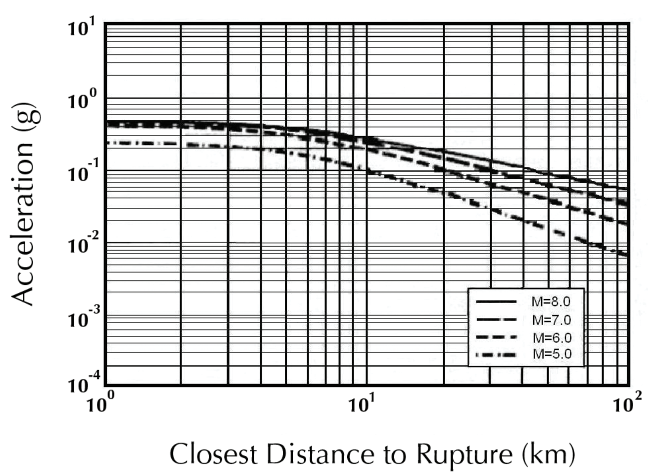

■ **Figure 3.3 Peak Ground Acceleration Attenuation Relationship from Campbell and Bozorgnia (2008)**

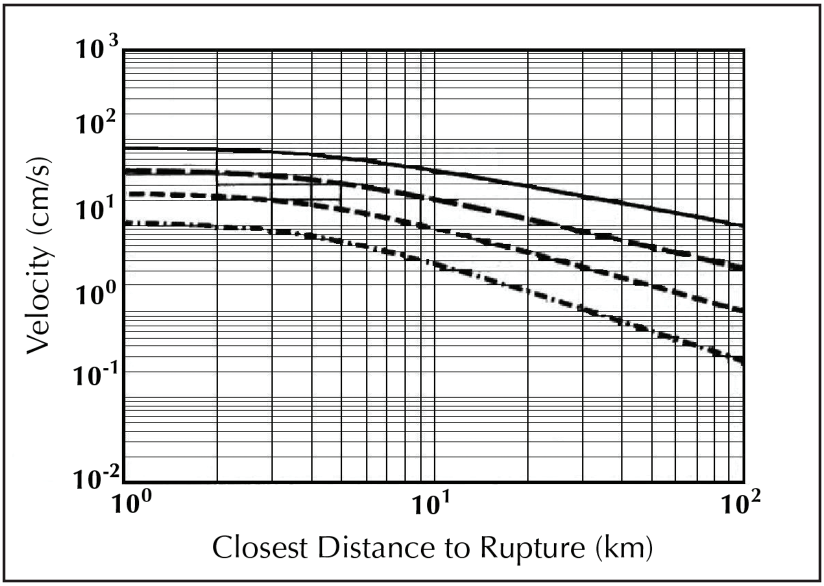

■ **Figure 3.4 Peak Ground Velocity Attenuation Relationship from Campbell and Bozorgnia (2008)**

For instances where only peak ground acceleration values are available for the site in question, the 2001 ALA Guidelines for Buried Steel Pipe (2001) provide convenient conversion ratios shown in Table 3.1.

■ **Table 3.1 Conversion Factors for Peak Ground Velocity**

Moment Magnitude, M_w	**Ratio of Peak Ground Velocity (cm/sec) to Peak Ground Acceleration (g) Source-to-Site Distance (km)**		
	0-20	**20-50**	**50-100**
Rock*			
6.5	66	76	86
7.5	97	109	97
8.5	127	140	152
Stiff Soil*			
6.5	94	102	109
7.5	140	127	155
8.5	180	188	193
Soft Soil*			
6.5	140	132	142
7.5	208	165	201
8.5	269	244	251

*The sediment types represent the following shear wave velocity ranges within the sediment layer: rock ≥ 750 meters per second, stiff soil is 200 meters per second - 750 meters per second, and soft soil < 200 meters per second. The relationship between the peak ground velocity and peak ground acceleration is less certain in soft soils.

3.3

Wave Propagation Velocity

Since onshore pipelines are typically buried 1 to 3 m below the ground surface, both body and surface waves are of interest. The following sections focus on the techniques for estimating effective propagation velocity for body and surface waves.

3.3.1 Body Waves

For body waves, we consider herein only S-waves since S-waves carry more energy and tend to generate larger ground motion than P-waves. For the S-wave, the horizontal propagation velocity (that is, the propagation velocity with respect to the ground surface) is the key parameter. For above ground structures, one often assumes that the seismic excitation is due to vertically propagating S-waves (infinite apparent propagation velocity with respect to the ground surface). That is, it is assumed that the entire base of the structure is subject to the same in-phase motion. For such structures, inertia effects are important and the relative displacements of the various floors with respect to the base are the response parameters of interest. For pipelines, inertia effects are not important since the weight of the pipe plus contents are roughly the same as the soil it replaces. As such, the out-of-phase (wave propagation) motion along the pipe length is important. Hence, for pipelines one must consider the small angle between the direction of body wave propagation and the vertical direction since this leads to out-of-phase motion along the pipe. M. O'Rourke et al. (1982) have studied the apparent horizontal propagation velocity, C, for body waves. They developed an analytical technique, utilizing all three components of motion at the ground surface and a ground motion intensity tensor, for evaluating the angle of incidence of S-waves. The apparent propagation velocity for S-waves is then given by:

$$C_S = \frac{V_S}{\sin\gamma_S} \tag{3.1}$$

where γ_S is the incidence angle of S-waves with respect to the vertical and V_S is the shear wave velocity of the surface soils.

Table 3.2 shows results by the ground motion intensity method for the 1971 San Fernando and the 1979 Imperial Valley events, as well as values for other events from more direct techniques. Note that the apparent propagation velocity for S-waves ranged from 2.1 to 5.3 km/sec with an average of about 3.4 km/sec.

Table 3.2 Summary of Apparent Horizontal Propagation Velocities for S-waves

Event	Site Conditions	Focal Depth (km)	Epicentral Distance (km)	C_S (km/s)	Method for Calculating C_S
Japan 1/23/68	60 m soft Alluvium	80	54	2.9	Cross-correlation array with common time
Japan 7/1/68	60 m soft Alluvium	50	30	2.6	Cross-correlation array with common time
Japan 5/9/74	70 m of silty clay, sand & silty sand	10	140	5.3	Cross-correlation array with common time
Japan 7/8/74	70 m of silty clay, sand & silty sand	40	161	2.6	Cross-correlation array with common time
Japan 8/4/74	70 m of silty clay, sand & silty sand	50	54	4.4	Cross-correlation array with common time
San Fernando 2/9/71	Variable	13	29 to 44	2.1	Ground motion intensity tensor (median value)
Imperial Valley 10/15/79	>300 m Alluvium	Shallow	6 to 57	3.8	Ground motion intensity tensor (median value)
Imperial Valley 10/15/79	>300 m Alluvium	Shallow	6 to 93	3.7	Epicentral distance vs. initial S-wave travel time

3.3.2 Surface Waves

For surface waves, we only consider R-waves since L-waves generate strains in buried pipelines, which will be shown to be significantly less than axial strain induced by R-waves. As indicated previously, R-waves cause the ground particles to move in a retrograde ellipse pattern within a vertical plane. The horizontal component of the ground motions for R-waves is parallel to the propagation path and thus will generate axial strain in a pipe laying parallel to the direction of wave propagation. Since R-waves travel parallel to the ground surface, the phase velocity of the R-waves, C_{ph}, is the apparent propagation velocity.

Note that the phase velocity is defined as the velocity at which a transient vertical disturbance at a given frequency, originating at the ground surface, propagates across the surface of the medium. The R-wave phase velocity is a function of the variation of the shear wave velocity with depth and, unlike body waves, is also a function of frequency. Like all traveling waves, the wavelength λ, frequency f and propagation phase velocity C are interrelated by:

$$C = \lambda f \tag{3.2}$$

The variation of phase velocity with frequency is typically quantified by a dispersion curve. Analytical and numerical solutions are available in the technical literature to generate dispersion curves for layered soil profiles (Haskell, 1953, Schwab and Knopff, 1977).

M. O'Rourke et al. (1984) developed a simple procedure for determining the dispersion curve for layered soil profiles for the typical case where the shear wave velocity increases with depth. Figure 3.5 presents a normalized dispersion curve for a uniform layer of thickness, H_S, with shear velocity, C_L, and Poisson's ratio, ν_L, over a half space with shear velocity, C_H, and Poisson's ratio, ν_H. The curves are for two values of the shear velocity ratio. The dispersion relationship is not strongly affected by the densities of the layer and half space, and those parameters are excluded from Figure 3.5.

Considering first the simplest case of a uniform layer over a half space, they found that at low frequencies ($H_S f / C_L \leq 0.25$), the wavelength is large compared to the layer thickness, and the phase velocity is slightly less than the shear wave velocity of the

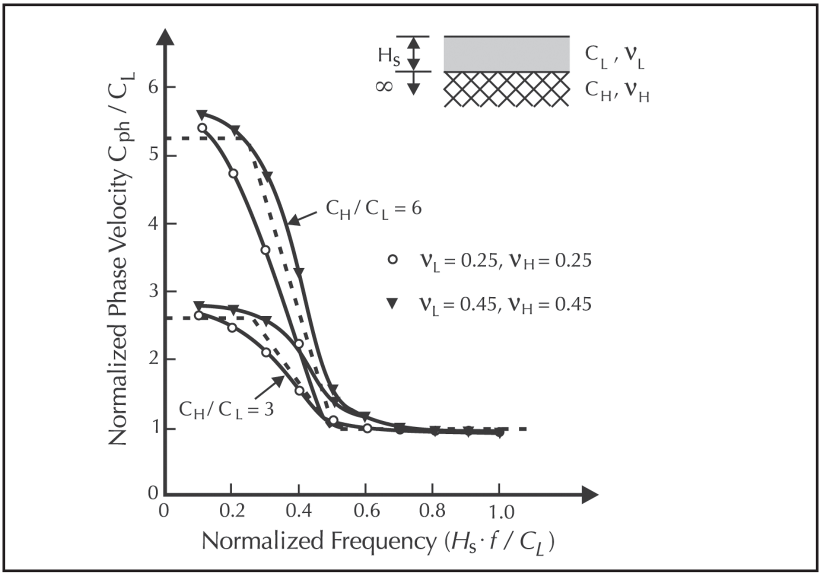

After M. O'Rourke et al., 1984

Figure 3.5 Normalized Dispersion Curve for Single Layer Over Half Space

stiffer half space. That is, for deep, large wavelengths the R-wave is not greatly affected by the "thin" layer. Conversely, at high frequencies ($H_s f/C_L > 0.5$), the wavelength is comparable to or smaller than the layer thickness, and the phase velocity is slightly less than the shear wave velocity of the layer. That is, the shallow small wavelength R-wave is contained primarily within the layer. The dispersion curve for an arbitrary single layer over a half space can be approximated by:

$$C_{ph} = \begin{cases} 0.875 C_{H}, & \dfrac{H_s f}{C_L} \le 0.25 \\ 0.875 C_H - \dfrac{0.875 C_H - C_L}{0.25}\left(\dfrac{H_s f}{C_L} - 0.25\right), & 0.25 \le \dfrac{H_s f}{C_L} \le 0.50 \\ C_{L}, & \dfrac{H_s f}{C_L} \ge 0.50 \end{cases} \tag{3.3}$$

where f is the frequency in Hz.

This technique can also be extended to multiple soil layers. For the two soil layer case shown in Figure 3.6(a), separate single layer models in Figure 3.6(b) for short wavelengths and in Figure 3.6(c) for long wavelengths are considered. The dispersion curves for each single layer model are combined to obtain the curve for the whole profile, as shown in Figure 3.7.

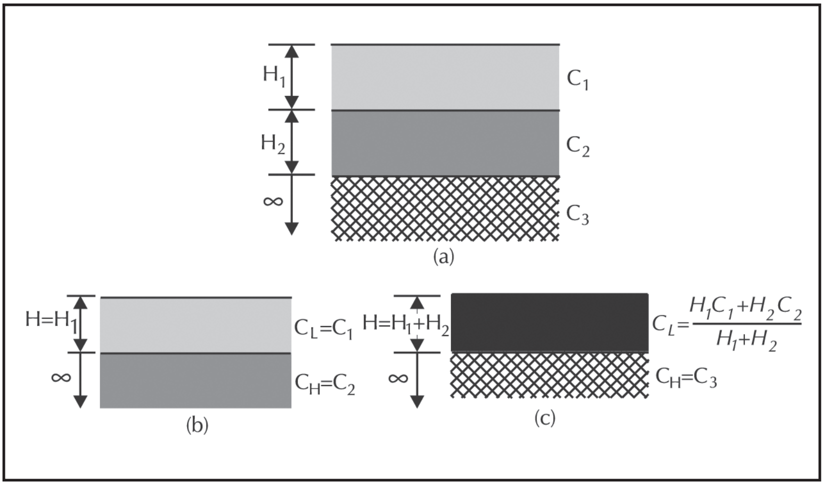

After M. O'Rourke et al., 1984

■ **Figure 3.6 Idealization of Complex Soil Profile**

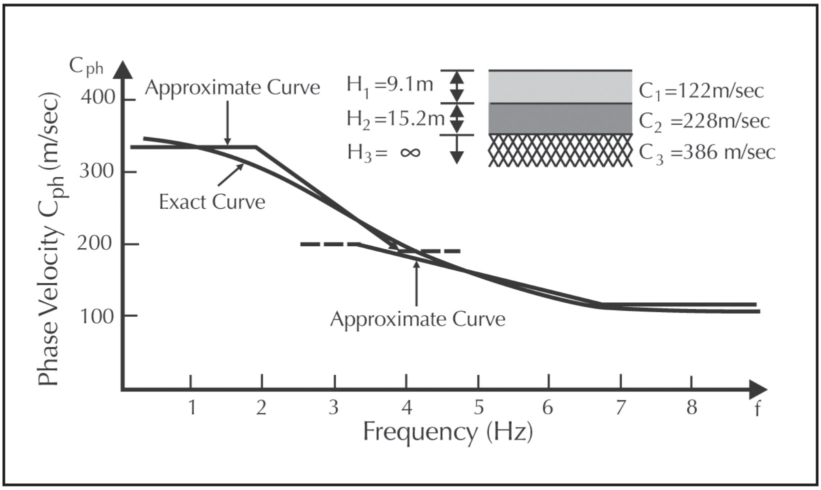

After M. O'Rourke et al., 1984

■ **Figure 3.7 Dispersion Curve for Two Layer Soil Profile**

3.4 Wavelength

The relationship between propagation velocity, frequency and wavelength is given in Equation 3.2. For body waves with a constant propagation velocity, the wavelength is inversely proportional to the frequency, or linearly proportional to the period of the wave. The situation for surface waves is a bit more complicated. For typical soil profiles, in which the material stiffness increases with depth, the propagation or phase velocity of the fundamental R-waves is an increasing function of the wavelength. That is, long wavelength waves travel faster than short wavelength waves.

For ground motions which contain a number of different frequencies or wavelengths, the question arises as to which frequency or wavelength leads to the largest ground strain. All other things being equal, for strain calculations with stations separated by a distance, L_S, a reasonable starting point might be $2L_S < \lambda < 4L_S$. As pointed out by Wright and Takada (1978), ground motion of two points due to a wave with $\lambda = 2L_S$ would be out-of-phase by 180°, leading to fairly large relative displacements and strains. Similarly, ground motion at two points due to a wave with $\lambda = 4L_S$ would be out-of-phase by 90°, again leading to somewhat smaller relative displacements and strains. If $\lambda = L_S$, the ground motions would be in-phase, and there would be no contribution to relative displacements and strains due to that wavelength. Thus, for R-wave propagation, the effective propagation velocity, C_{eff}, would appear to be the phase velocity, C_{ph}, for a wavelength equal to about two to four times the separation distance between stations.

Figure 3.8 presents back calculated values for the effective propagation velocity during the 1971 San Fernando event for a number of stations at the northern end of the Los Angeles Basin, as well as the phase velocity for the fundamental R-waves, calculated for $\lambda = 2L_S$ and $\lambda = 4L_S$. The R-wave model with $\lambda = 4L_S$ seems to provide a better overall match to the observed effective propagation velocity data than the R-wave model with $\lambda = 2L_S$.

As shown in Figure 3.8, for separation distances less than about 500 m (1,640 ft), the R-wave model with $\lambda = 4L_S$ matches fairly well with the observed effective propagation velocity data. For separation distances greater than 500 m, the R-wave model with $\lambda = 4L_S$

is conservative, i.e., an underestimation of the effective propagation velocity. However, these large separation distances are fast approaching the upper limit for engineering applications.

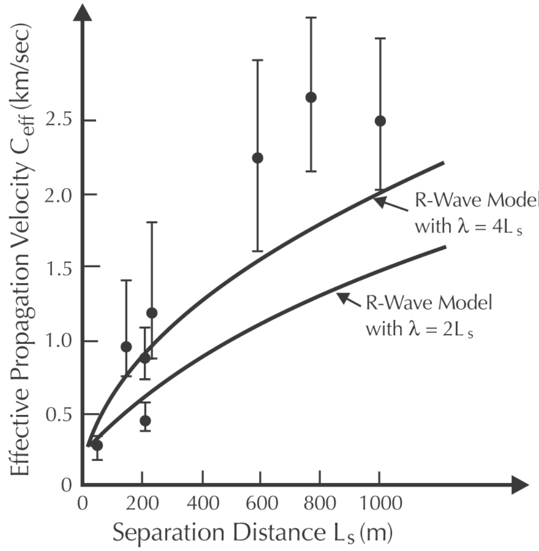

After M. O'Rourke et al., 1984

Figure 3.8 Effective Propagation Velocity vs. Separation Distance

3.5

Ground Strain and Curvature Due to Wave Propagation

For the analysis and design of buried pipelines, the effects of seismic wave propagation are typically characterized by the induced ground strain and curvature. Newmark (1967) developed a simplified procedure to estimate the ground strain. He considers a simple traveling wave with a constant wave shape. That is, on an absolute time scale, the acceleration, velocity and displacement time histories of two points along the propagation path are assumed to differ only by a time lag, which is a function of the separation distance between the two points and the speed of the seismic wave. The general form of a traveling wave is given by:

$$u = f\left(\frac{t}{T} + \frac{x}{\lambda}\right) \tag{3.4}$$

where T is the period of the repeating motion and λ is the wavelength. Note that the frequency f is the reciprocal of the period and that the frequency, wavelength and propagation velocity are related by the standard traveling wave relation in Equation 3.2. If u is the ground (particle) motion **parallel** to the direction of propagation (as would be the case for R-waves), then the derivative with respect to the spatial coordinate f'/λ is the ground strain along the direction of propagation, while the derivative with the respect to time f'/T is the ground or particle velocity. Utilizing Equation 3.2, we have:

$$\varepsilon_g = \frac{V_{max}}{C_R} \tag{3.5}$$

where V_{max} is the maximum horizontal ground velocity in the direction of wave propagation and C_R is the propagation velocity of the R-wave.

If u in Equation 3.4 is now the particle motion **perpendicular** to the direction of propagation (as would be the case for S-waves), the second derivative with respect to the spatial coordinate f''/λ^2 is the curvature along the direction of propagation, while the second derivative with respect to time f''/T^2 is the ground acceleration in a direction perpendicular to the direction of propagation. Again utilizing the standard relation between propagation velocity, frequency and wavelength in Equation 3.2, the curvature K_g is:

$$\mathrm{K}_g = \frac{A_{max}}{C_S^2} \tag{3.6}$$

where A_{max} is the maximum ground acceleration perpendicular to the direction of wave propagation and C_S is the propagation velocity of the S-wave.

These two relations for ground strain and curvature along the direction of wave propagation are relatively straight forward. The ground motion parameters V_{max} and A_{max}, the maximum particle velocity (parallel to direction of propagation), and acceleration (perpendicular to direction of propagation) can be obtained from earthquake records or from attenuation relations, discussed previously. For R-wave propagation, the ground strain parallel to the ground surface is given by Equation 3.5 where C_R, as shown above, can theoretically be taken as the phase velocity corresponding to a wavelength equal to two to four times the separation distance between the stations.

Hence, wave propagation with particle motion parallel to the pipeline would presumably induce significant axial strain in a pipe. On the other hand, an S-wave, again propagating parallel to the pipeline but with particle motion perpendicular to the pipe, would induce only bending strains. As will be demonstrated below, these bending strains are small. However, the energetic S-waves can induce axial strain if they travel **at an angle** with respect to the pipe axis. Consider an S-wave traveling in a horizontal plane at some angle with respect to a buried pipeline. Due to the angle, the S-wave particle motion (perpendicular to its direction of propagation) would have one component parallel to the pipe (inducing axial strain) and another perpendicular to the pipe (inducing bending strain). Yeh (1974) has shown the angle which maximizes the axial strain is 45°. The resulting relation for axial strain is:

$$\varepsilon_g = \frac{V_{max}}{2C_S} \tag{3.7}$$

where C_S is theoretically the apparent propagation velocity of the S-wave with respect to the ground surface given in Equation 3.1 and Table 3.2.

The simple relations in Equations 3.6 and 3.7 can be used to estimate pipe strain resulting from S-wave propagation. For a straight pipe running at 45° to the direct of wave propagation, it will be shown in Chapter 10 that Equation 3.7 is an upper bound for the axial strain in the pipe induced by wave propagation. Similarly, the product of the ground curvature in Equation 3.6 and half the pipe diameter is an upper bound for the bending strain in a pipe running parallel to the direction of S-wave propagation.

$$\epsilon_b \leq \frac{D}{2} \cdot \frac{A_{max}}{C_S^2} \tag{3.8}$$

where D is the pipe diameter. If one assumes that the ground motion is sinusoidal, then the ratio of peak ground acceleration to the peak ground velocity is given by:

$$\frac{A_{max}}{V_{max}} = 2\pi \cdot f \tag{3.9}$$

where f is now the predominate frequency of the ground motions. Applying this relation to the V_{max}/A_{max} ratios in Table 3.1 yields ground motion periods of 0.4 to 1.0 sec for rock, 0.6 to 1.2 sec for stiff soil, and 0.9 to 1.7 sec for soft soil, all of which seem reasonable. Utilizing the relation in Equation 3.2, the upper bound pipe bending strain in Equation 3.8 becomes:

$$\epsilon_b = \frac{\pi D}{\lambda} \cdot \frac{V_{max}}{C_S} \tag{3.10}$$

Note that the wavelength is typically two or three orders of magnitude larger than the pipe diameter. Hence, the pipe bending induced by S-wave propagation is roughly one or two orders of magnitude less than the pipe axial strain induced by S-wave propagation in Equation 3.7.

In summary, the bending strains induced in a pipe due to traveling waves (S-waves, L-waves or the vertical component of R-waves) are generally small. This is due to the fact that, as shown in Equation 3.10, they are proportional to the ratio of pipe diameter to wavelength, a small quantity. On the other hand, axial strains induced in the ground by traveling waves (an upper bound to axial strain in a pipe) can be fairly large. This is particularly true for R-waves since the effective propagation in Equation 3.5 (R-waves, ground strain parallel to the direction of propagation) is typically smaller than that for S-waves in Equation 3.7 (S-waves, ground strain at 45° to direction of propagation).

3.6

Observed Ground Strain and Effective Propagation Velocities

The theoretical relations for ground strain in Equations 3.5 and 3.7 are for the propagation direction for which the ground strain is a maximum (parallel to the direction of propagation for the R-wave relation in Equation 3.5, at 45° to the direction of propagation for the S-wave relation in Equation 3.7). If both wave types are present, the relations presuppose that one is able to determine the peak ground velocity, V_{max}, for each wave type. Finally, these equations are based upon the assumption that the seismic excitation can be modeled as a traveling wave, as given by Equation 3.4. That is, the relations neglect any incoherence or change in wave shape from point to point.

Given these conditions, it is instructive to review observed ground strains. Figure 3.9 presents peak ground strain values as determined by Paolucci and Smerzini (2008), plotted against peak ground velocity. The figure contains data from two earthquakes (Parkway #1 and Parkway #2) at the Parkway Valley array in New Zealand and two earthquakes (Parkfield and San Simeon) at the UPSAR array near Parkfield, California. The peak ground strain is the largest principle strain developed from a tensorial

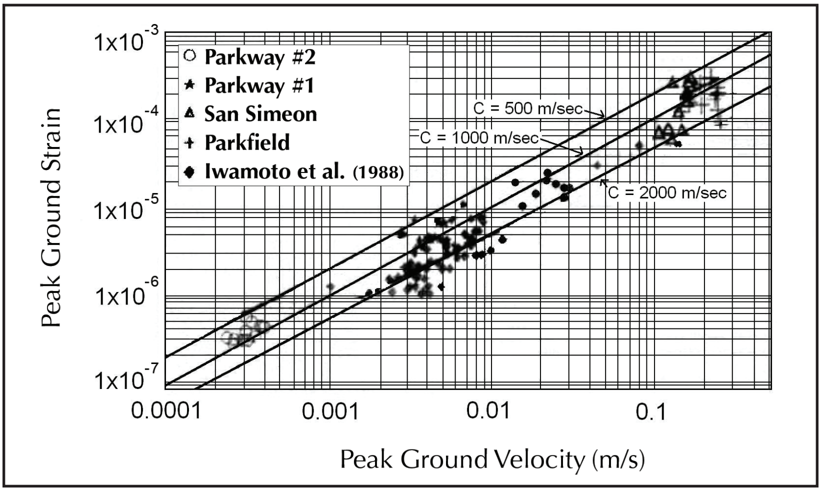

After Paolucci and Smerzini, 2008

Figure 3.9 Peak Ground Strain as function of Peak Ground Velocity

representation of ground strain in a horizontal plane. The ground strains in turn were determined from spatially interpolated displacement records.

The plot also contains pipe strains as recorded by Iwamoto et al. (1988). Paolucci and Smerzini correctly note that the pipe strain data tends to be somewhat lower than the others, since the pipe upon which the strain gage was placed may not have been orientated parallel to the direction of peak ground strain. It should also be mentioned that, as explained in more detailed Chapter 10, the ground strain is an upper bound for pipe strain, with pipe strain being lower than ground strain, particularly when there is slippage between the pipe and the surrounding soil. Nevertheless, Figure 3.9 shows an apparent linear relation over three orders of magnitude between ground strain and peak ground velocity as calculated by Paolucci and Smerzini.

Superimposed upon the data points in Figure 3.9 are the ground strain one calculates from Equation 3.5 using propagation velocities C = 500 m/sec, 1,000 m/sec and 2,000 m/sec. Note that the use of C = 500 m/sec provides a reasonable upper bound for the observed ground strains, C = 1,000 m/sec provides something close to the least squares line, and C = 2,000 m/sec provides a reasonable lower bound for the observed ground strains.

Similarly, Trifunac and Lee (1996) present useful information on the effective propagation velocity for calculation of peak ground strains. Specifically, they generate artificial accelerograms from the SYNACC computer program and evaluate ground strains in the radial direction. They then establish the following empirical relation between the peak ground strain and the peak particle velocity:

$$\begin{aligned} log_{10}\, \epsilon_{rr} &= (-0.26 - 0.67V_S) + (-0.00064 + 0.000467V_S)\, R_S \\ &+[(1 - 0.19V_S) + (-0.0043+0.0015V_S)\, R_S]\, log_{10} \frac{V_{max}}{V_S} \end{aligned} \qquad (3.11)$$

where V_{max} is the peak particle velocity in the radial direction (km/sec), R_S is the source-to-site distance in km, and V_S is the shear wave velocity (km/sec) in the top 50 meters of soil.

Note that the form of the relationship is consistent with surface wave propagation, that is, the ground strain in the radial direction (direction of propagation) is a function of the peak particle velocity in the same direction. The authors acknowledge that "surface waves play a prominent role" in their approach. As such, as the authors note the results are applicable to sites on soft sediments and for sources breaking the surface, conditions conducive to surface wave generation. Trifunac and Lee claim that other relationships would be needed for deeper events and when faulting does not reach the surface, that is for conditions that are not conducive to surface wave generation.

Equation 3.11 can be used to backcalculate the effective propagation velocity for various values of the source-to-site distance, the shear wave velocity of the top soil layer, and the peak particle velocities. These backcalculated effective propagation velocities are presented in Table 3.3. As one might expect, the effective propagation velocity for strain in the radial direction is an increasing function of the shear wave velocity of the top soil layer—the stiffer the soil, the larger the effective propagation velocity, and the smaller the ground strain for a given peak particle velocity.

Table 3.3 Backcalculated Effective Propagation Velocities from Trifunac and Lee Ground Strain Relation

Peak Particle Velocity V_{max} (cm/sec)	Effective Propagation Velocity (m/sec)			
	V_S = 100 m/sec		V_S = 500 m/sec	
	R_s = 10 km	R_s = 100 km	R_s = 10 km	R_s = 100 km
10	185	175	892	1265
100	194	195	1123	1462

For V_S = 100 m/sec, the effective propagation velocity in Table 3.3 ranged from $1.75V_S$ to $1.95V_S$ with an average of $1.87V_S$. While for V_S = 500 m/sec, the effective propagation velocity ranged from $1.78V_S$ to $2.92V_S$ with an average of $2.36V_S$. Hence, for sites subject to surface waves, one could argue that the effective propagation velocity for R-waves is roughly $2V_S$ or twice the average shear wave velocity of the top 50 meters of soil. This is consistent with Equation 3.3, as well as Figures 3.5 and 3.7, in that theoretically the shear wave velocity of the top soil layer is a lower bound for the R-wave phase velocity. The variation of effective propagation velocity with V_{max} seems to be an outgrowth of the specific functional form chosen by Trifunac and Lee (log of ground strain proportional to log of V_{max} / V_S).

The backcalculated Trifunac and Lee effective propagation velocities also seem generally consistent with the ground strain data from Paolucci and Smerzini in Figure 3.9. That is, the larger than average ground strains, which one would expect to be due to surface wave excitation, have effective propagation velocities in the 500 to 1,000 m/sec range. According to Trifunac and Lee, this range would correspond to V_S values in the 250 to 500 m/sec range which seem realistic. Hence, the observed ground strains from arrays and the simulated ground strain from a computer program are reasonably consistent with surface wave propagation theory.

However, there seems to be some inconsistency in relation to body wave propagation. Discounting the pipe strains from Iwamoto et al. in Figure 3.9, the upper bound for the effective propagation velocity is about 2,000 m/sec. While theory in Equation 3.7 suggests that the effective propagation velocity for body waves should be twice C_S or roughly 6,800 m/sec, using 3.4 km/sec as the average value of C_S from Table 3.2. Either all the ground strain values in Figure 3.9 are for surface waves (unlikely), or something is wrong with the theory for body waves, particularly the apparent propagation velocity. It seems likely that the traveling wave assumption—same shape from station to station—doesn't hold for body waves. That is, incoherence or changes in the body wave shape from point to point result in larger ground strain than predicted by body wave propagation theory. The incoherence induced larger than expected strains result in lower than expected effective propagation velocities. Work by Zerva and Harada (1997) generally supports this view. In subsequent chapters, a lower-incoherence influenced-effective propagation velocity for S-waves will be utilized. Specifically, ground strains from Equation 3.7 with C_S taken as 1,000 m/sec are shown in Chapter 10 to be consistent with observed damage to the Potrero Canyon gas pipeline. The same approach (Equation 3.7 with C_S = 1,000 m/sec) is used in Chapter 12 to develop fragility relations for segmented pipelines.

3.7 Transient Ground Strain Due to Variable Subsurface Conditions

The ground strains and curvatures described previously are due to wave propagation effects. The theoretical apparent propagation velocity relations presented apply to relatively uniform soil layering in the horizontal direction. However, as noted by Kachadoorian (1976) and Wang and M. O'Rourke (1978), damage to buried pipelines is often concentrated in areas with variable subsurface conditions (i.e., non-uniform soil properties in a horizontal direction). In a more recent example, Hall (1995) notes relatively large amounts of buried pipeline damage during the 1994 Northridge event in areas where an inclined ground surface or an inclined soil-rock interface exists. It is believed that ground strain for sites with variable subsurface conditions is due in large part to local differences in site response or site amplification.

3.7.1 Laboratory Results and Numerical Models

Nishio et al. (1983) carried out a series of laboratory tests to study the amplification response of ground due to an inclined soil-rock interface. Figures 3.10 and 3.11 show, for example, two basic models they considered. The bottom of the model was shaken as a unit, corresponding to vertically incident waves (i.e., no horizontal wave propagation effects). For the single inclined subsurface in Model No. 2 in Figure 3.10, the displacements were small where the soil layer was shallow, and large where the soil layer was deep. Somewhat similarly, the strains were very small atop the shallow layer and moderate atop the deep layer. However, the ground strain was largest near the inclined surface. For the valley situation (i.e., two inclined subsurfaces) in Model No. 3 in Figure 3.11, the ground displacements were again small atop the shallow layer and largest atop the center of the valley. However, as with Figure 3.10, the ground strains were largest over the inclined subsurface. Nishio et al. also performed a finite element analysis for these models. As shown in Figures 3.10 and 3.11, the numerical results match well with the experimental results.

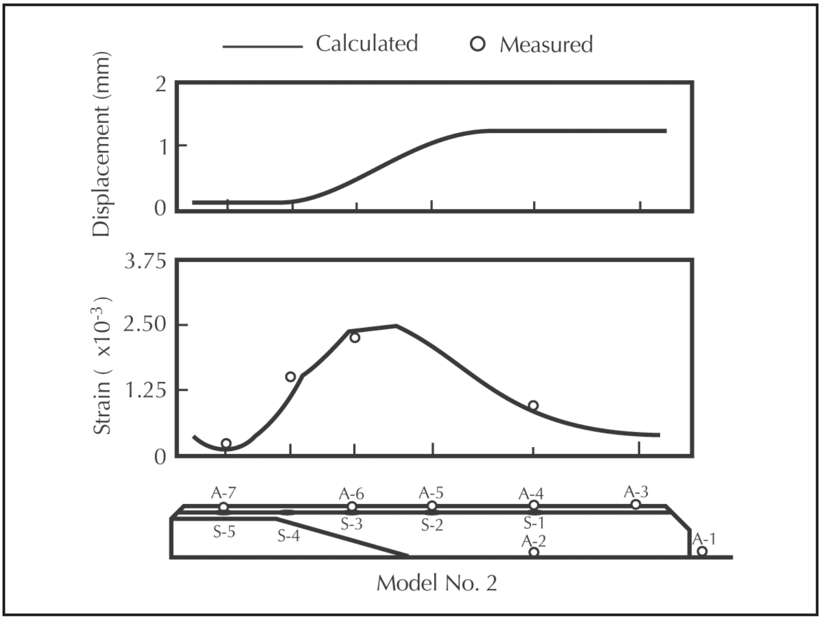

After Nishio et al., 1983

■ **Figure 3.10 Axial Strains and Model for a Half Valley**

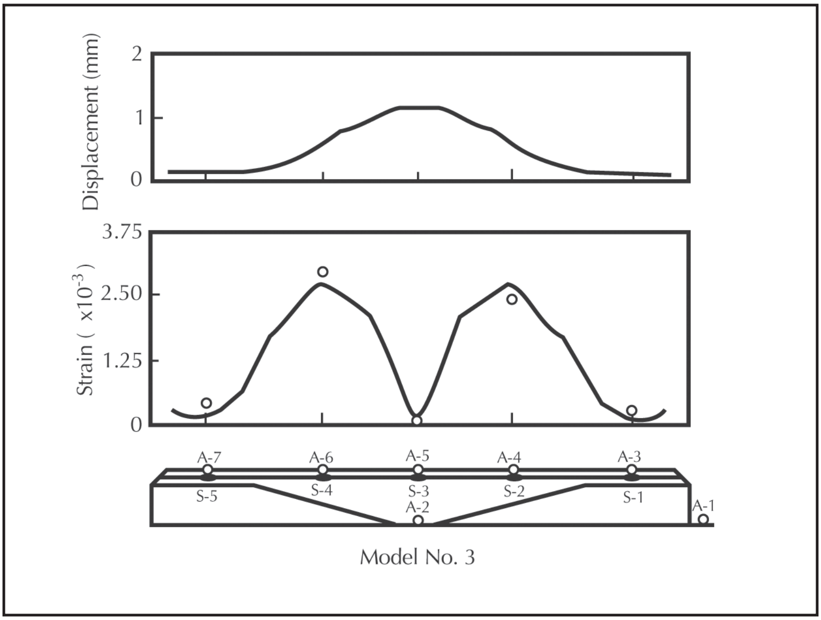

After Nishio et al., 1983

■ **Figure 3.11 Axial Strains and Model for a Valley**

For estimating the ground response of complex sites, approaches using 1-D, 2-D or 3-D finite element techniques have been pursued. For example, Ando et al. (1992) used a 2-D finite element program to analyze the dynamic response of the site shown in Figure 3.12. In this figure, the shaded area is embanked ground (fill deposits) with a shear velocity of 166 m/sec while the shear velocity for the original ground is 300 m/sec.

Using the 1978 Off Miyagi Prefecture earthquake record, which had a maximum ground acceleration of 25 gal, Ando et al. determined the ground and pipe strains, as shown in Figure 3.13.

Again, all points along the base of the model had the same motion without a time lag, modeling vertically propagating body waves. The ground strain was largest where the original ground surface (bottom surface of the fill deposits) is inclined (i.e., near PA3X), and where the top surface of fill deposits were inclined (i.e., to the right of location mark 170 m). The maximum ground strain is about three times that for the nominally uniform soil layer near GA3X. These results demonstrate that large ground strains are generated when the thickness of the soil layer varies. This can be due to either a nominally flat top surface and an inclined bottom surface, or an inclined top surface and a nominally flat bottom surface.

More recently, Liu and M. O'Rourke (1997a) used a numerical approach on an inclined subsurface model similar to Nishio et al.'s Model 2 in Figure 3.10. However, unlike the Nishio et al. model, Liu and M. O'Rourke considered the effects of material outside the immediate area of interest. Specifically, infinite elements are used in order to eliminate the reflection at the two boundaries. Shear waves are generated by inputting acceleration records or prescribed displacements along the base of the model.

Figures 3.14, 3.15 and 3.16 present peak ground displacement, peak ground velocity and peak horizontal ground strain near the ground surface for three inclined subsurface models with inclination angle, α, of 10°, 45° and 90°, respectively. The shear wave velocity is 150 m/sec for the surface soil layer and 1,250 m/sec for the rock in those cases. Like the Nishio and Ando results, the ground displacement is small over the shallow soil layer and large over the deeper soil layer. The ground velocities, which ranged roughly from 10 to 30 cm/sec, followed a similar pattern.

The ground strain was smaller (typically about 0.1×10^{-3}) atop the shallow soil layer, and larger (typically about 0.5×10^{-3}) atop the deeper soil layer. The largest horizontal ground strain occurred at the inclined subsurface. For inclination angles of 45º and 90º, the peak strain was roughly 50% larger than that for the deeper soil layer. For the shallow inclination angle at 10º, the peak strain wasn't greatly different than that atop the deep soil layer.

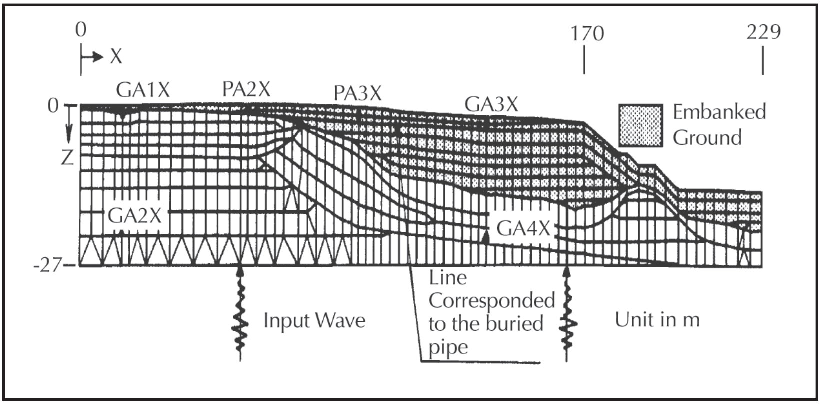

After Ando et al., 1992

Figure 3.12 Profile of a Complex Site

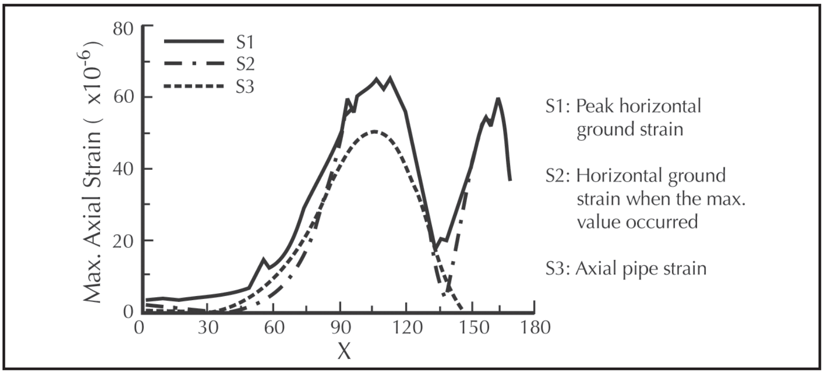

After Ando et al., 1992

Figure 3.13 Distributions of Strain for Complex Site

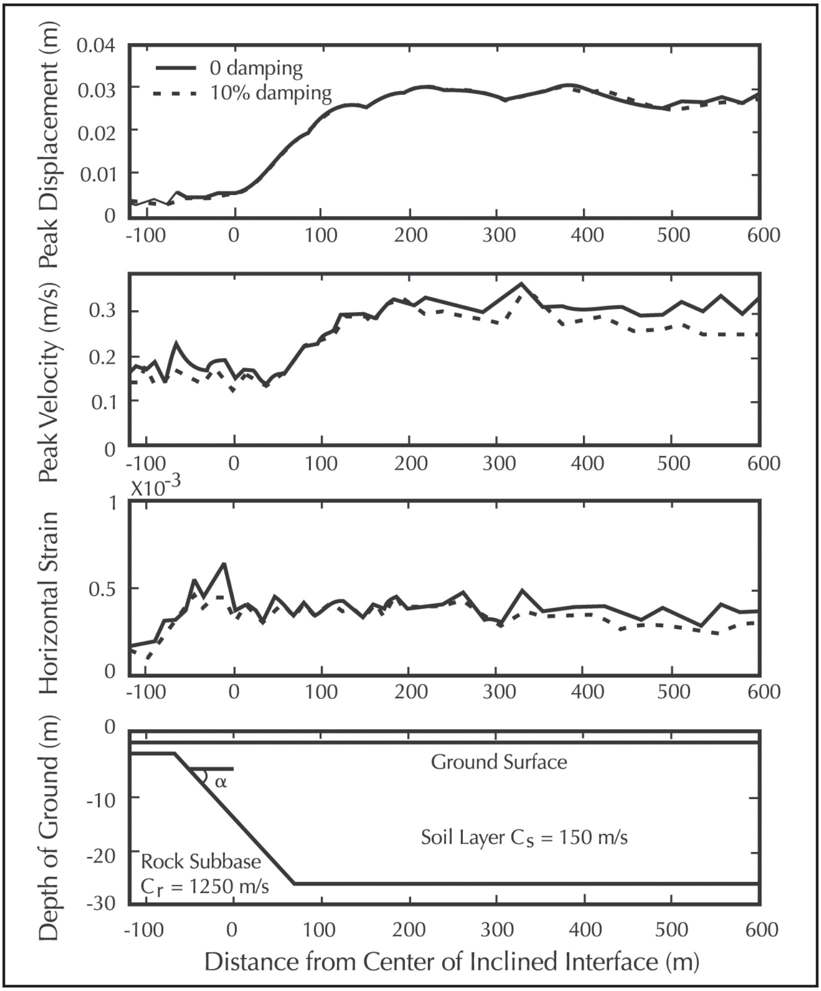

■ **Figure 3.14 Peak Ground Response for $\alpha = 10°$**

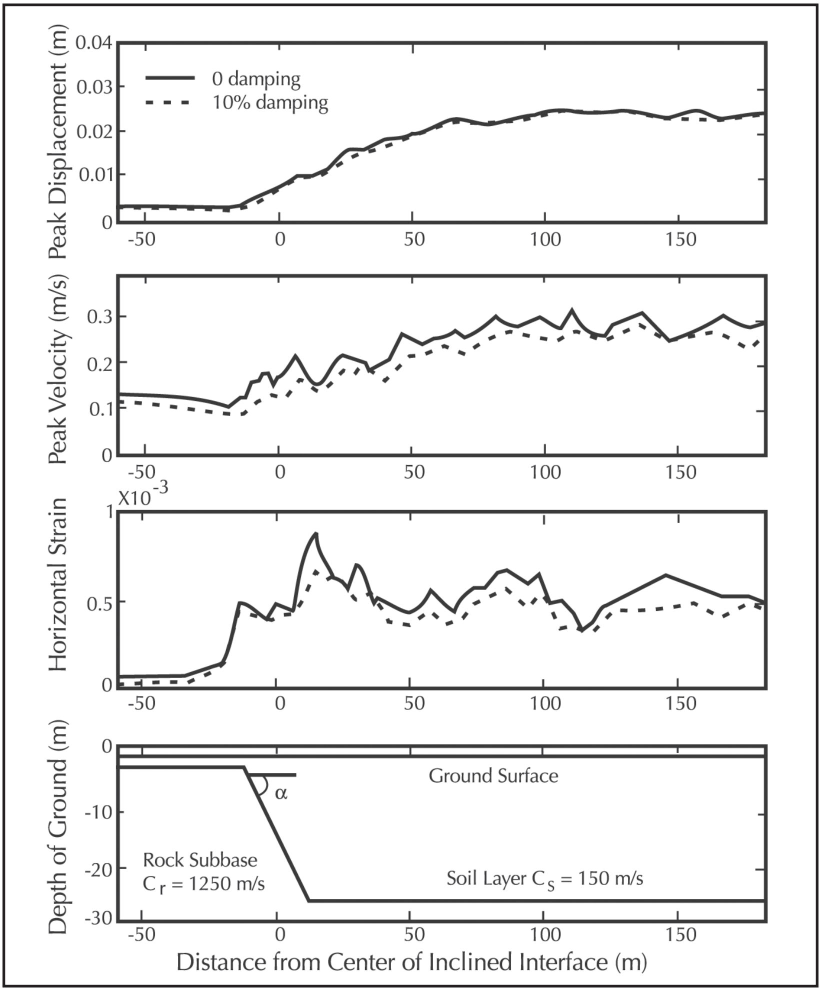

■ **Figure 3.15 Peak Ground Response for α = 45°**

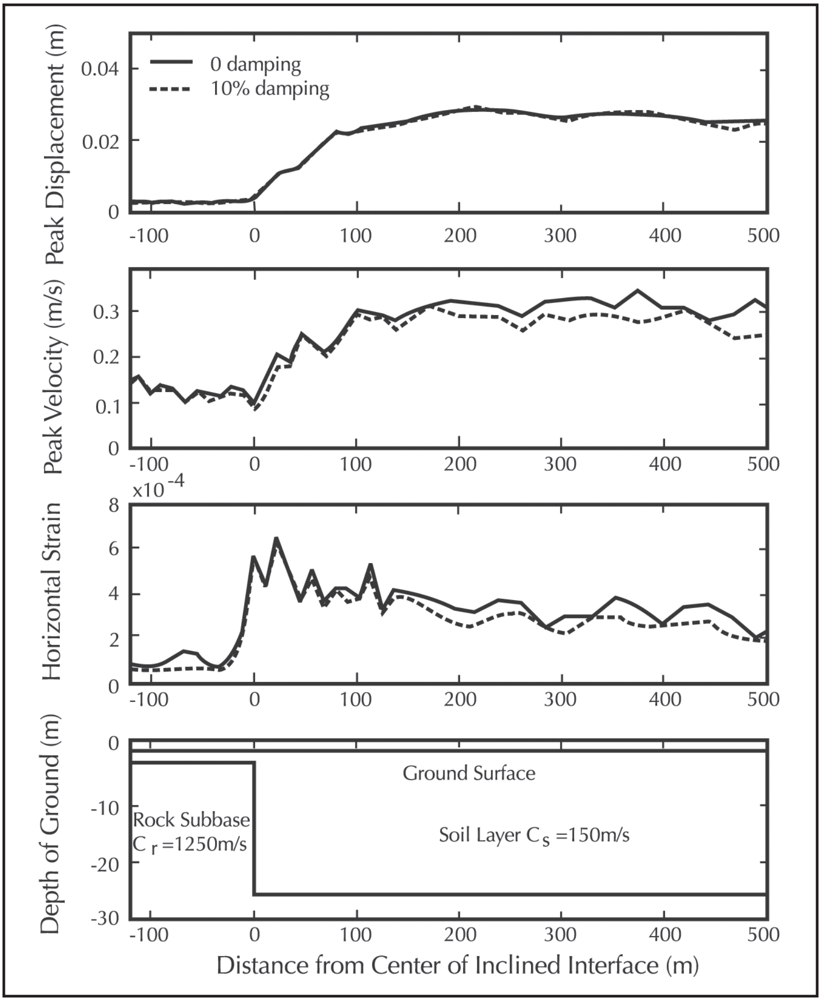

■ **Figure 3.16 Peak Ground Response for α = 90°**

3.7.2 Simplified Model

Liu and M. O'Rourke (1997a) have proposed a simplified model for estimating the ground strain for a site with an inclined soil-rock interface as shown in Figure 3.17, in which shear waves are propagating vertically from below.

In Figure 3.17, D_A is the peak ground displacement atop the shallow soil layer while D_B is the corresponding value for the deep soil layer. A simple estimate for ground strain over the inclined rock surface is the difference in the ground displacement divided by the separation distance. Assuming that the soil motions are in phase, and taking the horizontal projection of the inclined rock surface, L_{AB}, as the separation distance:

$$\varepsilon_g = \frac{D_B - D_A}{L_{AB}} \tag{3.12}$$

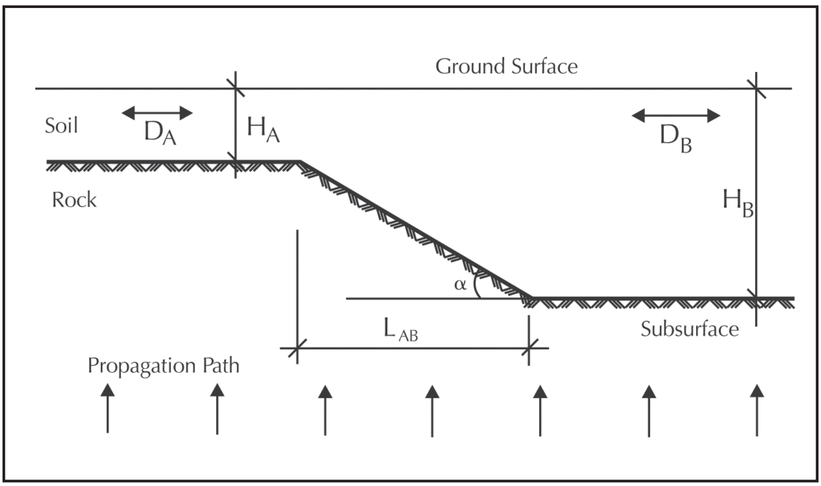

■ **Figure 3.17 Profile of a Site with Inclined Soil-Rock Interface (Shear Wave)**

A comparison of results from this simple relation with the numerical results given, for example, in Figures 3.15 and 3.16 indicated that Equation 3.12 provides reasonable estimates as long as the inclination angle α is less than 45°. For inclination angles greater than about 45°, Equation 3.12 overestimates peak ground strains from the numerical model. Note in this regard that for a vertical rock face (i.e., $\alpha = 90°$), L_{AB} is zero and Equation 3.12 gives infinite ground strain, which, of course, is not realistic.

In addition, the numerical results show that with an increase in the separate distance L_{AB}, the ground strain approaches a non-zero asymptotic value, while Equation 3.12 predicts the ground strain would approach zero.

Based upon these considerations, Equation 3.13 is suggested for estimating ground strain over an inclined rock surface.

$$\varepsilon_g = \begin{cases} (D_B - D_A) \cdot \left(\dfrac{0.5 \cdot \tan\alpha}{H_B - H_A} + \dfrac{\pi}{2TC_S}\right) & \alpha \leq 45° \\ (D_B - D_A) \cdot \left(\dfrac{0.5}{H_B - H_A} + \dfrac{\pi}{2TC_S}\right) & \alpha > 45° \end{cases} \tag{3.13}$$

where H_A is the thickness of the shallow soil layer, H_B is the thickness of the deeper soil layer, and T is the predominant period at the ground surface over the deep soil layer.

For an inclination angle $\alpha \leq 45°$, the peak ground strain is an increasing function of the inclined angle. For $\alpha > 45°$, ground strain is taken as the value for a 45° inclination angle.

3.7.3 Comparison

In order to test this simplified approach, Liu and M. O'Rourke calculated the ground strains for different sites with $\alpha \geq 3°$, $H_A \leq 5.0$ m (16 ft), $H_B \geq 10$ m (33 ft), 150 m/sec $\leq C_{S\text{-}soil} \leq$ 1,000 m/sec, $C_{S\text{-}rock} \geq$ 1,000 m/sec, using their finite element model. For example, Figure 3.18 shows the peak ground strain as a function of length L_{AB} for $C_{S\text{-}soil}$ = 150 m/sec, H_A = 2.0 m (6.6 ft), H_B = 26 m (85 ft) and $C_{S\text{-}rock}$ = 1,250 m/sec, while Figure 3.19 shows results for the same model with C_S = 210 m/sec.

Another type of comparison is shown in Figure 3.20. There the numerical strain from the model with $\alpha \geq 3°$ is plotted versus the estimated strain from Equation 3.13. Also included are the results from two San Fernando time histories scaled so that the peak accelerations match, as well as that from the Nishio et al. model in Figure 3.10.

Overall the match is reasonably good. Hence, Equation 3.13 can be used to estimate ground strain at a site with an inclined soil-rock interface.

Finally, it should be noted that the transient strains for the three earthquakes considered in Figure 3.20 ranged from roughly

0.1×10^{-3} to 1.0×10^{-3}. As such, they are comparable to wave propagation ground strain for reasonably large peak particle velocities in the 10 to 100 cm/sec range, as per Figure 3.9. Hence, transient ground strain due to variable subsurface conditions of and by themselves can lead to pipe damage rates comparable to those for seismic wave propagation. However, this additional damage would be restricted to areas with variable soil layer thickness while the wave propagation hazard exists to a greater or lesser degree over the whole pipe network.

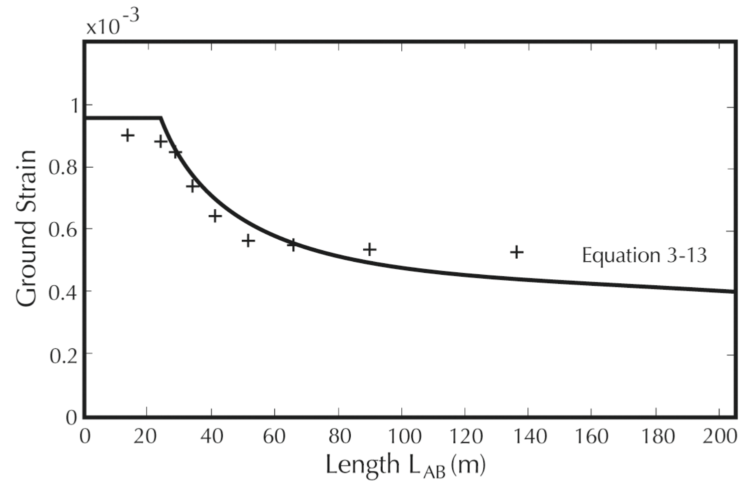

■ **Figure 3.18 Comparison of Ground Strain for C_s = 150 m/sec**

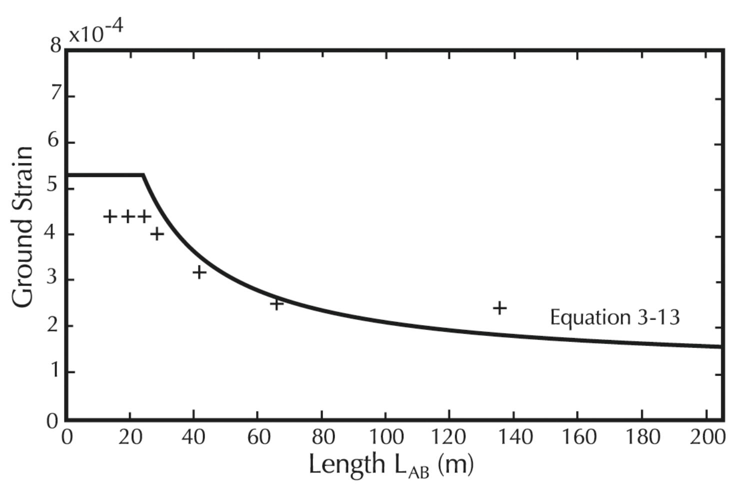

■ **Figure 3.19 Comparison of Ground Strain for C_s = 210 m/sec**

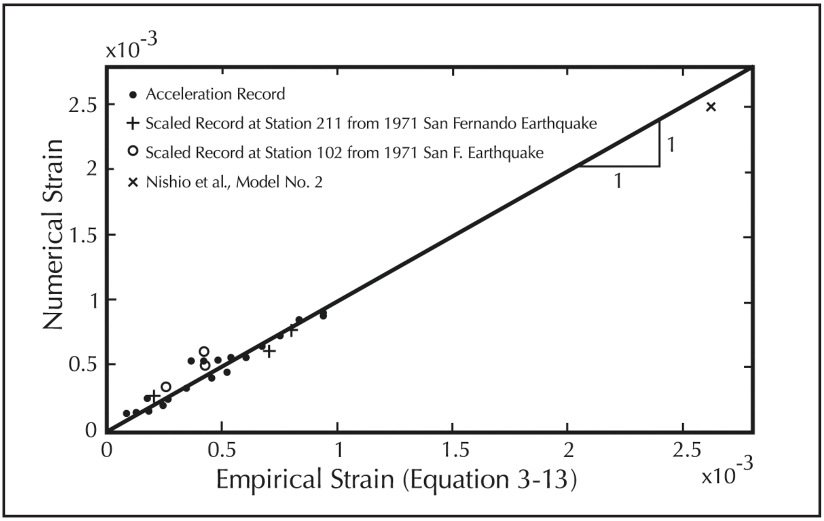

Figure 3.20 Comparison of Ground Strain

4

Pipe Limit States and Failure Criterion

This chapter describes the limit states for buried pipelines subject to seismic loading. The principal limit states or failure modes for corrosion-free **continuous** pipelines (e.g., steel pipe with welded joints) are rupture due to axial tension and/or bending, and local buckling due to axial compression and/or bending. If the burial depth is shallow, continuous pipelines in compression can also exhibit beam-buckling behavior. This limit state is particularly common for offshore pipelines in compression. Failure modes for corrosion-free **segmented** pipelines with bell and spigot type joints are axial pull-out at joints, crushing at the joints and round flexural cracks in pipe segments away from the joints.

Due to the nature of the hazards, different limit state criteria are often recommended for the PGD hazard (monotonic loading) than for the wave propagation hazard (cyclic loading). Similarly, different limit state criteria are recommended for butt-welded pipe (higher capacity) than for fillet/lap-welded pipe (lower capacity).

As will be shown, limit states for buried steel pipe often involve post-yield behavior. As such, a full description of the stress-strain behavior is needed. The Ramberg-Osgood model (1943) is the most widely used:

$$\varepsilon = \frac{\sigma}{E}\left[1 + \frac{n}{1+r}\left(\frac{\sigma}{\sigma_y}\right)^r\right] \tag{4.1}$$

where ε is the engineering strain, σ is the uniaxial tensile stress, E is the initial Young's modulus, σ_y is the apparent yield stress, and n and r are Ramberg-Osgood parameters. Commonly used values for σ_y, n and r for various grades of steel are listed in Table 4.1. Given the functional form of Equation 4.1, large increases in strain at stress levels only slightly above yield are associated with large values of r. That is, r = 100 results in a "distinct yield plateau" stress-strain curve. On the other hand, for r in the 10 to

20 range there is a more gradual (round-house type) increase in strain for stress levels above yield.

For modern pipe steel, the minimum elongation (ultimate strain) required by API 5L for line pipe varies from 12 to 18%, for test specimens with small cross-sectional area. As shown in Table 4.1, the higher the steel grade the lower is the required minimum elongation. However, the welds used to join the pipe segments have significant impact on the post-yield performance of continuous pipelines as discussed later.

Table 4.1 Yield Stress and Ramberg-Osgood Parameters for Mild Steel and X-Grade Steel Along with Minimum Elongation Required by API 5L (Small Cross-sectional Area Test Specimen)

	Grade-B	X-42	X-52	X-60	X-70	X-80
Yield Stress (MPa)	241	290	359	414	483	552
Minimum Elongation	18%	18%	16%	15%	13%	12%
n	10	15	9	10	5.5	16
r	100	32	10	12	16.6	16

4.1 Continuous Pipeline with Butt Welds

The principal failure modes for corrosion-free continuous pipeline with burial depth of about 3 ft or more are tensile rupture and local buckling. Onshore or offshore pipelines with burial depths less than about 3 ft (i.e., shallow trench installations), as well as offshore pipe laid directly on the seabed, may experience beam buckling behavior. Beam buckling has also occurred during post-earthquake excavation undertaken to relieve compressive pipe strain.

4.1.1 Tensile Rupture - PGD Hazard

When strained in tension, corrosion-free steel pipe with arc-welded butt joints is very ductile and capable of significant tensile yielding before rupture. On the other hand, older steel pipe with gas-welded joints often rupture at much smaller strain levels. For example, as described in Section 10.1.6.2, tensile tests on 30 specimens taken from a 1925 oxyacetylene-welded pipeline indicate about two-thirds had rupture strains of 1.0% or less, while about a third had rupture strains of 0.2% or less. That is, in some cases the welds failed before the pipe yielded. In addition, as discussed in detail in Section 4.2, steel pipe with welded slip joints does not perform as well as steel pipe with butt-welded joints. The 1994 Northridge event provides a case history of these differences in behavior. According to T. O'Rourke and M. O'Rourke (1995), none of the four arc-welded steel pipes along Balboa Blvd. with butt joints suffered tensile rupture when subjected to longitudinal PGD. However, three pipes with gas-welded slip joints suffered tensile rupture when subjected to the same PGD.

When the pipes are jointed with welds in the field, the weld material is typically stronger but less ductile than the parent material well away from the weld. In addition, due to the heat generated by the fusion welding process, the pipe material adjacent to the weld in the so-called heat affected zone (HAZ) also becomes less ductile. Two other factors that make the joint a 'weak' point in a continuous pipeline include tolerable defects in the welds and enhanced potential corrosion at joint coatings made in the field. For these reasons, the allowable tensile strains recommended in various guidelines are only a fraction (less than a third) of the minimum required elongation.

Over the years there have been a number of values suggested for the allowable tensile capacity of steel pipe with good quality butt welds. Newmark and Hall (1975) suggest 4% as the ultimate tensile strain for design purposes. The ASCE *Guidelines for the Seismic Design of Oil and Gas Pipeline Systems* (1984) permit longitudinal strains in the 3 to 5% range. In relation to a natural gas pipeline risk assessment project, Wijewickreme et al. (2005) use 3% and 10%, respectively, as the pipe strains corresponding to 10% and 90% probability of tensile rupture. Notice that these suggested tensile limits are given in terms of pipe strain. Since these limits are well above yield, small changes in stress are associated with large changes in strain, particularly for steel with a large Ramberg-Osgood r parameter. As such, strain is a better measure of pipe behavior.

In both the 2001 ALA Guidelines and the 2004 Pipeline Research Council International (PRCI) Guidelines for Gas and Liquid Hydrocarbon Pipelines (Honegger and Nyman 2004), the suggested tensile strain level for modern pipeline with high quality overmatched welds are a function of the performance goal. For pipelines where the performance goal is maintenance of pressure integrity (envisions a pipe that does not leak but may well have to be replaced after the design event), the tensile strain limit is 4 % in the ALA Guideline and 2 to 4% strain in the PRCI Guideline. If the performance goal is normal operability (post-event functionality of the pipe is expected), the ALA strain limit is 2% while the PRCI limit is 1 to 2%. For load-controlled conditions (hazards other than transient ground strain and PGD), the suggested tension strain limit in the PRCI Guideline is 0.5%.

The suggested tensile strain limits for onshore butt-welded modern steel pipe are summarized in Table 4.2.

For offshore pipelines, the Canadian Standard (CSA 2003) suggests a tensile strain limit of 2.5%. In the Norwegian Standard (DNV, 2000) the ordinary limit is 2%. However, a strain up to 4% is allowed if qualified by tensile tests and the Charpy V-notch test. Furthermore, in the Norwegian Standard the 2% strain limit is suggested for the normal operability performance goal. This limit is based in part on the corrosive offshore environment and difficulties in simply getting access to the pipeline.

Interestingly, even though the ultimate strain (maximum elongation) for the steel grades listed in Table 4.1 are different, the recommended allowable tensile strains for both onshore and offshore pipe are not functions of the steel grade nor the weld strength.

■ **Table 4.2 Recommended Maximum Tensile Strain for PGD – Onshore Steel Pipe with Good Quality Butt Welds**

Newmark & Hall (1975)	1984 ASCE Guideline	2001 ALA Steel Pipe Guideline	2004 PRCI Guideline	Wijewickreme et al. (2005)
4%	3 to 5%	4% – (pressure integrity goal) 2% – (normal operability goal)	2 – 4% (pressure integrity goal) 1 – 2 % (normal operability goal)	3% (10% probability of tensile rupture) 10% (90 % probability of tensile rupture)

4.1.2 Local Buckling - PGD Hazard

Buckling refers to a state of structural instability, in which an element loaded in compression experiences a sudden change from a stable to an unstable condition. Local buckling (wrinkling) typically involves inward kinking of the pipe wall adjacent to outward bulging for low to moderate internal pressures. For high internal pressure, an outward bulge is more common. The initiation of local shell wrinkling typically does not result in leakage or loss of the pressure boundary. However, all **further** geometric distortion caused by ground deformation or wave propagation tends to concentrate at the wrinkle. As noted by Das et al. (2000), as the wrinkle develops, the pipe strains at the wrinkle increase dramatically (with pipe strains reported in the 5 to 10% range) while the pipe strains beyond the wrinkle remain nominally the same. The resulting large curvatures in the pipe wall can lead to leakage. This is arguably a more common failure mode for steel pipe than tensile rupture. For example, lateral spreading at a river crossing caused a pipe wall tear in a liquid fuel pipeline during the 1991 Costa Rica event, as shown in Figure 4.1. Similar damage to water and gas pipelines was observed in the 1994 Northridge event.

As will be discussed in more detail later, the likelihood of a pipe wrinkle turning into a pipe wall tear is enhanced by the load reversals associated with wave propagation. As an example, wave propagation in the 1985 Michoacan event caused wrinkling and tearing of the Ciudad Nezahualcoyotl water pipe in Mexico City. Figure 4.2 shows a circumferential tear in the Ciudad Nezahualcoyotl pipe wall occasioned by high curvature at a local buckle, presumably in combination with load reversal. That is, the pipe may have winkled first under axial compression and then later cracked under axial tension.

■ **Figure 4.1 Pencil in Tear at Wrinkle in RECOPE Pipeline (Limon, Costa Rica, 1991)**

■ **Figure 4.2 Tear at Wrinkle in Ciudad Nezahualcoyotl Pipeline (Mexico City, 1985)**

4.1.2.1 Stress Limit

In Roark and Young (1975), the longitudinal compressive stress corresponding to elastic buckling of a long, thin walled tube with wall thickness *t*, radius *R* and modulus of elasticity *E*, is given as:

$$\sigma_{cr} = {}^{0.3Et}\!/_{R} \tag{4.2}$$

This test based result is 40 to 60% of the theoretical value. It applies to tubes which are thin walled with $D/t > 20$ and several times longer than the buckle half wavelength of $1.72\sqrt{Rt}$. For D/t ratios of 50 and 150, these half wavelengths correspond to 0.17*D* and 0.1*D,* respectively. That is, the wrinkles or buckles are short in comparison to the pipe diameter.

The **elastic** result in Equation 4.2 (buckling stress less than yield stress) holds only for *D/t* ratios much larger than commonly used for oil, gas or water pipelines. For example, in Equation 4.2 a critical stress of 50 ksi (345 MPa) or lower is only associated with *D/t* ratios of 340 or higher.

Hence, inelastic behavior is expected for pipe with typical *D/t* ratios (*D/t* ranging from 25 to 250). For the inelastic case, Schilling (1965) provides the critical compressive stress for local buckling of an unpressurized thin circular cylinder in air as:

$$\sigma_{cr} = \frac{acEt}{R} \tag{4.3}$$

where c is the local buckling imperfection parameter and a is the plasticity reduction factor. The local buckling parameter is a function of the R/t ratio as shown in Figure 4.3. The plasticity reduction is defined as:

$$a = 1.10\sqrt{\frac{E_s E_t}{E^2}} \tag{4.4}$$

where E_s and E_t are the secant and tangent modulus for the level of stress in question. Relations for E_s and E_t are:

$$\frac{E}{E_s} = 1 + \frac{3}{7}\left(\frac{\sigma}{\sigma_{0.7}}\right)^{n-1} \tag{4.5}$$

$$\frac{E}{E_t} = 1 + \frac{3}{7}n\left(\frac{\sigma}{\sigma_{0.7}}\right)^{n-1} \tag{4.6}$$

where $\sigma_{0.7}$ is the stress corresponding to the intersection of the $0.7E$ secant modulus line and the actual stress-strain curve. Unfortunately, since the plasticity reduction factor is a function of the level of stress, an iterative procedure is required to solve for the critical stress.

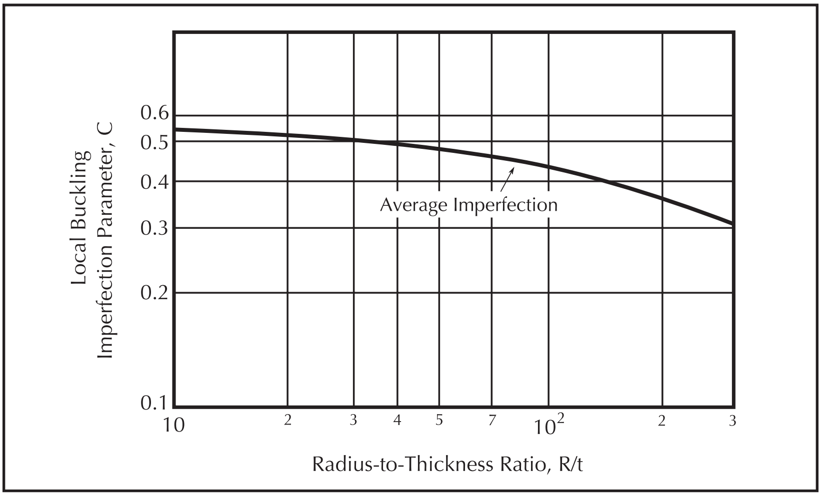

After Schilling, 1965

■ **Figure 4.3 Local Buckling Imperfection Parameter**

The relation is Equation 4.3 is for unpressurized pipe, while most oil, gas, and water pipes have internal pressure. As one might expect, internal pressure has the effect of increasing the local buckling stress. Harris et al. (1957) show that for moderate values of the normalized internal pressure $(P/E)\ (R/t)^2$ the percentage increase in the local buckling stress for an unstiffened circular cylinder is linearly proportional to the normalized internal pressure. Specifically, the percentage increase in buckling stress is zero for zero internal pressure and is about 61% for a normalized internal pressure $(P/E)\ (R/t)^2 = 0.169$ and above. The normalized pressure from Harris can be rewritten utilizing the Strength of Materials relation between the pipes hoop stress and internal pressure. Specifically:

$$\text{Normalized pressure} = (P/E)\ (R/t)^2 = \alpha_n\ \varepsilon_y \left(R/t\right) \tag{4.7}$$

where α_n is the ratio of the hoop stress to the yield stress and ε_y is the yield strain. Based upon the functional form in Equation 4.7, the increase in the critical wrinkling stress is largest for high grade steel with large D/t ratios. As an example, for a Grade B pipe with $D/t = 50$ the normalized pressure is $0.027\alpha_n$ while for X-72 pipe with $D/t = 150$ it is $0.1875\alpha_n$. Assuming that the earthquake occurs during normal operating conditions (as opposed to occurring, for example, during a hydrostatic test) one expects that α_n might be 0.25 or so. Using the Harris relation, the increase in critical buckling stress would be 2.5% for Grade B steel with $D/t = 50$. For X-72 steel and $D/t = 150$, the increase would be 17%.

A disadvantage of the stress-based relations in Equations 4.3 through 4.6 is that one must iterate to determine the critical compressive stress. Due to this drawback and the fact that laboratory instrumentation (strain gages) directly measures strain, limit states for axial compression (like those for axial tension) are often given in terms of strain. Although this eliminates the need to iterate, one still needs a stress-strain relation (e.g., Equation 4.1) since one typically determines the axial pipe strain for the PGD hazard by first calculating the pipe axial force.

4.1.2.2 Strain Limit

The local buckling limit state is a bit more complex than the tensile rupture limit state in that there are different stages of wrinkling: onset (initiation) of wrinkling (i.e., maximum load capacity), various stage of wrinkle formation (e.g., 5% internal diameter loss), up to tearing of the pipe wall. For the performance goal of normal post-event operability, the onset of wrinkling is commonly considered to be the appropriate limit state.

In 1995, Zimmerman et al. compared test data and various empirical curves for the onset of wrinkling (i.e., peak load condition). Based on this comparison, the empirical equation by Stephens et al. (1991) was judged to be the more appropriate lower bound:

$$\varepsilon_{cr} = 2.42(t/D)^{1.59} \tag{4.8}$$

Using Equation 4.8, the critical strain for a D/t ratio of 50 is equivalent to $0.24t/D$ (0.48%), while for D/t = 150 we have $0.126t/D$ (0.084%).

As noted above in the discussion of the Harris, internal pressure has the effect of increasing the local buckling strain. The empirical equation proposed by Gresnigt (1986) includes this effect.

$$\varepsilon_{cr} = 0.5\frac{t}{D} - 0.0025 + 3000\left[\frac{(P_i - P_e)\cdot D}{2tE_s}\right]^2 \tag{4.9}$$

where P_i is the internal pressure, assumed to be larger than the external pressure P_e.

However, after a strong earthquake event, a pipeline system may be shut down for inspection. During the inspection, the internal pressure may be reduced while the pipe strains due to PGD, such as fault movements or landslides, may still be present. That is, the increase in local buckling capacity due to internal pressure may not be present and, hence, it may be prudent to neglect it. Neglecting the increase in capacity due to internal pressure (last term in Equation 4.9), the critical strain becomes:

$$\varepsilon_{cr} = 0.5\,\frac{t}{D} - 0.0025 \tag{4.10}$$

For a D/t ratio of 50, the critical strain in Equation 4.10 corresponds to $0.375t/D$. While for D/t = 150, the critical strain corresponds to $0.125t/D$.

Utilizing α_n defined previously, the absolute increase in critical strain due to internal pressure in Equation 4.9 is:

$$\Delta\varepsilon_{cr} = 3000(\varepsilon_y\ \alpha_n)^2 \tag{4.11}$$

For $\alpha_n = 0.25$, the **percentage** increase in critical strain for a pipe with Grade B steel and $D/t = 50$ is only 3.2%. This suggests that the pressure term has a relatively small influence and may reasonably be neglected.

Finally, in a recent natural gas pipeline project, Wijewickreme et al. (2005) used $0.4t/D$ and $2.4t/D$ as the compression strain corresponding to 10% and 90% likelihood of reaching the local buckling limit state.

In relation to guidance documents for **onshore** pipelines, the 1984 ASCE Guidelines recommended a strain limit corresponding to the initiation of wrinkling of $0.3t/D$ to $0.6t/D$ for PGD effects on gas and oil pipelines. For the PGD hazard with the normal operability performance goal, the 2001 ALA Guidelines suggest Equation 4.9 with modification to *D,* which takes pipe out-of-roundness into account. For the pressure integrity performance goal a strain limit of $1.76t/D$ is recommended. These same suggested compression strain limits appear in the 2005 ALA Water Pipeline Guidelines, again for butt-welded steel pipe.

Finally, the 2004 PRCI Guidelines provide recommended compressive strains for gas and liquid hydrocarbon pipelines, again with butt-welded joints subject to PGD hazards. Like their tensile counterpart, two limited states are envisioned. For post-event operability and steels with rounded stress-strain curves:

$$\varepsilon_{cr} = 0.437\left(\frac{t}{D}\right)^{1.72} \left[1 - 0.89\left(\frac{p}{p_y}\right)\right]^{-1} \left(\frac{E}{\sigma_y}\right)^{0.70} \left(1.09 - \left(\frac{\Delta}{t}\right)^{0.09}\right) \tag{4.12}$$

while for steel with distinct yield plateaus:

$$\varepsilon_{cr} = 1.06\left(\frac{t}{D}\right)^{2.0} \left[1 - 0.50\left(\frac{p}{p_y}\right)\right]^{-1} \left(\frac{E}{\sigma_y}\right)^{0.70} \left(1.09 - \left(\frac{\Delta}{t}\right)^{0.09}\right) \tag{4.13}$$

with a limit of 2%. In Equations 4.12 and 4.13, p is the internal pressure, p_y is the internal pressure for hoop stress equal to yield, and Δ is a radial offset representing a fabrication tolerance (the difference in the as-built pipe radius across a girth weld joint).

The PRCI relations can be viewed as a basic value related to the pipes D/t ratio and three modification factors related to internal pressure, pipe material strength and fabrication imperfection, respectively. Equations 4.12 and 4.13 were originally developed by Dorey et al. (2000, 2006) for onset of wrinkling based upon **best fit** curve for the test data and FE simulation data. Hence, this strain limit is an "average" value from available data and is higher than the lower bound strain limit for the onset of wrinkling.

Like the 2001 and 2005 ALA Guidelines, the 2004 PRCI Guideline recommends $1.76t/D$ for the pressure integrity performance goal (wrinkling but no leakage). The compressive strain limits recommended for onshore pipe in various guidelines are summarized in Table 4.3.

Table 4.3 Recommended Maximum Compressive Strain for PGD - Onshore Steel Pipe with Good Quality Butt Welds

Item	1984 ASCE Guideline	2001 ALA Guideline	2005 ALA Water Pipeline Guideline	2004 PRCI Guideline	Wijewickreme et al. (2005)
Focus	Oil and gas pipelines	Oil and gas pipelines	Water pipelines	Oil and gas pipelines	Gas pipelines
Strain	0.3 t/D to 0.6 t/D	Eqn. 4.9-modified (normal operation) 1.76 t/D (pressure integrity)	Eqn. 4.9-modified (normal operation) 1.76 t/D (pressure integrity)	Eqn. 4.13 or 4.14 (normal operation) 1.76 t/D (pressure integrity)	0.4 t/D (10% prob. of limit state) 2.4 t/D (90% prob. of limit state)

Equations 4.8 and 4.9 provide strain limits corresponding to the **initiation** of a wrinkle or local buckle. They are arguably appropriate for the wave propagation hazard and the normal operability performance goal for the PGD hazard. The pressure boundary limit state, on the other hand, theoretically accepts initial wrinkling of the pipe wall but is intended to avoid tearing of the pipe wall. As discussed above, the pressure boundary limit state is typically addressed via a limiting pipe strain.

However, as noted in the 2005 ALA Guidelines, "once a wrinkle forms, additional shortening of the pipeline will tend to accumulate at the wrinkle." That is, the strain in the pipe away from the wrinkle does not change a great deal. In point of fact, in displacement controlled laboratory tests of welded slip joints, the strain in the pipe away from the wrinkle **reduced** after initial formation of the wrinkle.

As the wrinkle develops, the strain at the wrinkle increases greatly but the strain away from the wrinkle stays nominally the same. Hence, one could argue that any strain (e.g., $1.76t/D$) without a specified gauge length does not properly capture the potential for tearing of the pipe wall. Note in this regard that the PRCI strain criteria is associated with a gauge length of 1.0 to 1.5 pipe diameter.

Note in this regard that the additional displacement occurring after initial wrinkling, which results in tearing of the pipe wall, is expected to be in inches (millimeters) as opposed to feet (meters). For example, the 2005 ALA Guideline cites a test on a 30 in (760 mm) diameter pipe. It is noted that "average compressive strains over one pipe diameter, at the wrinkle, reached 3.5% without breach of the pressure boundary." However, one expects that the peak strain at the wrinkle is substantially larger than the average strain. Furthermore, 3.5% average strain over 30 in (760 mm) corresponds to a total displacement of only 1.05 in (26 mm). One suspects that a total displacement of possibly 3 to 4 in (76 to 102 mm) could result in a peak strain at the wrinkle comparable to the ultimate strain of the material and hence tearing of the pipe wall. If that were the case, the "additional displacement capacity" at the wrinkle would be only 3 to 4 in (76 to 102 mm).

Given the difficulty in calculating pipe strain after the onset of wrinkling, and the comparatively small expected additional displacement capacity (i.e., from wrinkle formation to tearing of the pipe wall), it may be prudent to use a **lower bound** strain for wrinkle formation as the appropriate limit state for the normal operability performance goal, and an **average** wrinkle formation strain for the pressure integrity performance goal.

For offshore pipelines, DNV (2000) developed an equation for pipelines with a D/t ratio smaller than 45 that considers internal pressure, yield stress and the yield to tensile ratio.

$$\varepsilon_{cr} = 0.78\left(\frac{t}{D} - 0.01\right)\left(1 + 5\ \frac{\sigma_h}{\sigma_y}\right)\alpha_h^{-1.5}\alpha_{gw} \quad D/t \leq 45,\ P_i < P_e \qquad (4.14)$$

where t is the remaining wall thickness after considering the corrosion allowance, σ_h is the hoop stress due to internal pressure, σ_y is the yield stress of the pipe, α_h is the maximum allowed yield stress to tensile strength ratio, and α_{gw} is the girth weld factor.

However, as demonstrated by full-scale test (Vitali et al., 2005), Equation 4.14 overestimates the critical strain for onset of wrinkling strain by more than 100%. Mohr (2003) concluded that if the $(1+5\ \sigma_h/\ \sigma_y)$ term is replaced by $(1+\ \sigma_h/\ \sigma_y)$, Equation 4.14 yields more reasonable results. Note that for *D/t* of 45 or more, CSA nominally recommend 0.35*t/D* as the strain limit. At smaller *D/t* ratios the CSA strain limit is somewhat larger than 0.35*t/D*.

Equations associated with the limit state of onset wrinkling are plotted in Figure 4.4 for a pipe with zero internal pressure. In the PRCI curve, Equation 4.13 is used with yield stress of 65 ksi and misalignment of 10%. Note the test data indicates that for both large and small *D/t* ratios, Stephens' limit serves well as a lower bound of the onset buckling strain. The PRCI relation with a misalignment of 10% provides a reasonable 'average' fit to the data.

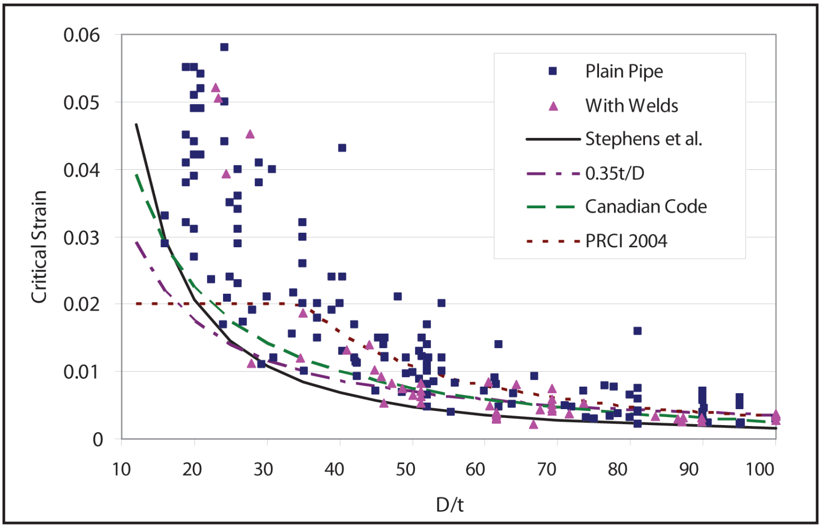

After Mohr, 2003

Figure 4.4 Maximum Compressive Strains - Zero Internal Pressure

4.1.3 Wave Propagation Hazard

There are significant differences between the PGD hazard and the wave propagation hazard. First of all, the wave propagation hazard occurs in every earthquake event and typically affects a significant portion of the whole pipeline network. The PGD hazard, on the other hand, may or may not occur during a particular event, and if it does it only affects a comparatively small portion of the network. Also, as noted above, the nature of the wave propagation hazard (alternating axial tension and compression) is different than that for the PGD hazard (monotonic loading with no load reversals). These differences result in different behavior with respect to the local buckling limit state. For example, Das et al. (2008) recently reported on laboratory tests of 305 mm (12 in) diameter X-52 grade steel pipe with $D/t = 45$. The pipe was subject to internal pressure, an axial compressive load and a bending moment. When the bending moment was increased monotonically, the post-wrinkling behavior was ductile (no leaks or fractures). However, when the axial load and bending moment were cycled (nominally full compression load to zero load to full compression load) the behavior was fairly brittle. Typically, it took about a half dozen cycles (specifically, 4 to 9 cycles) for a fracture or leak to form. One expects less capacity/earlier onset of fracture if the tests cycled from full compression to full tension and back to full compression. Unfortunately, most research on fatigue is directed at low stress and a large number of cycles, while for buried pipe subject to earthquake effects one is interested in high stress and a limited number of cycles.

As a result of these differences, guidelines have typically recommended lower limit state criteria for the wave propagation hazard than for the PGD hazard. Also, since wave propagation involves alternating tension and compression, and common onshore steel pipe has lower capacity for axial compression, the wave propagation limits typically are directed at the local buckling limit state. For example, the 1984 ASCE Guidelines recommend that half of the strain limit corresponding to the initiation of wrinkling be used for the wave propagation (ground shaking) hazard (i.e., $0.15t/D$ to $0.3t/D$). ALA (2001) suggests that 75% of the PGD strain limit for local buckling be used for wave propagation hazards for onshore pipelines in compression. The 2001 ALA Guidelines also establish a 0.5% strain limit for tension, although the compression limit would likely control for common onshore pipe D/t ratios. Table 4.4 lists the recommended strain limits for onshore pipe subject to wave propagation.

Table 4.4 Recommended Maximum Strain for Wave Propagation - Steel Pipe with Good Quality Butt Welds

Guideline	1984 ASCE Guideline	2001 ALA Guideline
Strain	$0.15t/D$ to $0.3t/D$	Tension: 0.5% Compression: 0.75 times local buckling from Eqn. 4.9

Neither the Canadian nor the Norwegian Standards specifically address the wave propagation hazard for offshore pipelines. However, since checks for dynamic loads and fatigue are required, one could argue that strains resulting from wave propagation should be checked. For offshore pipelines, the *D/t* ratio is typically less than 45, and the resulting critical buckling strains are well above 0.5%. Therefore, the 0.5% strain limit for both compression and tension may well be appropriate for the wave propagation hazard.

4.1.4 Beam Buckling

Beam buckling of a pipeline is similar to Euler buckling of a slender column in which the pipe/column undergoes a transverse displacement either upward or in the horizontal plane. The relative lateral movement occurs over a substantial length of pipe and, hence, the compressive pipe strains are not large. As a result, beam buckling of a pipeline in a ground compression zone is considered more desirable than local buckling, since the strains are less and the potential for tearing of the pipe wall is lessened.

4.1.4.1 Onshore Pipelines

Beam buckling of pipes has been observed in a few events. For example, during the period from 1932 to 1959, displacements on the order of 360 mm (14 in) accumulated across the Buena Vista reverse fault (Howard, 1968). This ground movement led to compression stresses in oil pipelines, which ranged in diameter from 51 to 406 mm (2 to 16 in). The oil pipelines buried at depths between 0.15 and 0.30 m (6 to 12 in), in loose to medium soil, lifted out of the ground as a result of compressive forces.

Another example occurred during the 1979 Imperial Valley earthquake. Two high-pressure pipelines, 219 mm (8.6 in) and 273 mm (10.7 in) in diameter, crossing the main trace of the Imperial fault were affected. No evidence of local buckling or beam buckling was observed immediately after the event. However, removal of cover during inspection after the earthquake caused both pipes to displace laterally in a beam buckling mode (McNorgan, 1989).

As opposed to tensile rupture, or wrinkling and associated tearing of the pipe wall, the pipes do not “fail” after beam buckling. The beam bucking of pipes may better be described as a serviceability problem since the pipe continues to serve its function of transmitting fluid without interruption. In that sense, it is difficult to establish a failure criterion for beam buckling strictly in terms of pipe material properties. Its occurrence depends on several factors, such as the bending stiffness and burial depth of the pipe, as well as initial imperfections. Intuitively, beam buckling is more likely to occur in pipelines buried in shallow trenches and/or backfilled with loose materials. That is, the critical load for beam buckling is an increasing function of the cover depth. Hence, if a pipe is buried at a sufficient depth, it will develop local buckling before beam buckling.

The general topic of beam buckling of buried pipelines has been the subject of analytical studies by Marek and Daniels (1971), Hobbs (1981), Kyriakides et al. (1983) and Ariman and Lee (1989).

Meyersohn (1991) arguably presents results for straight pipe in the most user friendly form. He determined a critical cover depth by setting the lowest beam buckling stress equal to the local buckling stress. Any pipe buried with less cover than the critical depth would experience beam buckling before local buckling. Conversely, if the pipe is buried at a depth more than the critical depth, it will experience local buckling. Figure 4.5 shows the critical cover depth for Grade B and X-60 steel pipes.

The shaded areas in the figure correspond to different degrees of backfill compaction. Note that critical depth for X-60 steel is substantially larger than that for Grade B steel (note the change in vertical scale). That is, stronger pipe are more susceptible to beam buckling. However, as noted by Meyersohn (1991), the t/D ratio is typically less than or about equal to 0.02 (D/t typically greater than or about equal to 50). Hence, from Figure 4.5, the likelihood of beam buckling of moderate temperature buried pipelines is small since the critical depth is less than typical burial depths.

4.1.4.2 Offshore Pipelines

Offshore pipelines typically have less restraint for lateral and vertical pipe movements than onshore pipelines. As a result, beam buckling is the principal “failure” mode for offshore pipes subject to compression due to PGD. Beam buckling includes upheaval buckling and lateral buckling (snaking). Upheaval buckling occurs typically for pipelines with significant lateral restraints (e.g.,

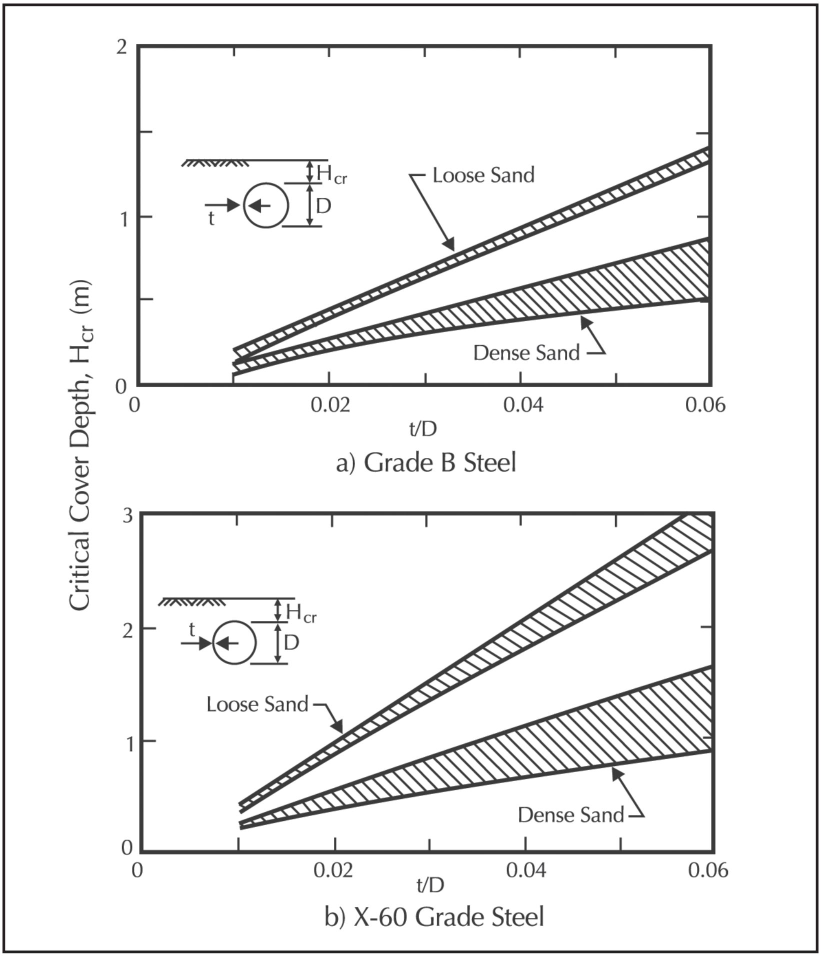

After Meyersohn, 1991

■ **Figure 4.5 Analytical Critical Cover Depth of Pipe for Grade B and X-60 Steel**

buried offshore pipelines). For pipelines laid on seabed, lateral buckling is more likely.

Upheaval buckling often requires treatment (e.g., reburial) because the suspended pipelines are venerable to third party damage (shipping anchors, fishing activity, etc.) and fatigue under hydrodynamic loads. Lateral buckling is acceptable for pipelines that require no protective soil cover, especially in deep water. Lateral buckling may be used as a means to release the compressive forces in the pipe. For example, lateral buckling is a desirable method to reduce the thermal expansion in high temperature – high pressure oil field pipelines (flowlines).

4.2

Continuous Pipeline with Welded Slip Joints

The failure criterion for steel pipelines with butt-welded joints is based on the strength of pipe material since properly detailed butt joints are stronger than the parent or base material away from the joint. This, however, is not the case for steel pipe with welded slip joints (WSJ). Figure 4.6(a) shows a WSJ with an exterior fillet weld, while Figure 4.6(b) shows the weld detail—specifically, the eccentricity e_c, the small gap between the outer surface of the spigot and the inner surface of the bell, g_p, and the length of the

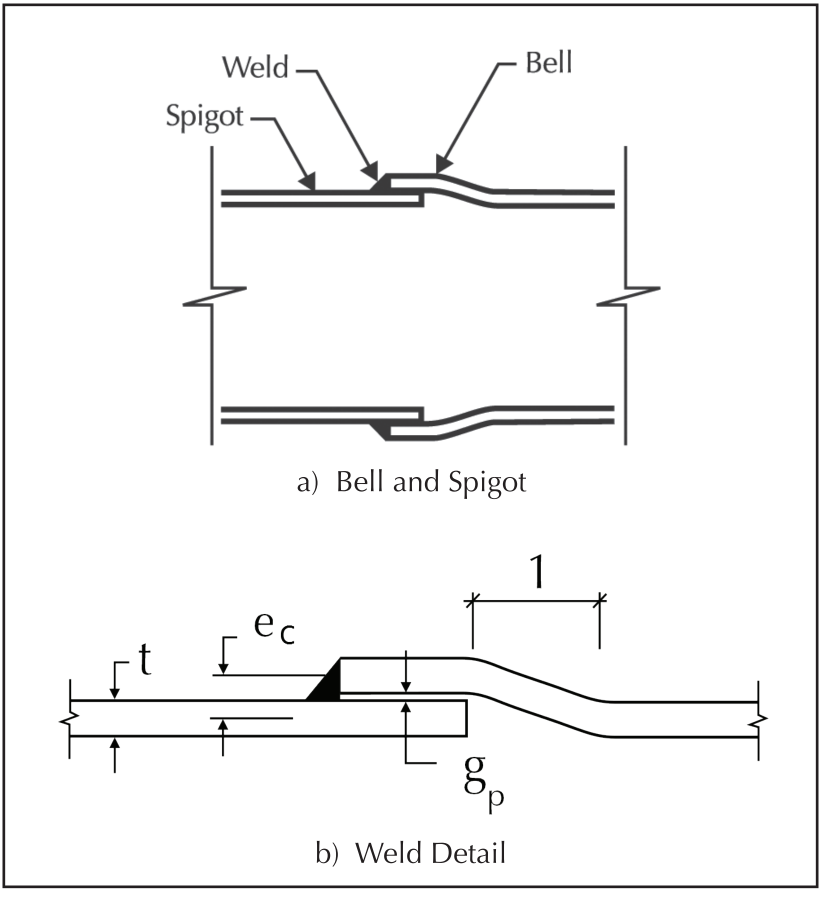

■ **Figure 4.6 WSJ with Exterior Fillet** curved bell, ℓ. Alternately, WSJs can have an interior fillet weld, or both exterior and interior fillets. Due to the eccentricity and the presence of the fillet weld, the load capacity of WSJs, is less than that for the parent material away from the joint, particularly for a WSJ subject to longitudinal compression. As such, pipelines with WSJs are susceptible to failure during earthquakes, as illustrated by the Balboa Blvd. example cited above.

4.2.1 Axial Tension

4.2.1.1 Analytical Models

Brockenbrough (1990) considered an unpressurized WSJ pipeline with an interior fillet weld subject to axial tension. His model evaluated a strength limit characterized by yielding at the weld. As one might expect, the joint efficiency (load capacity at WSJ normalized by yield load for unpressurized pipe away from the joint) is a decreasing function of the eccentricity. Specifically, the analytical relation is:

$$\text{joint efficiency} = (k^2 + 1)^{\frac{1}{2}} - k \tag{4.15}$$

where k is the ratio of the eccentricity to the wall thickness. For $k = 1.0$ (gap = 0) the efficiency is 0.41, while for $k = 1.25$ (gap = $0.25t$) the efficiency is 0.35. The expected joint efficiency for the limiting value of $k = 0$ (no eccentricity) is 1.0 as expected.

As noted above, Brockenbrough considered an unpressurized pipe subject to axial tension. However, one expects similar or slightly larger joint efficiencies if internal pressure is considered. That is, using the Von Mises criterion, the yield condition for biaxial tension (longitudinal tension and hoop tension) is a bit larger than that for uniaxial tension.

4.2.1.2 Experimental Results

As will be shown subsequently, experimental test results are particularly important in understanding the behavior of WSJ pipelines. Brockenbrough presents test data for WSJ pipe with closed ends subject to internal pressure. Due to these conditions, the longitudinal tension stress is always exactly half the hoop tension stress. Table 4.5 summarizes results from a 1958 and 1984 series of tests.

■ **Table 4.5 Internal Pressure Tests on WSJ Pipe with Closed Ends**

Year	No.	Diameter (in)	Wall Thickness (in)	Gap (in)	Weld Size (in)		Joint Efficiency
					Int.	Ext.	
1958	1	48	5/16	-	5/16	-	0.93
1958	2	48	5/16	-	5/16	-	1.00
1958	3	48	5/16	-	-	5/16	0.99
1958	4	48	5/16	-	-	5/16	0.99
1984	2	61	5/16	.05/.08	5/16	1/4	0.80
1984	3	61	5/16	.03/.10	1/4	5/16	0.78
1984	4	61	5/16	.05/.08	5/16	-	0.76
1984	5	61	5/16	.04/.10	-	5/16	0.76
1984	6	61	5/16	.09/.11	5/16	-	0.83

The 1958 tests as well as the single fillet 1984 tests (No.'s 4, 5, and 6) suggest that, at least for axial tension, the location of the fillet weld (exterior or interior) does not make a great deal of difference in terms of axial load capacity (joint efficiency). Also, surprisingly, the 1984 double fillet tests (exterior and interior fillets) suggest that double fillets are not significantly better than either a single exterior or a single interior fillet. However, this may be simply an artifact of the applied test loads. Note that both the double fillet tests, as well as Test No. 6 in the 1984 series, failed by longitudinal (hoop stress related) rupture. All the others failed by circumferential (longitudinal stress related) rupture or were discontinued before rupture (No.'s 3 and 4, 1958). Hence, the double fillets may well have increased the axial load capacity. The pipe may simply have failed due to large stress in the hoop direction, as opposed to a lack of strength in the longitudinal direction.

Both series have joint efficiencies at least double those predicted by the Brockenbrough theory in Equation 4.15. It seems likely that this is due to the fact that the Brockenbrough theory considered yielding while the experimental tests measured rupture and, as Brockenbrough describes it, a "decrease in eccentricity as the joint region tends to **straighten** under the action of the axial force." That is, as with the Tawfik and O'Rourke model discussed later, the Brockenbrough analytical model is a small deformation model. As such, the equilibrium equations are not reformulated based upon the deformed geometry of the WSJ. That is, the joint eccentricities remain the same throughout the analysis. For WSJ subject to axial tension, the deformed shape of the joint tends to reduce the eccentricity for a single fillet (either exterior or interior) joint. As a matter of fact, the observed joint efficiency nominally corresponds to the expected ultimate strength of a transversely loaded fillet weld without eccentricity.

$$\text{Weld Capacity} = 1.33\,(0.6F_{exx})\,(0.707t_w)\,(\pi D) \tag{4.16}$$

where $0.6F_{exx}$ is the ultimate shear strength of the electrode, $0.707t_w$ is the nominal throat dimension for the weld, and πD is the circumference of the pipe. The factor of 1.33 accounts for the 33% increase in capacity for transverse welds in comparison to longitudinal welds.

Recently, Mason and T. O'Rourke (2009) reported on a series of two unpressurized WSJ pipes with exterior fillets subject to axial tension. The pipe diameter was 12 in (0.32 m), the wall thickness was ¼ in (6.4 m) and the gap was 1/32 in (0.75 mm). The pipe failed at a circumference rupture well away from the WSJ. The failure loads were roughly 10% larger than the uniaxial yield load for the pipe away from the WSJ. Hence, from these tests, the joint efficiency was about 1.1. Note that the fillet weld throat dimension was reported to be 0.252 in. That is, the fillet weld was overbuilt, roughly 40% thicker than what one would presume for a ¼ in fillet. Again, as with the tests in Table 4.5, the estimated failure load for the "as-provided" fillet weld without eccentricity—including a 33% increase due to its transverse orientation (i.e., Equation 4.16)—was not greatly different than the observed failure load.

4.2.2 Axial Compression

4.2.2.1 Analytical Models

The first analytical investigation of WSJ behavior was undertaken by Tawfik and T. O'Rourke (1985). They considered a pressurized pipe having a WSJ with an exterior fillet weld subject to axial **compression**. They investigated two limit states. The first limit state (Mode I) involved yielding at the weld. For that limit state, the joint efficiency is a decreasing function of the eccentricity e_c. Specifically, for an eccentricity equal to the wall thickness ($e_c = t$, hence, gap = 0) the joint efficiency is about 0.29, while for an eccentricity equal to $1.25t$ (gap = $0.25t$) the efficiency is about 0.25. Tawfik and O'Rourke assume an internal pressure such that the hoop stress is half the material uniaxial yield stress.

The second limit state (Mode II) involves yielding of the curved bell. For that limit state, the joint efficiency is an increasing function of the length of the bell section. Tawfik and T. O'Rourke choose to use a normalized length, specifically the bell length divided by the pipe radius, l/R_0. For $l/R_0 = 0.25$, the joint efficiency was about 0.3, while for $l/R_0 = 1.0$ the joint efficiency was about 0.6. For very large bell lengths, the joint efficiency approaches 0.65, which is consistent with the expected axial compression capacity from the Von Mises yield criterion, for a tensile hoop stress of half the uniaxial yield stress.

Figure 4.7 shows the joint efficiency for Modes I and II plotted versus the normalized joint length, l/R_0, for an eccentricity of $e_c = 1.06t$ (gap = $0.06t$). Since the lower of the two strengths controls, Mode II (curved bell) controls the behavior for $l/R_0 < 0.3$, while Mode I (weld) controls for larger joint lengths. Note that Tawfik and O'Rourke investigated two **strength** related limit states, and the strength limit states were yielding either at the weld or in the curved portion of the bell. As such, they conservatively neglected any benefits related to strain hardening of steel beyond yield. On the other hand, they neglect all instability limit states such as local buckling.

In relation to a forensic investigation, Moncarz et al. (1987) presents inelastic finite element results for a WSJ pipeline with an interior fillet weld, subject to axial **compression**. The pipe di-

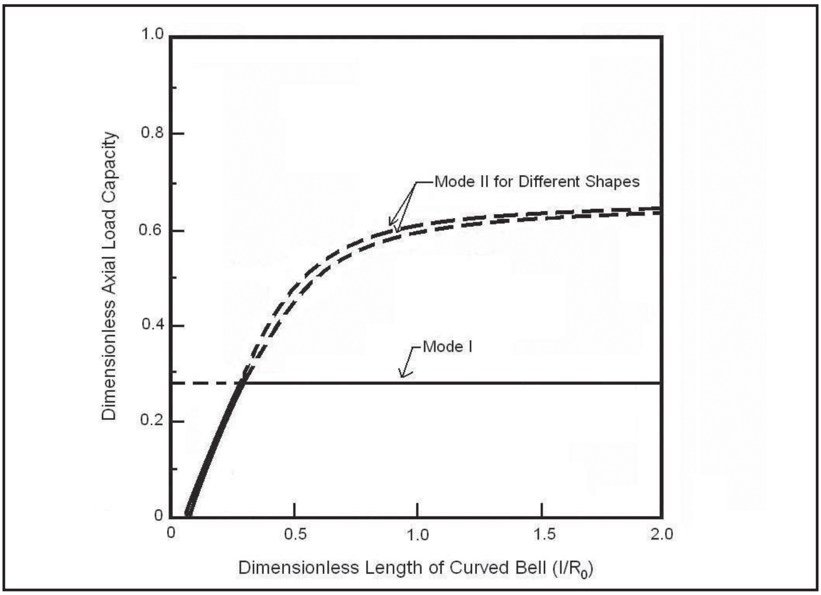

After Tawfik and T. O'Rourke, 1985

■ **Figure 4.7 Joint Efficiency of Slip Joints with Exterior Fillet Weld** ameter was 108 in (2.74 m), the wall thickness was 0.5 in (12.7 mm) and the material uniaxial yield stress was 42 ksi (290 MPa). For a hoop tensile stress of about 55% of uniaxial yield, the joint efficiency for a gap of 1/8 in (3 mm) was 0.40.

Finally, Eidinger (1999) presents finite element results for an unpressurized pipe with double fillet welds subject to axial **compression**. In this case, the analysis included large deformation ("large geometry") effects. The pipe material was mild steel with a uniaxial yield stress of 40 ksi and a strain at ultimate load of 21%. The pipe model had a *D/t* ratio of 66/0.375 or 176 and a total length of 36 in. Figure 4.8 presents the load versus axial shortening curve. At low levels of axial compression, elastic shortening was due mainly to elastic bending at the joint. When the axial shortening reached 0.1 in, the joint was at yield and plastic deformation within the joint then ensued. The axial compression load of 300 kips/radian corresponds to a strain level of 0.084% or about 60% of uni-axial yield. For axial shortening greater than 0.1 in, the axial load in the pipe decreases, presumably an artifact of the displacement controlled nature of the simulated test. During this time, all additional shortening is due to wrinkling at the joint. When the total shortening reached 1.0 in, the tensile strains at the joint (toe of exterior fillet, curved bell region) were about 14%. Hence, if the total axial shortening reached 2 in, one would expect tearing of the pipe wall and loss of the pressure boundary.

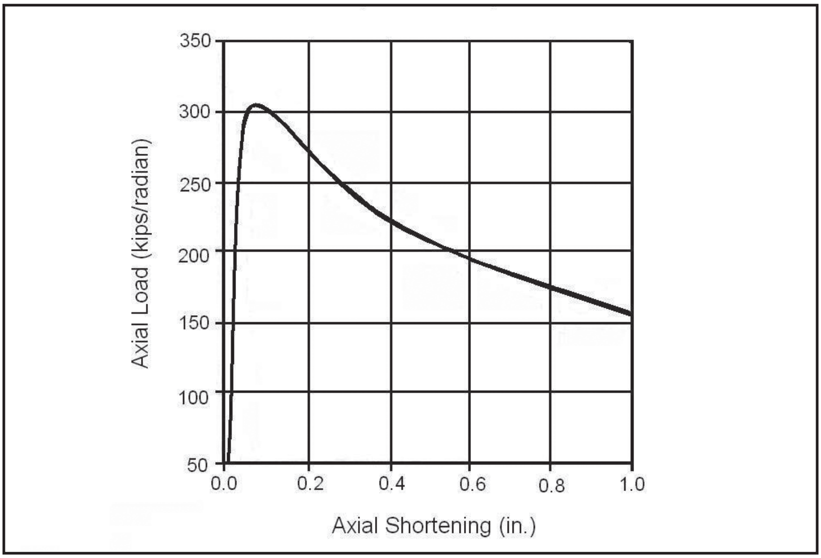

After Eidinger, 1999

Figure 4.8 Axial Load vs. Axial Shortening for WSJ Pipe Under Compression

4.2.2.2 Experimental Results

Mason et al. (2009) at Cornell report on a combined experimental and analytical investigation of unpressurized WSJ pipe subject to axial compression. The experimental portion involved five tests on pipe ranging in diameter from 12 to 36 in (300 to 910 mm), with *D/t* ratios ranging from 48 to 244. The smaller diameter pipe had exterior fillet welds, while the larger diameters (32 in and 36 in) had interior fillets. The length of the curved bell (see Figure 4.6(b)) was 3.5 to 4 in for the 12-inch-diameter specimens, and 4 and 11½ in for the 32- and 36-inch-diameter specimens, respectively.

The load-displacement curves for these Cornell tests are quite similar to that shown in Figure 4.8. As an example, for Test No. 5 the peak axial load occurred at an axial displacement of 0.1 in. After the peak load was obtained, the axial load **decreased** as the axial displacement increased. As noted above, this behavior is presumably a result of the displacement controlled nature of the tests. All tests were terminated at an axial displacement of 1.0 in (25.4 mm), and there was no observed tearing of the pipe wall. Finally, it should be noted that in all tests, the wrinkling occurred at the curved portion of the bell. That is, in relation to the 1985 Tawfik and T. O'Rourke model, Model II limit states were observed.

Table 4.6 presents the results of the compression tests wherein the axial capacity is characterized by the joint efficiency. Note the clear dependence on the specimen *D/t* ratio. As one might expect, the joint efficiency decreases with increasing *D/t*. Since both the smaller diameter specimens had exterior fillets and all the larger diameter specimens had interior fillets, one is unable to determine the effects of fillet weld location from the experimental tests alone.

Table 4.6 Axial Compression Tests on Unpressurized WSJ Pipe

No.	Diameter (in)	*D/t*	*l/t*	Fillet Weld	Joint Efficiency
1	12	48	15	exterior	0.78
2	12	48	15	exterior	0.81
3	32	244	32	interior	0.43
4	36	144	46	interior	0.66
5	36	144	46	interior	0.64

In Table 4.6, the l/t ratio is used to normalize the length of the curved bell. Since the offset or eccentricity is the wall thickness plus a presumably small gap, the l/t ratio quantifies the curvature in the bell. As such, the ratio is expected to properly quantify the influence of bell geometry. Unfortunately, since there are no test results in which the l/t ratio varied for a constant D/t ratio, one is unable to determine the influence of bell geometry from the experimental tests alone.

As noted above, the Cornell program included an analytical investigation of unpressurized WSJ under axial compression. A "large geometry" analysis was conducted with the length of the curved bell taken to be a constant, $\ell = 6$ in, for all simulations. As with the experimental tests, the limit state in the analytical simulations was buckling at the curved wall. Figure 4.9 presents the resulting joint efficiency for a WSJ pipe with exterior welds as a function of the pipe D/t ratio, for various values of the bell geometry (l/t) ratio. Similar results are presented in Figure 4.10 for WSJ pipe with interior welds.

As one might expect, the joint efficiency is a decreasing function of the pipe D/t ratio. Similarly, the joint efficiency (axial load capacity) is an increasing function of the bell geometry ratio l/t. Recall that the curvature in the bell region is an inverse function of the l/t ratio. Somewhat surprisingly, all other things being equal, the calculated joint efficiency of a WSJ with exterior welds is **larger** than the one with interior welds. It is thought that this unexpected behavior is related to the distribution of bending moment within the curved bell. For a WSJ with an exterior fillet, a simple statics model suggests that the bell portion is subject to double curvature bending (one portion of the curved bell tending to deform outward, the other tending to deform inward). For a WSJ with an interior fillet, the bell is subject to single curvature bending, with all portions tending to deform outward.

The normalized axial load capacities in Figures 4.9 and 4.10 are reasonably consistent with the Cornell experimental test results, as well as analytical results by others. For experimental tests No.'s 1 and 2 in Table 4.6, the joint efficiency was about 0.8 for a pipe with exterior fillet welds, a D/t of 48 and l/t of 15. Similar experimental tests No.'s 4 and 5 (interior fillets, $D/t = 144$, $l/t = 46$) are reasonably consistent with Figure 4.10. That is, the experimentally determined joint efficiency is larger than what one expects for $l/t = 24$. The same can be said for the Moncarz et al.

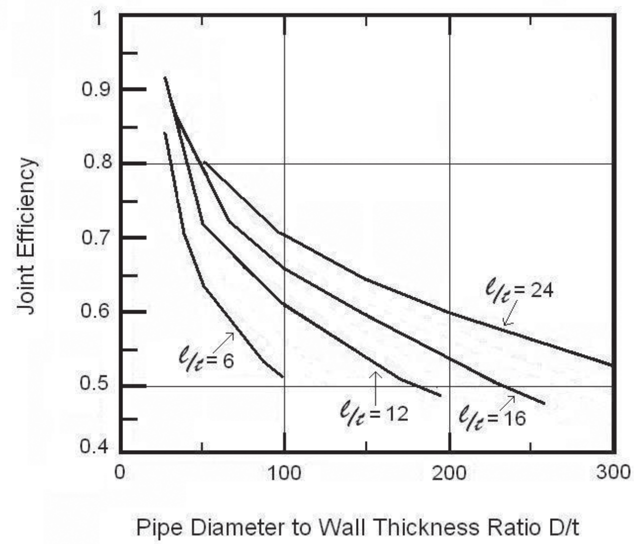

After Mason et al., 2009

■ **Figure 4.9 Joint Efficiency for WSJ Pipe in Compression with Exterior Welds**

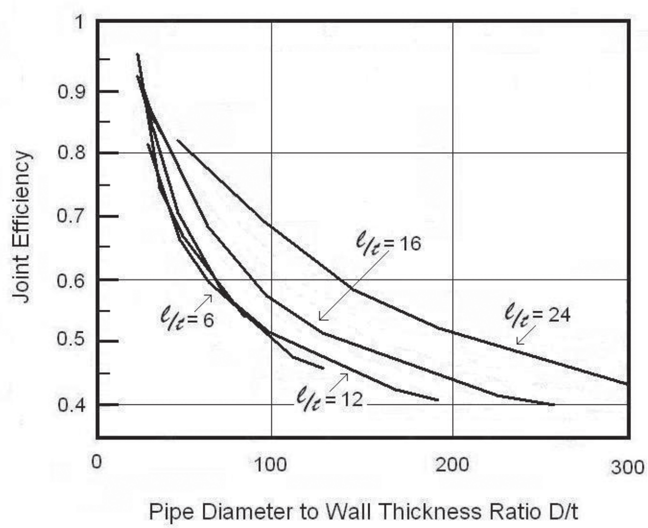

After Mason et al., 2009

■ **Figure 4.10 Joint Efficiency for WSJ Pipe in Compression with Interior Welds** analysis (interior fillet, $D/t = 216$, l/t = unknown, joint efficiency = 0.40), as well as the Eidinger analysis (double fillets, $D/t = 176$, l/t = unknown, joint efficiency = 0.6). The one possible exception is Test No. 3 in Table 4.6 (interior fillet, $D/t = 244$, $l/t = 32$, efficiency = 0.43). Figure 4.10 suggests that the expected joint efficiency should be something larger than 0.47. The Cornell program also included an analysis of steel pipe with cement liners. As one might expect, the axial load capacity increases if the liner is assumed to behave in a composite fashion with the steel pipe. However, field inspections of unreinforced cement liners (personal communication with J. Eidinger, August 2009) suggest that the assumption of composite action is likely unwarranted.

4.2.3 Recommended Limit States

In relation to guidance documents, the 2005 ALA Guideline is the only one that addresses WSJ pipe. For axial **tension** loading, they opine that "girth joints in single-lap welded steel pipe will generally not be strong enough to allow longitudinal tensile yielding in the main pipe." However, as demonstrated above, single-lap welded pipe (WSJ pipe with either an exterior or interior fillet) with **over-built welds** can have joint efficiencies of 1.0. That is, they can develop longitudinal yielding in the "main pipe." For double-lap welded steel pipe, ALA 2005 recommends that the allowable strain away from the WSJ should be limited to 2 to 4%. These suggested limits on the other hand, comparable to those for tensile loading of steel pipe with butt-welded joints, seem excessively unconservative. More realistic estimates of tensile capacity can be developed knowing weld size, electrode strength, and Equation 4.16.

For WSJ pipe in **compression**, ALA 2005 recommends limiting the axial strain in the main pipe away from the welds to 40% and 60% of yield for pipe with single and double fillets, respectively. These recommended limits seem reasonable in relation to the joint efficiencies shown in Figures 4.9 and 4.10.

4.2.4 Comparison with Butt Welds

In relation to the most common limit states for continuous onshore pipelines, the tensile capacity exceeds the compressive capacity, and the capacity of modern butt-welded pipe exceeds that for pipe with WSJs. For butt-welded pipe subject to axial tension, a commonly recommended maximum strain is 3%. For the same pipe subject to axial compression, a commonly recommended maximum strain would be roughly 0.6% for a pipe *D/t* slenderness ratio of 100 (roughly a fifth of the tensile capacity).

For WSJ pipe in axial tension, the expected capacity is a function of the fillet weld size. However, the axial capacity typically is less than that for longitudinal yielding in the parent material. As such, a maximum allowable axial strain may be on the order of 0.2% (a third of butt-welded pipe in compression, a fifteenth of butt-welded pipe in tension). For WSJ pipe in axial compression, the expected capacity is a function the pipe *D/t* ratio, the bell geometry (*l/t*), as well as the location of the fillet (interior or exterior). For a *D/t* ratio of 100, the axial capacity would be roughly 60% of that for longitudinal yielding. As such, a maximum allowable axial strain may be on the order of 0.12% (a fifth of that for butt-welded pipe in compression, a twenty-fifth of that for butt-welded pipe in tension).

4.3 Segmented Pipeline

For segmented pipelines, particularly those with large diameters and relatively thick walls, observed seismic failure is most often due to distress at the pipe joints. For example, in the 1976 Tangshan earthquake, Sun and Shien (1983) observed that around 80% of pipe breaks were associated with joints. As shown in Figure 4.11, M. O'Rourke and Ballantyne (1992) identified six types of damage mechanisms to segmented pipelines during the 1991 Costa Rica earthquake. For the CI and DI transmission pipelines in the Limon area, 52% repairs are due to pull-out at joints (Figure 4.11(f)) and 42% repairs are due to breaks at segments (Figure 4.11(a)).

Axial pull-out, sometimes in combination with relative angular rotation at joints, is a common failure mechanism in areas of tensile ground strain. This is due to the fact that the shear strength of joint caulking materials, or the friction force due to compression of the rubber gasket, is much less than the tensile strength of the pipe. That is, the segmented joint is the weak link. In areas of compressive ground strain, telescoping or crushing of the bell of bell and spigot joints is a fairly common failure mechanism in, for example, concrete pipes. For small diameter segmented pipes, circumferential flexural failure has been observed in areas of ground curvature. For example, as observed by T. O'Rourke et al. (1991), more than 80% of the breaks in cast iron pipes with small diameters (100 to 200 mm or 4 to 8 in) in the Marina District after the 1989 Loma Prieta event were round cracks in pipe segments close to joints.

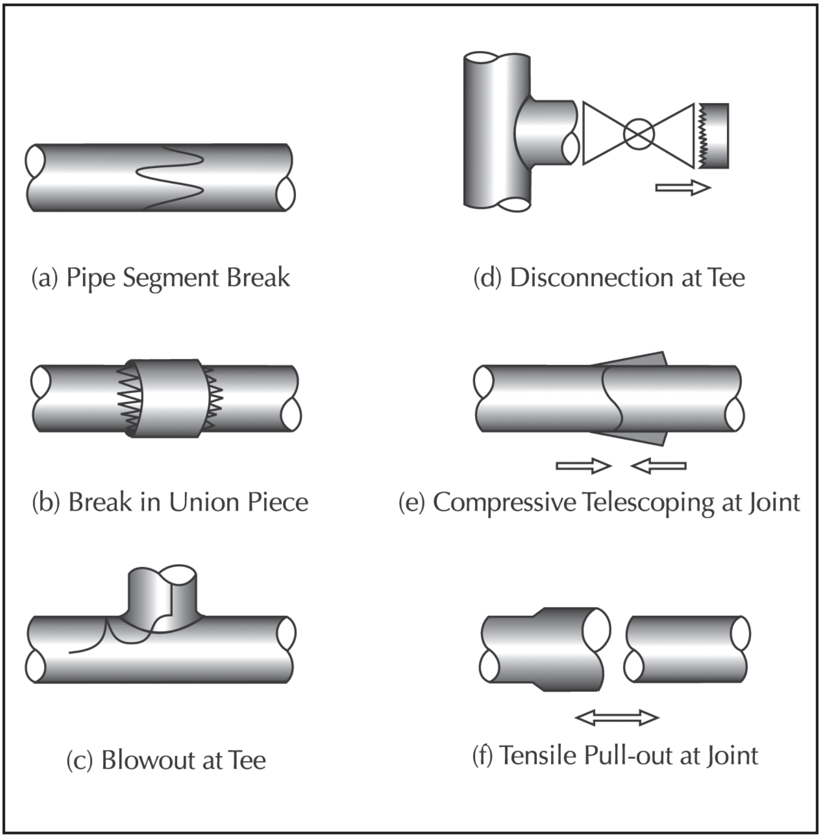

After M. O'Rourke and Ballantyne, 1992

■ **Figure 4.11 Damage Mechanisms for Segmented Pipelines**

4.3.1 Axial Pull-out

In terms of failure criterion, information for the various types of segmented pipes is not as well developed as for continuous pipes. El Hmadi and M. O'Rourke (1989) summarized the then available information on joint pull-out failure. Specifically, based on laboratory tests by Prior (1935), El Hmadi and M. O'Rourke (1989) established a cumulative distribution for leakage as a function of the normalized joint axial displacement u_j^u/d_p shown in Figure 4.12. Note that u_j^u is the joint opening for leakage and d_p is the joint depth.

As shown in Figure 4.12, the mean value of the joint opening corresponding to leakage at the joint is 0.52 d_p with a coefficient of variation of 10%. Hence, El Hmadi and M. O'Rourke suggest a relative joint displacement corresponding to 50% of the total joint depth as the failure criterion for pull-out of segmented pipelines with "rigid" joints.

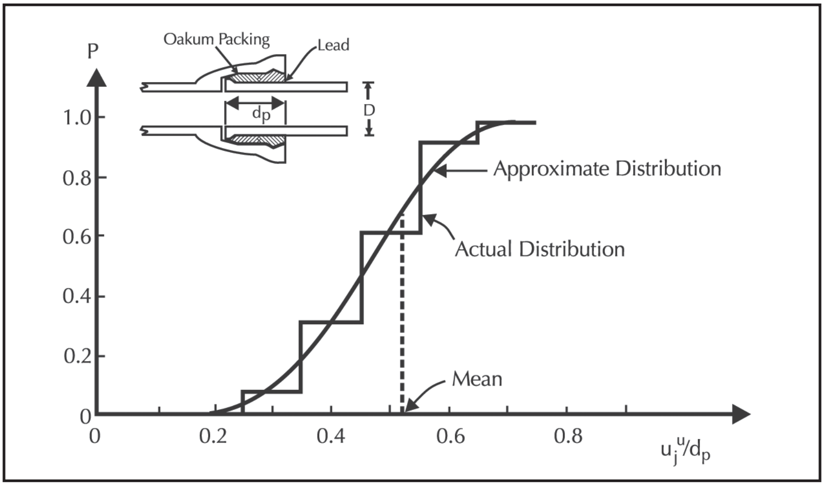

El Hmadi and M. O'Rourke, 1989

■ **Figure 4.12 Cumulative Distribution Function for Leakage of Lead Caulked Joints**

More recently, laboratory tests on concrete cylinder pipes with rubber gasketed joints by Bouabid and M. O'Rourke (1994) suggest that at moderate internal pressures the relative joint displacement leading to significant leakage corresponds to roughly half the total joint depth. Hence, it would appear that a relative axial joint extension of roughly half the total joint depth may be an appropriate failure criterion for many types of segmented pipes.

With this mechanism in mind, Table 4.7 lists the joint depth for various diameters for Ductile Iron Pipe (AWWA C151), pit-cast Cast Iron Pipe, and Concrete Cylinder Pipe (AWWA C-300 through C-302). As one might expect, the joint depth is an increasing function of nominal diameter. This suggests that for a given pipe type, damage rates due to joint pull-out would be a decreasing function of diameter.

Table 4.7 Joint Depth for Various Diameters of Ductile Iron, Cast Iron and Concrete Cylinder Pipe

	Joint Depth (in)		
Nominal Diameter (in)	Ductile Iron	Cast Iron	CCP
6	3.5	3.5	
12	4.25	4.0	
18	4.88	4.0	
24	5.12	4.0	
30	6.12	4.5	3.25
48		5.0	3.87
60		5.5	4.5
72		5.5	4.5

4.3.2 Crushing of Bell and Spigot Joints

As noted by Ayala and M. O'Rourke (1989), most of the concrete cylinder pipe failures in Mexico City occasioned by the 1985 Michoacan event were due to crushing or telescoping at the joints. The corresponding failure criterion, based on laboratory tests for crushing of bell and spigot joints, is apparently not well established at this time.

According to Bouabid and M. O'Rourke's observation in their 1993 axial compressive tests, joint failure in reinforced concrete cylinder pipes with rubber gasketed joints can start at either the inner concrete lining or the outer concrete lining. That is, a circumferential crack starts to form in the ends of the concrete lining when the applied load nears its ultimate value. After concrete lining cracks, the critical section then becomes the welded interface between the steel joint ring and the steel pipe cylinder. The eccentricity existing between these two elements causes some denting (or even local buckling) near this welded region. Such damaging action would eventually result in a leakage path and/or cause the section to burst. Hence, both Bouabid and M. O'Rourke

(1994), as well as Krathy and Salvadori (1978), proposed that the joint crushing failure criterion for concrete pipes can be taken as the ultimate compression force of the concrete core at joints F_{cr}. That is,

$$F_{cr} = \sigma_{comp} \cdot A_{core} \tag{4.17}$$

where σ_{comp} is the compressive strength of concrete and A_{core} is the area of the concrete core. For plain concrete pipes, A_{core} is the cross-section area, while for reinforced pipes, the transformed area of steel bars needs to be added.

However, as described in more detail in Sections 11.1 and 11.2, determination of the ground strain leading to axial pull-out or joint crushing is complicated. Among other things, realistic modeling requires consideration of joint properties (strength and stiffness) that **vary** from segmented joint to segmented joint. Specifically, one needs a statistical description of the load-displacement relation for the class of segmented joints under consideration. In this regard, Figure 4.13 shows a generic load-displacement relation for a joint in tension. It has the point of initial slip (load = P_s, displacement = Δ_s) shown as an open circle and the point of failure (load = P_u, displacement = Δ_u) shown as a closed circle. The pre-slip and post-slip stiffnesses are K_{pre} and K_{post}, respectively.

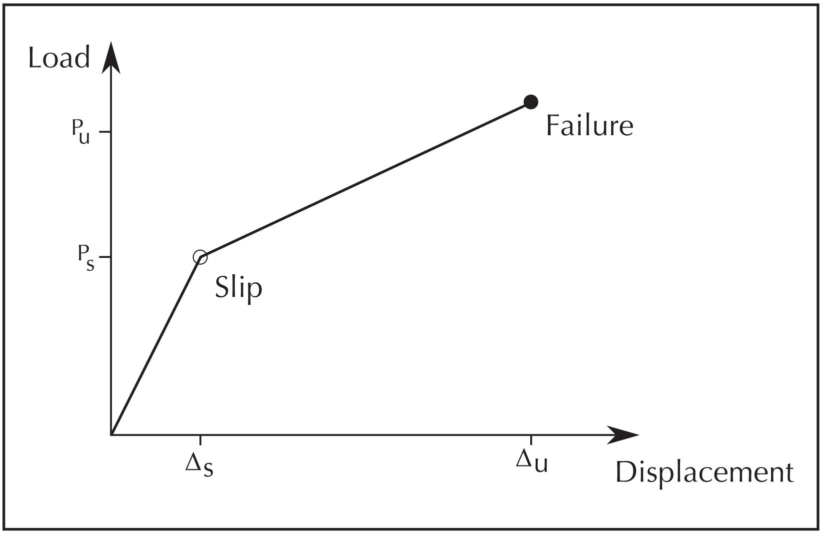

■ **Figure 4.13 Generic Load-Displacement Curve for a Joint in Tension**

In a series of papers in the early 1980s, Singhal and Benavides (1983) and Singhal (1984) present the results of axial pull-out tests on ductile iron (DI) pipe with rubber gasketed joints. These joints exhibited an elastic-plastic (yield plateau) type load-displacement curve. That is, the post-slip joint stiffness K_{post} was nominally zero. Table 4.8 presents the mean and standard deviation for the slippage force and the pre-slip stiffness. The individual force-displacement curves suggest that for a given diameter, large values of P_s were generally associated with larger values of K_{pre}. Also, Singhal (1984) presents an analytical relation for the pre-slip stiffness, which involves gasket compression and friction. Finally, in relation to the failure displacement Δ_u, Singhal observed that DI joints "get completely disassembled" for $\Delta_u \geq 1.2$ in, but that severe fluid leakage occurs at roughly a half inch of relative joint displacement. That is, for DI pipe, leakage occurs when the joint displacement is about 40% of the spigot embedment distance into the bell. More recently, Meis et al. (2003) conducted a series of laboratory tests on various types and diameters of pipe. The pipe joints were subject to axial tension or axial compression. Unfortunately, since duplicate tests were not performed, the variation in joint parameters is unknown. Table 4.9 presents the results for the more common joint types. Excepting polyethylene (PE) pipe, the joints in Table 4.9 are bell and spigot type. Ductile Iron and PVC pipe had push-on rubber gaskets. The Cast Iron pipe had lead-caulked joints, while the PE joint was butt fused. Since the fused joints in PE pipe are as strong or stronger than the material away from the joint, they should properly be considered continuous. Nevertheless, herein the Meis et al. test results for PE pipe are presented with the Meis et al. results for other pipe materials. For all the compression tests, again excluding PE pipe, the failure was due to the spigot telescoping or extruding into the bell, occasionally with fracture of the spigot end inside the bell. For PE pipe, the failure in compression was severe buckling of the pipe, while in tension (again for PE pipe) the failure occurred at one of the end flanges.

Finally, M. O'Rourke (2009) utilized a load-displacement relation for Cast Iron joints in developing an analytical fragility relation for segmented pipe. The simplified model was for 6-inch-diameter Cast Iron pipe with lead-caulked joints, arguably the most common joint type and diameter. In the simplified model, the displacement at slip, Δ_s was taken to be zero.

■ **Table 4.8 Load-Displacement Properties for Ductile Iron Pipe Joints Subject to Axial Tension Load**

Diameter (in)	Force at Slip P_s (lbs) mean	st. dev	Pre-Slip Stiffness K_{pre} (lbs/in) mean	st. dev
4	46	21	588	196
6	69	15	685	184
8	333	65	1,558	252
10	386	95	1,891	236

■ **Table 4.9 Load-Displacement Properties for Various Pipe Types**

Joint Type	Diameter (mm)	Loading	Force at slip P_s (kN)	Displacement at slip (cm)	Ultimate Force (kN)	Ultimate Displacement (cm)
Cast Iron	200	Comp.	1108	1.27	2046	2.46
Ductile Iron	100	Comp.	792	0.27	734	0.41
"	150	Comp.	1054	0.31	934	0.46
"	200	Comp.	1112	0.37	890	0.83
"	250	Comp.	1557	0.31	1179	0.48
PVC	150	Comp.	15	0.30		
"	200	Comp.	13	0.37		
"	300	Comp.	6	0.16		
PE	150	Comp.	186	3.90	125	5.50
"	200	Comp.	307	3.90	250	6.00
PE	150	Tension	133	1.50	157	6.20
"	200	Tension	125	0.87	232	4.30

The axial force at slippage, P_s, is based upon a model proposed by T. O'Rourke and Trautmann (1980):

$$P_s = C_a \pi D d_1 \tag{4.18}$$

where C_a is the adhesive strength at the pipe/lead interface and d_1 is the depth of lead caulking. C_a has a mean value of 252 psi and a coefficient of variation of 32%, while d_1 for a 6-inch-diameter pipe is 2.25 in. Hence, for the 6-inch-diameter pipe, the mean axial force at slippage is P_s = 10.7 kips and the standard deviation of P_s is 3.42 kips.

Based upon an analysis by El Hmadi and M. O'Rourke (1989) the joint force at leakage, P_u, is twice the slippage force. Finally, based upon Figure 4.12, the joint displacement at leakage Δ_u is taken to be a function of the joints embedment distance d_p. Specifically, the mean value of the ratio u_j^u/d_p was 0.45 and the standard deviation of the ratio was 0.13.

4.3.3 Circumferential Flexural Failure and Joint Rotation

When a segmented pipeline is subject to bending induced by permanent ground movement or seismic shaking, the ground curvature is accommodated by some combination of rotation at the joints and flexure in the pipe segments. The relative contribution of these mechanisms depends on the joint rotation and pipe segment flexural stiffnesses. For a flexible pipeline system such as DI pipe with Tyton joints or FLEX joints, stress in the pipe segments starts to increase greatly only after the joint rotation capacity, typically about 4° and 15°, respectively, is exceeded. On the other hand, for a more rigid segmented pipeline system, such as Cast Iron pipe with cement/lead joints, ground curvature is accommodated from the start by some combination of joint rotation and flexure in the segments (as will be discussed in more detail in Chapter 11).

In terms of failure criterion, it seems reasonable to base joint rotation failure/leakage criterion for "standard" segmented pipeline joints on some multiple (say 1.1 to 1.5) of the allowable angular offset for pipe laying purposes contained in manufacturer's literature. Table 4.10 contains a listing of such manufacturer's recommended allowable angular offsets.

For cast iron or asbestos cement pipes subject to ground curvature, round flexural cracks in segments are a major failure mechanism. On the other hand, for concrete pipes subject to ground curvature, cracks typically occur at the bell and spigot ends due in part to the joint ring eccentricity mentioned previously.

For round flexural cracks, it seems reasonable to use, as a failure criterion, the pipe curvature corresponding to the smaller of the ultimate tensile or compressive strains for the material. In this regard, El Hmadi and M. O'Rourke (1989) presented a listing of these mechanical properties for CI and DI pipe materials. Table 4.11 summarizes this information, as well as the properties for other common pipe materials.

Table 4.10 Typical Manufacturer's Recommended Allowable Angular Offset (Deg. and Min.) for Various Pipe Joints

D (in)	Cast Iron	Ductile Iron Push-on	Ductile Iron Mechanical	Prestressed Concrete	Concrete
4	4-00	5	8-18		
6	3-30	5	7-07		
8	3-14	4	5-21		
10		4	5-21		
12	3-00	4	5-21		
14		3	3-35		
16	2-41	3	3-35		2-19
18		3	3-00		2-04
20	2-09	3	3-00		1-52
24	1-47	2	2-23		1-34
27		2	2-23		1-24
30	1-26	2	2-23	1-44	1-15
33		1-30		1-35	1-09
36		1-30	2-05	1-28	1-03
42		1-30	2-00	1-16	1-03
48		1-30	2-00	1-06	1-03
60		1-30		0-56	
72		1-30		0-56	

■ **Table 4.11 Mechanical Properties for Common Pipe Materials**

Item	Cast Iron	Ductile Iron	Concrete	PVC	HDPE
Yield Strain $\times 10^{-3}$	1.0 to 3.0	1.75 to 2.17	0.1 to 1.3	17 to 22	22 to 25
Ultimate Strain $\times 10^{-3}$	5.0 to 40	100	0.25 to 3.0	50 to >100	50 to >100
Yield Stress (ksi)	14 to 42	42 to 52	0.32 to 4.0	5.0 to 6.5	2.2 to 2.5
Initial Modulus (ksi)	14,000	24,000	3,000	290-560	100-120

5

Soil-Pipe Interaction

Earthquake-induced axial forces and bending moments in buried pipelines and the resulting pipe strain are due to forces at the soil-pipe interface. That is, as the ground moves due to wave propagation or PGD, normal and friction forces at the soil-pipe interface load the pipeline. Hence, the overall seismic behavior of buried pipeline is directly related to, and strongly a function of, the force-deformation relation at the soil-pipe interface. Structural engineers tend to use the term “soil spring” when referring to these force-deformation relations, while geotechnical engineers tend to use the term “p-y curves.” For purposes of analysis, ground deformation can be decomposed into a longitudinal component (soil movement parallel to the pipe axis) and a transverse component (soil movement perpendicular to the pipe axis). Furthermore, the transverse component is typically decomposed into separate transverse-horizontal and transverse-vertical components. In relation to the transverse-vertical component, one must distinguish between upward and downward pipe movement since the interaction forces are quite different for these two cases. It is common practice to represent the load-deformation in each of these directions with separate, **independent** soil spring. Finally, for onshore pipeline, one must distinguish between pipe surrounded by competent, non-liquefied soil, and pipelines located in a liquefied layer.

Often offshore pipelines are simply laid on the seafloor. The resultant force-deformation relations are also discussed in this chapter.

5.1

Onshore Pipelines in Competent Non-Liquefied Soil

Interaction forces for a pipeline surrounded by competent, non-liquefied soil are reasonably well established. They are based upon a combination of laboratory tests and analytical studies. The 1984 ASCE Guidelines were arguably the first to present relations in a complete and user friendly fashion. They suggest, for the purpose of analysis, idealized elasto-plastic models as shown in Figure 5.1. Note that the elasto-plastic model is fully characterized by two parameters: 1) the maximum resistance t_u, p_u or q_u in the axial, transverse-horizontal and transverse-vertical directions, respectively, and 2) the maximum elastic deformation x_u, y_u or z_u. The resistance has units of force per unit length while, as expected, the deformation has units of length. As shown in Figure 5.1, the elasto-plastic force deformation relation is an idealization of the actual "roundhouse" type curve. As such, a ratio of the ultimate resistance to the maximum "elastic" deformation underestimates the actual effective stiffness. The 1984 ASCE Guidelines suggest using as the effective stiffness (units of force per unit area) twice the ratio of ultimate resistance to the maximum "elastic" deformation, for example, $2t_u/x_u$ for the axial spring. Note that for the elasto-plastic idealization, this spring coefficient is effective only for relative displacements less than half the maximum values of x_u, y_u and z_u, beyond which the resistance is assumed constant.

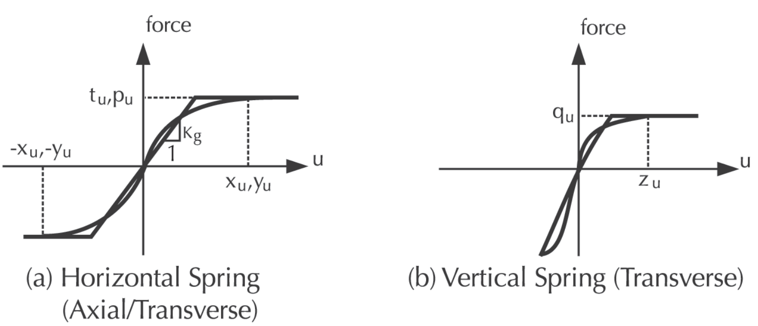

After ASCE, 1984

■ **Figure 5.1 Idealized Load-Deformation Relations at Pipe-soil Interface**

5.1.1 Longitudinal Movement

Relative movement parallel to the pipe axis results in longitudinal (axial) forces at the pipe-soil interface. The1984 ASCE Guidelines provide relations, in terms of the idealized elasto-plastic model, for sand (cohesionless) and clay (frictionless) materials.

For sand and other cohesionless materials, the longitudinal resistance is due to friction in the axial direction at the soil-pipe interface. The "normal" pressure which leads to the axial friction is over burden and lateral soil pressures. Specifically, in the 1984 ASCE Guidelines, the normal pressure is taken as the average of the vertical and at rest lateral soil pressures acting on the pipeline.

$$t_u = \pi D\bar{\gamma}H\left(\frac{1+k_o}{2}\right)\tan k\phi \qquad (5.1)$$

$$x_u = 0.1 \sim 0.2 \text{ in} = 2.5 \sim 5\text{mm} \qquad (5.2)$$

where D is the pipe diameter, $\bar{\gamma}$ is the effective unit weight of the soil, H is the depth to center-line of the pipeline, ϕ is the angle of shear resistance of the sand, k_o is the coefficient of lateral soil pressure at rest, and k is a friction factor. The magnitude of k_o for normally consolidated cohesionless soil has been reported to range from 0.35 to 0.47. However, one expects k_o to be somewhat larger because of compaction associated with the backfilling of soil around pipelines. T. O'Rourke et al. (1985) recommend k_o = 1.0 as a conservative estimate under most conditions of pipeline burial. Finally, the friction factor k depends on the surface characteristics. For example, if the pipe's outer surface is rough, slippage occurs at a soil-soil interface a bit beyond the soil-pipe interface. In that case, the friction factor k is 1.0 and slippage is related solely to the soils' angle of shearing resistance. That is, irrespective of the roughness of the soil-pipe interface, the effective friction for the buried pipe cannot exceed that for soil-soil slippage. Alternatively, if the pipe outer surface is smooth (slippery), then the slippage occurs at the soil-pipe interface, with an effective friction less than that associated with the soils' friction angle. The functional form tan ($k\phi$) with $k \le 1$ mathematically characterizes this behavior. Table 5.1 presents friction factors, as suggested in the 1984 ASCE Guidelines and the 2001 ALA Guidelines.

■ **Table 5.1 Friction Factor *k* for Peak Cohesionless Soil Resistance in the Axial Direction**

Pipe Material/ Coating	*k*
Concrete Cement Coated Steel Cement Coated Cast Iron	1.0
Coal Tar Coating	0.9
Rough Steel Cast Iron	0.8
Smooth Steel	0.7
Epoxy Coated Polyethylene	0.6

As will be shown subsequently, with the exception of the transverse vertical downward soil spring, the peak longitudinal resistance in Equation 5.1 has the same functional form as the other soil springs for cohesionless materials. Specifically, the peak resistance is proportional to a "depth times density" term ($\bar{\gamma}H$ in Equation 5.1), a geometry term (πD in Equation 5.1) and a dimensionless term related to the soils friction angle. The $\bar{\gamma}H$ term is the force per unit area at depth, and πD term is the length over which it acts resulting in a resistance with units of force per unit length.

For clay and other frictionless materials ($\phi = 0$), the longitudinal resistance (force per unit length) is proportional to the pipe diameter, the soils undrained shear strength, S_u and an adhesion factor, α, which itself is a decreasing function of S_u:

$$t_u = \pi \cdot D \cdot \alpha \cdot S_u \tag{5.3}$$

$$x_u = 0.2 \sim 0.4 \text{ in} = 5 \text{ to } 10 \text{ mm} \tag{5.4}$$

Figure 5.2 presents measured adhesion factors plotted as functions of the undrained shear strength S_u. An effective adhesion factor larger than one at the soil-pipe interface is unrealistic, since the slip can occur at an adjacent soil-soil interface. Also shown in Figure 5.2 are the adhesion factor curves recommended in the 1984 ASCE Guidelines and the 2001 ALA Guidelines. Note that both curves overestimate the measured adhesion data and that the 2001 ALA curve is nominally an upper bound for the measured data.

In general, using an upper bound value for the maximum soil resistance is conservative. That is, for a given amount of ground movement, the forces on the pipeline and the pipe strains are larger using “upper bound” soil springs. An exception to this general rule arises when the pipe mechanical properties change substantially in the area of interest. For example, consider a new fault crossing where high quality (expensive) butt welds are envisioned close to the fault, with less expensive WSJ’s envisioned only at some “safe distance” from the fault. In this case, it turns out that a **lower bound** estimate for the soil spring axial resistance should be used to establish the “safe distance.”

The peak resistance in Equation 5.3 is similar to those for the other soil springs for frictionless materials. Specifically, the resistance is proportional to S_u, a geometry factor (πD in Equation 5.3) and a non-dimensional factor (α in Equation 5.3).

If a soil has both frictional (non-zero ϕ) and cohesion (non-zero S_u) characteristics, then the peak axial resistance is the sum of Equations 5.1 and 5.3.

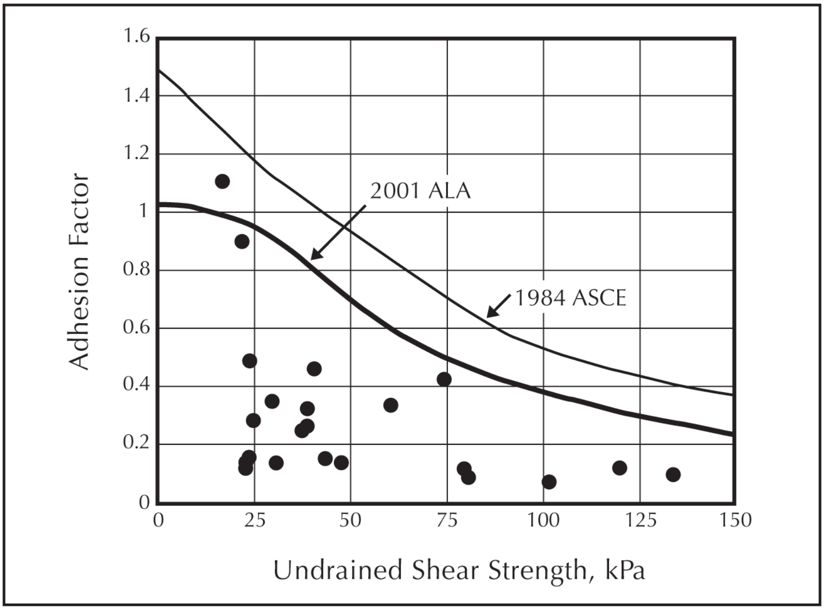

After Honegger and Nyman, 2004

■ **Figure 5.2 Measured Adhesion Factors for Longitudinal Soil Spring in Frictionless Soil**

5.1.2 Transverse-Horizontal Movement

Relative movement perpendicular to the pipe axis in the horizontal plane results in transverse-horizontal forces at the pipe-soil interface. The transverse-horizontal soil spring seems to have received more attention than the others. In this regard, Guo and Stolle

(2005) present a review of laboratory tests from four separate groups of researchers, as well as analytical results from a few others. To date, the lab tests and numerical models have been 2-D plane strain in nature. For example, in the Trautmann and O'Rourke (1985) tests, a rigid pipe was dragged horizontally through a specially built soil box. However, even for the 2-D case the behavior is fairly complex. As observed by Audibert and Nyman (1977), the failure mechanism is a function of the *H*/*D* ratio. For shallow burial depths (*H*/*D* < 3, according to Audibert and Nyman), lateral pipe movement eventually results in a log-spiral passive soil wedge above and in front of the pipe and a narrow active zone directly above the pipe. Both zones extend to the ground surface, as sketched in the simplified model for a cohesionless material in Figure 5.3. Applying equilibrium in the vertical direction, one can solve for the normal soil stress σ_N. Using $\mu = \tan\phi$ and solving for equilibrium in the horizontal direction, one can determine the peak lateral force on a pipe with shallow burial in a cohesionless material:

$$F_{max} = p_u = \frac{\frac{\bar{\gamma}}{2} \cdot \left(H + \frac{D}{2}\right)^2 \tan(45 + \phi/2)}{\cos\beta - \mu\sin\beta}\,[\sin\beta + \mu\cos\beta] \tag{5.5}$$

where β is the wedge angle (45°- ϕ/2). Note that the peak resistance in Equation 5.5 has the expected form, of a depth times density term (($\bar{\gamma}$)($H + D/2$)), a geometry term ($H + D/2$) and a complex non-dimensional term related to the soils friction angle. For $H/D = 2$, the simplified relation in Equation 5.5 yields peak lateral

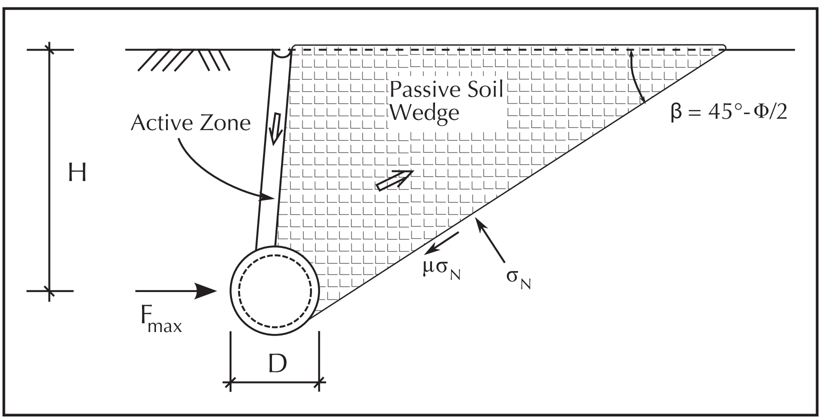

■ **Figure 5.3 Simplified Model for Transverse Soil Spring in Cohesionless Material at Shallow Burial Depths** resistance of 5.74 γHD and 9.03 γHD for soil friction angles of 35° and 45°, respectively.

For moderate burial depths ($3 \leq H/D \leq 12$, according to Audibert and Nyman), they describe a three-wedge failure mechanism consisting of a front passive wedge, a central soil wall wedge atop and a bit in front of the pipe, and an active caving wedge behind the pipe. As with the shallow burial mechanism, all three zones extend to the ground surface.

Finally, for deep burial ($H/D > 12$, according to Audibert and Nyman), they describe a completely below ground zone of soil flow. A simplified model for deep burial in a cohesionless material is sketched in Figure 5.4. A four-sided rigid block of soil (labeled abcde in Figure 5.4) moves to the right. The void left by the rigid block movement is filled by soil following around the rigid block. That is, soil above Side cd moves to the left, soil beyond Side bc moves downward to the left, etc. As such, the soil beyond Side bc is in a passive state, while the soil beyond Side de is in an active state.

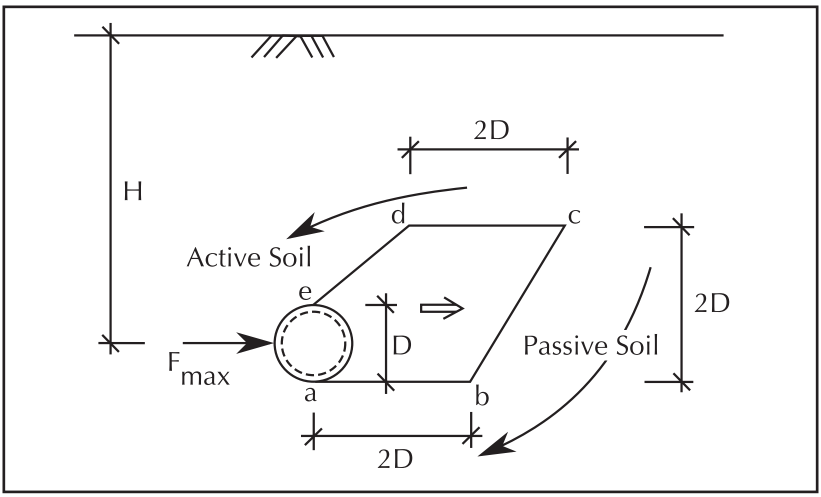

■ **Figure 5.4 Simplified Model for Transverse Soil Spring in Cohesionless Material at Deep Burial Depths**

For both horizontal surfaces (i.e., Sides cd and ab), the nominal soil pressure is simply the overburden pressure γH. Hence, the force per unit area resisting movement is the friction coefficient times the normal pressure. In the simple model, the normal pressure at the inclined sides (i.e., Sides bc and de) is taken as the average of the vertical and lateral soil pressures (i.e., $\gamma H (1 + k_p)/2$ along side bc, $\gamma H (1+ k_a)/2$ along side de). For the inclined surfaces, the force per unit area resisting horizontal movement is the sum of the horizontal components of the normal and friction pressures.

Summing the horizontal components on all four sides results in the following relation for the peak lateral force for a pipe with deep burial in a cohesionless material:

$$F_{max} = 4\mu\bar{\gamma}HD + \bar{\gamma}HD\,(1+k_p)(1+\mu)-1.12\bar{\gamma}HD(1+k_a)(0.44-.89\mu) \quad (5.6)$$

where k_p and k_a are the lateral pressure coefficients for passive and active conditions, respectively. Again, the peak resistance in Equation 5.6 has the expected form: a depth time density term ($\bar{\gamma}H$), a geometry term (D), and a non-dimensional term related to the soil friction angle. The simplified relation in Equation 5.6 yields peak lateral resistances of $11\bar{\gamma}HD$ and $18.2\bar{\gamma}HD$ for soil friction angles of 35° and 45°, respectively.

The simple model results in Equation 5.5 and 5.6 are not necessarily recommended for use in practice. Rather, they are presented to explain laboratory results and illustrate the influence of burial depth.

The 1984 ASCE guideline provides the following relation for sand (cohesionless material with $S_u = 0$):

$$p_u = \gamma H N_{qh}\, D \qquad (5.7)$$

$$y_u = \begin{cases} (0.07 \sim 0.10)(H + D/2) & \text{for loose sand} \\ (0.03 \sim 0.05)(H + D/2) & \text{for medium sand} \\ (0.02 \sim 0.03)(H + D/2) & \text{for dense sand} \end{cases} \qquad (5.8)$$

where N_{qh} shown in Figure 5.5 is the horizontal bearing capacity factor for sand from Trautmann and T. O'Rourke. Note first that the relation has the expected functional form. Secondly, although the bearing capacity factor is dimensionless and it is plotted versus a normalized depth, the relation for a given friction angle is not a straight line. This is due to the fact that different mechanisms control the behavior for different H/D ratios. That is, from the simplified relation for shallow burial depths in Equation 5.5, the peak resistance for a given soil friction angle is proportional to $(H + {}^{D}/_{2})^2$. While for deep burial, the peak resistance is proportional to $H \cdot D$ from Equation 5.6.

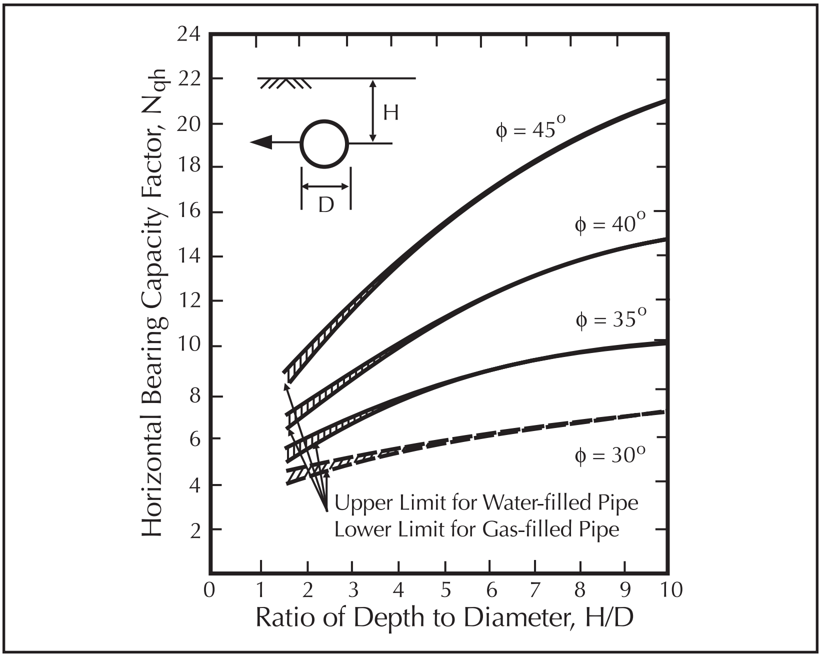

After Trautmann and T. O'Rourke, 1983

■ **Figure 5.5 Horizontal Bearing Factor for Sand vs. Depth to Diameter Ratio**

In both the 2001 ALA and the 2004 PRCI Guidelines, the peak transverse-horizontal resistance is given by Equation 5.7. However, in these later guidelines the Hansen (1961) horizontal bearing capacity factor, as shown in Figure 5.6, is recommended. The variation of the Hansen N_{qh} factor with *H/D* in Figure 5.6 is similar to that for the Trautmann and T. O'Rourke N_{qh} factor in Figure 5.5 for sands with $\phi = 30°$. However, for sands with $\phi = 45°$, the Hansen factors are more than twice as large as the Trautmann and T. O'Rourke factors for the same *H/D* ratio.

Complicating matters are test results for moist sand by T. O'Rourke and Turner (2006). There tests suggest that the N_{qh} factors for moist sand are roughly twice the Trautmann and T. O'Rourke N_{qh} factors for dry sand with the same ϕ angle and *H/D* ratio.

Fortunately, as part of a NSF-NEESR project at Cornell and Rensselaer, both full-scale and centrifuge tests on buried HDPE pipe subject to the fault offset hazard were undertaken. In both the centrifuge and full-scale tests, flexible pressure sensor sheets were used to measure the distribution of normal pressure both along the length and around the circumference of the pipe. Integrating the horizontal components of the measured normal and

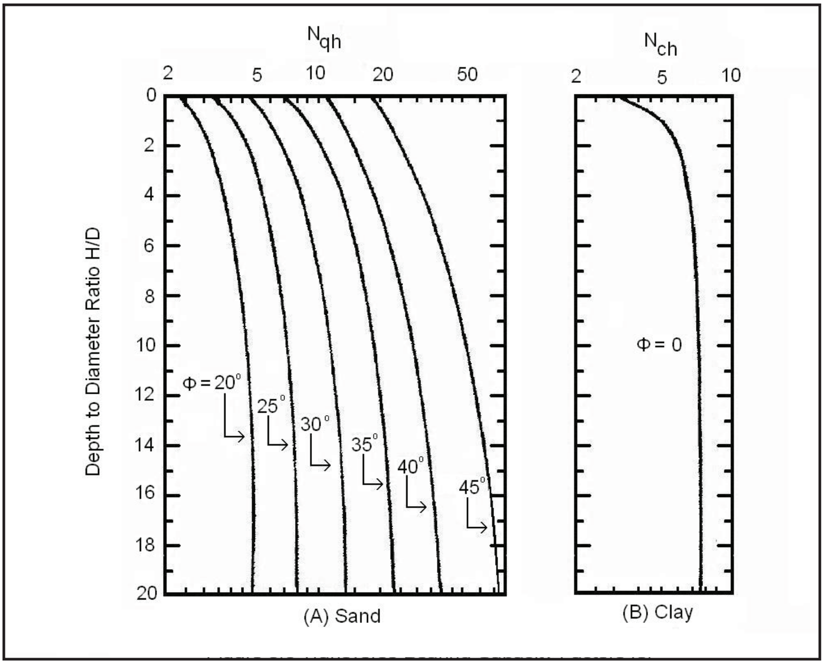

After Hansen, 1961

■ **Figure 5.6 Transverse Bearing Capacity Factors for Sand and Clay**

assumed tangential pressure, one can calculate the peak lateral resistance. As reported by Ha et al. (2008), the calculated N_{qh} factor from the centrifuge tests (4% moisture content, $\phi = 40°$, $H/D = 2.8$, and assumed coefficient of friction = 0.4) was roughly 8.5. This matches closely the value from Figure 5.5. This peak lateral resistance from the centrifuge tests ($N_{qh} \simeq 8.5$) was about half the Hansen, 2001 ALA, and 2004 PRCI N_{qh} value of 16.3 and about half the T. O'Rourke and Turner value for moist sand.

As noted above, the use of larger values for the peak resistance is generally conservative. In that sense, the apparent overestimation of N_{qh} by the Hansen or T. O'Rourke and Turner relations is "acceptable." However, the N_{qh} value measured by Ha et al. (2008) suggest that the N_{qh} values from T. O'Rourke and Trautmann may well be the most accurate.

Although the Cornell/Rensselaer tests provide benchmark information in relation to appropriate N_{qh} values, they also show that the actual soil-pipe behavior is not as simple as current models suggest. As noted above, current understanding of the peak lateral resistance in sand is based upon nominally plane strain (i.e., 2-D) laboratory tests and nominally plane strain analytical models. As such, they envision, for example, a straight north-south pipeline subject, over a substantial length, to the **same** east-west ground movement. Since each east-west slice is nominally the same, one expects plane strain behavior. However, for a pipeline subject to the generalized fault offset hazard, discussed in more detail in Chapters 8 and 9, plane strain conditions do not exist. First of all, the pipe closest to the fault is subject to larger relative soil movements than the pipe further from the fault. Secondly, due to curvature in the pipe, a vertical slice (perpendicular to the pipe longitudinal axis) near the fault is not parallel to a vertical slice away from the generalized fault. Hence, for the fault offset hazard, the behavior is inherently 3-D in nature.

This 3-D nature was evident in the Cornell/Rensselaer tests. As the fault offset increased, a passive soil failure zone developed on each side of the fault (south of the pipe on the west side, north of the pipe on the east side for an east-west pipe and right lateral offset). However, the horizontal (along pipeline) extent of the zones was limited. Apparently, as a result of this behavior, the soil springs away from the fault were weaker and more flexible than those close to the fault. For example, Figure 5.7 shows the load deformation data for one of the centrifuge tests. Note that for locations within roughly 3.5 pipe diameters (1.5 m) of the fault, the equivalent stiffness and peak resistance are larger than for locations more than 3.5 pipe diameters from the fault. The peak resistance for locations close to the fault matched reasonably well with the resistance expected from the Trautmann and T. O'Rourke relation in Figure 5.5, as discussed previously. In relation to the equivalent soil springs away from the fault, the expected reduction in strength and stiffness is not well established. Also note that it would be conservative to neglect the reduction.

Finally, although the peak resistance (i.e., P_u) for locations close to the fault are consistent with Equation 5.7 and the Trautman and T. O'Rourke N_{qh} values, the "yield" displacement between soil and pipelines (i.e., y_u) are much larger than those in Equation 5.8. It is believed that these differences are due in part to the behavior of the ground near the fault. The standard assumption is that each side of the fault acts as a rigid body that slides with respect to the opposite side. That is, all the offset occurs at the fault and a straight line crossing the fault before the offset becomes two offset straight lines with a gap after the fault move-

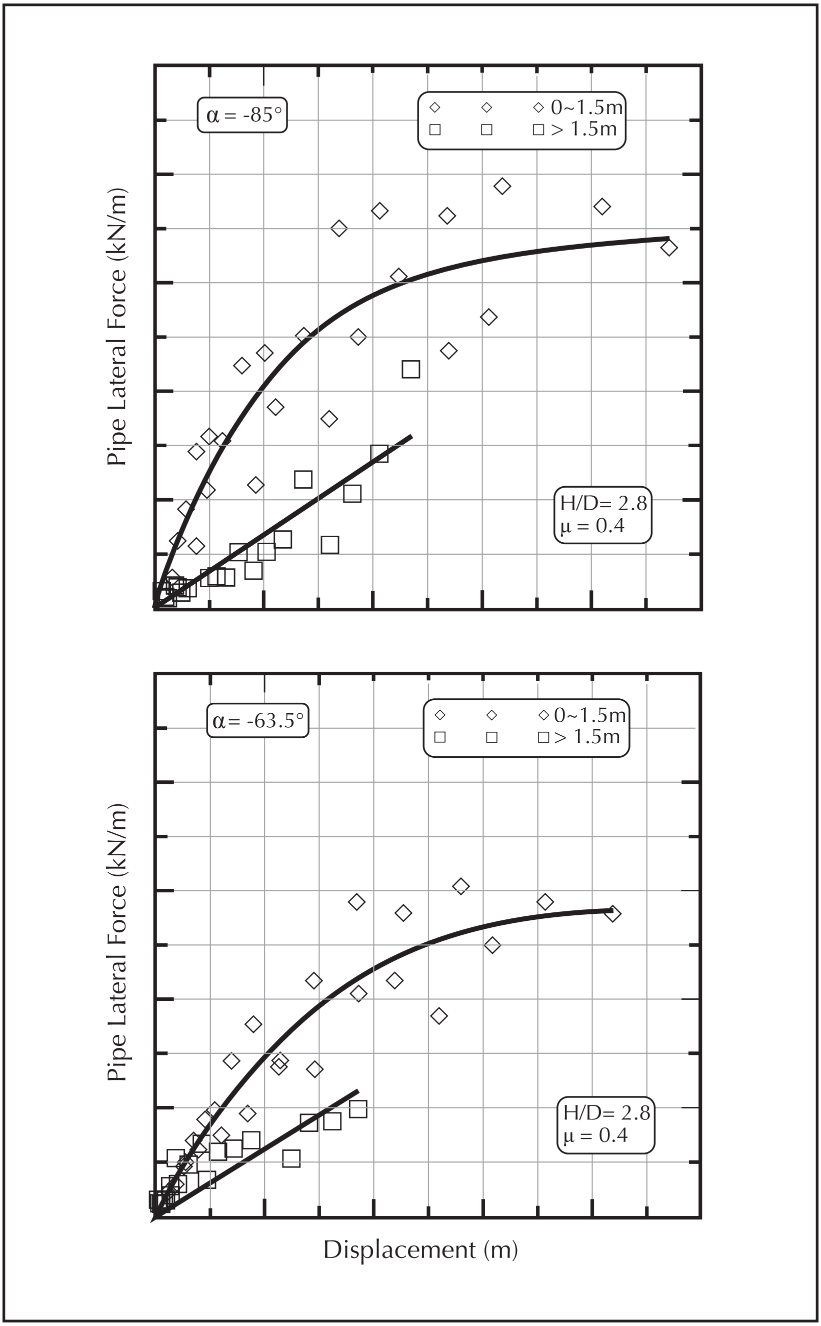

After Ha et al., 2008

■ **Figure 5.7 Transverse Force Deformation Relations for Locations Close To and Away From the Fault** ment. However, observation from the centrifuge tests suggest, as sketched in Figure 5.8, that the total offset is a combination of an abrupt contribution at the fault itself, plus shear type deformation within each block. This would result in smaller soil displacement at and near the fault than for the standard assumption. This in turn would explain why the apparent y_u values (based upon the standard assumption) seem to be high. However, as one might expect, the standard assumption is conservative.

There seems to be much less controversy for clay and other frictionless materials (i.e., $\phi = 0°$). The 1984 ASCE, 2001 ALA and 2004 PRCI guidelines all provide the same relations.

$$p_u = S_u N_{ch} D \tag{5.9}$$

$$y_u = (0.03 \sim 0.05)\,(H + D/2) \tag{5.10}$$

where N_{ch} is the horizontal bearing capacity factor for clay as presented in Figure 5.6(b). Note that the peak resistance in Equation 5.9 has the expected functional form for a cohesionless material: the undrained shear strength, a geometry term (D) and a non-dimensional term (N_{ch}).

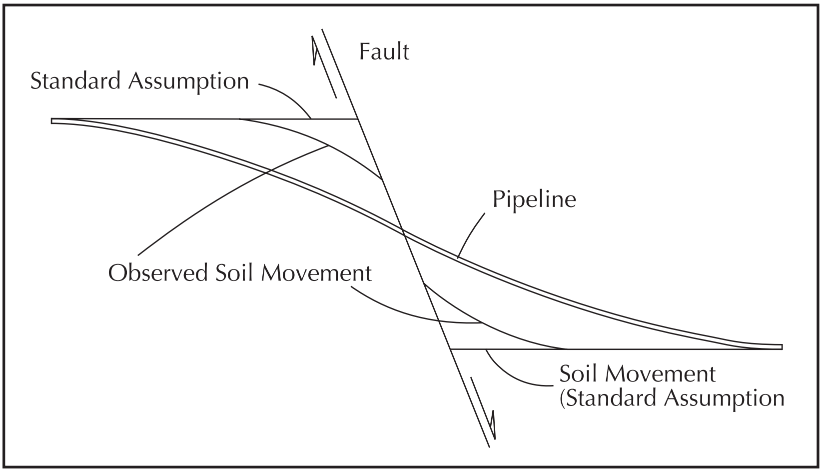

■ **Figure 5.8 Observed Soil Movement at a Fault**

5.1.3 Transverse Vertical Movement, Upward Direction

Relative upward movement perpendicular to the pipe axis results in vertical forces at the pipe-soil interface. The 1984 ASCE Guidelines provide the following relations for clay and sand.

For sand,

$$q_u = \bar{\gamma} H N_{qv} D \tag{5.11}$$

$$z_u = (0.01 \sim 0.015)H \tag{5.12}$$

where N_{qv} is the vertical uplift factor for sand as given in Figure 5.9.

In the 2001 ALA and 2004 PRCI guidelines, the peak resistance is given as:

$$q_u = \bar{\gamma} \cdot H^2 \cdot \tan\phi \tag{5.13}$$

which has the expected functional form and provides the same results as Equation 5.11 and Figure 5.9 for $\phi = 44°$ and 36°. Note

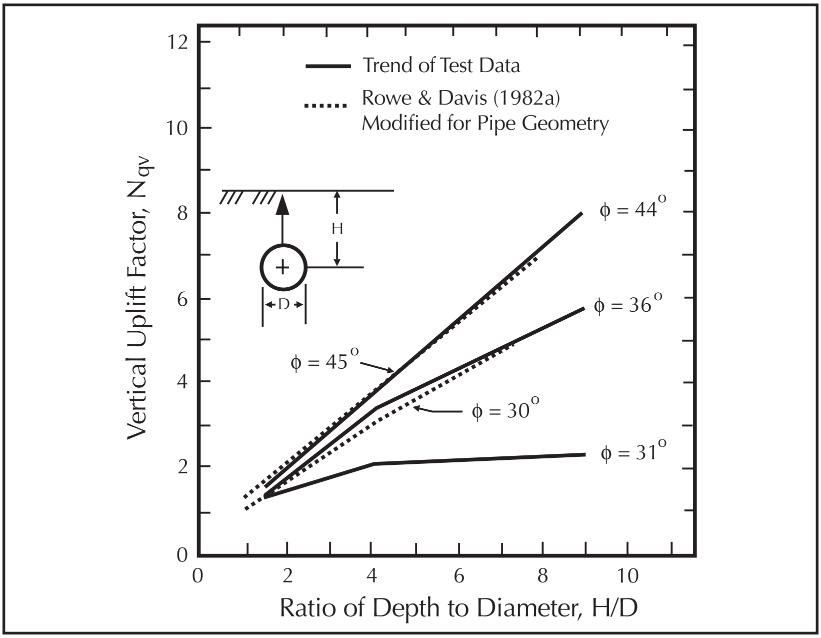

After Trautmann and T. O'Rourke, 1985

■ **Figure 5.9 Vertical Uplift Factor for Sand vs. Depth to Diameter Ratio** that the relation in Equation 5.13 nominally corresponds to the weight of an inverted triangle of soil with its apex at the centerline, a height equal to the burial depth, and a "base" at the ground surface corresponds to $2H \cdot \tan \phi$, as sketched in Figure 5.10. Furthermore, the maximum elastic deformation for sand, z_u is limited to no more than $D/10$.

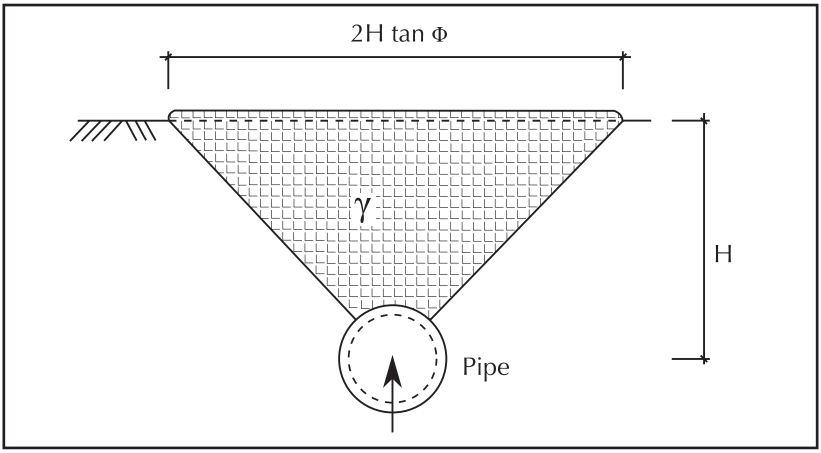

■ **Figure 5.10 Simplified Model for Vertical Uplift Factor for Sand**

For clay and other frictionless materials, the 1984 ASCE Guidelines provide the following relation:

$$q_u = S_u N_{cv} \cdot D \tag{5.14}$$

$$z_u = (0.1 \sim 0.2)H \tag{5.15}$$

where N_{cv} is the vertical uplift factor for clay given in Figure 5.11. In the 2001 ALA and 2004 PRCI guidelines, the peak resistance is given as:

$$q_u = 2S_u \cdot H \tag{5.16}$$

with a limit of 10 $S_u D$. Note that the peak resistance in both relations has the expected form. Furthermore, the relation in Equation 5.16 corresponds to the failure load for a vertical plug of soil with two vertical shear failure planes extending from the springline on each side of the pipe, vertically up to the ground surface, as sketched in Figure 5.12. This failure mode would control for lower buried depths. For larger burial depths, specifically $H/D >$

5 for the 2001 ALA/2004 PRCI Guidelines, the failure mechanism would be a bearing capacity failure immediately above the pipe. The 10 $S_u \cdot D$ limit is presumably intended to cover that failure mechanism. Furthermore, in the 2001 ALA/2004 PRCI Guidelines, the maximum elastic deformation for clay, z_u, is limited to no more than $D/5$.

Finally, like all the other soil springs, one should add resistance for sand and clay for a soil with $\phi \neq 0$ and $S_u \neq 0$.

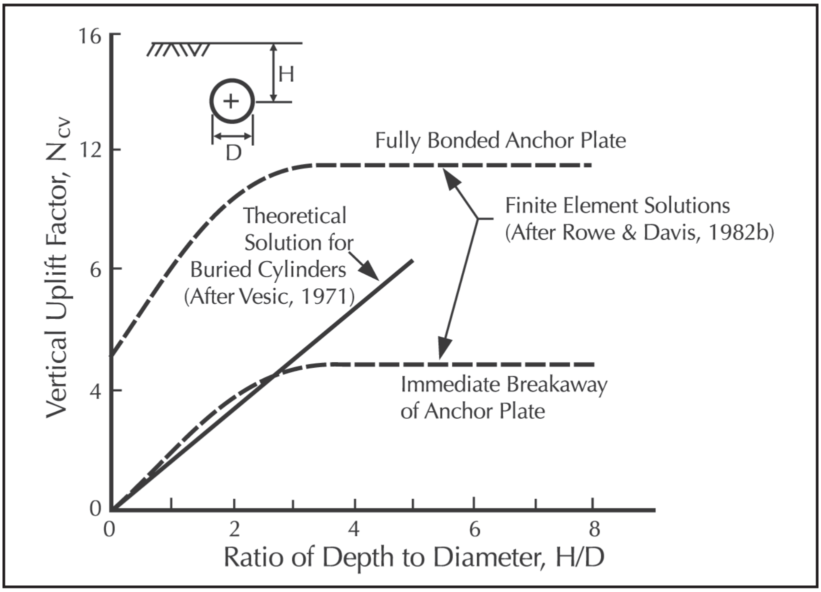

After ASCE, 1984

■ **Figure 5.11 Vertical Uplift Factor for Clay vs. Depth to Diameter Ratio**

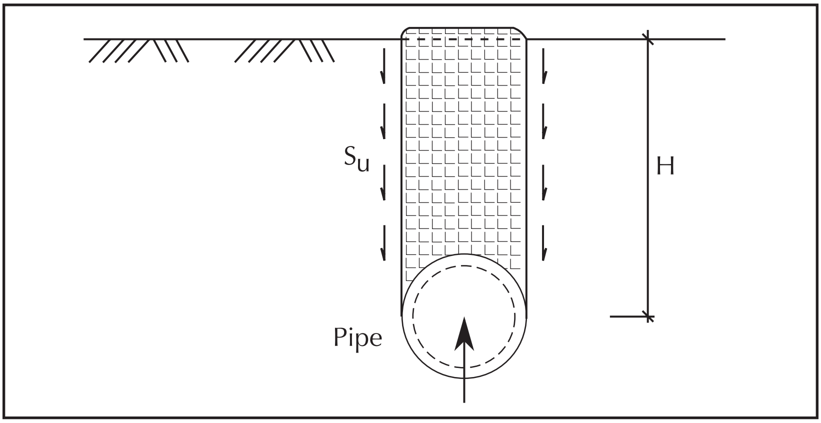

■ **Figure 5.12 Simplified Model for Vertical Uplift Factor for Clay**

5.1.4 Transverse-Vertical Movement, Downward Direction

Relative downward movement perpendicular to the pipe axis results in vertical forces at the pipe-soil interface. This corresponds to the vertical bearing capacity of a footing, a well-studied problem in soil mechanics. All three guidelines present the same relation.

For sand and other cohesionless materials:

$$q_u = \bar{\gamma} H N_q D + 1/2\, \bar{\gamma} D^2 N_y \tag{5.17}$$

$$z_u = (0.10 \sim 0.15)D \tag{5.18}$$

For clay and other frictionless materials:

$$q_u = S_u N_c D \tag{5.19}$$

$$z_u = (0.10 \sim 0.15)D \tag{5.20}$$

where γ is the total unit weight of sand, N_q and N_y are the bearing capacity factors for horizontal strip footings on sand loaded in the vertically downward direction, while N_c is the bearing capacity factor for horizontal strip footings on clay. The three bearing capacity factors are presented in Figure 5.13.

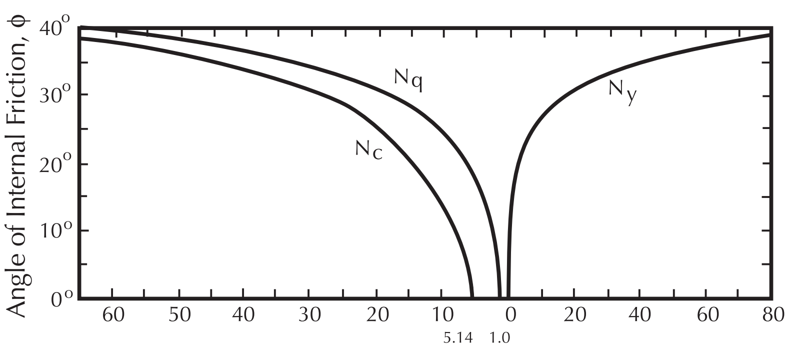

■ **Figure 5.13 Vertical Bearing Capacity Factors vs. Soil Friction Angle**

5.2 Onshore Pipelines in Liquefied Soil

Suzuki et al. (1988) and Miyajima and Kitaura (1989) have shown that pipe response is very sensitive to the stiffness of the equivalent soil springs for a pipeline located in a liquefied layer. This subsection will discuss the equivalent stiffness of soil springs for a pipe in liquefied soil.

Combining experimental data with analytical solutions based on a beam on an elastic foundation approach, Takada et al. (1987) developed an equivalent soil spring for a pipe in a liquefied soil. They indicate that the equivalent stiffness ranges from 1/1,000 to 1/3,000 of that for non-liquefied soil. On the other hand, Yoshida and Uematsu (1978), Matsumoto et al. (1987), Yasuda et al. (1987), and Tanabe (1988) suggest that the stiffness ranges from 1/100 to 3/100 of that for non-liquefied soil based on their model experiments.

For saturated sandy soil, T. O'Rourke et al. (1994) proposed a reduction factor, R_f, for a pipe or pile subject to transverse ground displacement, as:

$$R_f = \frac{N_{qh}}{K_c} \cdot \frac{1}{0.0055(N_l)_{60}} \tag{5.21}$$

where K_c is the bearing capacity factor for undrained soil and $(N_l)_{60}$ is the corrected SPT value. The reduced stiffness at the pipe-soil interface is then given by the stiffness for non-liquefied soil divided by the reduction factor. Their results suggest that the equivalent stiffness ranges from 1/100 to 5/100 of that for non-liquefied soil. As alluded to above, it is generally conservative to use a larger soil spring stiffness in calculations. Hence, if the actual depth and thickness of the liquefied layer is open to question, it may well be advisable to assume the pipe is in a competent soil layer (a.k.a. "cap layer"), which overrides the liquefied layer. However, if it is clear that the pipe will in fact be in the liquefied layer, it seems reasonable to use 3% of the "competent soil" spring stiffness in calculations.

For the approach described above, the liquefied soil is treated, more or less, as a very soft solid. A liquefied soil can alternately be viewed as a viscous fluid. For that model, the interaction force at the pipe-soil interface varies with the relative velocity between the pipe and surrounding soil. According to Sato et al. (1994), the transverse force imposing on the pipe per unit length is:

$$F = \frac{4\pi\eta V}{(2.0 - \log R_e)} \tag{5.22}$$

where η is the coefficient of viscosity for the liquefied soil, V is the velocity of the pipe with respect to the liquefied soil, $R_e = \gamma VD/\eta$ is the Reynolds number and γ is the density of liquefied soil.

Based on model tests, Sato et al. (1994) established a relation between the coefficient of viscosity and the liquefaction intensity factor, F_L. This relation is shown in Figure 5.14.

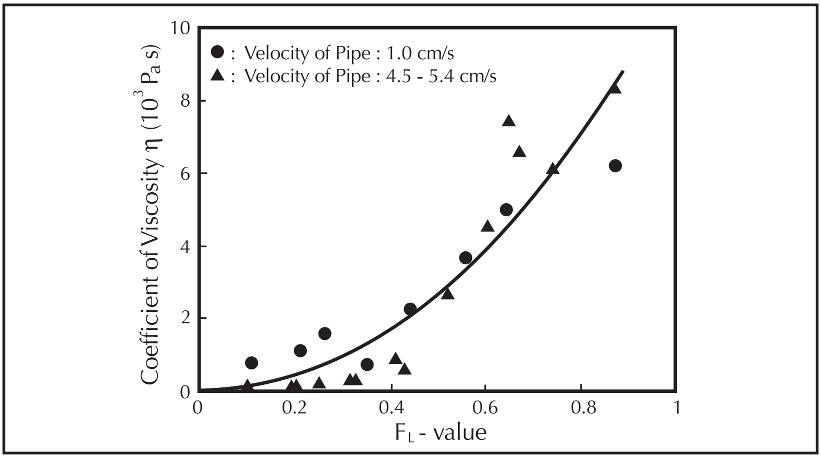

After Sato et al., 1994

■ **Figure 5.14 Coefficient of Viscosity vs. F_L-Value**

Japanese Road Association (1990) defined the factor of liquefaction intensity, F_L, as:

$$F_L = \frac{0.0042 D_r}{(a_{max}/g) \cdot (\sigma_v / \sigma'_v)} \tag{5.23}$$

where D_r is the relative density of the soil, a_{max} is the maximum acceleration of the ground, σ_v is the total overburden pressure and σ'_v is the effective overburden pressure.

Note that there are problems with modeling liquefied soil as a fluid. The biggest of these is the fact that the velocity of the soil, which is an upper bound for the velocity of the soil with respect to the pipeline, typically is unknown. Again, even if the pipe is likely to be in a liquefied layer, it is conservative to assume the pipe is located in the "cap layer."

5.3 Offshore Pipelines

For buried offshore pipelines, the formulae introduced in Section 5.1 can be used to determine the pipe-soil interaction forces. Specifically, for pipelines surrounded by sand, the effective soil density (i.e., submerged density = density of wet sand – density of water) should be used. For pipelines surrounded by clay, the undrained or in-situ shear strength should be used.

The more common situation in a deep water environment is a pipeline simply laid on the seabed. In that case, the soils at the top of the seabed are of interest. Due to erosion by ocean currents/waves, softer top soils are typically classified as sand, silt or clay. Sand tends to occur near coastlines where currents/waves are strong. Clay tends to occur in deep water and other locations where currents are weak. Silt occurs somewhere in between. Hard seabed soils can also be encountered at locations where loose softer top materials have been eroded away. Those hard soils are either corals, cemented sand, outcrops of hard clay or rock. These hard soils can be treated as non-cohesive materials.

In the following subsections, the equivalent soil springs for pipelines laid directly on the seabed are discussed. Due to the variety of soil properties, upper bound and low bound values are presented for the pipe-soil interaction forces. As with onshore buried pipelines, the use of upper bound values for pipe-soil interaction forces result in higher pipe forces and stresses and, hence, is conservative.

5.3.1 Pipe Embedment

Earthquakes are more likely to occur well after the pipeline has been installed. As such, one expects the pipeline to have embedded itself into the seabed and that the supporting soil has consolidated under the pipe weight.

Pipe embedment depends upon a number of factors. Intuitively, one would think that the embedment is due simply to the pipe submerged weight and soil strength. However, embedment values calculated from such simple static models underestimate observed values. As a pipeline is laid during installation, the maximum vertical loads in the seabed touchdown area are typically two to three times larger than the submerged weight of the pipe. In addition, dynamic motions of the pipeline, including lateral oscillation, cause cyclic loading/unloading in the touchdown area and, as a result, increase the pipe embedment (Randolph and White, 2008). Right after the pipeline is laid, a hydrotest is typically carried out. This results in further pipe embedment at support areas for free spans. Other factors affecting the embedment include movement due to hydrodynamic forces, erosion, and loose soil deposition during the service life of the pipeline.

Due to many uncertainties in soil properties, as well as installation and wave conditions, it is difficult to theoretically calculate the pipe embedment. However, empirical relations for pipe embedment have been developed. For example, Verley and Lund (1995) developed an empirical relation for pipe penetration in clay, as a function of the undrained shear strength S_u. Unfortunately, the relation is also a function of the amplitude of horizontal oscillations, which may be difficult to estimate. Fortunately, there are general rules of thumb for pipe penetration: $0.3D$ for sand, and $0.5D$ or more for very soft clay in deep water.

Similar to buried pipelines, the soils resistance to lateral movement of seabed-laid pipelines is an increasing function of the pipe movement. However, seabed-laid pipe eventually break out of the pseudo-trench (resulting from pipe embedment) in which they have been located. This breakout results in a significant reduction in the soil resistance (to possibly a half of the peak value), which remains relatively constant thereafter, as sketched in Figure 5.15.

As noted above, it is generally conservative to use upper bound values for the soil spring. Hence, for hand calculations, one may choose to neglect the “trench-breakout” all together. For more sophisticated analysis using the finite element method, a more realistic soil spring, including the trench breakout reduction, can be used. However, with such sophisticated analysis, one needs to ensure that local buckling of the pipe wall does not occur prior to breakout.

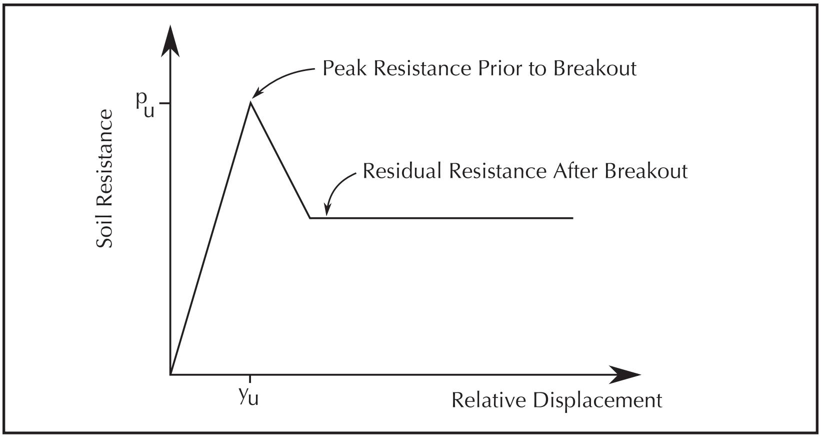

Figure 5.15 Variation in Lateral Resistance Due to Breakout from Pseudo-Trench

5.3.2 Longitudinal Movement

For pipelines laid on sandy soil or a hard seabed (stiff clay, cemented sand, coral, rock outcrops) where pipe embedment is negligible, the axial soil resistance is:

$$t_u = w_s \tan k\phi \tag{5.24}$$

$$x_u = \begin{cases} 0.002 \text{ m for a hard seabed} \\ 0.005 \text{ m for a sandy seabed} \end{cases} \tag{5.25}$$

where w_s is the submerged weight of the pipe per unit length (with contents), $\tan k\phi$ is the friction coefficient between the seabed and pipe, and k is the friction reduction factor as presented in Table 5.1. For a hard seabed, the friction angle ϕ typically ranges from 40° to 45°.

Since longitudinal pipe movement is parallel to the pseudo-trench, there is no "breakout" and the peak soil resistance remains relatively constant for relative displacement larger than x_u.

For sandy soil, pipe embedment leads to a larger percentage of the pipe circumference being in contact with the soil. The accompanying lateral pressures result in higher longitudinal resistance. However, for typical embedment depths (about 0.3D), the increase in longitudinal resistance is not substantial. For example, White and Randolph (2007) developed a relation which accounts for the increased contact area. The White and Randolph relation suggests there is a 10% increase in peak longitudinal resistance for an embedment depth of $0.3D$.

For both sandy soil and hard seabed, the initial resistance for relative displacements less than x_u is due to static friction. For larger relative displacements, the resistance is due to dynamic friction with an effective friction coefficient (i.e., tan $k\phi$) of roughly 80% of the static value. Again, it generally would be conservative to neglect this small difference.

For a pipeline laid on a **clay** seabed, the initial axial resistance is theoretically the product of the in-site shear strength, an adhesion factor and the contact area, which in turn is a function of the pipe embedment. Alternatively, as an outgrowth of "on-bottom stability" procedures (resistance to pipeline movement caused by wave and/or current action) offshore practioners often characterize resistance for all types of soils (clay included) by an effective friction coefficient. Using that approach, the peak resistance has an equivalent friction coefficient of 0.75 to 1.5. After initial slippage (typically at x_u of 0.01 m), "true" dynamic friction controls with a friction coefficient of 0.2 to 0.5.

5.3.3 Horizontal Transverse Movement

The initial lateral or transverse resistance for a pipeline laid on a **sandy** seabed consists of a friction component and passive soil resistance component. As one might expect, the passive soil/ pseudo-trench term is an increasing function of the pipe's normalized embedment z/D. Utilizing the empirical relation developed by Verley and Sotberg (1992), the initial total resistance is:

$$p_u = \tan(k\phi) \cdot w_s + \left(4.5 - 0.11\frac{\bar{\gamma}D^2}{w_s}\right)(\gamma D^2)\left(\frac{z}{D}\right)^{1.25} \tag{5.26}$$

$$y_u = 0.2D \text{ to } 0.5D \tag{5.27}$$

where the second term is the passive soil resistance due to pipeline embedded in the pseudo-trench. Once breakout occurs, the lateral resistance decreases as sketched in Figure 5.15. There are two effects at work. First, the friction component reduces somewhat. This is due to the fact that the pipeline is now in contact with unconsolidated sandy soil as opposed to the consolidated soil below the pipe in the pseudo-trench. In addition, the passive soil resistance term also changes after breakout. However, as opposed to dropping to zero, there is resistance associated with the small soil beam expected to form in front of the laterally displacing pipe. As a first approximation, the post-breakout lateral resistance can be estimated by considering only the first term in Equation 5.26 with an equivalent friction coefficient of 0.4 to 0.8 (smaller value for smooth pipe, larger value for rough pipe).

Like the relation for a sandy seabed, the lateral or transverse resistance for a pipe laid on a **clay** seabed is composed of both frictional and passive soil resistance components. A recent relation by Bruton et al. (2006) seems to work well for a range of embedment depths, z:

$$p_u = 0.2 \cdot w_s + 3z\sqrt{(D \cdot S_u \cdot \bar{\gamma})} \tag{5.28}$$

$$y_u = 0.1D \tag{5.29}$$

where $\bar{\gamma}$ is the effective unit weight of the soil (density of saturated soil minus density of seawater) and the soil shear strength at $1.0D$ below the surface is takes as representative. The estimated lateral displacement for breakout ($0.1D$ in Equation 5.28) is from Dingle et al. (2008).

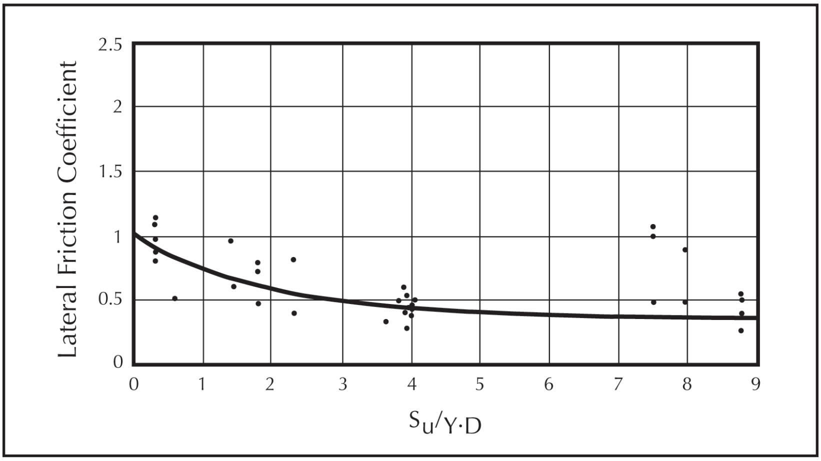

After Bruton et al., 2008

■ **Figure 5.16 Equivalent Lateral Friction Coefficient**

Once the pipeline breaks out of the pseudo-trench, the remaining lateral soil resistance depends upon the dynamic friction (as shown in Figure 5.16 for clay) and the remaining berm ahead of the pipe. An equivalent friction coefficient may be used to calculate the remaining soil resistance (Bruton et al., 2008). Notice that the variation of the lateral force in Figure 5.16 is similar to the adhesion factor in Figure 5.2. Both are decreasing functions of the clay shear strength.

5.3.4 Vertical Transverse Movement, Upward Direction

For an offshore pipeline laid directly on a sandy or hard seabed, there is no soil directly above the pipe to resist vertical movement. That is, a force equal to the submerged unit weight will cause the pipe to move upward. For consistency with the characterization of soil springs, a small relative displacement of perhaps 0.001 m may be used for the maximum elastic deformation, beyond which the upward resistance remains constant.

For a pipeline laid on a clay seabed, the initial break-out resistance needs to consider adhesion at the pipe-soil interface. For quick vertical motions, suction (negative pore water pressure) tends to increase this resistance. For simplicity, one may assume the vertical resistance equal to the submerged weight plus the adhesion coefficient times S_u times the contact width.

$$q_u = w_s + \alpha \cdot S_u \cdot D \cdot \sin\theta \tag{5.30}$$

where $\theta = cos^{-1}(1 - 2z/D) \leq 90°$. Once the breakout takes place at a displacement of about 0.002 m, the submerged weight of the pipe is the only resistance for further upward movements.

5.3.5 Vertical Transverse Movement, Downward Direction

For a pipeline laid on **hard** seabed, the downward resistance is large and the downward movement is small (e.g., several millimeters). For simplicity, a high downward stiffness (e.g., 10^7 N/m^2 level) may be assumed.

Sand

For a pipeline laid on a **sandy** seabed, the downward soil resistance is similar to that in Equation 5.17 except that $H = 0$. That is,

$$q_u = \tfrac{1}{2} \gamma N_y B^2 \qquad (5.31)$$

where B is the contact width of the pipe, which depending on the embedment of the pipe (Brown, 1995). As indicated in relation to Equation 5.30, contact width B can be calculated as $D \cdot \sin \theta$.

Clay

For pipelines laid on a soft **clay** seabed, there are a number of expressions for the resistance to downward movement. For example, Murff et al. (1989), Merifield et al. (2008), and Randolph and White (2008) have addressed this problem.

However, the results are not greatly different than those from the relation for onshore pipeline given in Equation 5.19. For example, using Murff et al. (1989), one calculates upper and lower bounds of 5.9 DS_u and 5.4 DS_u for rough pipe with $z/D = 0.5$. For smooth pipe with the same embedment ratio, the bounds are 5.6 DS_u and 4 DS_u. Using Equation 5.19, one calculates a resistance of 5.1 DS_u.

Furthermore, since that there is no “breakout” for downward movement of the pipe, results for onshore buried pipe are applicable, in this instance, to the case of surface laid offshore pipeline.

5.3.6 Variable Properties for Normal/Reverse Fault

As shown above, due to common practice in the offshore industry, soil resistance is often characterized using an effective friction coefficient in combination with the submerged weight of the pipeline. For many seismic hazards, this approach does not present a problem. However, the effective friction approach results in complications for offshore, seabed-laid pipeline subject to normal or reverse faults. In that case, the normal force for the pipe on the upthrown side is much larger than the pipes submerged unit weight. This increase in normal force would then affect axial and lateral soil springs based upon the effective friction approach.

6

Response of Buried Continuous Pipelines to Longitudinal PGD

For purposes of analysis, PGD can be decomposed into longitudinal and transverse components. This chapter discusses the response of continuous pipeline subject to longitudinal PGD (soil movement parallel to the pipe axis). Subsequent chapters will cover the response of continuous pipeline to transverse PGD (soil movement perpendicular to the pipe axis) and to abrupt offsets, such as at a fault crossing, as well as the response of segmented pipe to various types of PGD.

Under longitudinal PGD, a corrosion-free continuous pipeline may fail at welded joints, may buckle locally (wrinkle) in a compressive zone, and/or may rupture in a tensile zone. When the burial depth is very shallow, a pipeline in a ground compressive zone may buckle out of the ground like a column, as discussed in Chapter 4.

Two separate models of buried pipe response to longitudinal PGD are presented herein. In the first model, the pipeline is assumed to be linear elastic. This model is often appropriate for buried pipe with slip joints since, as shown in Chapter 4, slip joints typically fail at load levels for which the rest of the pipe is linear elastic. In the second model, the pipeline is assumed to follow a Ramberg-Osgood type stress-strain relation, as given in Equation 4.1. This model is often appropriate for pipe with arc-welded butt joints, since the local buckling or tensile rupture failure modes for these more rugged pipes typically occur when the pipe is beyond the linear elastic range. Conditions leading to local buckling failure are presented, as well as those for tensile rupture. Finally, the effect of flexible expansion joints and the effects of bends or elbows are discussed. For each of these situations, case history comparisons are presented when available.

6.1

Elastic Pipe Model

The pattern of ground deformation has a mild effect upon the response of continuous pipelines to longitudinal PGD. Examples of observed longitudinal patterns were presented in Figure 2.16. For the purpose of analysis, M. O'Rourke and Nordberg (1992) have idealized five patterns as shown in Figure 6.1. That is, the Block pattern in Figure 6.1(a) is an idealization of the relatively uniform longitudinal pattern in Figure 2.16(a) (Section Line N-2),while the Ramp, Ramp-Block, Symmetric Ridge and Asymmetric Ridge patterns are idealizations of the observed patterns in Figures 2-16(b), (c), (d) and (e), respectively. In all cases, the length of the longitudinal PGD zone (i.e., the plan dimension of a landslide or lateral spread in the direction of ground movement) is L and the maximum amount of ground movement is δ. For a Block pattern, all the soil within the PGD zone experiences the same ground movement. This results in tensile ground cracks of the head of the zone, and a compression mound at the toe. For a Ridge pattern, the maximum ground movement occurs at the center of the zone, with uniform tensile ground strain α on one side and uniform compressive ground strain α on the other.

Assuming elastic pipe material and using either elasto-plastic or rigid-plastic force-deformation relations at the soil-pipe interface, M. O'Rourke and Nordberg (1992) analyzed the response of buried steel pipeline to three idealized patterns of longitudinal PGD (i.e., Ramp, Block and Symmetric Ridge). They found that the response for a simplified rigid-plastic model of the soil-pipe interaction gives essentially the same results as a more complex elasto-plastic model for the soil-pipe interface.

For a rigid plastic soil model, the axial force per unit length at the soil-pipe interface is taken to be constant irrespective of the amount of relative displacement between the pipe and the surrounding soil. This is considered reasonable since the amount of PGD movement, δ in Figure 6.1, is typically a meter or so, while the amount of relative displacement at the soil-pipe interface needed for plastic behavior of the soil spring is typically millimeters. The maximum pipe strain, ε, for all three patterns, normalized by the equivalent ground strain, α, is plotted as a function of

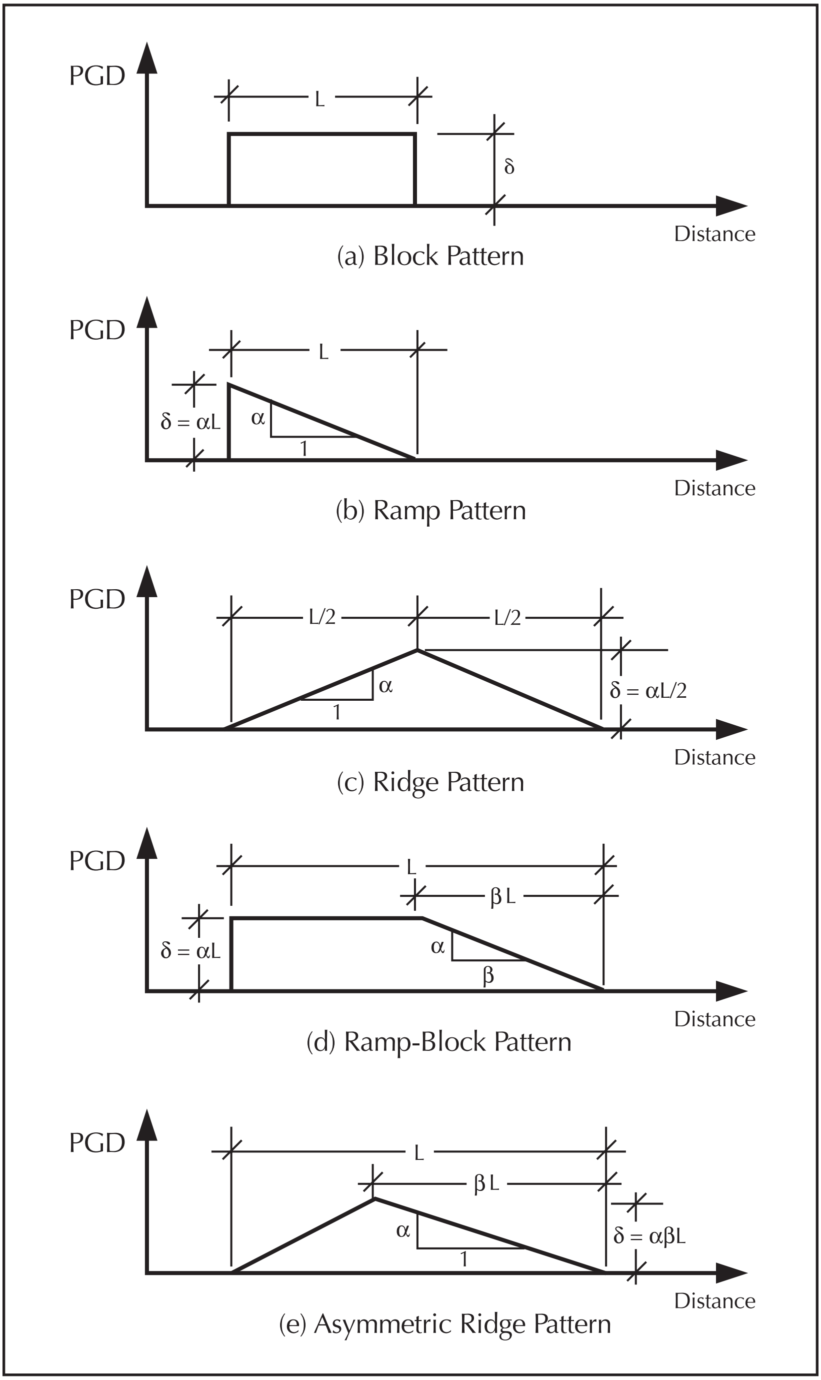

M. O'Rourke et al., 1995

■ **Figure 6.1 Five Idealization Patterns** the normalized length of the PGD zone in Figure 6.2. The length of the PGD zone is normalized by the embedment length, L_{em}, which is defined as the length over which the constant slippage force t_u must act to induce a pipe strain equal to the equivalent ground strain. Note that the Block pattern results in the largest strain in an elastic pipe.

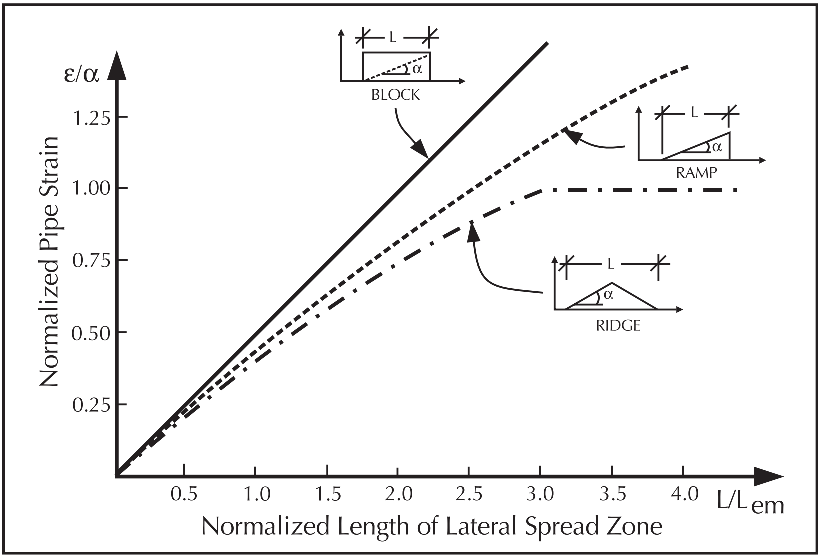

After M. O'Rourke and Nordberg, 1992

Figure 6.2 Normalized Pipe Strain as Function of Normalized Length of the Lateral Spread Zone for Three Idealized Patterns of PGD

For the Block pattern of PGD, the strain in an elastic pipe (tension at the head zone, compression at the toe) is then given by:

$$\varepsilon = \begin{cases} \dfrac{\alpha L}{2L_{em}} = \dfrac{t_u L}{2AE} & L < 4L_{em} \\ \dfrac{\alpha L}{\sqrt{LL_{em}}} = \sqrt{\dfrac{\delta t_u}{AE}} & L > 4L_{em} \end{cases} \tag{6.1}$$

where

$$L_{em} = \frac{\alpha EA}{t_u} \tag{6.2}$$

For $L < 4\ L_{em}$, the pipe strain is controlled by the length of PGD zone, L, while for $L > 4\ L_{em}$ the pipe strain is controlled by the amount of ground movement, δ.

Flores-Berrones and M. O'Rourke (1992) extended the model for a linear elastic pipe with a rigid-plastic "soil spring" (i.e., maximum resistance t_u for any non-zero relative displacement at the soil-pipe interface) to the Ramp-Block and Asymmetric Ridge patterns. They assigned the most appropriate of the five idealized patterns in Figure 6.1 to each of the 27 observed patterns presented by Hamada et al. (1986) and determined the peak pipe strain. They found that the idealized block pattern (that is, Equation 6.1) gave a reasonable estimate of pipe response for all 27 of the observed patterns. This is shown in Figure 6.3 wherein the calculated maximum strain in two elastic pipes (ϕ = 27°, H = 0.9 m (3 ft), t = 1.9 cm (3/4 in) for Pipe 1 and ϕ = 35°, H = 1.8 m (6 ft), t = 1.27 cm (1/2 in) for Pipe 2) with the appropriate idealized PGD pattern are plotted against the value from Equations 6.1 (i.e., an assumed Block pattern).

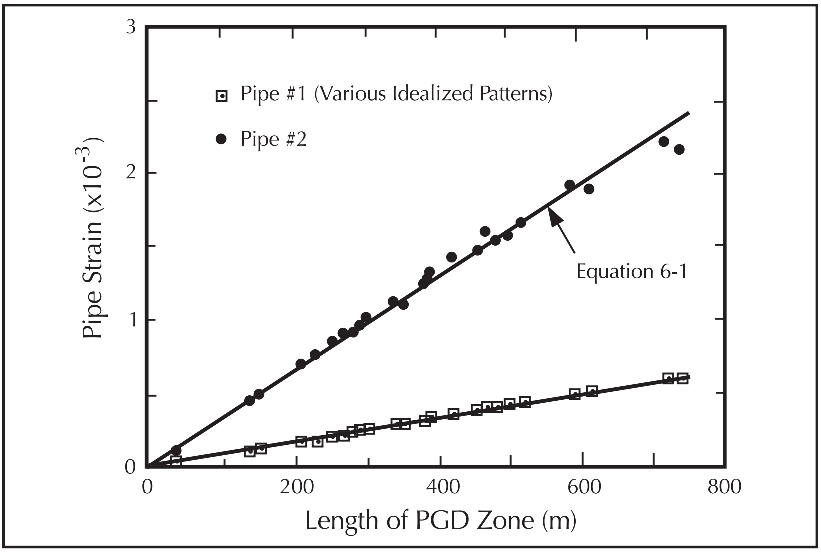

After Flores-Berrones and M. O'Rourke, 1992

■ **Figure 6.3 Maximum Strain in Two Elastic Pipes**

Some of the pipeline damage in the 1994 Northridge earthquake provide case histories for comparison with the elastic pipe model. Three out of seven pipelines along Balboa Blvd. were damaged due to longitudinal PGD. Figure 6.4 shows a map of the PGD zone and the locations of the pipe breaks on Balboa Blvd., in which the two parallelograms are the margins of the PGD zone. According to T. O'Rourke and M. O'Rourke (1995), the length or

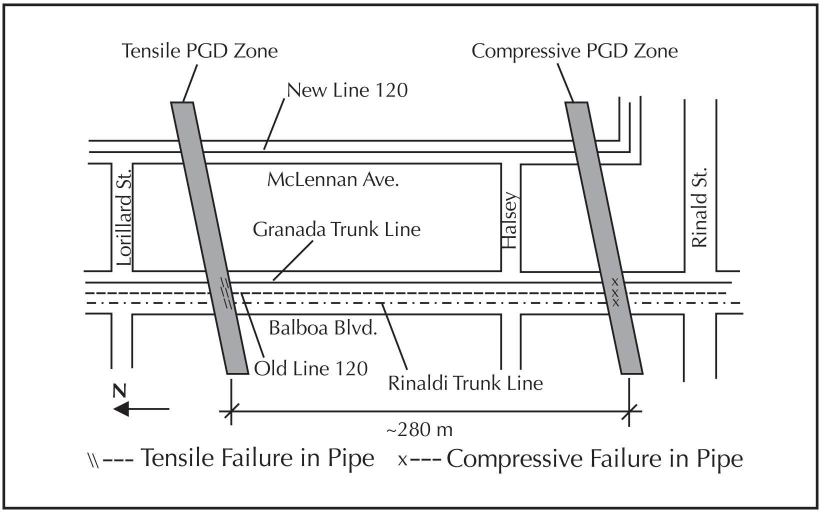

■ **Figure 6.4 Map of Ground Deformation Zones and Locations of Pipeline Damage on Balboa Blvd.**

spatial extent of the PGD zone along Balboa Blvd. was 280 m (918 ft) and the amount of movement was about 0.50 m (20 in).

The properties of those three damaged pipelines are shown in Table 6.1. Note that all these pipelines are made of Grade-B steel.

Due to the relatively low strength of slip joints and unshielded arc-welded joints, the linear elastic pipeline model discussed above can be used to analyze the behavior of these pipelines.

■ **Table 6.1 Properties of Three Damaged Pipelines**

Pipeline	Diameter (mm)	Thickness (mm)	σ_y (MPa)	Burial Depth (m)	Coating	Joints
Granada Trunk Line	1260	6.4	249	1.8	Cement Mortar	Slip joints
Rinaldi Trunk Line	1730	9.5	249	2.7	Cement Mortar	Slip joints
Old Line 120	560	7.1	242	1.5	Coal Tar Epoxy	Unshielded Arc Welded

The interaction force at the pipe-soil interface is evaluated using Equation 5.1, and assuming $\phi = 37°$ for dense sand, $k = 0.87$ for coal tar epoxy, $k = 1.0$ for cement mortar coating and $\bar{\gamma} = 1.88 \times 10^4 N/m^3$ (115 pcf). For the two water trunk lines, the joint efficiency of 0.40 is assumed, which is reasonable based upon results in Figures 4.9 and 4.10 for a D/t ratio of about 190. For unshielded arc-welded Line-120, the yield strain of the pipe steel is conservatively used as the critical strain since the compressive and tensile strength of these type of joints are less than those determined from the yield strength of the pipe steel (T. O'Rourke and M. O'Rourke, 1995). Table 6.2 shows the critical strain for the pipes (i.e., failure condition based on joint efficiency, etc.) as well as the induced seismic strain calculated from Equation 6.1. Since the calculated seismic strain is larger than the critical strain, failure is predicted for each of these pipes, which, as mentioned previously, was the observed behavior.

Table 6.2 Computation for Three Damaged Pipelines Along Balboa Blvd.

Pipeline	k	Frictional Coefficient	Joint Efficiency	Critical Strain	L_{em} (m)	Seismic Strain	Predicted Behavior
Granada Trunk Line	1.0	0.75	0.40	0.48×10^{-3}	50.0	2.1×10^{-3}	Failure
Rinaldi Trunk Line	1.0	0.75	0.40	0.48×10^{-3}	51.0	2.1×10^{-3}	Failure
Old Line 120	0.87	0.63	1.0	1.2×10^{-3}	78.7	1.59×10^{-3}	Failure

6.2 Inelastic Pipe Model

As mentioned above, failure of arc-welded pipelines with typical burial depths and diameter-to-wall thickness ratios requires a model in which the pipe material is inelastic. Since the Block pattern appears to be the most appropriate model for elastic pipes, M. O'Rourke et al. (1995) assumed a Block pattern for determination of the circumstances leading to a longitudinal PGD failure in a pipe with a more realistic Ramberg-Osgood material model. The idealized Block pattern, shown in Figure 6.1(a), corresponds to a mass of soil having length *L*, moving down a slight incline. The soil displacement on either side of the PGD zone is zero, while the soil displacement within the zone is a constant value δ. As shown for example in Figure 6.5, a block of soil between Points B and D moves to the right, tending to drag the pipe along with it. That is, the soil forces acting on the pipe within the PGD zone are to the right. However, the soil between Points A and B near the head, and between Points D and E near the toe, resist the pipe movement and these soil restraint forces are directed to the left. The combined soil-pipe interaction forces result in a region of pipe axial tension near the head and a region of axial compression near the toe. Since the longitudinal force per unit length at the soil-pipe interface is assumed constant, the pipe axial force varies linearly with maximum tension of the head (Point B) and maximum compression at the toe (Point D). The resulting pipe strains are related to pipe stress through the aforementioned Ramberg-Osgood relation.

The situation sketched in Figure 6.5 (Case I) corresponds to the case where the ground displacement, δ, is comparatively large and the length of the PGD zone, *L,* is comparatively short. In that case, the maximum pipe displacement is less than the ground displacement and the pipe strain is controlled by *L*.

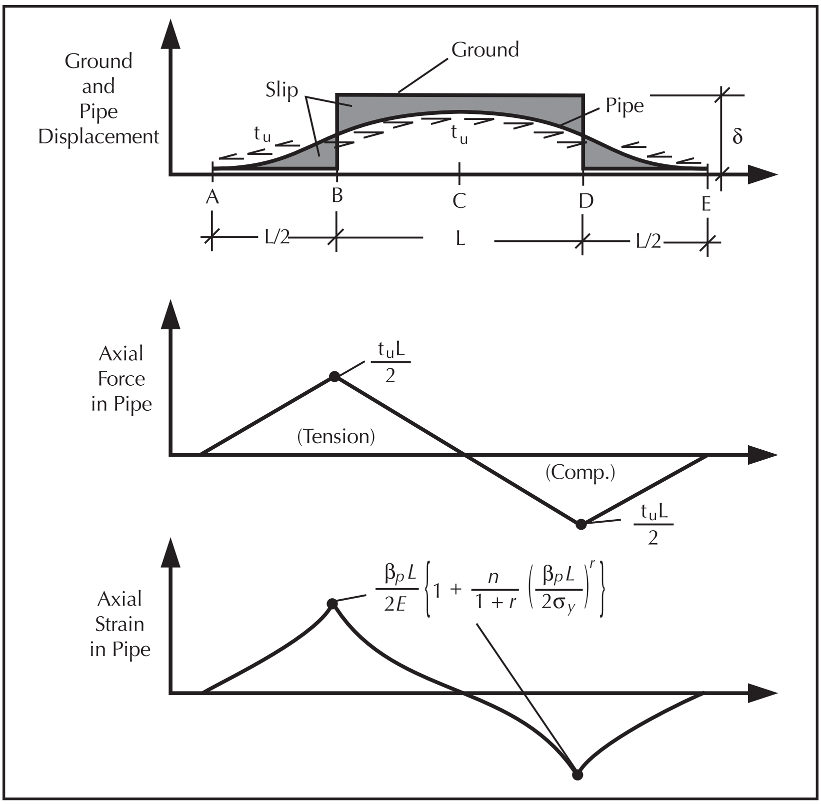

After M. O'Rourke et al., 1995

■ **Figure 6.5 Distribution of Pipe Axial Displacement, Force and Strain for Case I**

The other possibility (Case II) is sketched in Figure 6.6. There, the length of the PGD zone is comparatively large while the amount of ground displacement is comparatively short. There is still axial pipe tension at the head and compression at the toe, however, the zone is long enough that the pipe displacement matches that of the ground between Points C and D where the axial force and strain in the pipe are zero.

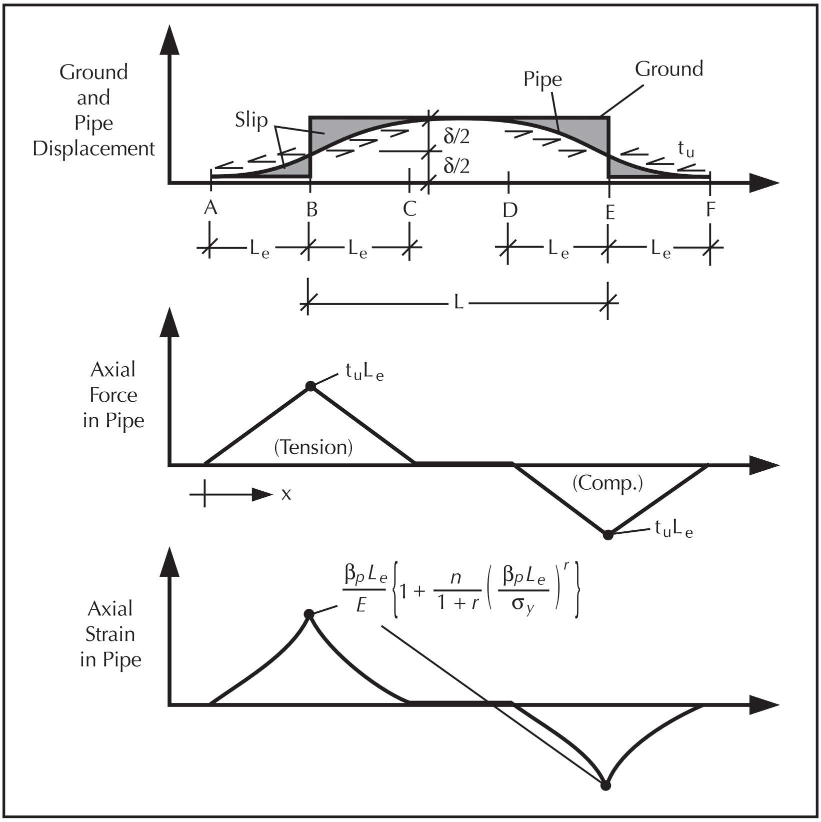

After M. O'Rourke et al., 1995

■ **Figure 6.6 Distribution of Pipe Axial Displacement, Force and Strain for Case II**

As shown in Figures 6.5 and 6.6, the force in the pipe over the segment AB is linearly proportional to the distance from Point A. Using a Ramberg-Osgood model, the pipe strain and displacement can be expressed as follows:

$$\varepsilon(x) = \frac{\beta_p x}{E}\left\{1 + \frac{n}{1+r}\left(\frac{\beta_p x}{\sigma_y}\right)^r\right\} \tag{6.3}$$

$$\delta(x) = \frac{\beta_p x^2}{E}\left\{1 + \frac{2}{2+r}\cdot\frac{n}{1+r}\cdot\left(\frac{\beta_p x}{\sigma_y}\right)^r\right\} \tag{6.4}$$

where n and r are Ramberg-Osgood parameters discussed in Chapter 4, E is the modulus of elasticity of steel, σ_y is the effective yield stress and β_p is the pipe burial parameter, having units of pounds per cubic inch, defined as the friction force per unit length t_u divided by the pipe cross-sectional area A.

For sandy soil ($S_u = 0$), with k_0 in Equation 5.1 taken as 1.0 the pipe burial parameter β_p is defined as:

$$\beta_p = \frac{\mu\gamma H}{t} \tag{6.5}$$

where the frictional coefficient μ is given by:

$$\mu = \tan k\phi \tag{6.6}$$

For clay, the pipe burial parameter β_p can be expressed as:

$$\beta_p = \frac{\alpha S_u}{t} \tag{6.7}$$

where α is the adhesion factor for clay (see Figure 5.2).

As one would expect, the relations for a Ramberg-Osgood (R.O.) pipe in Equations 6.3 and 6.4 are consistent with those for an elastic pipe (i.e., R.O. parameter $n = 0$) in Equation 6.1. For example, the peak pipe strain in Equation 6.3 (i.e., for $x = L/2$) matches that in Equation 6.1 for $L < 4\ L_{em}$.

In the following subsections, Equations 6.3 and 6.4 will be used to identify the specific combinations of longitudinal PGD length L and ground displacement δ, which lead to either a local buckling or tensile rupture failure in the pipe.

6.2.1 Wrinkling

Substituting a critical local buckling strain into Equation 6.3, one can obtain the critical length of PGD zone L_{cr}. This can then be used to calculate the critical ground movement δ_{cr} from Equation 6.4. Using the Ramberg-Osgood pipe material model, M. O'Rourke et al. (1995) develop critical values for δ and L, which result in wrinkling of the pipe wall in compression (critical strain in compression taken to be 0.175 t/R). Table 6.3 shows these critical values for Grade-B (n = 10, r = 100) and X-70 (n = 5.5, r = 16.6) steel and a variety of burial parameters and R/t ratios (radius of pipe/thickness).

A pipe fails in local buckling when both the length and displacement of the PGD zone are larger than the critical values given, for example, in Table 6.3.

Table 6.3 Critical Length and Displacement for Compressive Failure of Grade-B and X-70 Steel and Various Burial Parameters and *R/t* Ratios

		β_p = 1.0 pci		β_p = 2.5 pci		β_p = 5 pci		β_p = 15 pci		β_p = 25 pci	
	R/t	L(m)	δ(m)	L(m)	δ(m)	L(m)	δ(m)	L(m)	δ(m)	L(m)	δ(m)
GR-B	10	1762	1.32	704	0.53	352	0.26	117	0.09	70	0.05
	25	1744	1.12	698	0.45	349	0.23	116	0.08	70	0.045
	50	1728	1.05	691	0.42	346	0.21	115	0.07	69	0.042
	100	1704	1.00	682	0.4	341	0.20	114	0.066	68	0.04
	150	1660	0.94	664	0.38	332	0.19	111	0.063	66	0.037
X-70	10	4488	10.3	1795	4.1	898	2.10	299	0.69	180	0.41
	25	4182	6.87	1673	2.75	836	1.37	279	0.46	167	0.28
	50	3833	5.18	1533	2.1	768	1.04	256	0.35	153	0.21
	100	2577	2.25	1031	0.90	515	0.45	172	0.15	103	0.09
	150	1718	1.0	687	0.4	344	0.2	115	0.067	69	0.04

As a case history, two X-52 grade steel pipelines (Line 3000 and Mobil Oil) with arc-welded joints subject to the longitudinal PGD at Balboa Blvd. during the 1994 Northridge earthquake are considered. These two pipelines are a 0.76 m diameter (30 in) gas pipeline and a 0.41 m diameter (16 in) oil pipeline, as listed in Table 6.4.

Based on the ASCE Guidelines (1984), the friction reduction factor is taken as 0.6 for a pipe with epoxy or polyethylene coatings. The corresponding burial parameter is 10 pci (0.28 kgf/cm^3) for the gas line and 4 pci (0.11 kgf/cm^3) for the Mobil line. The critical displacement δ_{cr} and the critical length L_{cr} for both wrinkling and tensile rupture were determined and listed in Table 6.4. For tensile rupture, the critical strain was taken as 4%. Since the calculated critical length is larger than the observed length of the

PGD zone, the M. O'Rourke et al. (1995) model predicted successful behavior of those two X-52 grade steel pipelines along Balboa Blvd. Note, however, that the procedure suggests that one of the lines (Line 3000) is close to incipient wrinkling.

Table 6.4 Computation for Three Undamaged Pipelines Along Balboa Blvd.

Pipeline	D (m)	t (mm)	β_p (pci)	Compression		Tension	
				L_{cr} (m)	δ_{cr} (m)	L_{cr} (m)	δ_{cr} (m)
Line 3000	0.76	9.5	10	281	0.31	362	1.57
Mobil Oil	0.41	9.5	4	815	1.25	960	4.2

6.2.2 Tensile Failure

For typical pipe diameter to wall thickness ratios, D/t, the axial strain for initiation of local buckling of the pipe wall (i.e., wrinkling) is less than that for tensile rupture. Since the peak tensile and compressive strains for longitudinal PGD are equal, as shown in Figures 6.5 (Case I) and 6.6 (Case II), one expects wrinkling to occur first. However, depending upon the performance objectives for the pipe system, wrinkling of the pipe wall without subsequent rupture of the pressure boundary may be acceptable performance. For such conditions tensile rupture may be the limit state of interest. One can determine the conditions for an initial tensile rupture by substituting a tensile rupture strain into Equation 6.3. This gives the critical length of the longitudinal PGD zone, which in combination with Equation 6.4 yields the critical ground displacement. Note that the critical parameters L_{cr} and δ_{cr} for tensile failure are larger than that for compression failure.

These values can be used to evaluate the likelihood of a subsequent tensile failure. By subsequent tensile failure, we mean a tensile rupture failure in the pipe near the head of the PGD zone, **after** a local buckling failure in the compression region near the toe. For Case II shown in Figure 6.6, the tension critical parameters can be used directly to determine the potential for a subsequent tensile rupture. In that case, L is large enough and δ is small enough so that a compression failure at Point E does not affect the state of stress in the tensile region around Point B. For Case I shown in Figure 6.5, the critical parameters for tensile failure need to be modified to evaluate the potential for subsequent tensile failure. In reference to Figure 6.5, a compressive failure which limits the pipe force at Point D increases the tension force at Point B. That is, from equilibrium, the point of zero pipe force (Point C) would no longer be midway between B and D, but would shift towards D.

If the tensile rupture strain is only slightly larger than the compressive wrinkling strain, the peak tensile force at B would then be due to friction forces acting over a distance slightly larger than $L/2$. Subsequent tensile rupture would occur if the actual length of the PGD zone is slightly less than initial tension L_{cr} described above. Alternately, if the compressive wrinkling strain is much smaller than the tensile rupture strain, the point of zero pipe force would be very close to the toe of the slide (Point D) and the tensile force at B would be due to t_u acting over a distance slightly less than L. For that case, subsequent tensile rupture occurs if the actual length of the PGD zone slightly larger than **half** the initial tension L_{cr} described above.

6.3 Influence of Expansion Joints

M. O'Rourke and Liu (1994) studied the influence of flexible expansion joints in a continuous pipeline subject to longitudinal PGD. As used herein, an expansion joint allows differential axial movement across the joint but doesn't transmit axial force across the joint. Depending upon the location of the expansion joints, they may have no effect, have a beneficial effect or have a detrimental effect. For example, referring to Figure 6.5 (Case I) if the expansion joint is located at a distance larger than L away from the center of the PGD zone (i.e., to the left of Point A or to the right of Point E in Figure 6.5), an expansion joint would have no effect on the pipe stress and strain induced by the longitudinal PGD. That is, the joint would be beyond the zone of influence since the axial force in the pipe would be zero there even with no expansion joints. Similarly for Case II shown in Figure 6.6, an expansion joint to the left of Point A, to the right of Point F, or between Points C and D would have no effect.

Figures 6.7 through 6.9 illustrate the beneficial effects of two expansion joints close to the head and toe areas of a longitudinal

PGD zone. In one case (Figure 6.7), both expansion joints are located beyond (outside) the slide, in another (Figure 6.8) both are inside the slide, while in the last (Figure 6.9) one is inside and the other outside. In all three cases, an expansion joint is located within a distance $L_1(L_1 < L/2)$ of the head of the PGD zone (Point B) and another within $L_2(L_2 < L/2)$ of the toe (Point E). This placement is beneficial since the peak tension and compression forces are limited to $t_u L_1$ and $t_u L_2$, respectively.

Figure 6.10 illustrates the potential detrimental effects of a single expansion joint close to the head of a PGD zone. For Case I shown in Figure 6.10(a), the tensile stress is reduced to $t_u L_1$ but the compression stress is increased to $t_u L_3$. That is, a single expansion joint made the situation worse since the total soil drag load $t_u L$ is no longer shared equally at both the compression and tension zones. The reverse occurs for a single expansion joint near the toe region. That is, for Case I the compression stress is reduced but the tensile stress increases. For Case II shown in Figure 6.10(b), the tensile stress is still reduced to $t_u L_1$ but the compression stress is unchanged.

The use of expansion joints presupposes that they are able to accommodate the imposed relative expansion and contraction. For example, if the distance L_1 and L_2 in Figure 6.9 are small (expansion joints very close to the head and toe of the PGD zone), the required expansion and contraction capability would be essentially the same as the ground displacement δ. For an expansion joint at distance $L_1(L_1 < L/2)$ away from the head or toe, the required expansion or contraction capacity is $\delta - t_u L_1^2/(AE)$, as shown in Figure 6.10.

If the amount of ground movement and required expansion/contraction capability are larger than the allowable movement of the expansion joint, the pipeline will likely be damaged. This type of damage has been observed in past events. For example, T. O'Rourke and Tawfik (1983) note that during the 1971 San Fernando earthquake, two water mains containing flexible joints were damaged at mechanical joints. However, in that particular case, the pipe was subject to transverse PGD in combination with a small amount of longitudinal PGD.

In summary, the use of expansion joints to mitigate against the effects of longitudinal PGD on continuous pipelines must be done with care. In general, to be effective, at least two expansion joints are needed, one close to the head of the PGD zone and the other

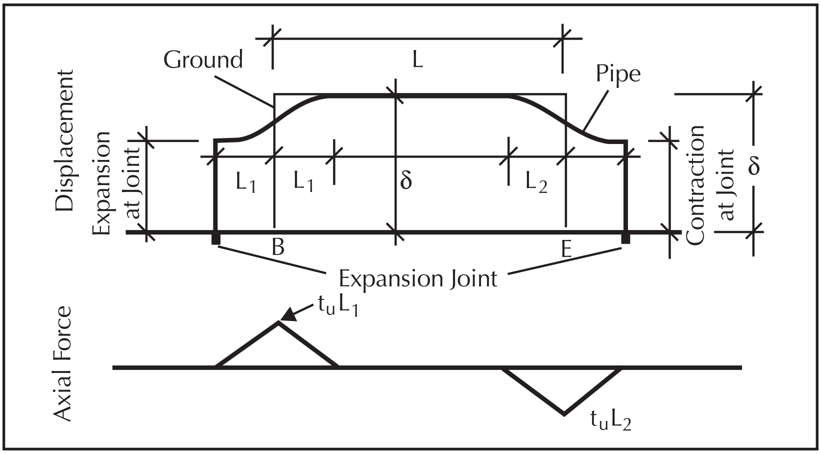

■ **Figure 6.7 Pipe and Soil Displacement with Two Expansion Joints Outside PGD Zone**

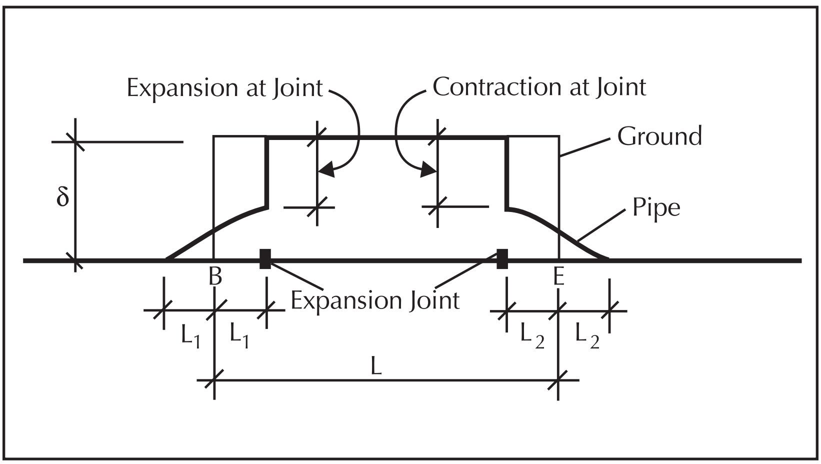

■ **Figure 6.8 Pipe and Soil Displacement with Two Expansion Joints Inside PGD Zone**

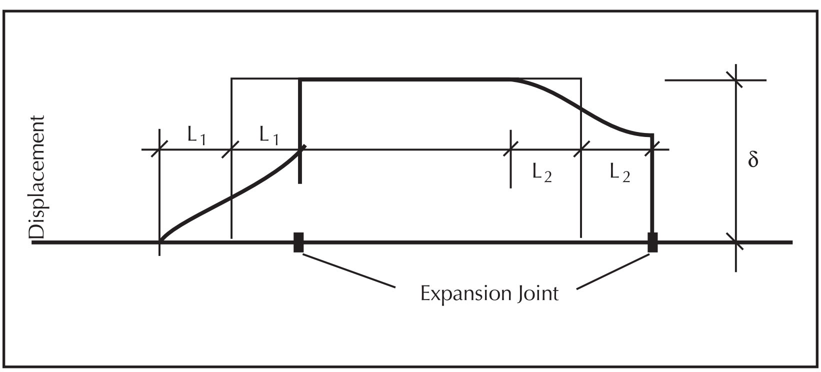

■ **Figure 6.9 Pipe and Soil Displacement with One Inside and One Outside PGD Zone** close to the toe. In addition, the expansion and contraction capability of the joints themselves needs to be comparable to the amount of ground deformation δ. Finally, one needs a reasonably accurate estimate of both the location and extent of the PGD zone.

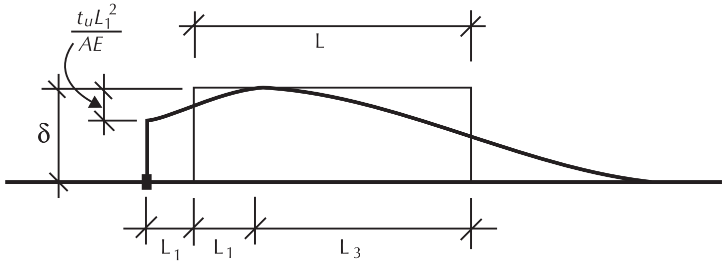

(a) One Expansion Joint Near Head, Case I

(b) One Expansion Joint Near Head, Case II

Figure 6.10 Pipe and Soil Displacement with a Single Expansion Joint

6.4

Influence of an Elbow or Bend

An elbow or bend located close to, but beyond the margins of a longitudinal PGD zone, will influence pipe response. In addition to the PGD-induced axial stresses generated in the straight section of pipe, bending stresses are generated at the elbow. Furthermore, because of the presence of the elbow, the soil drag force is no longer equally distributed between the tension at the head and compression at the toe. The case of a 90° bend in the horizontal plane is considered here. The longitudinal PGD causes the elbow to move in the direction of ground movement. This elbow movement is resisted by transverse soil springs along the transverse leg (i.e., the leg perpendicular to the direction of ground motion). The soil loading on the transverse leg results in bending moments, M, at the elbow as well as a concentrated force, F (an axial force in the longitudinal leg equal to the corresponding shear force in the transverse leg). Similar to the models in Figures 6.5 and 6.6, two cases are considered herein as shown in Figure 6.11.

In both cases, the elbow is located at a distance L_0 from the compression area (i.e., the ground movement is in a direction towards the elbow). In Case I, the length of the PGD zone, L, is small and the pipe response is controlled by the length of the PGD zone, as shown in Figure 6.11(a). In Case II, the length of the PGD zone is large and pipe response is controlled by the displacement of the PGD zone, δ, as shown in Figure 6.11(b).

In the analytical development which follows, the pipe is assumed to be elastic and the axial force per unit length along the longitudinal leg is taken as t_u. Assuming that the lateral soil spring along both the longitudinal and transverse legs are elastic, a beam on elastic foundation model of the elbow results in the following relation between the imposed displacement δ' and the resulting force F:

$$\delta' = \frac{1}{2\xi^3 EI}\,(F - \xi M) \tag{6.8}$$

where,

$$\xi = \sqrt[4]{\frac{K_g}{4EI}} \tag{6.9}$$

and M is the resulting moment at the elbow, given by:

$$M = \frac{F}{3\xi} \tag{6.10}$$

For a given force F at the elbow, equilibrium of the longitudinal leg near the compression margin requires:

$$F = (L_1 - L_0)t_u \tag{6.11}$$

where L_1 is the distance from the compression margin of the PGD zone to the point of zero axial pipe stress within the PGD zone (Point A in Figure 6.11(a)).

For a small L case (Case I in Figure 6.11(a)), the pipe response is controlled by the length of PGD zone. The maximum pipe dis-

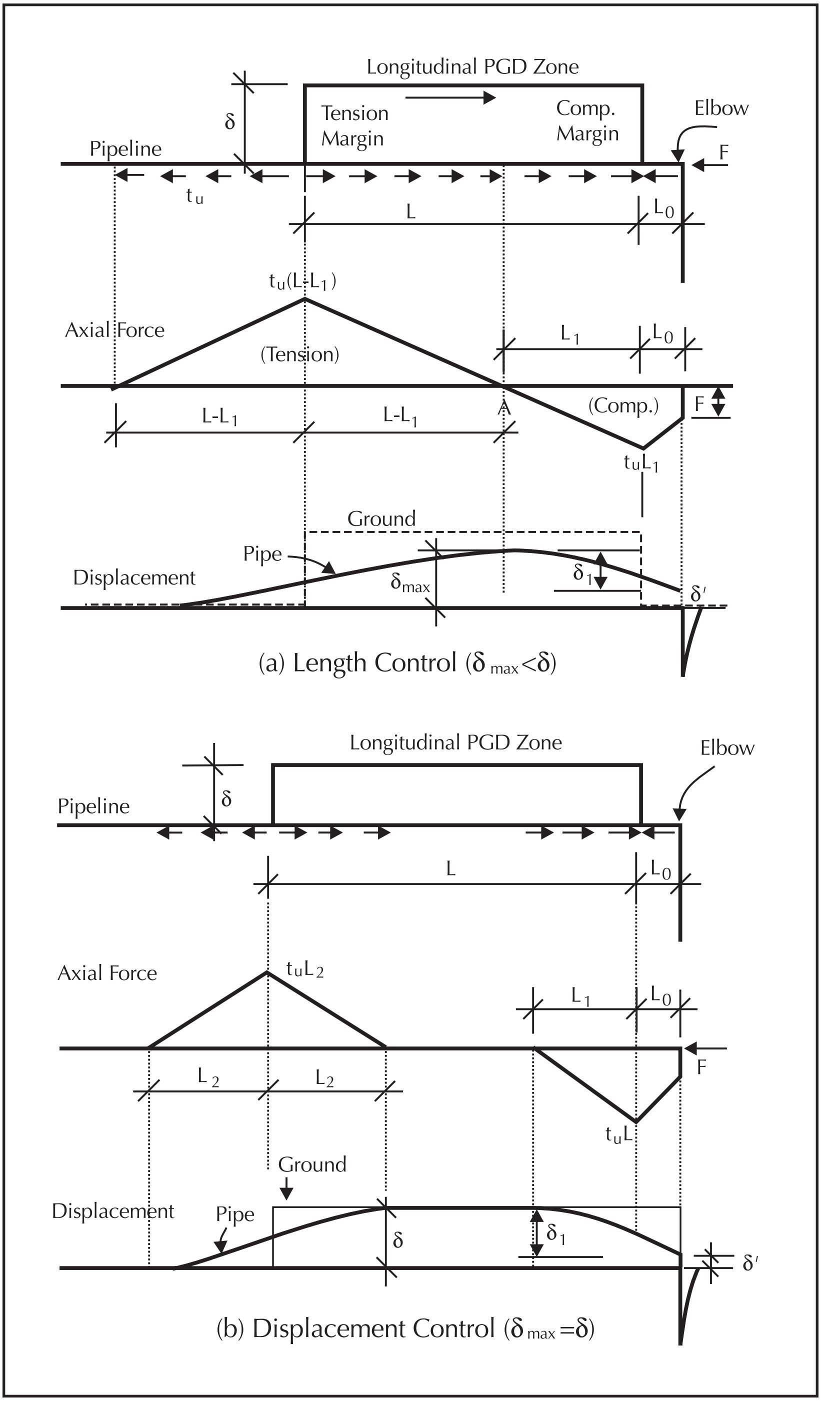

Figure 6.11 Pipeline with Elbow Subject to Longitudinal PGD

placement δ_{max} is less than the ground displacement δ. Considering pipe deformation near the compression margin,

$$\delta_{max} = \delta' + \delta_1 \tag{6.12}$$

where δ' is given by Equations 6.8 and 6.10, and

$$\delta_1 = \frac{FL_0}{AE} + \frac{t_u L_0^2}{2AE} + \frac{t_u L_1^2}{2AE} \tag{6.13}$$

is the displacement due to pipe strain between Point A and the elbow.

Considering pipe deformation near the tension margin, that is integrating pipe strain to the left of Point A gives,

$$\delta_{max} = \frac{t_u (L - L_1)^2}{AE} \tag{6.14}$$

hence,

$$\frac{t_u (L - L_1)^2}{AE} = \frac{F}{3EI\xi^3} + \frac{FL_0}{AE} + \frac{t_u L_0^2}{2AE} + \frac{t_u L_1^2}{2AE} \tag{6.15}$$

For a large length case (Case II in Figure 6.11(b)), the pipe response is controlled by the maximum ground displacement. That is,

$$\delta_{max} = \delta = \delta' + \delta_1 \tag{6.16}$$

or

$$\delta = \frac{F}{3EI\xi^3} + \frac{FL_0}{AE} + \frac{t_u L_0^2}{2AE} + \frac{t_u L_1^2}{2AE} \tag{6.17}$$

The force F at the elbow and the effective length L_1 can be obtained by simultaneously solving Equations 6.11 and 6.15 (Case I) or Equations 6.11 and 6.17 (Case II). The moment can then be calculated by Equation 6.10. When the elbow is located near the compression margin, the maximum pipe stress at the elbow is then given by:

$$\sigma = \frac{F}{A} \pm \frac{MD}{2I} \tag{6.18}$$

When the elbow is located beyond the PGD zone but close to the tension margin, the same relation applies but the force at the elbow, *F*, would be tension.

McLaughlin (2003) investigated the effects of an elbow on the response of a pipe subject to longitudinal PGD. Specifically, he considered the case where the transverse soil springs were elastic-plastic, as opposed to the assumption of elastic behavior used above. This was accomplished through the introduction of an analytically derived flexibility factor. Table 6.5 presents a comparison of results, elastic-plastic transverse spring versus elastic transverse spring, for a model corresponding to the New Line 120 case history. As shown in Figure 6.12, New Line 120 was subject to longitudinal PGD along McLennan Avenue during the 1994 Northridge earthquake. There is an elbow at about 40 m (131 ft) away from the southern (compression) margin of the PGD zone. The length of the PGD zone was about 280 m (918 ft) and the amount of ground displacement was reported to be about 0.50 m (20 in). This line is X-60 grade steel pipe with D = 0.61 m (24 in), t = 0.0064 m (1/4 in) and H = 1.5 m (5.0 ft). For the pipe with fusion bounded epoxy coating (μ = 0.38), the axial friction force per unit length is estimated to be 1.8×10^4 N/m (103 lbs/in) from Equation 5.1 while the lateral (transverse) spring coefficient is estimated to be 3.3×10^6 N/m^2 (482 lbs/in^2).

Table 6.5 Pipe Strains for New Line 120 with Elasto-Plastic and Elastic Transverse Soil Springs for Two Values of L_o

	Elastic Spring		Elasto-Plastic Spring	
	L_o = 10 m	L_o = 40 m	L_o = 10 m	L_o = 40 m
Elbow Axial Strain	6.3×10^{-4}	4.8×10^{-4}	2.9×10^{-4}	2.6×10^{-4}
Elbow Bending Strain	4.8×10^{-3}	3.7×10^{-3}	4.8×10^{-3}	3.6×10^{-3}
Elbow Total Strain	5.5×10^{-3}	4.2×10^{-3}	5.1×10^{-3}	4.1×10^{-3}
Tensile Strain at Head	1.25×10^{-3}	1.21×10^{-3}	1.7×10^{-3}	1.49×10^{-3}
Compressive Strain of Toe	7.0×10^{-4}	7.5×10^{-4}	3.5×10^{-4}	5.2×10^{-4}
Maximum Pipe Displacement	.24 m	.21 m	.39 m	.31 m

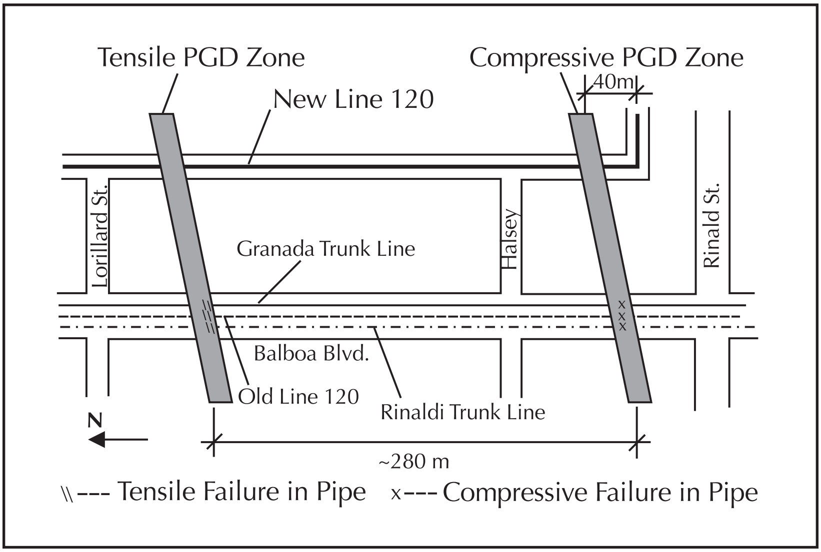

■ **Figure 6.12 Observed PGD and Location of Pipeline**

As one might expect, the presence of an elbow near the toe results in tensile strain at the head being larger than compressive strain at the toe. Also, as the distance from the compression margin to the elbow, L_0, increases the tensile pipe strain at the head decreases while the compressive strain at the toe increases. At the elbow, the flexural strains dominate and decrease with increasing L_0. For the case considered, the largest strain is at the elbow.

The comparison between elastic and elasto-plastic results is also as one might expect. Since the more realistic elasto-plastic springs are softer, the tensile pipe strains at the head increase while the compressive pipe strains at the toe decrease. Similarly, the axial strains at the elbow decrease. However, for the case considered, the flexural strains at the elbow are nominally unchanged. For the specifics of the New Line 120 case history (L_0 = 40 m), the peak tensile strain at the head is 1.49×10^{-3}, the peak compressive strain at the toe is 5.2×10^{-4}, while the peak compressive strain at the elbow is 4.1×10^{-3}. For this X-60 grade steel pipe, the tensile rupture strain is frequently taken to be 0.04. Hence, tension rupture at the head is not expected. For a *D/t* ratio of 96, the local buckling strain is about 1.8×10^{-3} and the reduction in elbow strain resulting from the assumption of elasto-plastic transverse soil spring behavior is less than 10%.

The authors understand that the line was inspected after the Northridge event and is currently in service. No distress was noted at either the tension or compression margin. However, the elbow region was not inspected.

Although all possible combinations of pipe and soil parameters were not considered, it is clear at least for the New Line 120 case that an elbow located fairly close to the compression margin acts as a net stress riser. Hence, it seems prudent to layout the pipe route such that elbows and bends are located well away from potential longitudinal PGD zones.

7 Response of Buried Continuous Pipelines to Transverse PGD

Transverse PGD refers to permanent ground movement perpendicular to the pipe axis. When subject to transverse PGD, a continuous pipeline will stretch and bend as it attempts to accommodate the transverse ground movement. The failure mode for the pipe depends then upon the relative amount of axial tension (stretching due to arc-length effects) and flexural (bending) strain. That is, if the axial tension strain is small, the pipe wall may buckle in compression due to excessive bending. On the other hand, if axial tension is large, the pipe may rupture in tension due to the combined effects of axial tension and flexure. T. O'Rourke and Tawfik (1983) present a case history from the 1971 San Fernando event of continuous pipe failure due to PGD. The transverse component of PGD was approximately 1.7 m. Line 1001 (Pipeline 5 in Figure 2.17) was abandoned because of multiple breaks. Line 85 (Pipeline 4 in Figure 2.17) was repaired at several locations within the PGD zone. The records indicate that three repairs near the eastern boundary of the soil movement were due to tensile failure and two other repairs near the western boundary were due to compressive failure. Note that, besides the large lateral movement, there was a small longitudinal component toward the west and that tension failure near the eastern margin, coupled with compression failures near the western margin, are consistent with pipe response to longitudinal PGD to the west. Hence, although the larger ground movements were transverse, the pipe failure modes may well have been controlled by the smaller in magnitude longitudinal movements. As will be seen, transverse PGD without abrupt transverse offsets at the margin typically do not result in pipe failure.

Similar to longitudinal PGD, pipeline response to transverse PGD is in general a function of the amount of PGD δ, the width of the PGD zone as well as the pattern of ground deformation. Figure 7.1 presents sketches of two types of transverse patterns considered herein.

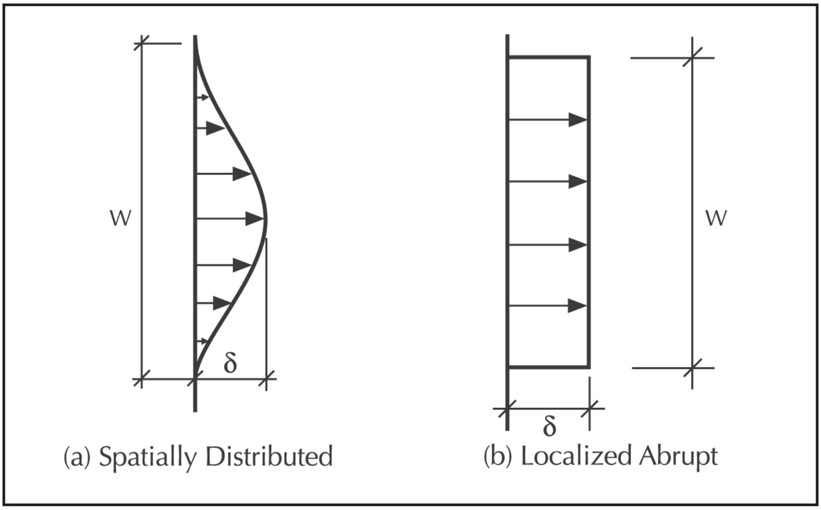

■ **Figure 7.1 Patterns of Transverse PGD**

Observed examples of **spatially distributed** transverse PGD (sketched in Figure 7.1(a)) have previously been presented in Figure 2.17 near Pipeline 2. In these cases, the pipe strain is a function of both the amount and width of the PGD zone. Observed examples of **abrupt** transverse PGD (sketched in Figure 7.1(b)) have previously been presented in Figure 2.17 near Pipelines 4 and 5. In these cases, the pipe strain is a function of δ and, in some cases, the width of Zone W. That is, if the zone is wide, the movement at each margin of the PGD zone corresponds more or less to a fault offset where the fault/pipeline intersection angle is 90°.

Another type of onshore transverse PGD occurs due to bouyancey when a pipe is surrounded by liquefied soil. In addition to the potential pipe deformation in the horizontal direction due to lateral spreading of liquefied soil, it may also uplift due to buoyancy (transverse deformation in the vertical direction). This mechanism has caused pipe damage in past events. For example, Suzuki (1988) and Takada (1991) mentioned that some pipes, with or without manholes, were uplifted out of the ground due to buoyancy effects during the 1964 Niigata earthquake. This in all likelihood would require replacement of the lines even if the pipe were still able to transmit fluids.

In this chapter, we discuss in detail continuous onshore and continuous offshore pipeline response to transverse PGD. This distinction is necessary due to the differences in onshore and offshore pipe response. These differences in response are due to differences in the soil strengths. For example, according to Nodine et al. (2006), the shear strength of under-consolidated clay at the sea floor in the Mississippi River Delta is about 50 psf with an increase of 8 psf per ft depth. These offshore soil strengths are an order of magnitude **less** than S_u for onshore frictionless materials. The stronger soils result in beam-like behavior for onshore pipelines. That is, axial tension and flexure are both important. However, the weaker soils in the offshore environment result in pipes that behave like a cable. That is, axial tension controls the behavior.

7.1 Idealization of PGD Patterns

In this section, the various analytical idealizations of transverse PGD that have been used are reviewed. Analytical and numerical models of pipe response to spatially distributed transverse PGD are then discussed. The cases of a pipeline in a competent soil layer and in a liquefied layer are presented separately. Also, the effects of the buoyancy force are discussed. Finally, the conditions whereby abrupt transverse PGD may be modeled as a special case of fault offset are presented. The topic of pipe response to fault offset is discussed in Chapter 8.

One of the first items needed to evaluate pipeline response to spatially distributed transverse PGD is the pattern of ground deformation, that is, the variation of ground displacement across the width of the PGD zone. Different researchers have used different patterns in their analyses.

T. O'Rourke (1988) approximates the soil deformation with the beta probability density function:

$$y(x) = \delta[s/s_m]^{r'-1}[(1-s)/(1-s_m)]^{\tau-r'-1} \quad 0 < s < 1 \tag{7.1}$$

where s is the distance between the two margins of the PGD zone normalized by the width W, s_m is the normalized distance from the margin of the PGD zone to the location of the peak transverse ground displacement, δ, while r' and τ are parameters of the distribution. In his analysis, the following values were used: s_m = 0.5, r' = 2.5 and τ = 5.0. Figure 7.2 shows the resulting idealized soil deformation.

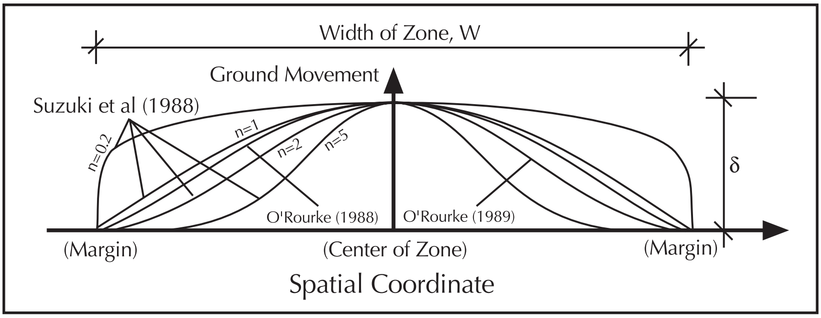

■ **Figure 7.2 Assumed Patterns for Spatially Distributed Transverse PGD**

Suzuki et al. (1988) and Kobayashi et al. (1989) approximate the transverse soil deformation by a cosine function raised to the power *n*.

$$y(x) = \delta \cdot \left(\cos \frac{\pi x}{W}\right)^n \tag{7.2}$$

where the non-normalized distance *x* is measured from the center of the PGD zone. Figure 7.2 also shows the Suzuki et al. and Kobayashi et al. model for $n = 0.2$, 1.0, 2.0 and 5.0.

M. O'Rourke (1989) assumes the following function for spatially distributed transverse PGD:

$$y(x) = \frac{\delta}{2}\left(1 - \cos \frac{2\pi x}{W}\right) \tag{7.3}$$

where *x* is the non-normalized distance from the margin of the PGD zone. This gives the same shape as both the Suzuki and Kobayashi et al.'s models with $n = 2.0$ (note, origin of *x* axis is shifted).

As shown in Figure 7.2, all the patterns are similar in that the maximum soil deformation occurs at the center of the PGD zone and the soil deformation at the margins is zero. The patterns differ in the variation of ground deformation between the center and the margins. Note that the Suzuki and Kobayashi models with $n = 0.2$ result in something like the abrupt offset case in Figure 7.1(b).

7.2

Onshore Pipe Subjected to Spatially Distributed PGD

Onshore pipelines are typically buried about 1.0 m (3 ft) below the ground surface. Often, the ground water level and the top surface of the liquefied soil layer are both below the bottom of the pipe. In these cases, the force-deformation relations at the soil-pipeline interface correspond to a pipe in competent non-liquefied soil which overrides a liquefied soil layer. Some authors refer to this as the pipe being in the "cap layer."

In the following subsections, results from various analytical approaches and nonlinear finite element approaches will be presented and compared. Results for pipes in liquefied soil are presented in Section 7.3.

7.2.1 Finite Element Methods

The finite element method allows explicit consideration of the nonlinear characteristics of pipe-soil interaction in both the transverse and longitudinal directions as well as nonlinear stress-strain relations for pipe material. T. O'Rourke (1988), Suzuki et al. (1988) and Kobayashi et al. (1989), as well as Liu and M. O'Rourke (1997b), have used the finite element approach to evaluate buried onshore pipe response to spatially distributed transverse PGD. Assumptions and numerical results from each group are presented here.

T. O'Rourke

T. O'Rourke (1988) simulated the soil deformation by the beta probability density function given in Equation 7.1. Figure 7.3 shows the deformation of both the soil and the pipe.

As shown in Figure 7.3, L_a is the distance from the margin of the PGD zone to an assumed anchored point in the undisturbed soil beyond the PGD zone. The anchored point in the T. O'Rourke (1988) model was located where the bending strain is less than 1×10^{-5}. This modeling assumption will be discussed later.

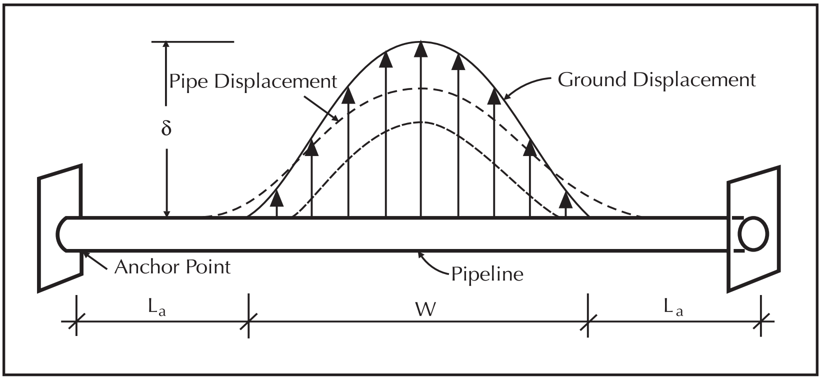

After T. O'Rourke, 1988

■ **Figure 7.3 Parameters for T. O'Rourke's Model**

Figure 7.4 presents the maximum tensile strain versus the maximum ground displacement for various widths of the PGD zone for an X-60 pipe with 0.61 m (24 in) diameter, 0.0095 m (3/8 in) wall thickness and burial depth H = 1.5 m (5 ft). For the three widths considered, as shown in Figure 7.4, the width of 10 m (33 ft) results in the largest tensile strain in the pipe for any given value of δ.

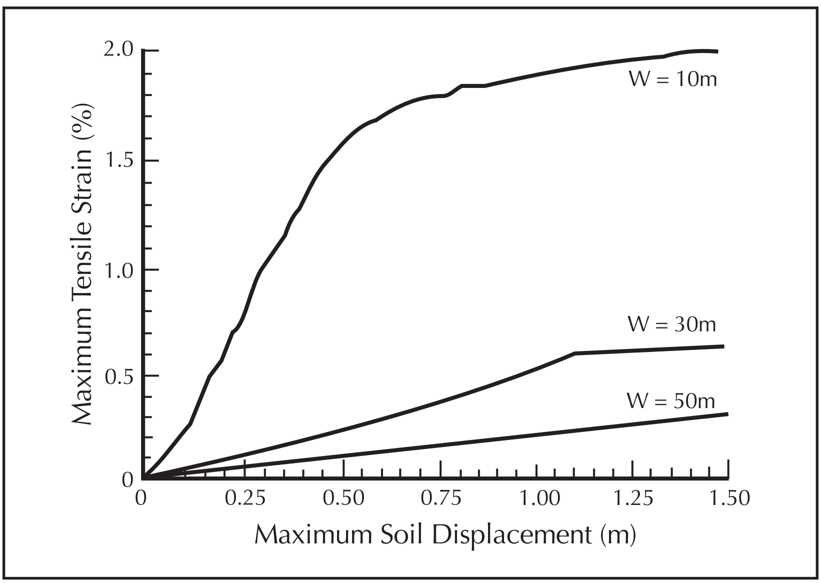

After T. O'Rourke, 1988

■ **Figure 7.4 Maximum Tensile Strain vs. Maximum Ground Displacement for Various Width of PGD Zone**

Figure 7.5 presents the maximum compressive strain as a function of δ for a width of 30 m. In this plot, the soil density ranged from 18.8 to 20.4 kN/m^3 (115 to 122 pcf) and the soil friction angle ranged from 35° to 45°. Note there is no difference in pipe response for $\delta < 0.5$ m (1.6 ft), and only a 30% difference for $\delta =$ 1.5 m (5 ft). Based on these observations, T. O'Rourke (1988) correctly concludes that the width of the PGD zone has a greater influence on the magnitude of pipe strains than the soil properties.

From Figures 7.4 and 7.5, the peak tensile and compressive strains for a width of 30 m (98 ft) and $\delta = 1.5$ m (5 ft) are about 0.61% and 0.32%, respectively. This indicates that the induced axial pipe strain, at least in the T. O'Rourke (1988) model, is significant.

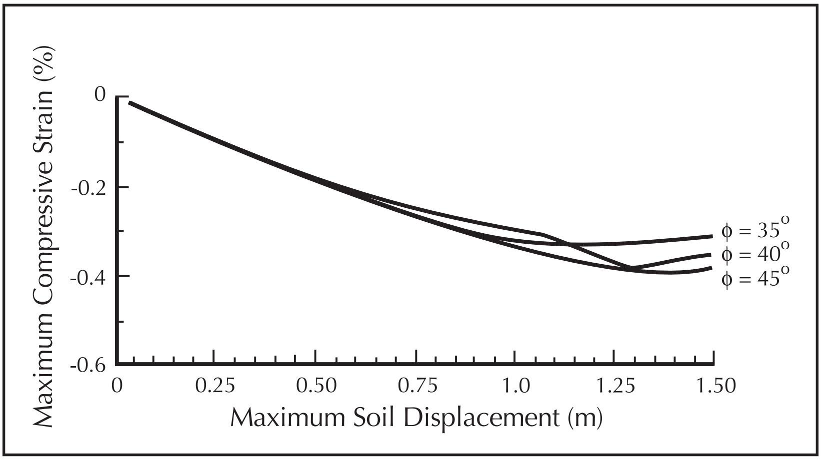

After T. O'Rourke, 1988

■ **Figure 7.5 Maximum Compressive Strains vs. Maximum Ground Displacement for Different Soil Friction Angles**

Suzuki et al.

Suzuki et al. (1988) expressed the pattern of transverse ground displacements by the cosine function raised to the *n* power, as given in Equation 7.2. The normalized patterns for four values of *n* are shown in Figure 7.2. The patterns for *n* close to zero approximate abrupt transverse PGD, while the patterns for $n \geq 1$ correspond to spatially distributed transverse PGD.

Suzuki et al.'s physical model is similar to T. O'Rourke's shown in Figure 7.3, except for the PGD pattern and the anchored length L_a. Suzuki et al. correctly note that L_a needs be long enough such that the axial friction at the pipe-soil interface can fully accommodate the axial movement of the pipe due to the PGD. That is, there should be no flexural nor axial strain in the pipe at the anchor points. It turns out that the anchored length in Suzuki et al.'s model is much larger than that in the T. O'Rourke (1988) model.

Figure 7.6 presents the influence of the width of the PGD zone on pipe strain for X-52 grade steel, 0.61 m (24 in) diameter, 0.0127 m (1/2 in) wall thickness and H = 1.5 m (5 ft). For given values of W and δ, the tensile and compressive strains are about equal. This suggests that the axial strain in the pipe is small. A certain width of the PGD zone somewhere around 30 m (98 ft) results in the largest pipe strain. Note that although the pipes are somewhat different, the tensile pipe strains in Figures 7.4 and 7.6 are somewhat similar for W = 30 and 50 m, but vastly different for W = 10 m.

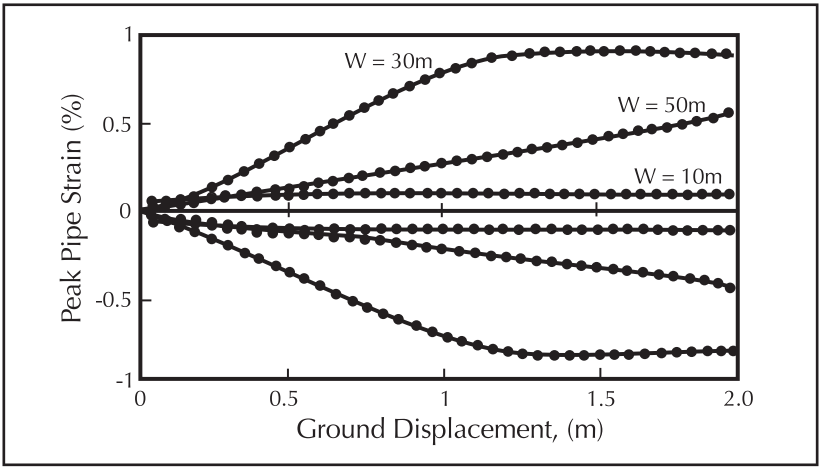

After Suzuki et al., 1988

■ **Figure 7.6 Maximum Strain vs. PGD for Different Width of PGD Zone; X-52 Grade Steel**

Kobayashi et al.

Kobayashi et al. (1989) used the same shape function and followed the same procedure as Suzuki et al. They consider an X-42 grade steel onshore pipe with 0.61-m (24-in) diameter and 0.0095-m (3/8-in) wall thickness. Kobayashi et al.'s results for the peak tensile strain are shown in Figure 7.7 for various widths of the PGD zone. Note that the largest pipe strain occurs for a width of about 19 m (62 ft) in their model.

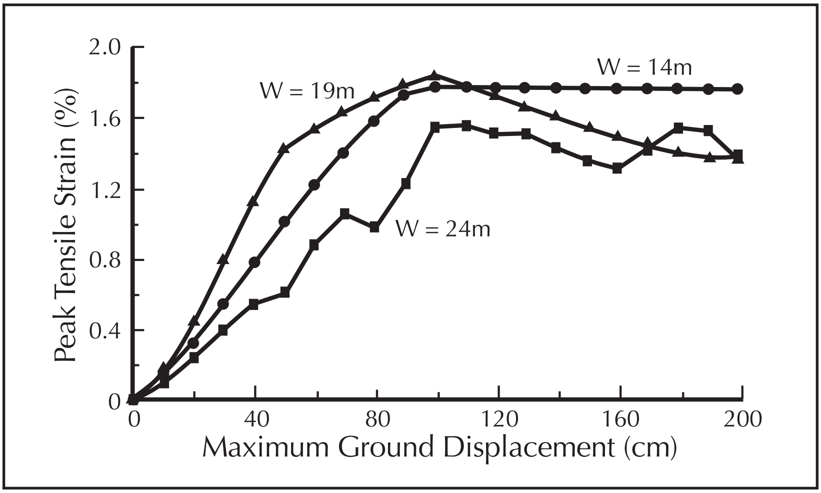

After Kobayashi et al., 1989

■ **Figure 7.7 Peak Tensile Strain vs. Maximum Ground Displacement; X-42 Grade Steel**

Liu and M. O'Rourke

Liu and M. O'Rourke (1997b) developed a finite element model, utilizing large deformation theory, nonlinear pipe-soil interaction forces (soil springs) and Ramberg-Osgood stress-strain relations for the onshore pipe material. The onshore pipe is modeled as a beam coupled by both axial and lateral soil springs. The anchor length of the pipe is long enough (up to 400 m (1,312 ft)) such that both the flexural and axial pipe strain are essentially zero at the two anchor points. The pipe is assumed surrounded by loose to moderately dense sand (friction angle $\phi = 35°$ and soil density $\gamma = 1.87 \times 10^4$ N/m^3 (115 pcf)) with a burial depth $H_c = 1.2$ m (4 ft) from ground surface to the top of the pipe. The resulting elasto-plastic soil springs are based on the TCLEE Guideline (ASCE, 1984) and have peak transverse, p_u, and longitudinal, t_u, resistance of 1.0×10^5 and 2.4×10^4 N/m (571 and 137 lbs/in), respectively. The relative displacements between pipe and soil at which the peak transverse and longitudinal soil resistances are mobilizing are 0.06 and 3.8×10^{-3} m (2.4 and 0.15 in), respectively.

Figure 7.8 shows the maximum tensile and compressive strains in the pipe versus the ground displacement for W = 10, 30 and 50 m, while Figure 7.9 shows the maximum pipe displacement versus the maximum ground displacement. Both these figures are for an X-52 grade steel pipe with D = 0.61 m (24 in), t = 0.0095 m (3/8 in) and the ground deformation pattern given in Equation 7.3. Except for W = 10 m, Figure 7.8 indicates that the peak tensile strain is substantially larger than the peak compressive strain, particularly for larger values of δ. Also, for the three widths considered, the pipe strains are largest for W = 30 m. Although the pipes are somewhat different, the peak tensile strains shown in Figure 7.8 match reasonably well with Suzuki et al.'s shown in Figure 7.6 for all three widths. Also, both the peak tensile and compressive strains match reasonably well with the T. O'Rourke (1988) results for W = 30 and 50 m. Finally, as shown by all the other numerical analyses, the peak pipe strain remains relatively constant beyond some value of the ground displacement. For example, as shown in Figure 7.8 for W = 30 m, neither the peak tensile nor peak compressive strains increase for ground displacement greater than about 1.3 m.

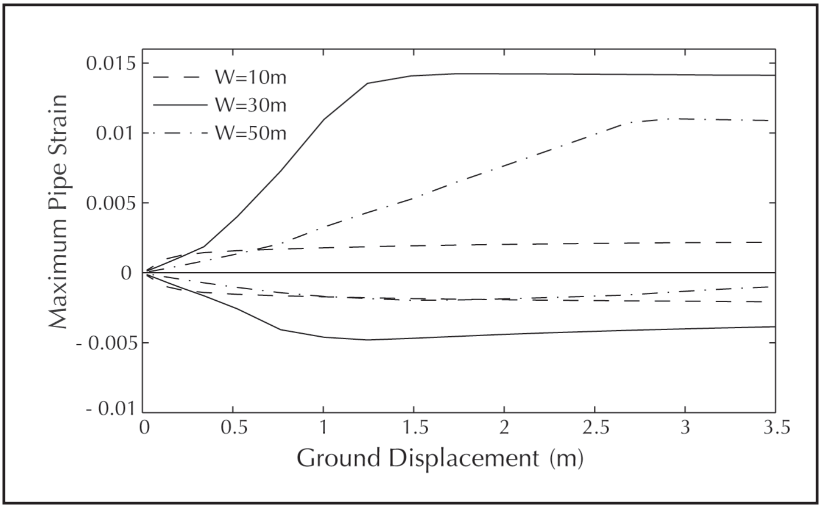

After Liu and M. O'Rourke, 1997b

■ **Figure 7.8 Maximum Pipe Strain vs. Ground Deformation; X-52 Grade Steel**

As shown in Figure 7.9, the maximum pipe displacement more or less matches the ground deformation up to a certain critical displacement δ_{cr}. Thereafter, the pipe strain remains relatively constant while the pipe displacement increases more slowly with ground deformation. For ground deformation greater than δ_{cr}, the onshore pipe bending strain varies slightly (increasing for small widths and decreasing for large widths) and axial strain increases slowly, which results in the maximum tensile strain remaining more or less constant.

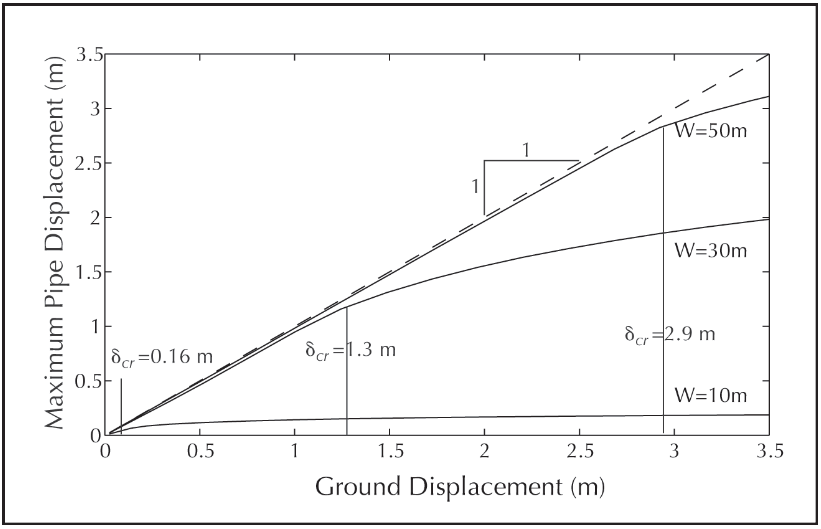

After Liu and M. O'Rourke, 1997b

Figure 7.9 Maximum Pipe Displacement vs. Ground Displacement; X-52 Grade Steel

For a fixed value of the width of the PGD zone (W = 30 m), Figure 7.10 shows the spatial distribution of pipe and soil displacement for $\delta = 0.5\delta_{cr}$, δ_{cr}, and $2\delta_{cr}$.

Note that the pipe deformation matches fairly well with the ground deformation over the whole width of the PGD zone for $\delta \leq \delta_{cr}$. However, for $\delta > \delta_{cr}$, the maximum pipe displacement is less

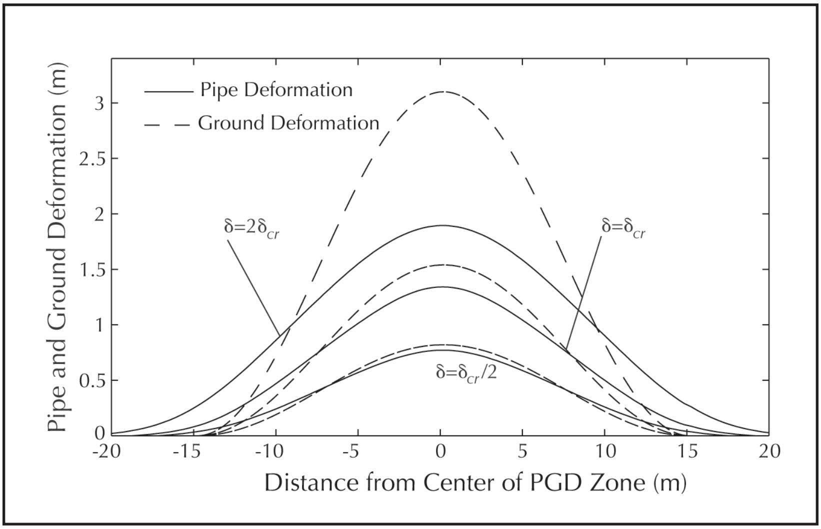

After Liu and M. O'Rourke, 1997b

Figure 7.10 Pipe and Ground Deformation for *W* = 30 m; X-52 Grade Steel

than the maximum ground displacement (from Figure 7.10, 40% less for $\delta = 2\delta_{cr}$), and "width" of the deformed pipe (i.e., length over which the pipe has noticeable transverse displacement) is larger than the width of the PGD zone. As a result, the curvature of the pipe is substantially less than the curvature of the ground for $\delta > \delta_{cr}$. As shown in Figure 7.10 for W = 30 m, the pipe curvature at $\delta = 2\delta_{cr}$ is comparable to the pipe curvature at $\delta = \delta_{cr}$.

Figures 7.11 and 7.12 show the distribution of bending moments and axial forces in the pipe at $\delta = \delta_{cr}$ for W = 10, 30 and 50 m. As one might expect, the bending moments in Figure 7.11 are symmetric with respect to the center of the PGD zone and similar to those for a laterally loaded beam with built-in (i.e., fixed) supports near the margins of the PGD zone. That is, there are positive moments near the center of the PGD zone and negative moments near the margins. The moments vanish roughly 10 m beyond the margins. Note that the bending moments for W = 30 m are larger than those for W = 10 m or 50 m.

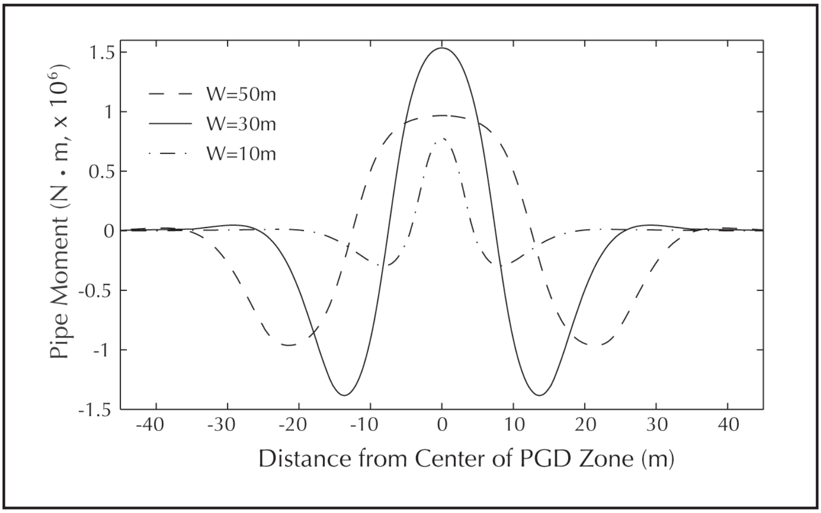

After Liu and M. O'Rourke, 1997b

■ **Figure 7.11 Distribution of Bending Moment for Three Widths ($\delta = \delta_{cr}$)**

The axial forces in the pipe shown in Figure 7.12 are, as expected, also symmetric about the center of the PGD zone. The axial forces are maximum near the center of the zone and decrease in a fairly linear fashion with increasing distance from the center of the zone. Unlike the moments, the axial forces become small only at **substantial** distances beyond the margins of the zone (note the different distance scales in Figures 7.11 and 7.12). Also, for the three widths considered, the axial force was an increasing function of the width of the PGD zone (i.e., largest for W = 50 m and smallest for W = 10 m).

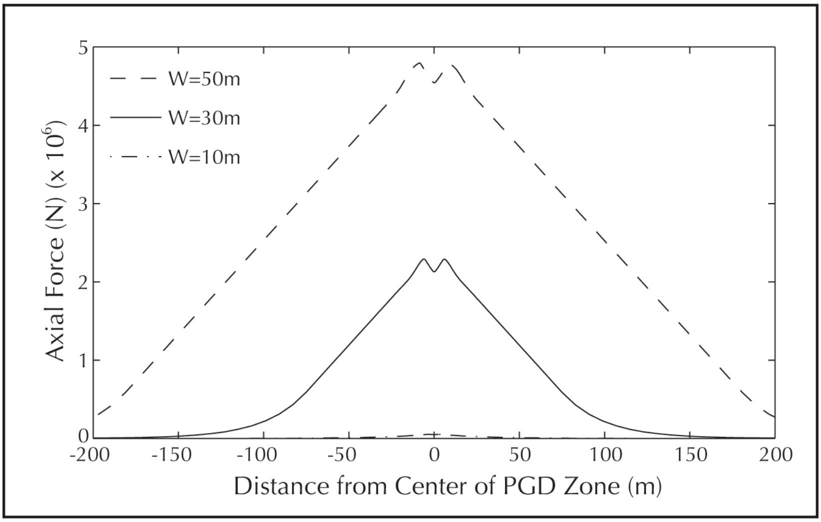

After Liu and M. O'Rourke, 1997b

■ **Figure 7.12 Distribution of Axial Force for Three Widths ($\delta = \delta_{cr}$)**

The transverse loading on the pipe also results in axial movement of the pipe, that is, inward movement towards the center of the PGD zone. This inward movement is generally an increasing function of the ground movement δ, as shown in Figure 7.13. For δ = 4 m (13 ft), this inward movement at the margins of the PGD zone for the pipe under consideration was 0.002, 0.07 and 0.15 m (0.08, 2.8 and 5.9 in) respectively for W = 10, 30 and 50 m. That is, both the inward movement at the margin (Figure 7.13) and the axial force in the pipe (Figure 7.12) are increasing functions of the width of the zone.

The influence of other parameters upon the pipe behavior was also determined and is shown in Figures 7.14 through 7.20. Unless otherwise indicated, these results are for W = 30 m, X-52 grade steel, D = 0.61 m (24 in), t = 0.0095 m (3/8 in), $p_u = 1.0 \times 10^5$ N/m, (571 lbs/in), $t_u = 2.4 \times 10^4$ N/m (137 lbs/in) and the M. O'Rourke (1989) pattern of ground deformation. Figure 7.14 shows, for example, the influence of diameter on peak tensile and compressive strains. Note that both the peak tensile and compressive strains are increasing functions of diameter.

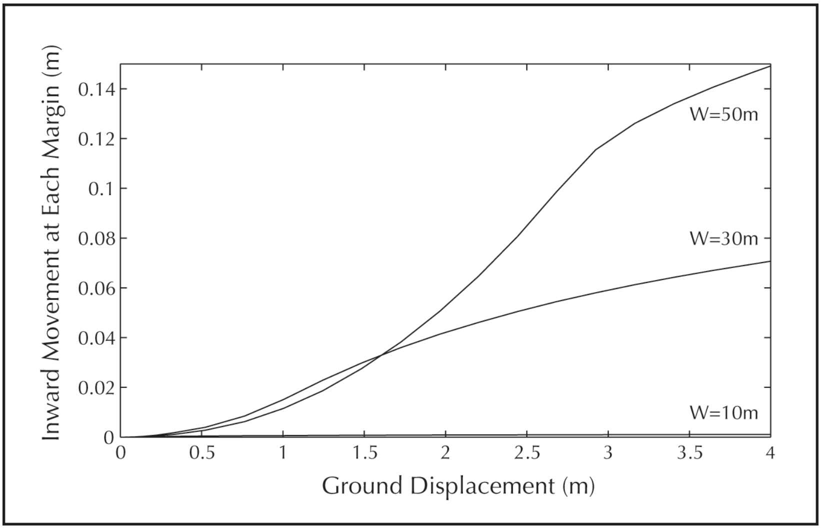

After Liu and M. O'Rourke, 1997b

■ **Figure 7.13 Pipe Inward Movement at Each Margin of PGD Zone**

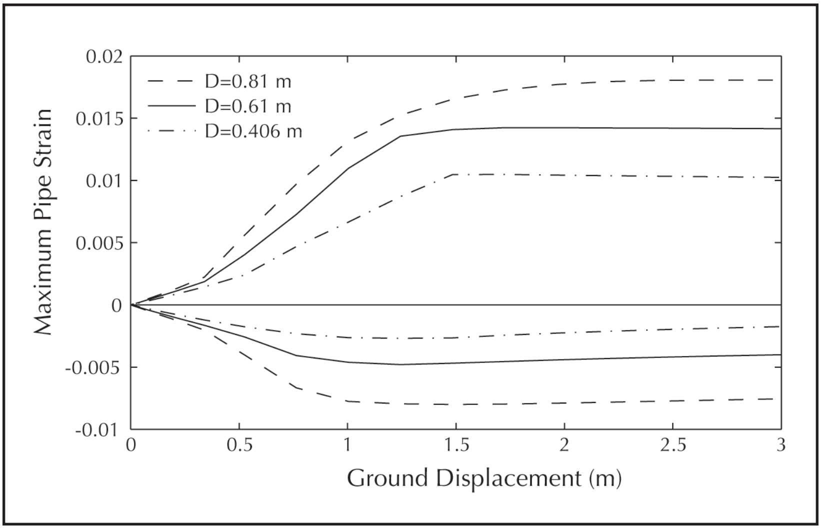

After Liu and M. O'Rourke, 1997b

■ **Figure 7.14 Influence of Pipe Diameter, *D***

For the onshore pipe model considered, the peak tensile strain is to a greater or lesser extent a function of all the parameters shown in Figures 7.14 through 7.20. However, the peak compressive strain is essentially independent of the wall thickness, as shown in Figure 7.15, and the steel grade, as shown in Figure 7.18.

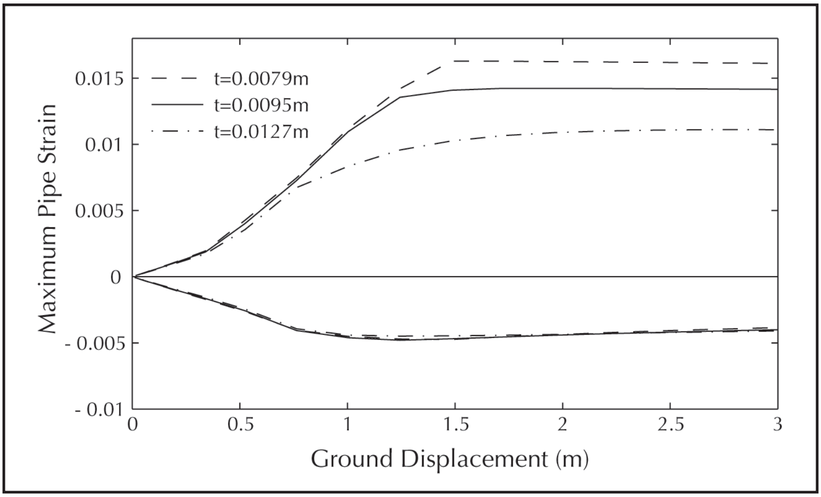

After Liu and M. O'Rourke, 1997b

■ **Figure 7.15 Influence of Wall Thickness, *t***

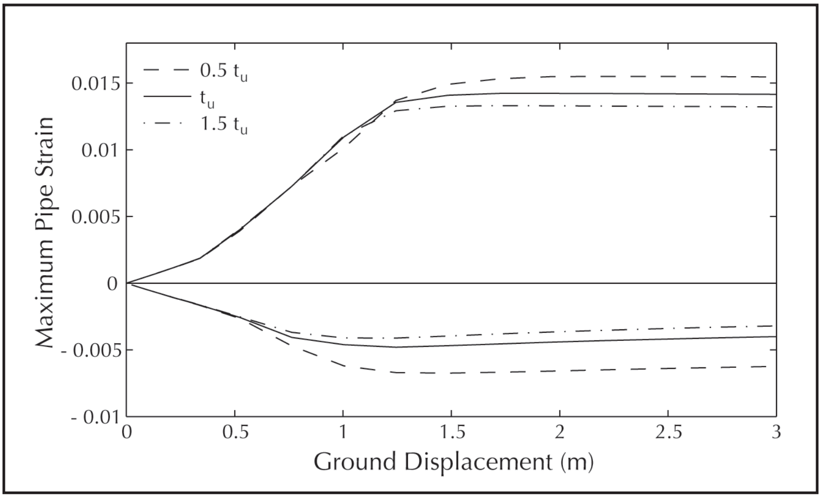

After Liu and M. O'Rourke, 1997b

■ **Figure 7.16 Influence of Peak Longitudinal Soil Resistance, t_u**

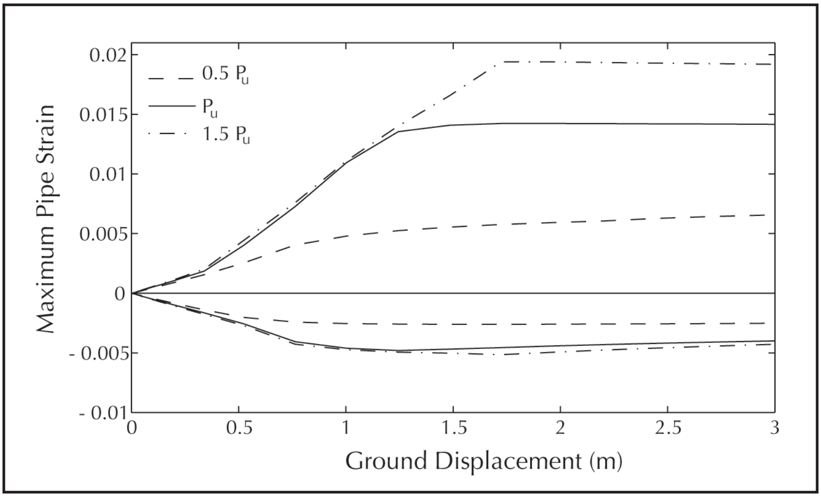

After Liu and O'Rourke, 1997b

■ **Figure 7.17 Influence of Peak Transverse Soil Resistance, p_u**

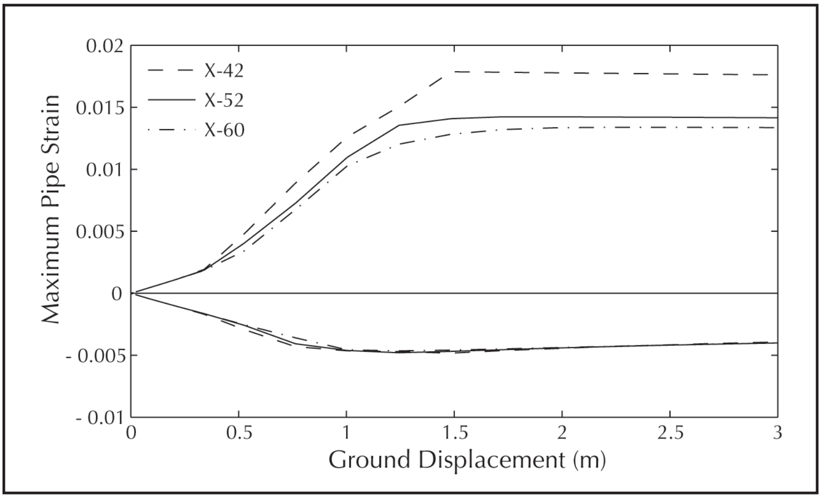

■ **Figure 7.18 Maximum Pipe Strain for Three X-Grade Steel Materials**

The peak tensile strain is an increasing function of the pipe diameter and the transverse (lateral) soil spring resistance. It is a decreasing function of the pipe wall thickness, the steel grade and to a lesser extent the longitudinal (axial) soil spring resistance.

In terms of anchor length L_a, a zero anchor length resulted in substantially larger pipe strain than for L_a = 15 m (49 ft) or 400 m (1,312 ft), as shown in Figure 7.19.

The parameter which most strongly influences the tensile strain is the width of the PGD zone, followed by the transverse soil spring resistance, pipe diameter, steel grade, wall thickness, PGD pattern, anchor length of the pipe and longitudinal soil spring resistance. The critical ground displacement δ_{cr} was found to be an increasing function of width of the PGD zone and the lateral pipe-soil interaction force, but a decreasing function of steel grade, pipe diameter, axial pipe-soil interaction force and pipe wall thickness.

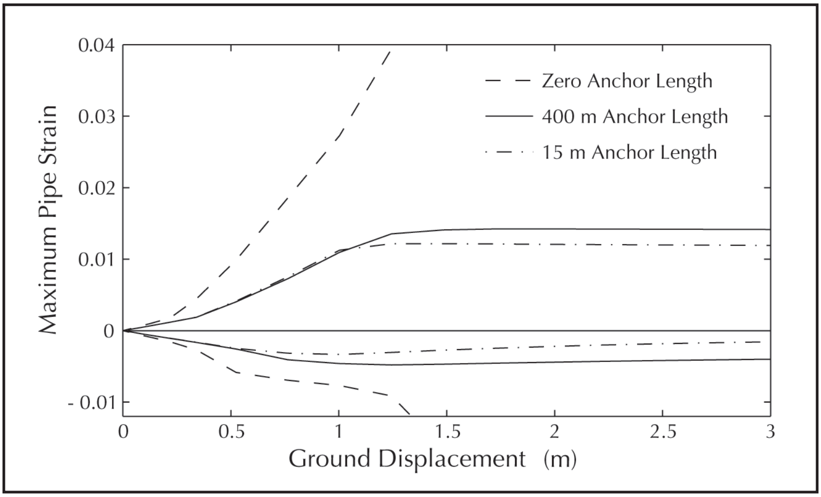

■ **Figure 7.19 Effect of Anchored Length Outside of PGD Zone L_a**

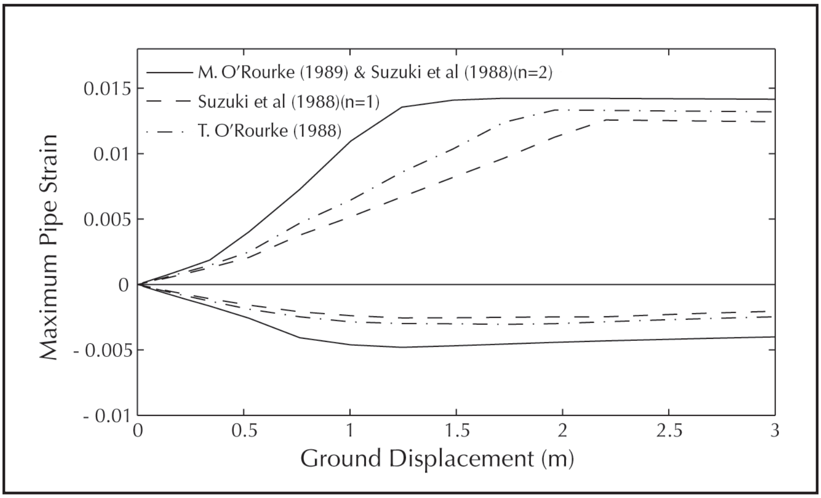

■ **Figure 7.20 Effects of Spatially Distributed PGD Patterns**

Miyajima and Kitaura

Miyajima and Kitaura (1989) model an onshore pipe subject to spatially distributed transverse PGD as a beam on an elastic foundation, as shown in Figure 7.21. The equilibrium equations for the pipe are expressed as follows:

$$EI\,\frac{d^4y_1}{dx^4} + K_1 y_1 = K_1\,\delta\left(1-\sin\frac{\pi x}{W}\right)\quad\left(0<x<\frac{W}{2}\right) \tag{7.4}$$

$$EI\,\frac{d^4y_2}{dx^4} + K_2 y_2 = 0 \tag{7.5}$$

where y_1 and y_2 are the transverse pipe displacement in and outside the PGD zone, K_1 and K_2 are the equivalent lateral soil spring coefficients in and outside the PGD zone, and EI is the flexural rigidity of the pipe cross-section. The equivalent soil springs K_1 and K_2 are based upon recommended practice in Japan (Japan Gas Association, 1982), in which nonlinear characteristics are taken into consideration.

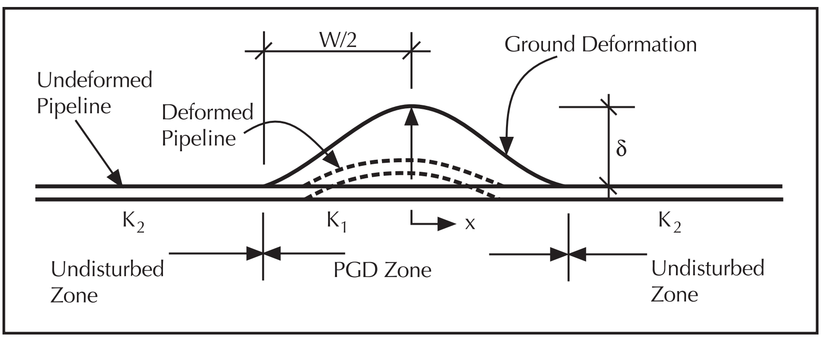

After Miyajima and Kitaura, 1989

■ **Figure 7.21 Analytical Model for Pipeline Subject to Spatially Distributed Transverse PGD**

Miyajima and Kitaura's equations provide a clear mechanical model and are solved by using a modified transfer matrix method. The maximum bending stress for a 16-inch (40-cm) diameter and 1/4-inch (0.6-cm) wall thickness steel pipe in a competent soil layer above the liquefied layer (i.e., $K_1 = K_2$) is shown in Figure

7.22 as a function of the width of the PGD Zone *W* for three values of ground deformation δ.

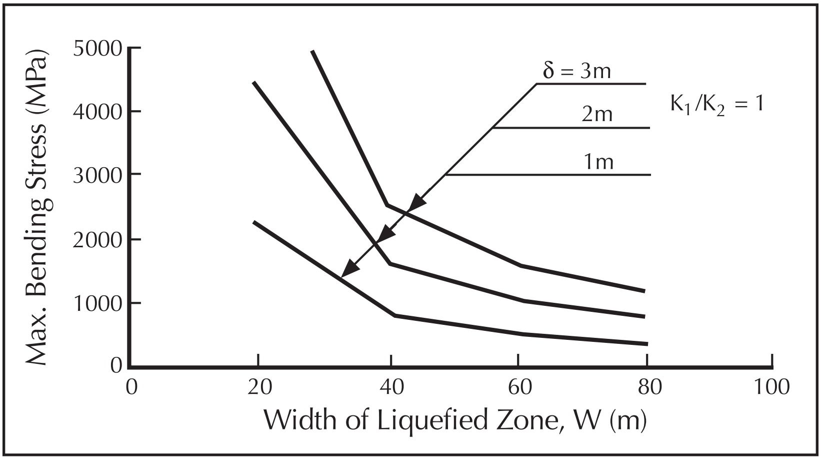

After Miyajima and Kitaura, 1989

■ **Figure 7.22 Maximum Bending Stress vs. Width of PGD Zone for Three Values of Ground Deformation**

As one might expect intuitively, the pipe stress is an increasing function of the ground deformation δ. For a given value of δ, the stress is a decreasing function of *W* for the range of widths considered by Miyajima and Kitaura. Note that they used small deformation flexural theory, which does not account for axial strain due to arc-length effects.

M. O'Rourke

M. O'Rourke (1989) developed a simple analytical model for onshore pipeline response to spatially distributed transverse PGD. He considered two types of response, as shown in Figure 7.23. For a wide width of the PGD zone, the pipeline is relatively flexible and its lateral displacement is assumed to closely match that of the soil. For this case, the pipe strain was assumed to be mainly due to the ground curvature (i.e., displacement controlled). For a narrow width, the pipeline is relatively stiff and the pipe lateral displacement is substantially less than that of the soil. In this case, the pipe strain was assumed to be due to loading at the soil-pipe interface (i.e., load controlled).

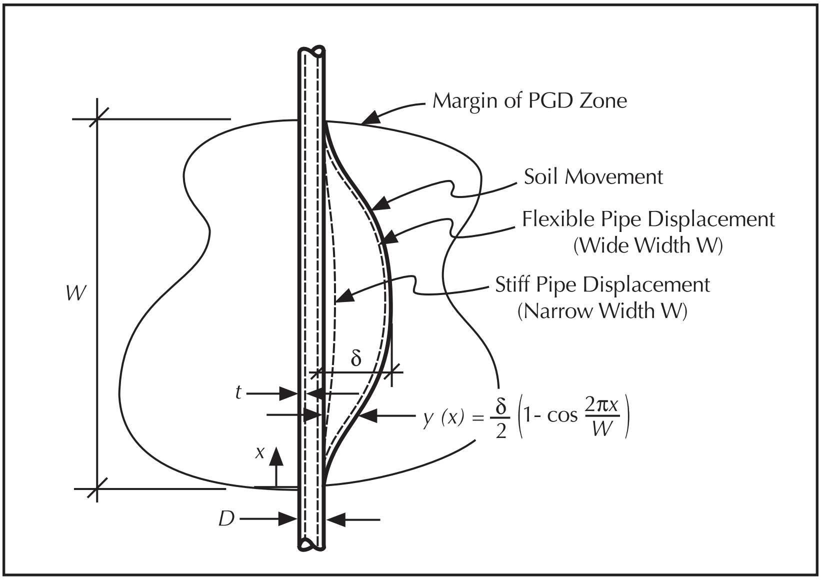

After M. O'Rourke, 1989

■ **Figure 7.23 M. O'Rourke's Analytical Model for Pipeline Subject to Spatially Distributed Transverse PGD**

For the wide PGD width/flexible pipe case, the onshore pipe is assumed to match the soil deformation given by Equation 7.3. The maximum bending strain, ε_b, in the pipe, is given by:

$$\varepsilon_b = \pm\frac{\pi^2 \delta D}{W^2} \tag{7.6}$$

In this simple model, the axial tensile strain is based solely upon the arc-length of the pipe between the PGD zone margins. Assuming the pipe matches exactly the lateral soil displacement, the average axial tensile strain, ε_a, is approximated by:

$$\varepsilon_a = \left(\frac{\pi}{2}\right)^2 \left(\frac{\delta}{W}\right)^2 \tag{7.7}$$

For the narrow width/stiff pipe case, the onshore pipe is modeled as a beam, built-in at each margin (i.e., fixed-fixed beam), subject to the maximum lateral force per unit length p_u at the soil-pipe interface. For this case, the axial tension due to arc-length effects is small and neglected. Hence, the maximum strain in the pipe is given by:

$$\varepsilon_b = \pm \frac{p_u W^2}{3\pi E t D^2} \tag{7.8}$$

Note that M. O'Rourke (1989) assumes that the pipe is fixed at the margins and hence neglects any inward (i.e., axial) movement of pipe at the margin of PGD zone. As a result, Equation 7.7 overestimates the axial strain in the pipe, as will be shown later.

Liu and M. O'Rourke

Based on the Finite Element results described previously, Liu and M. O'Rourke (1997b) found that onshore pipe strain is an increasing function of ground displacement for ground displacement less than a certain value, δ_{cr}, and pipe strain does not change appreciably thereafter. For example, for W = 30 m as shown in Figure 7.8, the maximum tensile strain is an increasing function of maximum soil displacement up to a value of δ = 1.3 m (4.3 ft). For larger values of δ, the maximum tensile strain remains at a relatively constant value of roughly 0.014. Similar behavior is observed for other widths.

In reality, the pipe resistance to transverse PGD is due to a combination of flexural stiffness and axial stiffness. The analytical relations developed below are for an elastic pipe. Although the inelastic pipe case is more complex, the elastic relations provide a basis for interpreting finite element results and, as will be shown later, are directly applicable to transverse PGD case histories from Niigata.

For small widths of the PGD zone, the critical ground deformation and pipe behavior are controlled by bending. The mechanism is the same as that in the M. O'Rourke (1989) model for the stiff pipe case (i.e., two-end fixed beam with constant distributed load). The critical ground deformation is given by:

$$\delta_{cr-bending} = \frac{p_u W^4}{384 E I} \tag{7.9}$$

which is the midspan deflection for a build-in beam of length W, subject to a uniform load p_u.

For very large widths of the PGD zone, the onshore pipe behaves like a flexible cable (i.e., negligible flexural stiffness). For this case, the critical displacement is controlled primarily by the axial force. For a parabolic cable shown in Figure 7.24, the relation between the axial force T at the ends and the maximum lateral deformation (or sag) δ is:

$$T = \frac{p_u W^2}{8\delta} \tag{7.10}$$

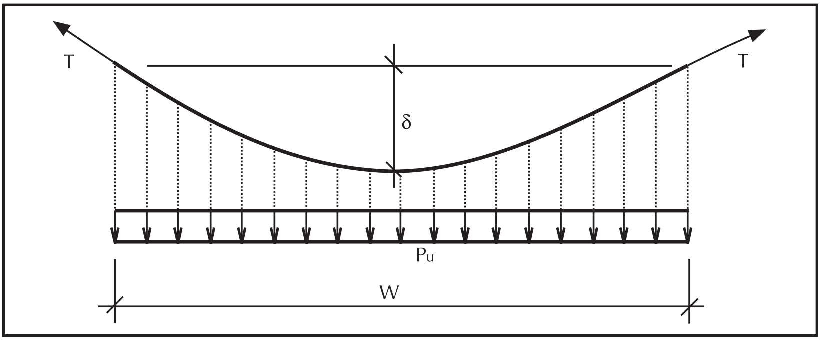

■ **Figure 7.24 Flexible Cable System**

As shown in Figure 7.10, the ground displacement is larger than the pipe displacement in the middle region of the PGD zone. Herein, the width of this middle region is assumed to be $W/2$. The distributed load over the middle region is the resistance per unit length, p_u, at the pipe-soil interface. Taking the "sag" over this middle region to be δ/2, the interrelationship between the tensile force, T, and ground displacement, δ, is given by:

$$T = \pi D t \sigma = \frac{p_u (W/2)^2}{8(\delta/2)} = \frac{p_u W^2}{16\delta} \tag{7.11}$$

where σ is the axial stress in the pipe (assumed to be constant within the PGD zone).

Inward movement of the pipe occurs at the margin of the PGD zone due to this axial force. Assuming a constant longitudinal friction force, t_u, beyond the margins, the pipe inward movement at each margin is:

$$\Delta_{inward} = \frac{\pi D t \sigma^2}{2Et_u} \tag{7.12}$$

The total axial elongation of the pipe within the PGD zone is approximated by the average axial strain given by Equation 7.7 (i.e., arc-length effect) times the width W. This elongation is due to stretching within the zone ($\sigma W/E$) and inward movement at the margins from Equation 7.12. That is,

$$\frac{\pi^2\delta^2}{4W} = \frac{\sigma W}{E} + 2 \cdot \frac{\pi D t \sigma^2}{2Et_u} \tag{7.13}$$

The critical ground deformation, $\delta_{cr\text{-}axial}$ for "cable-like" behavior and the corresponding axial pipe stress, σ, can be calculated by simultaneous solution of Equations 7.11 and 7.13. These values are presented in Table 7.1 for three values of the width W and the standard properties mentioned previously (i.e., D = 0.61 m, t = 0.0095 m, $p_u = 1.0 \times 10^5$ N/m, $t_u = 2.4 \times 10^4$ N/m). Note that the critical ground deformation is controlled by axial force for this case, and that the maximum axial stress at $\delta = \delta_{cr}$ is an increasing function of width of the PGD zone.

Table 7.1 Critical Ground Displacements and Stresses for "Cable-Like" Elastic Pipe

Item	W = 10 m	W = 30 m	W = 50 m
$\delta_{cr\text{-}axial}$ (Equations 7.11 and 7.13)	0.37 m	1.5 m	2.85 m
σ (Equations 7.11 and 7.13)	92.8 MPa	206 MPa	301 MPa

For any arbitrary width of the PGD zone, somewhat between small and very large, resistance is provided by both flexural (beam) and axial (cable) effects. Considering these elements to be acting in parallel,

$$\delta_{cr} = \frac{1}{\dfrac{1}{\delta_{cr-bending}} + \dfrac{1}{\delta_{cr-axial}}} \tag{7.14}$$

Table 7.2 lists the resulting critical displacements of an elastic pipe (D = 0.61 m, t = 0.0095 m, etc.) for W = 10, 30 and 50 m, along with the corresponding elastic finite element results. For W = 30 and 50 m, the critical displacement from Equation 7.14 matches that from the elastic finite element model. However, for W = 10 m, the critical displacement from Equation 7.14 is an order of magnitude less than that from the elastic finite element model. This is due, in part, to the assumption of a constant transverse load p_u on the pipe for bending effects in the simplified approach. The finite element model, on the other hand, uses transverse elasto-plastic soil springs. As noted previously, one obtains the full load p_u from the soil spring only after 0.06 m (2.4 in) of the relative transverse displacement between the pipe and the soil. However, since the fully loaded pipe deflects in bending only 0.015 m (0.6 in) for W = 10 m, the soil spring force is less than the full transverse resistance p_u.

■ **Table 7.2 Critical Ground Displacements for Elastic Pipe**

Item	*W* = 10 m	*W* = 30 m	*W* = 50 m
$\delta_{cr\text{-}bending}$ (Equation 7.9)	0.015 m	1.22 m	9.6 m
$\delta_{cr\text{-}axial}$ (Table 7.1)	0.37 m	1.5 m	2.85 m
δ_{cr} (Equation 7.14)	0.015 m	0.67 m	2.2 m
δ_{cr} (F.E. Approach)	0.16 m	0.70 m	2.1 m

Note that the critical displacements for both the simplified elastic and elastic finite element models in Table 7.2 underestimate δ_{cr} for an inelastic pipe shown, for example, in Figure 7.8. This is due to the fact that, for the inelastic pipe model, the steel modulus decreases after yielding and the pipe must undergo larger deformations such that the strain energy in the pipe equals the work done by the distributed soil springs.

The maximum strains in an elastic pipe are due to the combined effects of axial tension (cable behavior – first term) and flexure (beam behavior – second term), and can be expressed as:

$$\varepsilon_{elastic} = \begin{cases} \dfrac{\pi\delta}{2} \cdot \sqrt{\dfrac{t_u}{AEW}} \pm \dfrac{\pi^2 \delta D}{W^2} & \delta \le \delta_{cr} \\[2ex] \dfrac{\pi\delta_{cr}}{2} \cdot \sqrt{\dfrac{t_u}{AEW}} \pm \dfrac{\pi^2 \delta_{cr} D}{W^2} & \delta > \delta_{cr} \end{cases} \tag{7.15}$$

where A is the pipe cross-sectional area.

7.2.3 Comparison Among Approaches

Table 7.3 presents a summary of the pipe properties and the pipe-soil interaction forces used in the approaches mentioned above.

■ **Table 7.3 List of Parameters in Seven Approaches**

Item	M. O'Rourke (1989)	Miyajima & Kitaura (1989)	T. O'Rourke (1988)	Suzuki et al. (1988)	Kobayashi et al. (1989)	Liu & O'Rourke (1997b)
Method	Analytical	Analytical	F.E.	F.E.	F.E.	Both
Diameter (m)	0.50, 1.01	0.406	0.61	0.61	0.61	0.61
Thickness	0.0127, 0.0063	0.006	0.0095	0.0127	0.0095	0.0095
Material	Mild Steel	Elastic	X-60	X-52	X-42	X-52
t_u(N/m)	-	-	2.4×10^4	1.9×10^4	1.9×10^4	2.4×10^4
p_u(N/m)	8.7×10^4	-	7.7×10^4	1.5×10^5	1.15×10^5	1.0×10^5

Comparing the approaches is difficult since the models have different diameters, wall thickness, pipe-soil interaction parameters, etc. Nevertheless, the bending strains can be compared since the analytical relation for bending strain given in Equation 7.15 (second term on the right hand side in both equations) suggest that it is only a function of δ, D and W.

Figure 7.25 shows the pipe bending strain for $W > 20$ m, back calculated from the different approaches, plotted as a function of $\delta D/W$. Herein, the bending strain is calculated as one half of the sum of the tensile and compressive pipe strains. Note that the Kobayashi et al. (1989) approach is not included since they did not present compressive strain. In this figure, the straight line with a slope of π^2 is the analytical relation given in Equation 7.6. Note that the Suzuki et al. (1988), as well as the Liu and M. O'Rourke (1997b) results, both match the analytical relation fairly well. The T. O'Rourke (1988) flexural strain are somewhat less (roughly two thirds) than the analytical results, while the Miyajima and Kitaura (1989) results are somewhat (roughly 60%) higher.

Another type of comparison involves the general trends in results from the various approaches. For example, the Liu and M. O'Rourke (1997b) results suggest that axial effects are important in that the tensile strains are larger than the compressive strains. This agrees with the numerical results by T. O'Rourke (1988). In addition, for the three widths considered the tensile strains are largest for $W = 30$ m, which agrees with the numerical results by Suzuki et al. (1988). However, the Liu and M. O'Rourke (1997b) numerical results described above differ from those by T. O'Rourke (1988), specifically for the width of the PGD zone $W = 10$ m. Similarly, the Liu and M. O'Rourke (1997b) numerical results differ from those by Suzuki et al. (1988) in that the tensile pipe strains are significantly larger than the compressive strains. It is believed that this difference is due to the comparatively heavy wall thickness used in the Suzuki et al. (1988) model (note, as shown in Figure 7.15, that a heavier wall thickness reduces the peak tensile strain but essentially has no effect on the peak compressive strain) in combination with a relatively weak longitudinal soil spring.

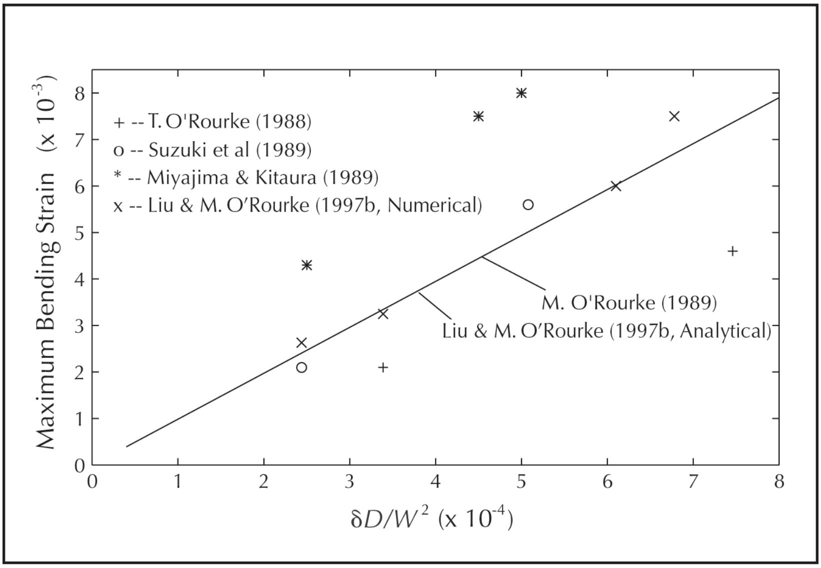

■ **Figure 7.25 Comparison of Pipe Bending Strain**

7.2.4 Expected Response

Although the approximate method (Liu and M. O'Rourke, 1997b) described above is strictly applicable to elastic pipe and widths of 30 m or greater, they prove useful for many realistic design situations. Suzuki and Masuda (1991) present values for the width W and the amount of movement δ, for transverse onshore PGD observed in the Niigata Japan after the 1964 event. Based on roughly 40 separate sites, the amount of ground movement δ ranged from about 0.3 m to 2.0 m, while the width of the PGD zone W ranged from about 100 m to 600 m.

For $W \geq 100$ m (328 ft), steel pipe with $D = 0.61$ m (24 in), $t = 0.0095$ m (3/8 in), the critical ground deformation from Equation 7.14 is 6.0 m (20 ft) or more, which is much larger than the maximum observed ground displacement of 2.0 m (6.6 ft). Also, the estimated peak tensile (i.e., combined axial and flexural) strain for $\delta = 2$ m from Equation 7.15 is less than the yield strain for X-grade steel but slightly above the yield strain for GR-B grade steel. Hence, an X-grade pipe behaves elastically and the strain can be estimated by Equation 7.15.

The maximum pipe strains are shown in Figure 7.26 as a function of the ground deformation using both the simplified analytical and numerical models by Liu and M. O'Rourke (1997b). The finite element results for both X-grade and GR-B grade steels are identical for δ less than about 1.6 m. At that location there is a kink in the GR-B curve, indicating the onset of inelastic behavior in that material. Note that the analytical model (i.e., Equation 7.15) results compare favorably with the finite element values.

The approximate analytical approach does overestimate to some degree the peak tensile strain and underestimates the peak compressive strain. This suggests that the estimated axial strains are somewhat too large. However, the differences are relatively small, particularly in light of the accuracy of geotechnical predictions for expected values of the spatial extent and ground movement of PGD zones.

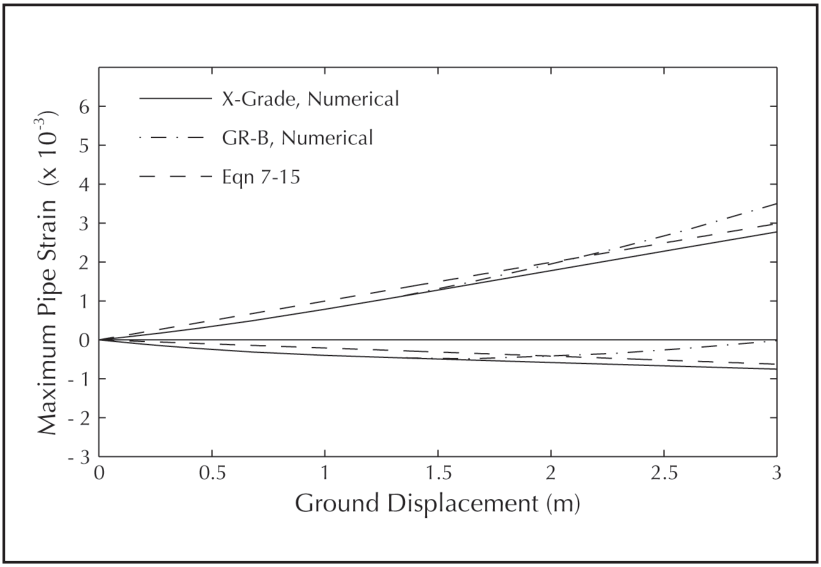

After Liu and M. O'Rourke, 1997b

■ **Figure 7.26 Maximum Pipe Strain vs. Ground Displacement for *W* = 100 m**

7.2.5 Comparison with Onshore Case Histories

The performance of buried pipelines subject to the transverse onshore PGD during the 1971 San Fernando earthquake provides case histories to test the approaches described above. In the case history shown in Figure 2.17, a water transmission pipeline (Pipeline 2), made of Grade-C steel with 1,370 mm (54 in) diameter and 7.9 mm (5/16 inch) wall thickness, was subjected to spatially distributed transverse PGD with the maximum ground displacement δ of 0.7 m (2.0 ft) and a width W of about 400 m (1,312 ft). From Equation 7.6, the bending strain in the pipe with W = 400 m and δ = 0.7 m (2.3 ft) would be 6.0×10^{-5}, while the axial tension strain would be 7.6×10^{-6} and the critical displacement δ_{cr} is over 10 m (33 ft). Hence, the maximum tension strain is 6.8×10^{-5} while the net compression strain is 5.2×10^{-5}. Since these values are below the tensile rupture and local buckling strain respectively for the pipe, one expects the pipe would not be damaged by this transverse PGD. The expected behavior matches the observed behavior in that there was no failure within the PGD zone. Note, however, that one break was observed at a location close to but outside the PGD zone, where the pipeline was connected to a ball valve by a mechanical joint at a reinforced concrete vault. According to T. O'Rourke and Tawfik (1983), the mechanical joint was severely deformed and showed signs of repeated impacts. This evidence of repeated impacts suggests that the damage may have been due to wave propagation as opposed to PGD effects.

In summary, although there has been a fair amount of research activity directed at the problem of buried onshore pipe subject to distributed transverse PGD, case histories of continuous pipeline failure due solely to distributed transverse PGD without abrupt offsets at the margins are rare. In contrast, pipeline damage due to longitudinal PGD is fairly common. This is due, in part, to the fact that pipe is relatively easy to bend (flexurally compliant) while difficult to stretch or compress axially. Also, a typical δ/W ratio for transverse PGD may be roughly 1/300, based on the Suzuki and Masuda data. In terms of beam design, this deflection over span ratio is easy to accommodate.

7.3

Onshore Pipelines in Liquefied Soil

As mentioned previously, the top of the liquefied soil layer is commonly located below the bottom of onshore pipes. However, when the pipe is buried in saturated sand, such as at a river bed, the soil surrounding the pipe may liquefy during strong seismic shaking. In this case, the pipe may deform laterally following the flow of liquefied soil down a gentle slope, or move upward due to buoyancy, especially when a manhole is present or a compressive load acts on the pipe. For example, according to Suzuki et al. (1988) and Takada (1991), a sewage pipe with manhole and a gas pipe (150 mm in diameter) were uplifted out of the ground due to buoyancy in combination with a compressive load caused by longitudinal permanent ground deformation during the 1964 Niigata earthquake. A compressive load can also be induced by temperature change and/or internal operating pressure in a pipe restrained against longitudinal expansion.

7.3.1 Horizontal Movement

When an onshore pipeline is surrounded by liquefied soil, the pipe may move laterally due to the flow of liquefied soil downslope. Using the same model as shown in Figure 7.3, Suzuki et al. (1988) studied the response of a buried pipe surrounded by liquefied soil, subject to spatially distributed transverse PGD. The presence of the liquefied soil was modeled by assuming that the lateral soil coefficient (K_1) for a pipe surrounded by liquefied soil is some fraction of the corresponding value (K_2) for competent, non-liquefied soil. Figure 7.27 shows the peak pipe strain as a function of the amount of PGD, δ, for three values of the reduction factor. For this plot, the width of the PGD zone is 30 m, while the pipe properties are the same as those listed in Table 7.3 for the Suzuki et al. approach.

As one might expect, the peak pipe strain for competent non-liquefied soil (i.e., $K_1/K_2 = 1$, also see Figure 7.6 for $W = 30$ m) is in all cases larger than that for liquefied soil. As a rough approximation, the pipe strain for $\delta \geq 1.5$ m (5 ft) is proportional to the soil coefficient reduction factor.

As noted in Section 5.3, the equivalent soil spring coefficient for liquefied soil, according to Takada et al. (1987), ranges from 1/1,000 to 1/3,000 of that for non-liquefied soil, while other scholars suggest that the ratio is from 1/100 to 5/100. Hence, for the same amount of PGD and width of the PGD zone, an onshore pipe surrounded by liquefied soil is much less likely to be damaged by spatially disturbed transverse PGD. Hence, for design purpose it seems reasonable to conservatively assume that onshore pipe subject to spatially distributed transverse PGD is located in a competent non-liquefied soil (cap layer), which overlays the liquefied layer.

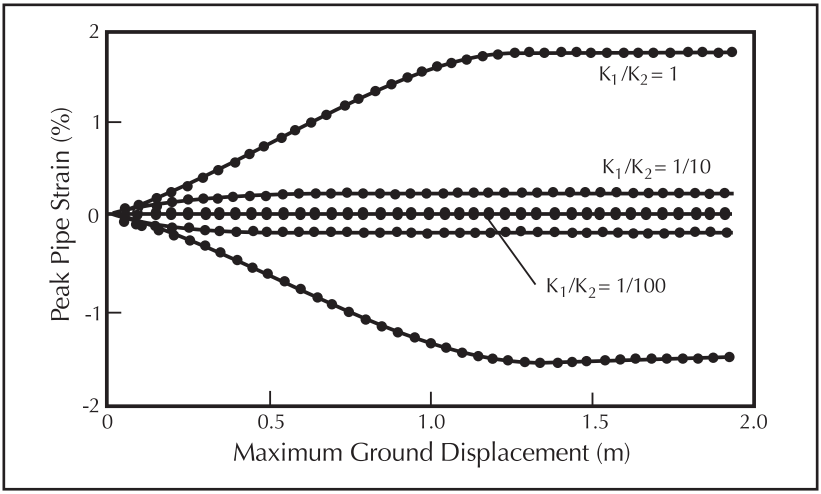

After Suzuki et al., 1988

■ **Figure 7.27 Maximum Strain vs. δ for Three Soil Spring Constants**

7.3.2 Vertical Movement

If the soil immediately surrounding an onshore buried pipe liquefies, the pipe may uplift due to the buoyancy. A few studies have been done regarding this uplifting response. Takada et al. (1987) conducted a series of laboratory tests and estimated the liquefied soil spring constant by combining the test values with analytical solutions. Yeh and Wang (1985) analyzed the dynamic (i.e., seismic shaking and buoyancy effects) pipe response by using a simplified beam-column model for the pipe. They concluded that the dynamic displacement is relatively small (less than 20% of static pipe displacement due to the buoyancy) when the surrounding soil is liquefied.

Using 2 cm (0.8 in) diameter polyethylene pipeline, Cai et al. (1992) carried out a series of laboratory tests and observed pipe response due to soil liquefaction. Figure 7.28 shows the two system models. The model in Figure 7.28(a) is a pipeline without a manhole, while (b) is for a pipeline with a manhole. In both models, the end of the pipe can be fixed, elastically constrained, or free. The model pipe is 1.2 m (4 ft) in length, which would correspond to a prototype length of 50 m (164 ft) for a prototype diameter of 83 cm (32 in). In these tests, only the shaking and uplifting response can be observed since the simulated ground surface before and after liquefaction is normally flat. That is, lateral response of the pipe is not modeled. For an elastically restrained case, they found that the dynamic strain due to shaking is less than 10% of the static strain due to uplifting and, hence, can be neglected when estimating the maximum uplifting strain in the pipe. When a manhole and/or an axial compressive force are introduced, the upward response is larger. For elastically constrained ends, the pipe keeps uplifting till a portion of pipe near the center of PGD zone is at the ground surface. However, when a non-liquefied soil layer (60 mm in thickness) is used as cover, the pipe came to rest at the interface of the non-liquefied and liquefied layers.

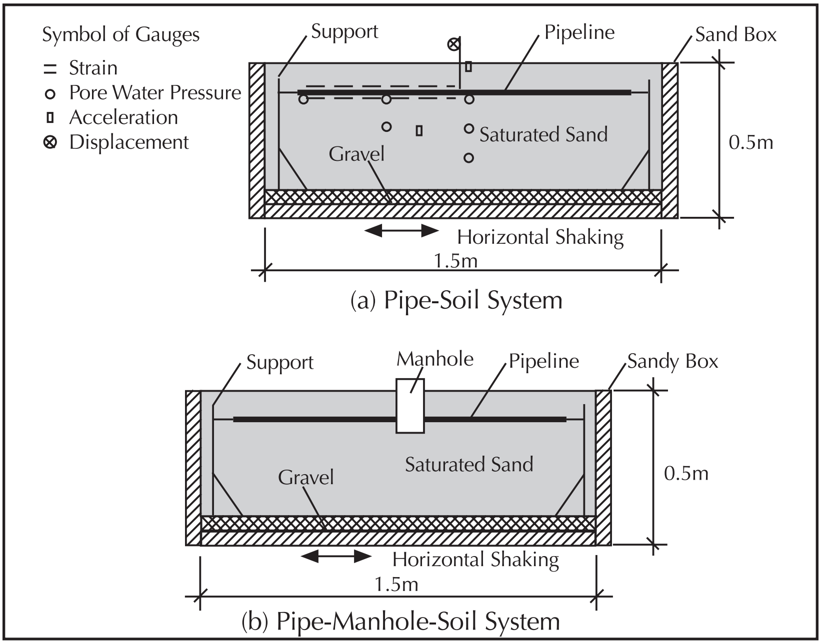

After Cai et al., 1992

■ **Figure 7.28 Model System of Buried Pipeline in Liquefied Soil**

Hou et al. (1990) analyzed onshore pipe strain due to buoyancy effects by a finite element approach. In the analysis, the nonlinearity of both steel material and interaction force at the pipe-soil interface outside the liquefied zone are considered. The uplifting force per unit length, P_{uplift}, acting on the pipe within the liquefied zone, can be expressed as:

$$P_{uplift} = \frac{\pi D^2}{4} (\gamma_{soil} - \gamma_{contents}) - \pi D t \gamma_{pipe} \tag{7.16}$$

where γ_{soil}, γ_{pipe}, and $\gamma_{contents}$ are the weights per unit volume of liquefied soil, pipe and pipe contents (i.e., water, gas, etc.), respectively. Note that the uplifting force will decrease when a portion of the pipe is at the ground surface.

The pipe is constrained beyond the margins of the liquefied zone by restraint due to the non-liquefied soil. That is, the behavior is similar to a beam, built in at each margin, subject to a uniform upward load.

The maximum strain in a steel pipe is shown in Figure 7.29 as a function of the length of the liquefied zone for $\gamma_{soil} = 2.0 \times 10^4$ N/m^3, (120 pcf), $\gamma_{contents} = 0.8 \times 10^4$ N/m^3 (48 pcf), $t = 0.0079$ m (0.31 in) and three separate pipe diameters. Note that the initial stress ($\sigma_{initial} = 180$ MPa) in compression is due to restrained thermal expansion. As shown in Figure 7.29, the maximum pipe strain occurs at a certain width of the liquefied zone, W_{cr}. For the width less than W_{cr}, the pipe strain is an increasing function of the width, while the pipe strain decreases with the increasing width thereafter. Their results also indicate that the pipe uplifting displacement and pipe strain are an increasing function of the initial compressive stress.

In fact, the buoyancy per unit length given in Equation 7.16 is less than 10% of the lateral pipe-soil interaction for a pipe surrounded by non-liquefied soil. That is, the curve $K_1/K_2 = 1/10$ in Figure 7.27 can be considered as an upper bound. A comparison of Figures 7.27 and 7.29 indicates that the Suzuki et al.'s results match Hou et al. (1990) reasonably well. That is, for $W \geq 30$ m and $D = 0.61$ m (24 in) in Figure 7.27, the peak pipe strain is about 0.2%, while for $D = 0.53$ m (21 in) in Figure 7.29, the peak pipe strain is 0.19%. Since the maximum strain is less than both critical strain of tensile failure and local buckling, the pipe is unlikely to be damaged due to the buoyancy, although it may uplift out of the ground when the width of the liquefied zone is large.

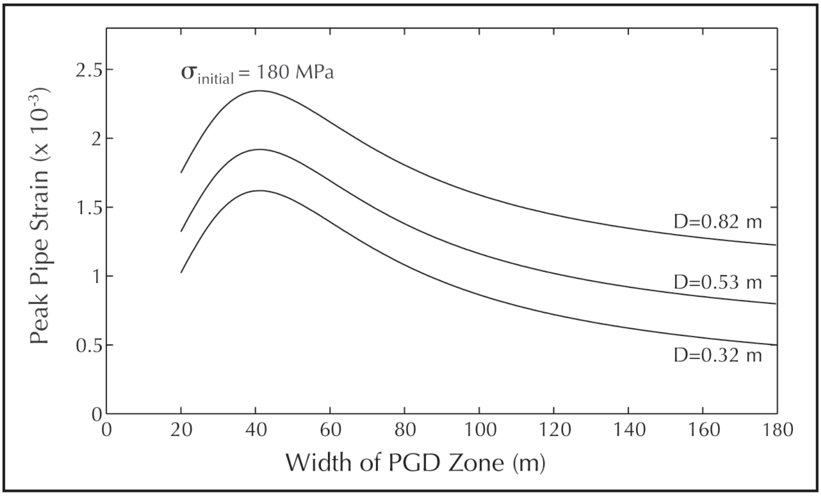

After Hou et al. 1990

■ **Figure 7.29 Maximum Strain vs. Width of Liquefied Zone**

Typically, liquid pipelines have small uplift potential due to the high unit weight of the contents. Uplifting behavior has been observed only for large diameter water pipelines (e.g., over 1 m diameter) and oil pipelines with initial compressive loads. The initial compressive forces in an oil pipeline are due to restrained thermal expansion, and increase the uplift potential. As oil temperature increases, the pipeline may even experience upward buckling and pop up out of the ground. In this case, the buoyancy serves as the initial imperfection and the upheaval buckling is mainly caused by the thermal compressive loads.

Gas pipelines have high uplift potential due to the small unit weight of the contents when its surrounding soil is liquefied. Pipeline performance during past earthquakes also indicates that steel pipelines are unlikely to be damaged by the buoyancy, but may become exposed. For situations where a large uplifting displacement or pipe exposure is not desirable (for example, for submarine pipelines), the following equation derived from the principle of conservation of energy can be used to determine the maximum uplift displacement and/or the spacing for piles or other pipe restraints:

$$A\delta_{max}^{\ 3} + 16 \cdot I\delta_{max} - \frac{16 P_{uplift} W_s^4}{E\pi^5} = 0 \qquad (7.17)$$

where A is the cross-section area, and W_s is the spacing of the piles as, shown in Figure 7.30.

The peak pipe strain is then given by:

$$\varepsilon_{max} = \pm \frac{\pi^2 \delta_{max} D}{W_s^2} + \frac{\pi^2 \delta_{max}^2}{4 W_s^2} \tag{7.18}$$

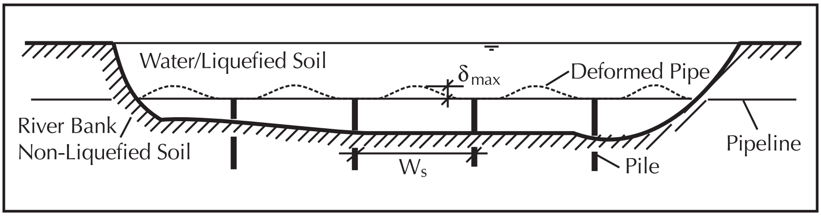

Figure 7.30 Profile of Pipeline Crossing Liquefied Zone

For a 0.61 m (24 in) OD gas pipeline with a wall thickness of 9.5 mm, the buoyancy force per unit length in liquefied soil is around 4.4 kN/m. The maximum pipe uplift displacement and peak pipe strains are calculated using Equations 7.17 and 7.18, and listed in Table 7.4 for three sets of pile spacing.

For the 0.61 m OD pipeline with 1 m burial depth in liquefiable sand, results in Table 7.4 suggest that the spacing of piles needs to be less than 70 m in order to avoid exposure of the pipeline. Again, the pipe strains are less than 0.2% and hence no pipe structural failure is expected. Note that initial stresses are not considered in Equations. 7.17 and 7.18. Initial compressive loads tend to increase the uplift displacement, while initial tensile loads tend to reduce the uplift movement.

Table 7.4 Pipe Displacement and Strain vs. Spacing for Piles

Spacing (m)	Uplift (m)	Bending Strain (%)	AxialStrain (%)	Total Strain (%)
53.0	0.50	0.107	0.022	0.129
72.8	1.00	0.114	0.047	0.160
92.3	1.50	0.106	0.065	0.171

7.4 Onshore Pipe Subject to Abrupt PGD

Two patterns of transverse PGD are shown in Figure 7.1. The spatially distributed pattern in Figure 7.1(a) has been discussed extensively above. In relation to the localized abrupt pattern shown in Figure 7.1(b), it was noted that this corresponds more or less to a pair of fault offsets, provided that the PGD zone is sufficiently wide. Hence, a key question involves determining the minimum width of the PGD zone, above which the fault crossing models discussed in more detail in Chapter 8 are applicable. Recall that data gathered by Suzuki and Masuda (1991) and shown in Figure 2.13 suggest that PGD zone widths are typically larger than 80 m. A lower bound width of 50 m is considered herein. Figure 7.31 shows the bending moment and axial force in a continuous buried pipeline subjected to a localized abrupt pattern of transverse PGD. The amount of ground movement $\delta = 1.0$ m (3.3 ft) while the width of the PGD zone, W, is 50 m. The pipe and soil properties are $D = 0.61$ m (24 in), $t = 0.0095$ m (3/8 in), $\gamma_{soil} = 1.8 \times 10^4$ N/m^3, $\phi = 35°$.

Note that the bending moment is essentially zero over a distance of roughly 20 m (66 ft) near the center of the PGD zone. Hence, in terms of flexure, the continuous pipe behaves as if it was subject to two separate fault offsets both having a pipe-fault angle of 90° with no interaction between them. The pipe axial force near the center depends on the width of the PGD zone. It would be zero if the width is large enough such that all the axial force resistance is provided by the friction at the pipe-soil interface within the PGD zone. In that case, the pipe behavior (both tension and flexure) due to a localized abrupt pattern of transverse PGD is the same as that for a pipe crossing a fault with intersection angle of 90°. That is, the procedures described in Chapter 8 could be used directly in that case.

If the axial force near the center of the zone is non-zero (as shown in Figure 7.31(b)), the peak axial force at the margins would be larger than that for two separate fault offsets. That is, by symmetry the center of the zone acts as an effective anchor point and, as will be noted in Chapter 8, an anchor near a fault increases the stress in a pipe subject to movement at the fault.

In summary, there are significant differences in pipe behavior between spatially distributed and localized abrupt transverse PGD. Unfortunately, for designers, the authors are not aware of procedures for discriminating, apriori, between these two patterns.

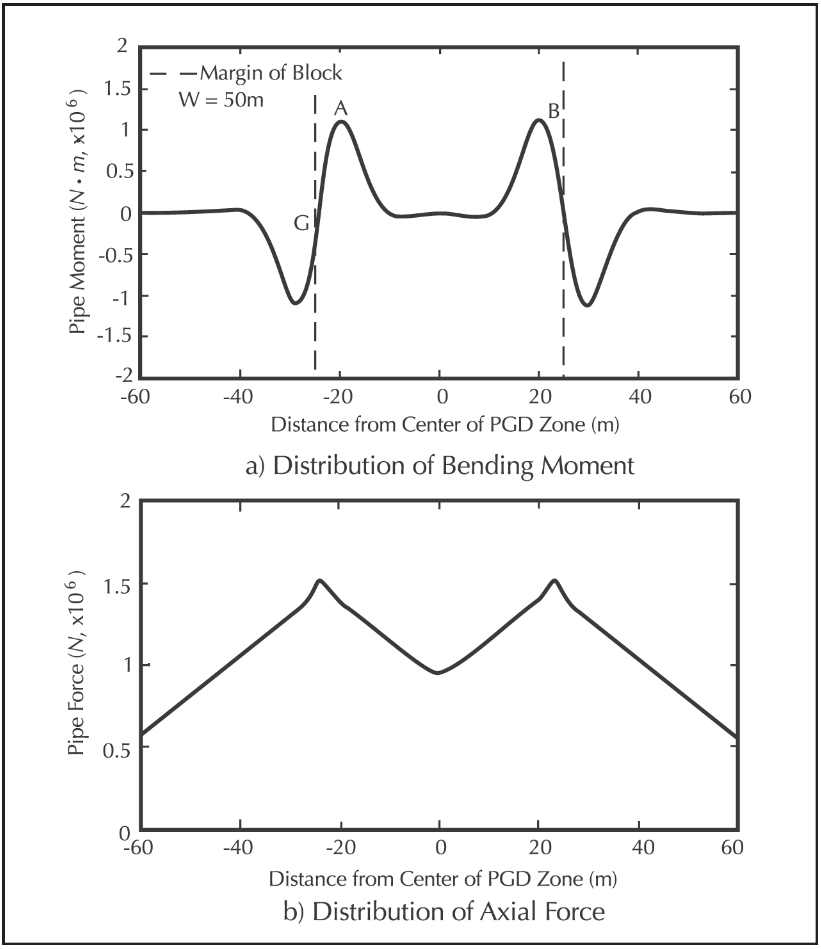

■ **Figure 7.31 Distribution of Pipe Bending Moment and Axial Force**

7.5

Offshore Pipelines

As noted above, the larger widths and low soil strength associated with offshore landslides result in pipe behavior that is more like that for a chain or cable (axial tension only) than for a beam (axial tension and bending).

Parker et al. (2008) develop relations for offshore pipe subject to transverse PGD. Figure 7.32(a) is a sketch of the general behavior. It envisions a landslide of width $2W_1$ (distance from Point C to Point E in Figure 7.32). Within this width the pipeline is subject to a lateral force per unit length P_{u1}. This lateral load is equilibrated by soil resistance forces P_{u2} over a distance W_2 on each side of the landslide zone (i.e., from Point B to Point C to the left, and from Point E to Point F on the right, in Figure 7.32). Hence, from horizontal equilibrium in the direction of pipe movement:

$$P_{u1}W_1 = P_{u2}W_2 \tag{7.19}$$

The axial tension in the line is assumed to be a constant value T_0 within the offshore landslide zone. Beyond the margins the pipe axial tension decreases linearly at Points C and E to zero at Points A and G, as shown in Figure 7.32(b).

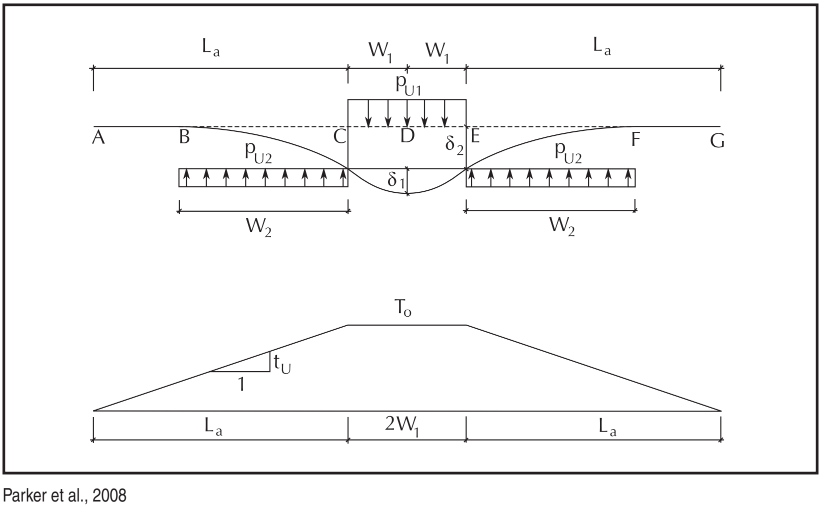

Parker et al., 2008

■ **Figure 7.32 Model for Offshore Pipe Subject to Transverse PGD**

The downslope movement of the pipe at the center of the landslide zone is composed of two parts: the downslope movement δ_1 between the center and the margins of the zone, and the downslope movement δ_2 of the pipeline at the margin.

With the aid of a few simplifying assumptions, the downslope movement can be determined from equilibrium. Figure 7.33 shows the portion of the pipeline/cable between the Points D and E, subject to transverse soil load P_{u1}. As noted above, the pipe tension within the landslide zone is assumed constant. That is, soil friction forces along the pipe between Points D and E are neglected. Taking moments about Point E results in:

$$\delta_1 = \frac{P_{u1} W_1^2}{2T_0} \tag{7.20}$$

The same relation is used for the convex portion of the pipe beyond the margin:

$$\delta_2 = \frac{P_{u2} W_2^2}{2T_0} \tag{7.21}$$

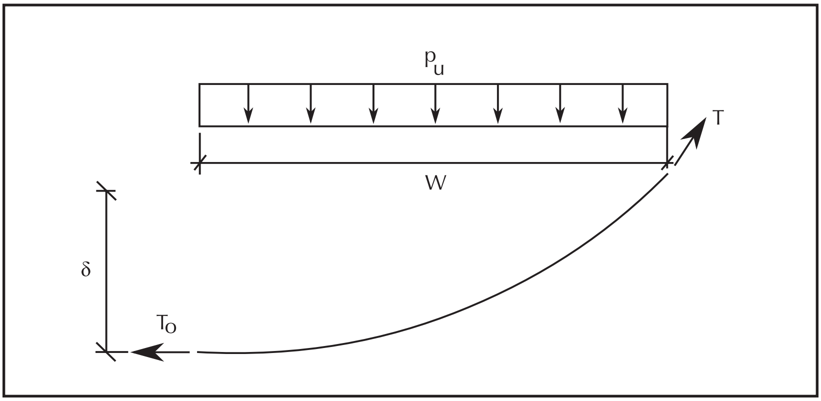

■ **Figure 7.33 Free Body Diagram of Pipe-Midspan to Margin of PGD Zone**

Note Equation 7.21 assumes that the pipe tension is constant between Points E and F, which is nominally correct if the distance W_2 is small in comparison with L_a.

Assuming a parabolic shape for the pipeline/cable in Figure 7.33, the **change** in length due to arc-length effects from Point D to E is:

$$\Delta L_1 = \frac{2\delta_1^2}{3W_1} \tag{7.22}$$

While from Point E to F:

$$\Delta L_2 = \frac{2\delta_2{}^2}{3W_2} \tag{7.23}$$

It can be shown that the total change in length due to pipe/cable deformation (Point B to Point F) is:

$$\Delta L = \frac{4\delta_1{}^2}{3W_1} + \frac{4\delta_2{}^2}{3W_2} = \frac{4\delta_1{}^2}{3W_1} \; (1+P_{u1}/P_{u2}) \tag{7.24}$$

Further algebraic manipulation using Equation 7.20 results in:

$$\Delta L = \frac{1}{3} P_{u1}{}^2 W_1^3 \left(1 + P_{u1} / P_{u2}\right) / T_0^2 \tag{7.25}$$

However, the total change in length of the pipe/cable can also be determined by integrating the axial strain over the total affected length of the pipe. Using the Ramberg-Osgood stress-strain relation in Equation 4.1, the change in length is:

$$\Delta L = \frac{2W_1T_0}{AE}(1+\chi) + \frac{T_0{}^2}{AEt_u}\left(1 + \frac{2}{2+r}\cdot\chi\right) \tag{7.26}$$

In Equation 7.26, the first term is the change in length over the width of the PGD zone where the axial strain is assumed constant (from Point C to Point E), the second term is the change in length over the two regions beyond the margin of the PGD zone where the axial tension is assumed to vary in a linear fashion and:

$$\chi = \frac{n}{1+r}\left(\frac{T_0}{A\sigma_y}\right)^r \tag{7.27}$$

One obtains the Parker et al. (2008) relations for elastic pipe by taking χ to be zero.

For a given pipe, soil and width of the PGD zone, the peak axial tension T_0 can be calculated by simultaneous solution of Equations 7.25 and 7.26.

Similar to Equation 6.3, the axial pipe strain is calculated as:

$$\varepsilon_a = \frac{T_0}{AE}\left[1+\frac{n}{1+r}\left(\frac{T_0}{A\sigma_y}\right)^r\right] \tag{7.28}$$

The bending strain in the pipe may be estimated as:

$$\varepsilon_b = \frac{D}{2}\frac{P_{u1}}{T_0} \tag{7.29}$$

which will be developed in more detail in relation to Equations 8.5 and 8.6. The total pipe strain in the pipe is the summation of the axial strain and bending strain.

Note that the Parker et al. (2008) model has much in common with Liu and O'Rourke model discussed in Section 7.2.2 above. The main difference is that Parker et al. consider the downslope pipe movement at the margin of the PGD zone, while Liu and O'Rourke take δ_2 to be zero.

An example problem in Chapter 14 will illustrate the use of the Parker model as modified herein for inelastic response.

8

Response of Buried Continuous Pipelines to Faulting

Chapters 6 and 7 present the response of continuous pipelines subject to longitudinal and transverse PGD, respectively. As mentioned previously, arbitrary PGD can be decomposed into two components, one parallel to the pipe axis (i.e., longitudinal PGD) and the other perpendicular to the pipe axis (i.e., transverse PGD). This chapter presents the response of continuous pipelines subject to fault offsets, which in the general case involves both longitudinal and transverse response.

Two cases are discussed herein. In the first case (nominal tension), pipes are distressed due to bending (caused by transverse component) and axial **tensile** force (caused by longitudinal component). A normal fault is an example of this case. The pipe failure mechanism, particularly for thick wall pipe where the tensile and compression failure strains are closer in value, would likely be tensile rupture since the largest pipe strains are tensile in this case. In the second case (nominal compression), pipes are distressed due to bending and axial **compressive** force. A reverse fault is an example of this second case. The pipe failure mechanism would be buckling of some sort since the largest pipe strains are compressive and, as noted in Chapter 4 for steel pipe, failure strains for compression are never larger than those for tension, regardless of the pipe *D/t* ratio. A strike slip fault could place a pipe in either nominal tension or nominal compression depending upon the intersection angle between the fault trace and pipe axis and the relative movement at the fault. For example, the right lateral movement of the fault in Figure 8.1 (other side appears to be moving to the right) results in the pipe on either side moving towards each other and, hence, the nominal compression case. On the other hand, a left lateral fault offset would result in the nominal tension case.

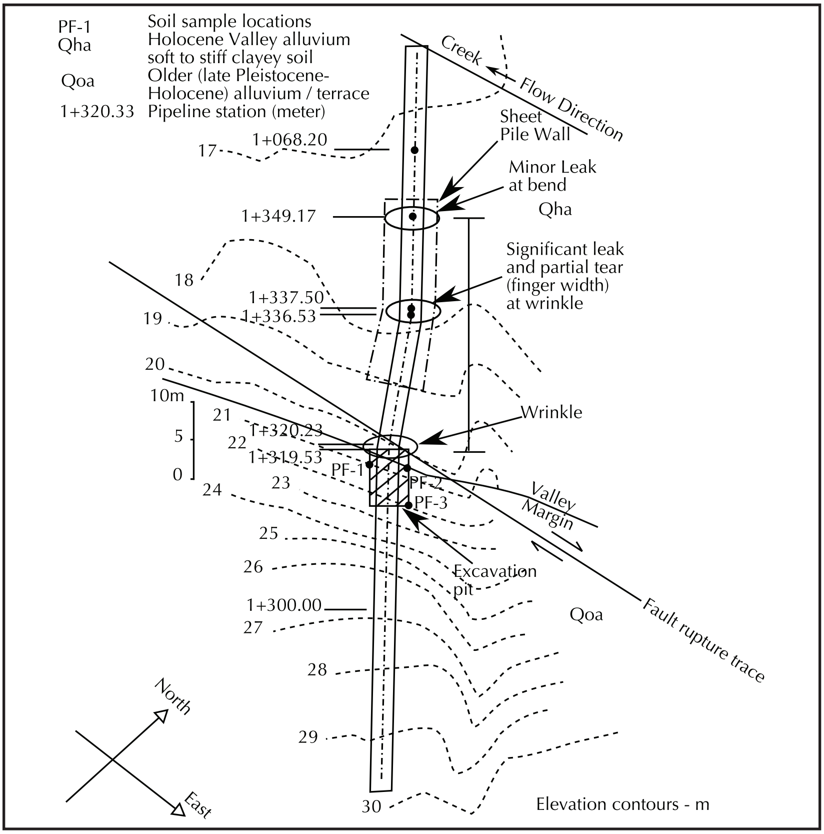

After Eidinger et al., 2002

■ **Figure 8.1 Thames Water Pipeline after Right Lateral Fault Offset**

8.1

Pipe Damage Observations

Surface faulting has accounted for many pipe breaks during past earthquakes. For example, much of the surface faulting during the 1971 San Fernando earthquake occurred in urban and suburban communities. Although only a half of one percent of the area was influenced by the surface faulting, the fault movements resulted in over 1,400 breaks in water, natural gas and sewer pipelines (McCaffrey and T. O'Rourke, 1983). Among the three fault zones (the Mission Wells Segment, the Sylmar Segment and the Harding School Segment), the 3 km long (1.9 mi) Sylmar Segment had the largest ground displacement, which was composed of 1.9 m (6.2 ft) of left-lateral slip, 1.4 m (4.6 ft) of vertical offset and 0.6 m (2.0 ft) of thrust. Most of the left-lateral slip and thrust were concentrated along the southern, 25 to 80-m-wide (82 to 262 ft) section of the fault zone, where the failure mode of local buckling of the pipe wall was dominant. On the other hand, vertical offsets and extension fractures are predominant in the northern section, where most of the breaks were due to tensile rupture.

Arguably the best documented case study of buried pipe response to fault offsets is the Thames Water Pipeline during the 1999 Izmit (Turkey) event. As described in more detail in Eidinger et al. (2002), the pipe material was API Grade B Steel, with a diameter of 2.2 m and wall thickness of 1.8 cm (D/t = 122). The pipeline crosses the Spanaca Segment of the North Antolian Fault at an angle $\beta = 125^o$. The 3 m of right lateral offset results in 2.45 m of lateral offset and 1.72 m of longitudinal compressive shortening after the earthquake. The pipe experiences three areas of damage: 1) a major wrinkle about 1 m southeast of the fault trace, 2) another major wrinkle about 17 m northwest of the fault, and 3) a third minor bend at 29 m northwest of the fault. As shown by the contour lines in Figure 8.1, the fault is nominally along the margin of a valley, with the flat area to the northwest and a ridge to the southeast. The pipeline underwent asymmetric behavior with significant differences in the distance from the fault trace to the major wrinkles. This behavior is due to differences in the stiffness of the local soil, with softer Holocene alluvium (Qha) in the valley and stiffener Pleistocene terrace (Qoa) in the ridge.

Figure 8.2 shows a view of a major wrinkle from inside the pipe. Note that the pipe distortion seems to accumulate at the wrinkle locations, with little or no observed distress away from the wrinkles. The wrinkles were severe enough to result in tearing of the pipe wall, however, the leakage was estimated to be only about 1% (about 1,000 gpm) of its original flow capacity. Somewhat more significant in terms of the pipeline operation was a wrinkle-induced reduction in effective diameter, down to roughly 1.4 m from the 2.2 m original diameter.

A finite element analysis indicated a peak compressive pipe strain of 9.6% and a peak tensile pipe strain of 3.0%. Both these peak pipe strains were located on opposite sides of the wrinkles, which in the FE analysis were separated by a distance of 14 m (in comparison to the observed wrinkle separation distance of about

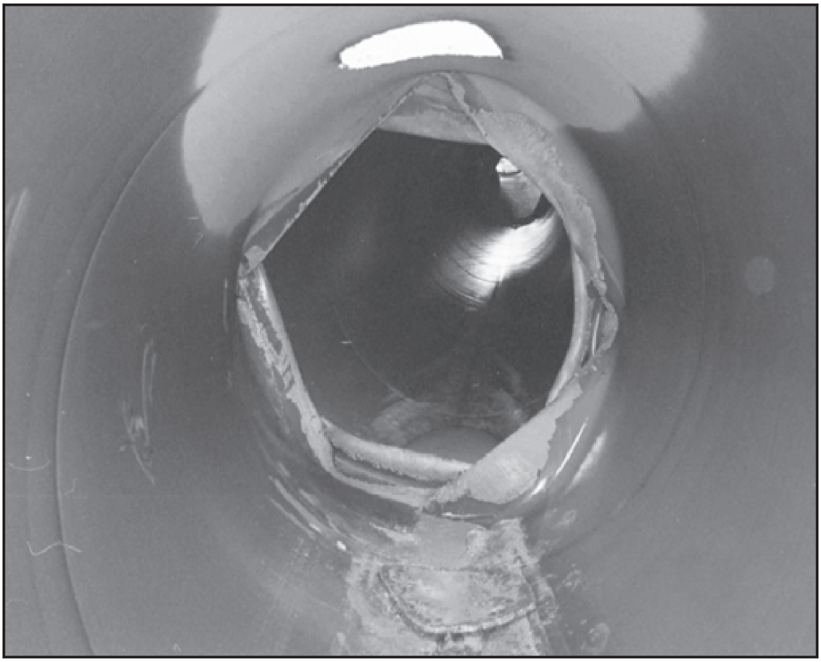

After Eidinger et al., 2002

■ **Figure 8.2 Internal View of Thames Water Pipeline at a Major Wrinkle**

18 m). The pipe material model was inelastic and induced strain hardening effects. The model did not, however, include the effects of wrinkling. As will be shown later, as wrinkles form pipe deformation concentrates at the wrinkles. The wrinkle locations behave like hinges in relation to bending effects, and behave like expansion/ compression joints in relation to axial effects. That is, both transverse and longitudinal offsets are accommodated by increasing deformation at the wrinkles. As such, the pipe region between the wrinkles and beyond the wrinkles tends to unload. Since wrinkling effects are not included in the FE model, one expects that the actual peak tensile and compressive pipe strains at the wrinkles are well in excess of the 3% and 9.6% values reported above. Nevertheless, the FE analysis would suggest that wrinkling was likely or almost certain to occur since the critical local buckling strain using, for example the relation in Equation 4.8, is only 0.11%.

In general there are three potential failure modes for a continuous pipeline fault crossing. They are: tensile rupture, local buckling (wrinkling) in compression, and beam buckling in compression. The beam buckling mode is discussed in detail in Section 4.1.4. Although this is a realistic failure mode for offshore pipelines laid on the ocean floor, onshore pipelines are typically buried 1.0 m (3.0 ft) or more below the ground surface. Since this burial depth is larger than the critical burial depth shown in Figure 4.5, the onshore pipe wrinkles rather than buckles like a beam when subject to compressive PGD. Hence, this chapter focuses on tensile rupture of a pipe due to bending and tension, and wrinkling of the pipe wall due to bending and compression.

8.2 Strike Slip Fault – Nominal Tension

People rarely question pipe behavior information gleaned from full-scale case histories, such as the Thames Water Pipeline mentioned above. There are drawbacks, however, with case histories. For example, to confirm the condition leading to initial local buckling of the pipe wall, it would have been better if the fault offset was roughly a tenth of the actual value. Laboratory test programs, such as the Cornell-Rensselaer NEESR project, provide the opportunity to investigate such behavior.

8.2.1 Centrifuge Tests – Nominal Tension

Figure 8.3 shows axial and flexural strains measured on HDPE pipe subject to various amounts of strike-slip fault offset, as reported by Ha et al. (2008). The angle, β, between the fault and the pipe were 85° and 63.5°, respectively. Hence, both pipes are subject to bending due to the transverse component of fault offset, and axial tension due to the longitudinal component. The tests were conducted in the Rensselaer split-box with the pipe pinned to the split-box end wall, as shown in Figure 8.4. As such, the tests simulate a prototype situation with thrust blocks at the end of the pipe test specimen. The results shown in Figure 8.3 were for tests at a 12.2 g level. Hence, in prototype scale the simulated thrust blocks are 7.8 m (0.64 m times 12.2 = 7.8 m) from the fault.

For both pipe fault angles, the axial pipe strain is an increasing function of the offset, as one would expect. Also, the induced axial strains for the near perpendicular offset ($\beta = 85^{o}$) are much smaller, roughly a fifth of those for $\beta = 63.5^{o}$. This ratio of roughly

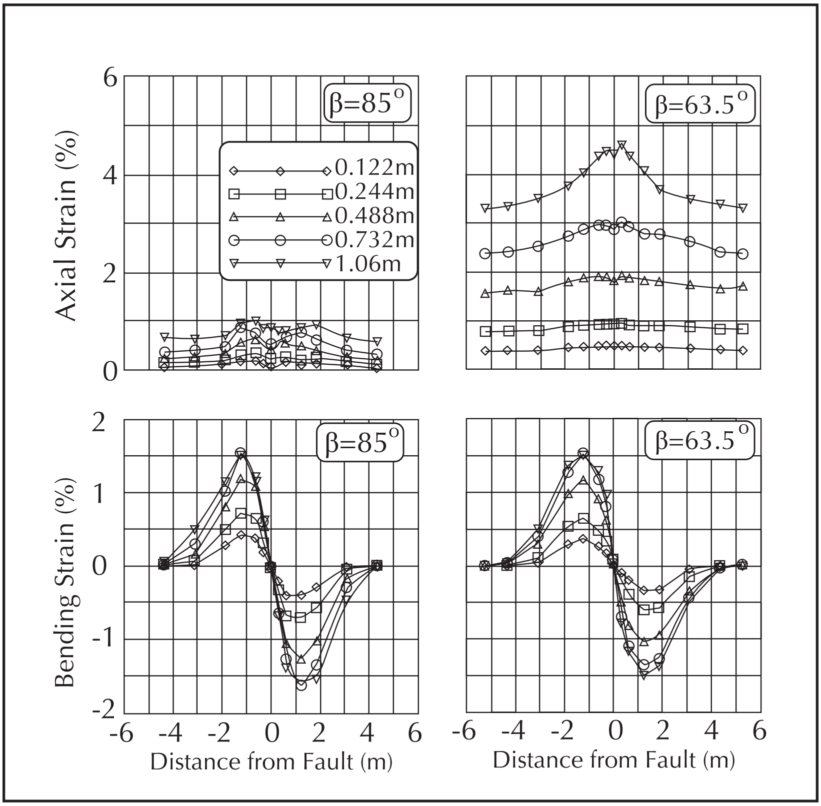

After Ha et al., 2008

■ **Figure 8.3 Measured Axial and Bending Strains in HDPE Pipe Subject to Nominal Tension Strike-Slip Offsets**

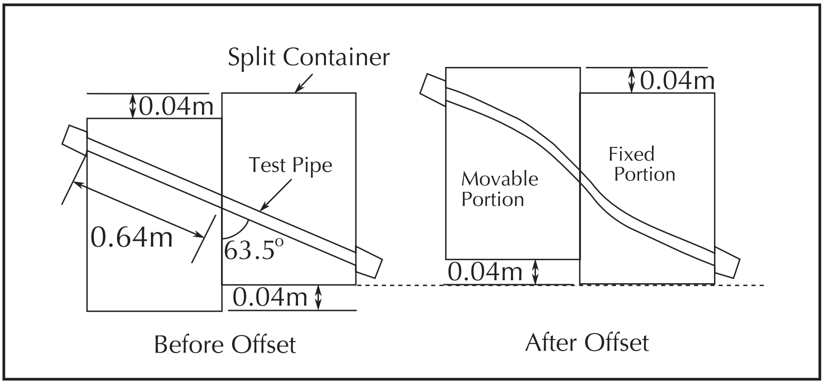

After Ha et al., 2008

■ **Figure 8.4 Plan View of Centrifuge Split-Box with Pipe-Fault Angle β = 63.5° - Dimensions are in Model Scale** a fifth is consistent with the ratio of longitudinal components of offset (cos 85 / cos 63.5 = 0.195). The axial pipe strains are largest near the fault, and decrease in a somewhat linear fashion with distance from the fault.

The measured bending strains in Figure 8.3 are consistent with double curvature bending-convex on one side of the fault, concave on the other, with an inflection point at the fault itself. At low values of the offset, up to about 0.49 m for the test shown in Figure 8.3, the flexural strains for the near perpendicular model ($\beta = 85^o$) are slightly larger than those for $\beta = 63.5^o$ (sin 85/sin 63.5 = 1.11). Note, however, that unlike the axial strain, the bending strains reach a maximum of roughly 1.5% at a 0.73 m offset. Tactile pressure sensor data indicated that this limit or plateau for pipe bending strain occurs when the nonlinear soil spring transition from linear elastic behavior to plastic behavior. That is, for ever increasing offsets, the axial strains continue to increase while the bending strains remain at a plateau. Other centrifuge tests reported by Abdoun et al. (2009) indicate that neither the fault offset rate nor the soil moisture content significantly influenced the magnitudes or location of the peak pipe strains. On the other hand, the burial depth had a significant influence on pipe strain, particularly the bending strains. As one might expect, deeper burial depths result in large pipe bending strains.

8.2.2 Analytical Models – Nominal Tension

A number of investigations have been performed regarding tensile and bending behavior due to large abrupt fault movements. These include the Newmark-Hall approach, and the Kennedy et al. approach, among others. Herein, these analytical approaches are reviewed and the results are compared to those from an FE model.

Newmark and Hall (1975) were the first to formally analyze the fault crossing problem, apparently in relation to the Alyeska Pipeline project. They considered the model shown in Figure 8.5 with a total fault movement δ_f, in which a pipeline intersects a right lateral strike-slip fault at an angle β. For a pipe-fault intersection angle $\beta \le 90°$, the strike-slip fault results in tensile strain in the pipe. They assume that the pipe is firmly attached to the soil (i.e., no relative displacement between pipe and soil) at two anchor points located at L_a from the fault trace. Anchors correspond to thrust blocks and other features, which develop substantial resistance to pipe axial movement.

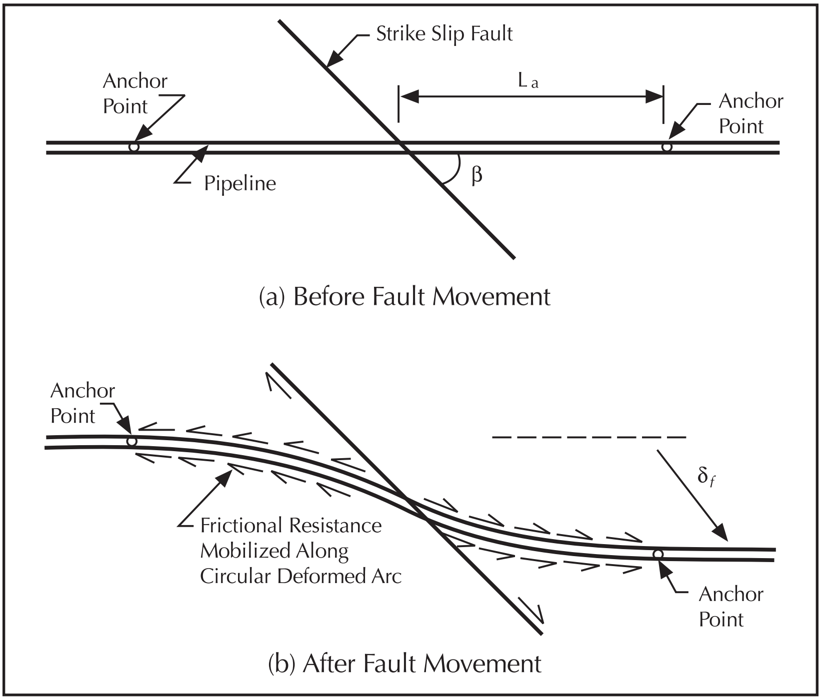

After Newmark and Hall, 1975

Figure 8.5 Plan View of the Newmark-Hall Model for Pipeline Crossing a Right Lateral Strike-Slip Fault

The authors neglect the bending stiffness of the pipe as well as lateral interactions at the pipe-soil interface. That is, they envision shallow burial in a trench with sloping side walls for which only longitudinal interaction at the pipe-soil interface is considered. The total elongation of the pipe is composed of two components. The first is due to the axial component of fault movement ($\delta_f \cos \beta$). The second is due to arc-length effects caused by lateral component of fault movement ($\delta_f \sin \beta$).

Because of symmetry, only one side of the fault trace is considered. The average pipe strain, $\bar{\varepsilon}$, is:

$$\bar{\varepsilon} = \frac{\delta_f}{2L_a} \cos \beta + \frac{1}{2}\left(\frac{\delta_f}{2L_a} \sin \beta\right)^2 \tag{8.1}$$

where L_a is the effective unanchored length, that is, the distance between the fault trace and the anchor point. The first term accounts for the longitudinal component of the fault offset, that is, the average strain for a total displacement of 0.5 $\delta_f \cos \beta$ over a distance L_a. The second term accounts for arc-length effects and can be derived by applying the Pythagorean and Binomial Theorems. Note that Equation 8.1 assumes that both the longitudinal and transverse effects occur over the same horizontal distance L_a from the fault. This is an unconservative assumption in relation to the transverse component in that the distance over which bending strains are important is typically smaller than the corresponding distance for axial strains induced by the longitudinal component.

When no thrust blocks or other constraints are located near the fault, the friction forces at the pipe-soil interface provide all the axial resistance. In this case, L_a can be estimated by:

$$L_a = L_e + L_p \tag{8.2}$$

where L_e is the pipe length over which elastic strain develops, while L_p is the length over which plastic strain develops.

L_e, L_p are given by:

$$L_e = (E_i \varepsilon_y \pi D t)/t_u \tag{8.3}$$

$$L_p = [E_p(\varepsilon - \varepsilon_y)\, \pi D t]/t_u \tag{8.4}$$

where ε_y is the material yield strain, E_i and E_p are the modulus before yield and after yield, ε is the plastic tensile strain in the pipe and t_u is the axial friction force per unit length at the pipe-soil interface. That is, L_a is the total length over which the axial friction force t_u must act, to develop a particular level of axial strain in the pipe. Failure in the Newmark and Hall approach is assumed to occur when the average strain $\bar{\varepsilon}$ is greater than 4%.

For a 0.61-m-diameter (24 in) pipe made of X-60 grade steel, the relation between the tolerable fault movement and the intersection angle using the Newmark and Hall approach is shown in Figure 8.11 along with similar information from other approaches, which will be discussed later. The Newmark and Hall model provides valuable insight into the mechanics of this problem, and allows one to evaluate the most influential parameters. However, as will be shown later, this approach overestimates the tolerable fault movement for pipelines since it uses the average strain as a failure criterion and neglects the lateral interaction at the pipe-soil interface.

Kennedy et al. (1977) extended the ideas of Newmark and Hall, and incorporated some improvements in the method for evaluating the maximum axial strain. Specifically, they considered the effects of lateral interaction in their analysis. Also, the influence of large axial strains on the pipe's bending stiffness is considered. That is, the pipe bending stiffness becomes very small (roughly 0.5% of the initial stiffness) when axial strain is well beyond the yield strain.

Figure 8.6 presents the Kennedy et al. model, for one side of the fault. Note the bending strain occurs in the curved region where a constant curvature, $1/R_c$, is assumed. That is, unlike the Newmark-Hall model, bending and corresponding arc-length effects occur relatively close to the fault, while the axial friction forces extend well beyond this near fault region.

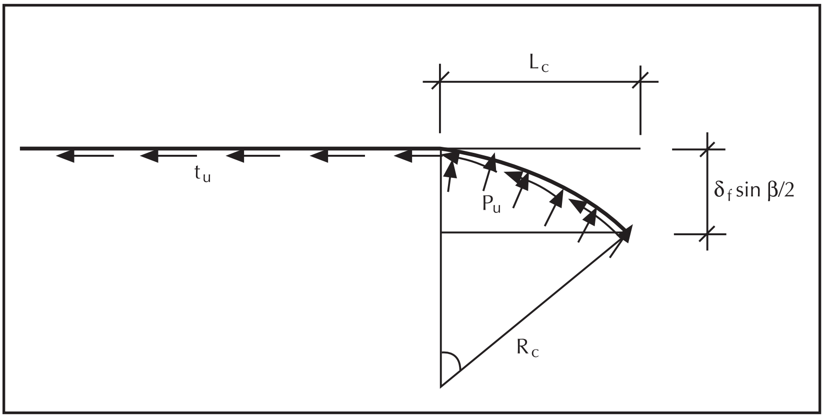

After Kennedy et al., 1977

■ **Figure 8.6 Kennedy et al. Model of Buried Pipeline on One Side of the Fault**

The bending strain, ε_b, is expressed as:

$$\varepsilon_b = \frac{D}{2R_c} \tag{8.5}$$

where R_c is the radius of curvature of the curved portion, which can be evaluated by using an analogue to internal pressure in a cylinder:

$$R_c = \frac{\sigma \pi D t}{p_u} \tag{8.6}$$

where σ is the axial stress at fault crossing, and p_u is the peak lateral soil-pipe interaction force per unit length (see Equation 5.7 for sand or Equation 5.9 for clay). That is, the Kennedy et al. model assumes that the offset is large enough that the soils lateral resistance is fully mobilized.

The total strain in the pipe is given by:

$$\varepsilon = \varepsilon_a + \frac{D}{2R_c} \tag{8.7}$$

where ε_a is the maximum axial strain due to the elongation of the pipe. The total elongation of the pipe, ΔL, which can be estimated by:

$$\Delta L = \delta_f \cos\beta + \frac{(\delta_f \sin\beta)^2}{3L_c} \tag{8.8}$$

Like the Newmark-Hall approach, the first term is the elongation due to the axial component of the fault movement, while the second term is the elongation due to arc-length effects induced by the lateral component of the fault movement. However, unlike the Newmark-Hall approach, L_c is the horizontal projection length of the laterally deformed pipe shown in Figure 8.6, which can be approximated by:

$$L_c = \sqrt{R_C \delta_f \sin\beta} \tag{8.9}$$

Also, unlike Newmark-Hall where the arc-length term is based upon a right triangle approximation, the Kennedy et al. term is based on an assumed circular arc.

Based on the Ramberg-Osgood relation in Equation 4.1, the total elongation can be expressed in terms of an integral of axial strain. That is,

$$\Delta L = \frac{2}{E}\int_0^{L_a} \sigma \left[1 + \frac{n}{1+r}\left(\frac{\sigma}{\sigma_y}\right)^r\right] dx \tag{8.10}$$

Integrating Equation 8.10, one can obtain the relation between the axial movement and effective length L_a. Combining Equation 6.3, Equation 6.4 and Equation 8.8, one can obtain the relation between fault offset and pipe strain for any intersection angle β, which is shown later in Figure 8.11.

Figure 8.7 shows the tolerable fault movement for a 42-in-diameter (1.07 m) pipe as a function of unanchored length. The burial depth from the ground surface to the top of the pipe are 3 ft (0.91 m) and 10 ft (3 m), respectively. The pipe wall thickness is 0.014 m (0.55 in); it's made of X-60 steel and surrounded by loose to moderately dense sand with $\gamma = 1.76 \times 10^4$ N/m^3 (110 pcf) and $\phi = 34°$.The critical tensile strain in the Kennedy et al. model is 4.5% for a burial depth, H_c, of 0.9 m and 3.5% for a burial depth of $H_c = 3.0$ m. The difference accounts for the substantial increase in bending strains and hoop ovaling for the deeper burial depth.

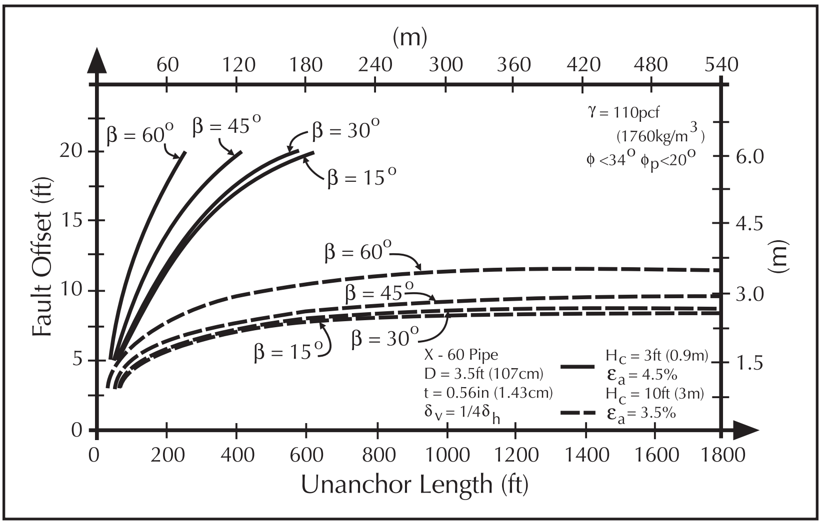

After Kennedy et al., 1977

■ **Figure 8.7 Tolerable Fault Movement vs. Unanchored Length**

As shown in Figure 8.7, the tolerable fault offset for the pipe is an increasing function of unanchored length and pipe-fault intersection angle, but a decreasing function of burial depth. The influence of unanchored length is easily understood. Accommodating a given longitudinal displacement demand over a larger pipe length results in lower pipe axial strain. The influence of crossing angle is related to the relative importance of the longitudinal component of fault offset (larger for small β) in comparison to the transverse (large for β close to 90°). That is, since L_C is typically large with respect to δ_f the second term in Equation 8.8 is smaller compared to the first (longitudinal stretch) term for equal amounts of transverse and longitudinal offset (i.e., β = 45°). Finally, deeper burial means larger axial and lateral soil restraint forces, which in turn leads to shorter lengths over which the offset is accommodated, and larger bending strains.

For the pipe-fault intersection angle of β = 60°, Figure 8.8 shows the maximum axial strain as a function of unanchored length. As shown in Figure 8.8, the pipe axial strain is a decreasing function of the wall thickness and unanchored length. For a given wall thickness, the axial strain is an increasing function of the pipe diameter, which is due to the corresponding increase in the interaction forces at the pipe-soil interface.

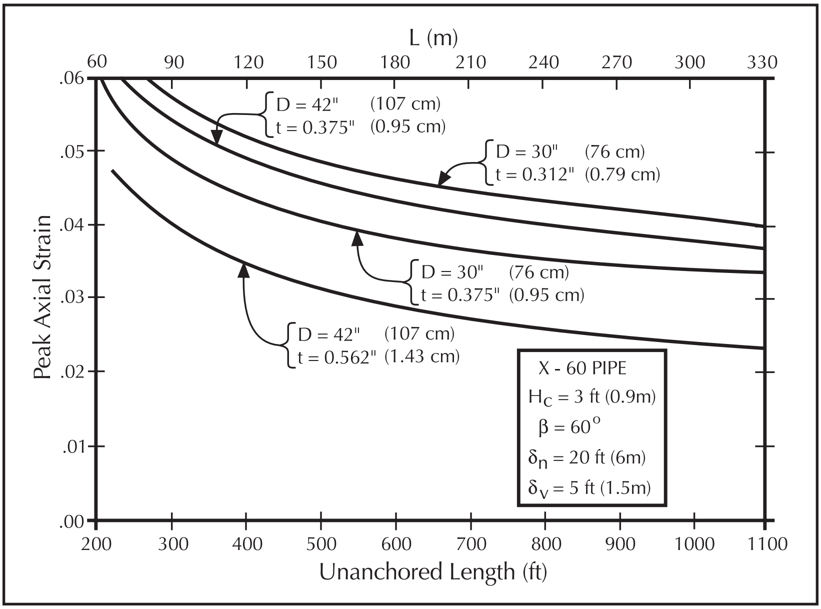

After Kennedy et al., 1977

Figure 8.8 Maximum Axial Strain vs. Unanchored Length

Subsequent to the above studies, Wang and Yeh (1985) introduced some additional modifications. Specifically, they use a beam on an elastic foundation (BEF) model for the "straight" portion of the pipeline beyond the constant curvature region. Furthermore, they subdivide the constant curvature region into elastic strain and inelastic strain regions.

Wang and Yeh apparently neglect the influence of pipe axial stress on pipe bending stiffness, and conclude that the pipe fails at the start of the BEF region. This seems somewhat unlikely since one expects tensile rupture to occur at or very near the location of maximum tensile strain that is closer to the fault.

Most recently, Karamitros et al. (2007) extend the Kennedy model and incorporate some ideas from the Wang-Yeh model. Specifically, like Wang and Yeh, they use a beam-on-elastic foundation model for the "straight" pipe region. As a simplification, they neglect the "sin β" term of Equation 8.1 or 8.8 in evaluations of the pipe elongation. To account for situations with comparatively small offsets and low axial strain, they calculate the bending strain as follows:

$$\frac{1}{\varepsilon_b} = \frac{1}{\varepsilon_b^{\mathrm{I}}} + \frac{1}{\varepsilon_b^{\mathrm{II}}} \tag{8.11}$$

where ϵ_b^{II} is the "curvature" bending strain from Equation 8.5 and ϵ_b^{I} is the strain due to the bending moment.

$$\varepsilon_b^{\mathrm{I}} = \frac{M_{max} \cdot D}{2EI} \tag{8.12}$$

As such, the Karamitros relation is applicable for both small offsets (offset over diameter less than 1.0) as well as larger offsets envisioned by the Kennedy et al. procedure.

Interestingly, they provide an explanation for the small increase in axial strain as one moves away from the fault. The increase can be seen in the axial strain plot for β = 63.5° in Figure 8.3. At low offsets when the pipe is still elastic (offset less than or equal to 0.24 m), the axial strain decreases monotonically with distance from the fault. However, for larger offsets (0.49 m and larger in Figure 8.3) where the pipe is inelastic, the axial strain has a local minimum at the fault itself. The peak axial strain occurs between the fault (point of peak axial force) and the point of peak bending moment. As noted by Karamitros et al. (2007), in the inelastic region where the combined axial and flexural strain is limited by the yield strain, the axial strain increases so that the integral of stress over the pipe cross-session equals the applied axial force.

8.2.3 Finite Element Models

Assuming a constant radius of curvature for the curved portion of the pipe, Ariman and Lee (1991) evaluated pipe strain using the finite element method. The pipe is modeled as a thin cylindrical shell, which is essentially semi-infinite. For a 42-in-diameter pipe made of X-60 steel, they present the bending strain as a function of soil angle of shearing resistance, burial depth, and pipe diameter in Figure 8.9(a), (b) and (c), respectively. The amount of fault offset is 6.1 m and the intersection angle is 70° in their calculation. As shown in Figure 8.9, the Ariman and Lee model suggests that the bending strain in the pipe is an increasing function of the soil friction angle, burial depth and pipe diameter.

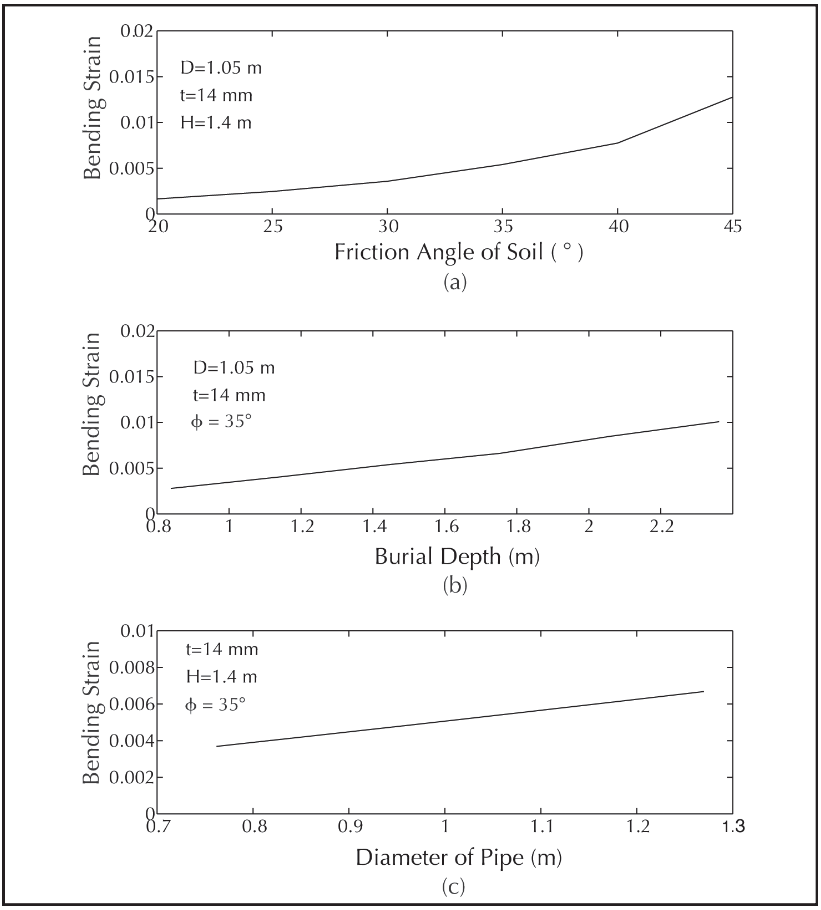

After Ariman and Lee, 1991

■ **Figure 8.9 Pipe Bending Strain as a Function of Soil Friction Angle, Burial Depth and Pipe Diameter**

In order to evaluate the various approaches, an ABAQUS FE model was used herein to estimate the pipe strain. The pipeline model is fixed at the point 500 m (1,640 ft) away from the fault. This unanchored length is sufficiently long such that both axial strain and bending strain are zero at the anchor point. All the bases of soil springs to the left of fault trace are fixed. To the right of the fault trace, all the bases of lateral soil springs move a distance of $\delta_f \sin \beta$ in the transverse direction, while all the bases of axial soil springs move a distance of $\delta_f \cos \beta$ in the longitudinal direction.

Considering the non-linear interaction at the pipe-soil interface (Equation 5.1 and Equation 5.7) and the Ramberg-Osgood stress-strain relationship (Equation 4.1), the response of an X-60 grade pipe (0.61 m in diameter, 0.0095 m in wall thickness) subject to a strike-slip fault is analyzed.

The peak pipe strain for an intersection angle of 90° is shown in Figure 8.10 as a function of fault offset. The peak compression strain occurs for a fault offset of approximately 2 m (6.6 ft) and decreases thereafter. This decrease of compression strain is due to the decrease of bending strain/stiffness caused by the large axial strain. Three stages can be identified for the response of a buried pipeline subject to an abrupt lateral fault offset as shown in Figure 8.10. In Stage I (small offsets), both axial and bending strains are important, and both increase with fault offsets. Bending strains are large enough such that there is a non-zero net compressive strain. In Stage II (intermediate offsets), the axial strain is beyond

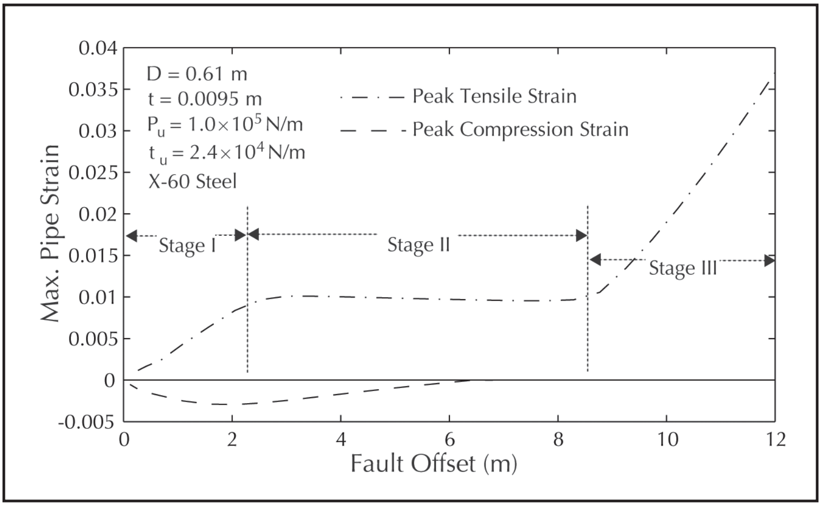

■ **Figure 8.10 Pipe Strain vs. Fault Offset (for 90° Intersection Angle)** yield, and bending stiffness (and hence bending strain) are decreasing and the net compressive strains approach zero. In Stage III (large offsets), the bending strain remains constant while axial strain increases with increasing fault offsets.

8.2.4 Comparison Among Approaches

In this section, two comparisons are made between results from analytical models and finite element results. The first comparison is in terms of the allowable fault offset, that is the design limit where the pipe is at its peak capacity. The second comparison is in terms of pipe strains at smaller offsets.

For strike-slip offsets which place the line in nominal tension, Figure 8.11 presents the tolerable fault offset from four approaches as a function of the intersection angle between the pipe axis and fault trace. As shown in Figure 8.11, the results obtained from the ABAQUS numerical approach match that from Kennedy et al.'s analytical approach very well for intersection angles less than 60°. For intersection angles larger than 60°, the tolerable fault offset from the ABAQUS model is only slightly less than that from Kennedy et al.'s approach.

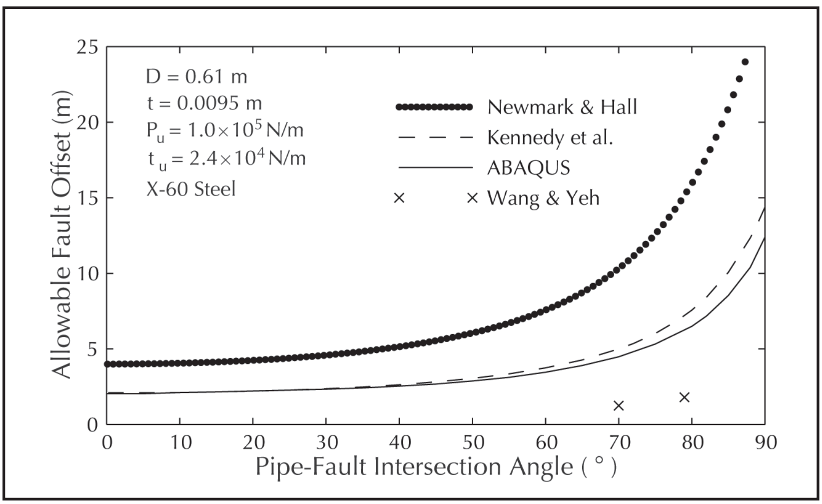

Figure 8.11 Comparison of Results from Four Approaches

Newmark and Hall's approach overestimates the tolerable fault offset by roughly a factor of two. This is believed to be due to the use of the average strain for the failure criterion. Note that the maximum strain in the pipe is at least twice the average strain used in their approach. Moreover, Newmark and Hall neglect the bending strain in the pipe and the influence of bending strain on the axial stiffness of the pipe. Note that Newmark and Hall's curve is based on Equation 8.1 with an unanchored length of 50 m (164 ft).

Wang and Yeh's approach appears to underestimate the tolerable fault offset for the pipeline by a factor of four. This is believed to be due to their assumption that the pipe strain in a portion of the curved region is elastic and a reduced bending stiffness at high axial strain is neglected. In fact, the finite element results suggest that the axial strain in that region does exceed the yield strain and the bending stiffness is, in fact, greatly reduced. Hence, Wang and Yeh's approach overestimates the bending strain in the pipe, and underestimates the tolerable fault offset for the pipe.

Peak pipe strain for smaller offsets are compared in Figure 8.12, for intersection angles $\beta = 30^o$ and 60^o. Specifically, the peak strains from various approaches for a X-65 grade steel pipe with

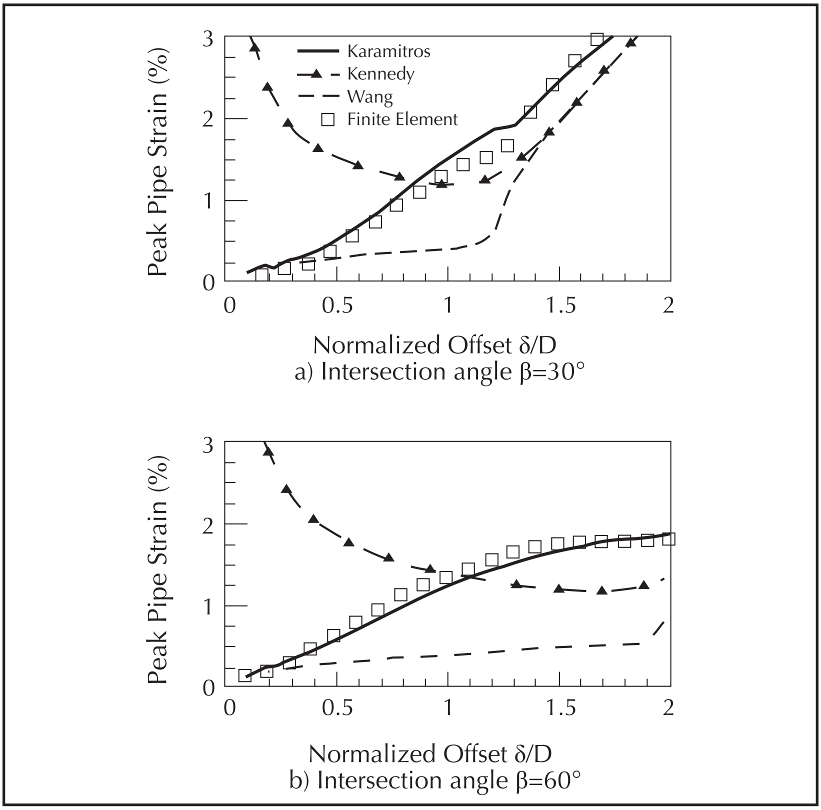

After Karamitros et al., 2007

■ **Figure 8.12 Comparison of Peak Pipe Strain for Small Offsets** diameter $D = 0.914$ m (36 in), wall thickness $t = 0.012$ m (0.47 in), burial depth of 1.3 m in soil with a friction angle = 36° and unit weight = 18 kN/m^3, are plotted versus the normalized fault offset.

As one might expect, the peak strain from the finite element model are larger for an intersection angle $\beta = 30°$ from those for 60°, particularly for normalized offsets larger than 1.0. The Karamitros et al. model compares favorably to the finite element results for all normalized offsets considered. The Kennedy et al. model provides reasonable strain estimates for normalized offsets larger than about 1.25. As the normalized offsets decrease, the Kennedy et al. peak strain becomes larger. As shown by Karamitros et al. (2007), this incorrect result is due to bending strains. As noted in relation to Equations 8.5 and 8.6, Kennedy et al. assume that the offset is large enough that the soils lateral resistance is fully mobilized, which clearly is not the case at small offsets. The Karamitros et al. model avoids this difficulty through the use of Equation 8.11. The Wang and Yeh model provides reasonable results for $\beta = 30°$ and normalized offsets greater than about 1.25. For $\beta = 60°$, the Wang and Yeh model appears to significantly underestimate peak pipe strain.

Hence, in terms of available analytical approaches, either the Kennedy et al. or the Karamitros et al. methods seem reasonable for evaluation of design capacity. The Karamitros et al. approach would be recommended for determination of the state of pipe strain at smaller fault offsets, on the order of the pipe diameter itself.

8.3 Strike-Slip Fault – Nominal Compression

There has been more research effort directed at the nominal tension case than the nominal compression case. This is likely an outgrowth of the fact that in design the nominal tension case is preferred since the tensile strain capacity of steel pipe is larger than compressive strain capacity. In addition, as will be shown shortly, the nominal compression case is more complicated. However, right-of-way constraints often result in pipe being subject to strike slip faulting with nominal compression. The Thames Water Pipeline in Figure 8.1 is one such example. Similarly, two of the four large diameter Bay Division Pipelines within the Hetch-Hetchy Water System, which supplies San Francisco Peninsula communities, cross the Hayward Fault such that the lines are in nominal compression.

Figure 8.13 shows centrifuge tests results from Ha et al. (2010) for HDPE pipe subject to either nominal compression (intersection angle $\beta = 120^o$) or nominal tension ($\beta = 63.5^o$) offsets. The prototype pipe diameter was 0.41 m (16 in), the H/D ratio was 2.75 and the *D/t* ratio was 17. At low offsets (0.254 m or less in Figure 8.13), the behavior is quite similar to that for the nominal tension case described previously. As a matter of fact, the $\beta = 63.5^o$ (nominal tension) results in Figure 8.3 are the same as those shown in Figure 8.13, plotted with a different vertical scale.

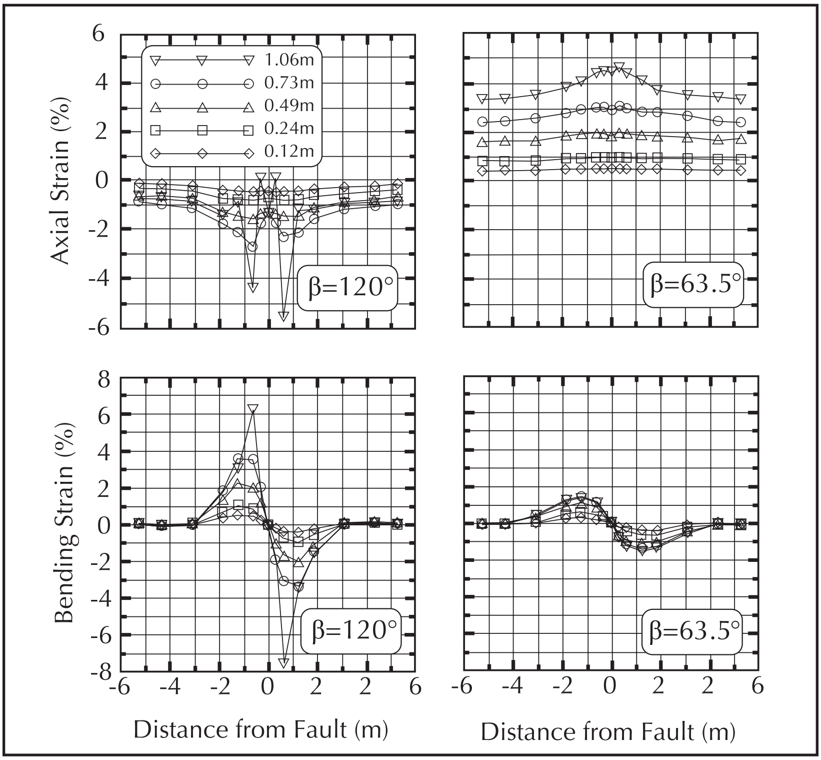

After Ha et al., 2010

■ **Figure 8.13 Measured Axial and Bending Strains in HDPE Pipe Subject to Nominal Compression and Nominal Tension Strike-Slip Offsets**

However, the nominal tension and compression behavior differ substantially for offsets of 0.49 m or larger. For nominal compression, both the axial and bending strains become quite large at two locations close to the fault. Shown in Figure 8.14 is a close-up photo of the two buckles after the over burden soil has been removed. As these buckles form, the portion of pipe between them unloads, as evidenced by the reduced axial strain in the pipe segment between the two buckles. That is, the axial displacement and rotation demands are accommodated primarily at the two buckles.

From Figure 8.13, the buckles begin to form at offsets between 0.24 and 0.49 m. The corresponding total strain (axial compression plus flexural compression) were between 1.8% (offset = 0.24 m) and 3.5% (offset = 0.49 m). The HDPE pipe material has a round-house type stress-strain curve and, hence, a somewhat ill defined "yield" strain. However, for the offset rate used in there tests, the nominal yield strain (onset of significant inelastic behavior) is about 2%. Hence, it appears that the buckles were initiated by material yielding as opposed to classical local buckling of the pipewall.

After Ha et al., 2010

■ **Figure 8.14 Close-up View of Two Buckles in HDPE Pipe Subject to Strike Slip-Nominal Compression Faulting (View After Overburden Soil Removed)**

Normal and Reverse Faults

As with the strike-slip nominal compression case, there is very little available in the technical literature on pipe behavior for either normal or reverse faulting. The one exception is a set of centrifuge test of HDPE pipe subject to offsets along a vertical fault plane.

Figure 8.15 shows measured axial and bending strains for two different fault offsets, as reported by Abdoun et al. (2008). The first is strike slip-nominal tension with pipe fault intersection angle at β = 85°, while the second is normal faulting along a vertical fault plane.

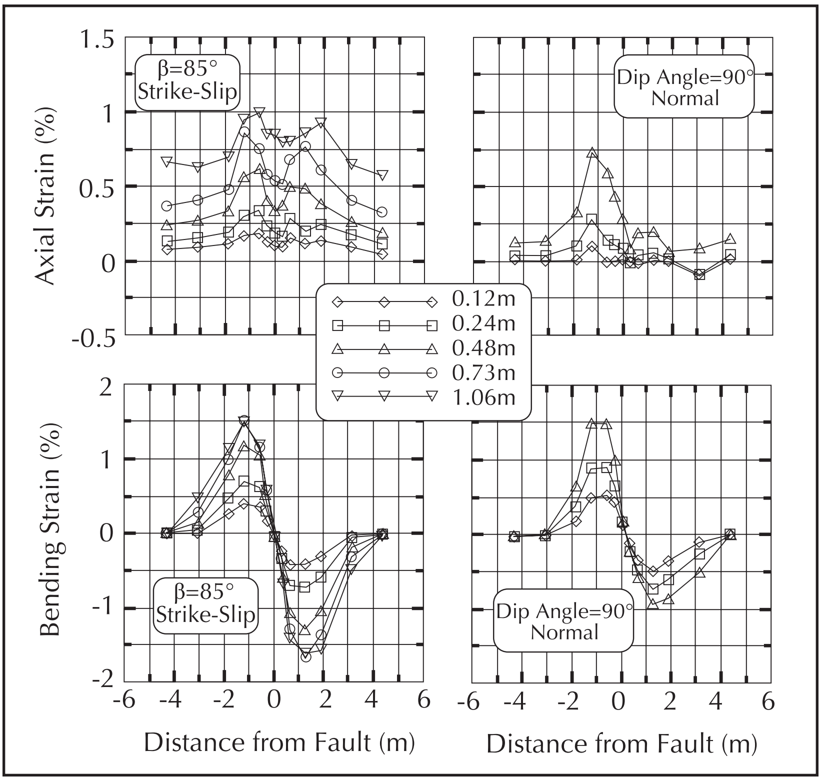

After Abdoun et al., 2008

■ **Figure 8.15 Measured Axial and Bending Strains in HDPE Pipe at Various Distances from the Fault for Strike-Slip Nominal Tension and Normal/Reverse Faulting**

The strike slip behavior is the same as described above in relation to Figure 8.3. As a matter of fact, the plots for $\beta = 85^o$ are identical, with the exception that the axial strain is plotted at a different scale.

The behavior for normal/reverse faulting is different than that for strike slip-nominal tension faulting. In the first place, the strain distribution is no longer symmetric with respect to the fault, the differences in axial strain being most noticeable. For both axial and bending, the larger strains are on the upthrown side, as one might expect. Secondly, the bending strains for strike slip faulting reach a plateau at an offset of 0.73 m. There is no apparent plateau in bending strains for the normal/reverse fault. Note, however, that due to limitation of the split-box equipment, the largest prototype vertical offset was 0.48 m. Finally, although the behavior is different, with the normal/reverse faulting case being more complex, the measured strains in Figure 8.15 suggest that the strike slip strains for near perpendicular horizontal offsets provide a reasonable but somewhat unconservative estimate for axial and bending strains induced by vertical near-perpendicular offsets.

8.5 Comparison with Case Histories

The 1979 Imperial Valley earthquake provides case histories which can be used to benchmark the finite element approaches for strike slip-nominal tension and strike slip-nominal compression faulting. During this earthquake, three natural gas pipelines were affected by the localized abrupt offsets at the Imperial Fault, as shown in Figure 8.16. The maximum co-seismic right lateral slip along the fault was 0.55 to 0.60 m (1.8 to 2.0 ft) at Heber Dunes. Up to 0.29 m (1.0 ft) of afterslip was measured at McCale Road 160 days after the earthquake, according to Roth et al. (1990).

The material properties of those pipelines, the amount of fault offset as well as the pipe-fault intersection angles are listed in Table 8.1. The No. 56 coating consists of layers of red oxide primer, filled asphalt, two spiral wraps of cellulose acetate, filled asphalt and paper wrapper. The somastic coating is composed of asphalt, aggregate and fiber mixture. In this case study, Equations 5.1 and

5.7 are used for estimating maximum axial and lateral interacting forces at the pipe-soil interface. We assume the angle of shear resistance of the sand $\phi = 35°$ and $k = 0.7$ for No. 56 coating and $k = 0.9$ for somastic coating.

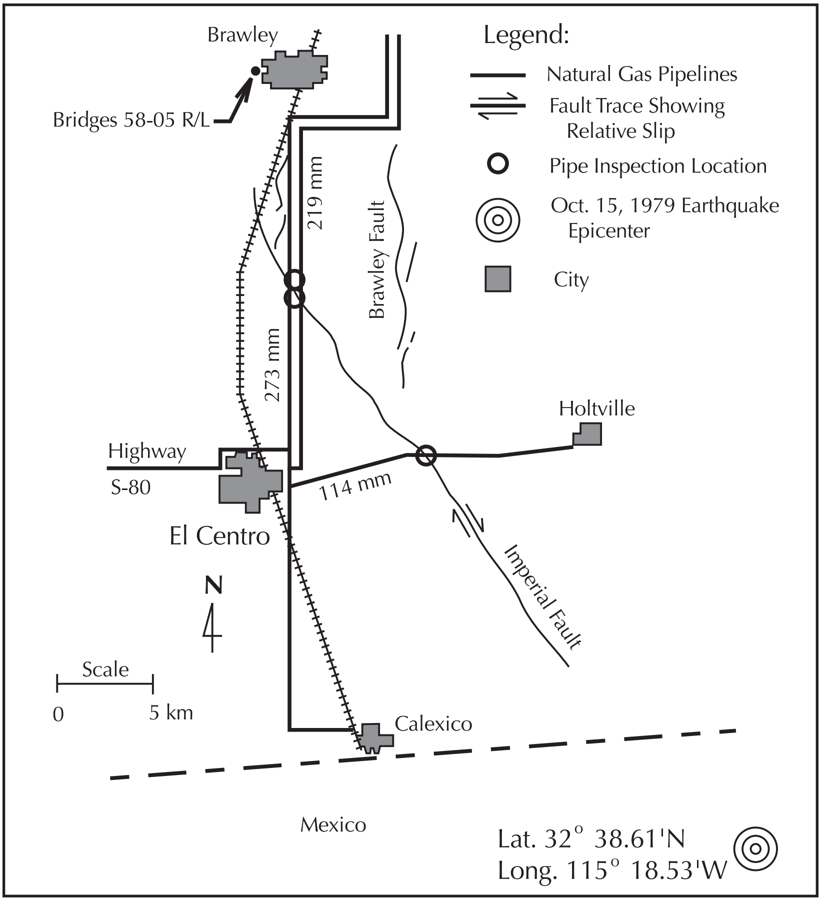

After Roth et al., 1990

■ **Figure 8.16 Three Gas Pipelines Intersected by the Imperial Fault**

Two cases are considered herein. In Case I, the fault is assumed to be a single abrupt fault (i.e., the width of offset zone is zero). In Case II, the 9.6 m (32 ft) of actual fault width is used, and linear distribution of ground movement across the width is assumed. The maximum pipe strains from the finite element model as well as the critical strain are listed in Table 8.1. The critical strain for the Holtville-El Centro Line (angle 55°) is taken as a tensile rupture strain of 4%, while the critical strains for Lines

6000 and 6001 are taken as 0.175t/R. The predicted behavior matches the observed behavior in that the maximum strain for Case II (actual width used) are less than the critical values, and the pipes did not, in fact, fail. Note that the tensile strains for the Holtville-El Centro Line for both cases are relatively close. However, for the other two pipelines, the compressive strain for the zero-width fault is much larger that for the 9.6-m-wide fault. This suggests that the width of the fault can be a key parameter, particular for compressional movements. That is, the finite element results suggest that the two pipelines in compression would have wrinkled if the width of the fault were small (e.g., less than about 3.0 m (10 ft)).

Table 8.1 Pipe and Fault Properties and Strain Analyses

Characteristic	Holtville-El Centro Line	Line 6000	Line 6001
Diameter	114 mm	219 mm	273 mm
Wall Thickness	5 mm	7 mm	5 mm
Material	A-25 Steel	GR-B Steel	X-42 Steel
Yield Stress	170 MPa	240 MPa	290 MPa
Operating Pressure	2.8 MPa	2.8 MPa	2.8 MPa
Depth of Cover	0.9 m	0.9 m	0.9 m
Weld Type	Acetylene	Electric Arc	Electric Arc
Coating	No. 56	Somastic	No. 56
Fault Offset	0.6 m	0.4 m	0.4 m
Intersection Angle	55°	120°	120°
Max. Tensile Strain (Case I)	0.015	-	-
Max. Tensile Strain (Case II)	0.0126	-	-
Max. Compressive Strain (Case I)	-	> 0.06	0.0335
Max. Compressive Strain (Case II)	-	0.00736	0.00326
Critical Strain	0.04	0.0112	0.0064

Response of Segmented Pipelines to PGD

In this chapter, the response of segmented pipelines subject to PGD will be discussed. Segmented pipes typically have bell and spigot joints and can be made of cast iron, ductile iron, steel, concrete or asbestos cement. As indicated in Section 4.3, there are three main failure modes for segmented pipelines: axial pull-out at joints, crushing of the bell and spigot joints, and round flexural cracks in the pipe segment away from the joints.

Similar to the response of continuous pipelines, the behavior of a given buried segmented pipeline is a function of the type of PGD (e.g., longitudinal or transverse), the amount of ground movement δ, the spatial extent of the PGD zone and the pattern of ground movement within the zone.

In reference to the type of PGD, Suzuki (1988) concluded that damage due to longitudinal PGD was more common than damage due to transverse PGD based on observed behavior of segmented gas pipelines during the 1964 Niigata earthquake. In these cases, the joints were pulled out in the ground tension region and buckled in the ground compression region. In the ALA Guidelines (2005), an assertion is made that the damage rate for non-seismically designed pipes subject to longitudinal PGD is 5 to 10 times larger than that for similar pipe subject to transverse PGD.

In terms of the pattern, if the ground movement within the PGD zone is relatively uniform (i.e., an idealized block pattern of longitudinal PGD in Figure 6.1(a)), one expects that a few pipe joints near the head and toe of the zone would have to accommodate essentially all the abrupt differential ground movement. On the other hand, if the ground movement varies within the PGD zone (i.e., an idealized ridge pattern of longitudinal PGD in Figure 6.1(c)), the rate of change of ground displacement along the segmented pipeline leads to an "equivalent" ground strain. One expects that all joints within the zone, to a greater or lesser extent, would then experience relative axial displacement.

9.1 Longitudinal PGD

As with continuous pipeline, longitudinal PGD induces axial effects in segmented pipeline, specifically axial strain in the pipe segments and relative axial displacement at the joints. However, in contrast to the response of continuous pipelines, damage to segmented pipelines subject to longitudinal PGD typically occurs at pipe joints since the strength of the joints is generally less than the strength of the pipe segment between joints. Whether the joints fail depends on the strength and deformation capacity of the joints as well as the characteristics of the PGD.

One particularly important characteristic is the pattern of longitudinal PGD. Herein, two types of patterns are considered in detail. For the distributed deformation case (such as the idealized ridge pattern in Figure 6.1(c)), ground strain exists over a significant portion of the PGD zone. For the abrupt deformation case (such as the idealized block pattern in Figure 6.1(a)), relative movement exists only at the margins of the PGD zone, and the ground strain between the margins is zero.

9.1.1 Distributed Deformation

The response of segmented pipelines subject to a distributed deformation pattern of longitudinal PGD is similar to that for segmented pipelines subject to wave propagation, in that the spatially distributed PGD results in a region of ground strain. That is, the ridge, asymmetric ridge and ramp patterns in Figure 6.1 result in ground strain over the whole length of the PGD zone, while the ramp-block pattern results in uniform ground strain over a portion (i.e., length βL) of the zone. For example, the ground strain for the ridge pattern (tensile strain to the left of the peak ground displacement point in Figure 6.1(c), compressive ground strain to the right) is:

$$\varepsilon_g = \frac{2\delta}{L} \tag{9.1}$$

By assuming that pipe segments are rigid and all of the longitudinal PGD is accommodated by extension or contraction at the joints, the average relative displacement at the joints is given by the ground strain times the pipe segment length, L_o:

$$\Delta u_{avg} = \frac{2\delta L_o}{L} \tag{9.2}$$

Equation 9.2 envisions conditions prior to joint pull-out in tension or joint lock-up in compression. Although Equation 9.2 represents the average behavior, the joint displacements for uniform ground strain varies somewhat from joint to joint due to variation in joint stiffness. That is, in a region of tensile ground strain a relatively flexible joint is expected to experience larger joint displacements than adjacent stiffer joints. A more detailed discussion of the effects of variable joint properties on the response of segmented pipe to ground strain is presented in Sections 11.1 (tensile ground strain) and 11.2 (compressive ground strain).

Using realistic variations of joint stiffness, El Hmadi and M. O'Rourke (1989) determined, as presented in Table 9.1, the mean joint displacement, $\Delta\bar{x}$, in centimeters, and coefficients of variation, μ, in percentage, as a function of ground strain for various diameters of Cast Iron pipe with lead-caulked joints (CI) and Ductile Iron pipe with rubber gasketed joints (DI). The values in Table 9.1 assume that the pipe segment length L_o for all types was 6.0 m (20 ft) and that neither joint pull-out nor lock-up occurs. Note that the mean values for both CI and DI pipes are about equal to the value given in Equation 9.2 (that is, $\varepsilon_g L_o$).

■ **Table 9.1 Mean Joint Displacement and Coefficient of Variation for Segmented Pipe Subject to Uniform Ground Strain**

Ground Strain	CI D = 40 cm (16 in)		CI D = 76 cm (30 in)		CI D = 122 cm (48 in)		DI D = 40-122 cm (16-48 in)	
	$\Delta\bar{x}$ (cm)	μ(%)	$\Delta\bar{x}$ (cm)	μ(%)	$\Delta\bar{x}$ (cm)	μ(%)	$\Delta\bar{x}$ (cm)	μ(%)
0.001 (1/1,000)	.54	64	.56	54	.58	52	.59	2
0.002 (1/500)	1.14	56	1.17	49	1.17	43	1.19	2
0.005 (1/200)	2.92	39	2.95	24	2.97	14	3.00	1
0.007 (1/150)	4.12	26	4.16	19	4.16	16	4.19	1

However, the coefficients of variation, μ for DI joints are quite small in comparison to those for CI joints. This is due to the fact that DI joints are substantially more flexible than CI joints. As a result, the joint opening or closure for DI pipelines would be relatively constant over the length of the PGD zone, while there would be more variability of joint displacement for CI pipe. Hence, for tensile ground strain one expects little or no damage in DI pipe until the ground strain equals the average joint displacement for leakage divided by the pipe segment length. For compressive ground strain, and DI pipe, the "tipping point" is ground strain equal to the joint contraction for lock-up divided by the pipe segment length. On the other hand, one expects damage to CI pipe at lower levels of ground strain since some of the CI joints will have axial displacement well above the average value given in Equation 9.2.

Hence, a key issue is whether ground strains due to distributed deformation patterns of longitudinal PGD are larger or smaller than these tipping points. M. O'Rourke et al. (1995) present a summary of longitudinal PGD patterns observed in Noshiro City after the 1983 Nihonkai Chubu event. The **minimum** ground strain due to distributed longitudinal PGD was 0.008. The resulting joint opening is 5 cm (2 in), for a pipe segment length of 6.0 m. This is larger than the tensile joint capacity of typical segmented pipelines, as noted in Section 4.3 (i.e., segmented joints typically leak for relative displacement on the order of half the total joint depth). Hence, expected ground strains for distributed deformation patterns of longitudinal PGD are large compared to tensile ground strains resulting in damage to a typical or average joint. Similar behavior for compressive strains is expected. That is, one expects joint damage when a segmented pipeline crosses a potential longitudinal PGD zone. Hence, consideration should be given to replacement by a continuous pipeline or segmented pipelines with special joints (having large contract/expansion capacity and/or anti-pull-out restraints).

9.1.2 Abrupt Deformation

As used herein, abrupt longitudinal PGD refers to ground movements with large relative offsets at localized points. The block pattern in Figure 6.1(a) is an example. In this case, the ground strain is zero away from the margins of the PGD zone, there is a tensile opening or gap at the head of the zone and a localized compressive mound at the toe. The ramp and ramp-block patterns in Figure 6.1(b) and (d) also have an abrupt offset, but for these patterns the abrupt offset is only at one end of the PGD zone.

At the head of the zone (i.e., the tension gap), pipeline failure for typical bell and spigot joints is probable. In the simplest model, all the abrupt offset is accommodated by opening at the one pipe joint closest to the head of the PDG zone. With that model, one expects joint leakage or pull-out if the ground offset (that is δ in Figure 6.1) is larger than the relative joint displacement corresponding to these limit states. For the 17 idealized block, ramp or ramp-block patterns studied by M. O'Rourke et al. (1995), the minimum abrupt offset, δ, was 1.2 m (4 ft). Typically, bell and spigot joints pull-out for this level of displacement. Hence, one expects joint pull-out in typical segmented pipe at tension gaps at least for the examples of longitudinal PGD considered by M. O'Rourke et al. (1995).

The expected behavior at the toe of the zone (i.e., at the compression mound) is different. At the toe, a number of pipe joints would lock-up in an attempt to accommodate the abrupt ground offset. As explained in more detail in Chapter 11, this joint lock-up is accompanied by a large increase in axial compression force in the pipe segments themselves, which leads to telescoping and/or crushing at the joints.

Hence, whether subject to a distributed deformation pattern or an abrupt deformation pattern of longitudinal PGD, one expects damage to ordinary segmented pipe.

One potential mitigation approach would involve the use of axially restrained joints (e.g., gasketed joints with an anti-pull-out device). For spatially distributed PGD, the restrained joints should be used throughout the PGD zone. For an abrupt pattern of longitudinal PGD, the axially restrained joints are needed at both sides of the head (tensile ground deformation area) to accommodate the offsets. As presented in the ALA Guidelines (2005), if $\acute{\Delta}$ is the relative joint displacement before the joint becomes "restrained", then the required number, n, of "chained" restraint joints near the head of the zone is:

$$n = \delta / \Delta' \tag{9.3}$$

The pipe segments and the restrained joints must be capable of withstanding the resultant axial forces. The ALA Guidelines recommend a safety factor of two. Hence, the peak axial force, largest near the center of the chain of restrained joint, is the longitudinal soil friction force per unit length, t_u, times the distance from the start of the chain to its' middle, times the safety factor:

$$F_a = 2 \cdot t_u \cdot \frac{n+1}{2} \cdot L_o \tag{9.4}$$

9.2 Transverse PGD

In considering the response of segmented pipelines subject to transverse PGD, one must differentiate between spatially distributed transverse PGD and localized abrupt transverse PGD, as sketched in Figure 7.1. Localized abrupt PGD is a special case of fault offset, which is discussed in Section 9.3.

9.2.1 Spatially Distributed PGD

For segmented pipelines subject to spatially distributed transverse PGD, the failure modes include round cracks in the pipe segments and crushing of bell and spigot joints due to the bending, and pull-out at the joint due to axial elongation (i.e., arc-length effects).

For an assumed sinusoidal variation of ground movement across the width of the PGD zone, as given by Equation 7.3 and shown in Figure 7.23, M. O'Rourke and Nordberg (1991) studied the maximum joint opening due to both joint rotation and axial extension of segmented pipelines. Figure 9.1(a) and (b) present a pipeline subject to transverse PGD, where Δx_t and $\Delta\theta$ are the joint extension and relative joint rotation between the adjacent segments.

Assuming that the pipe segments are rigid (i.e., $EA = \infty$, $EI = \infty$) and that the lateral displacement at the midpoint of the rigid pipe segment exactly matches the spatially distributed PGD at that point, they developed the relative axial displacement at a joint.

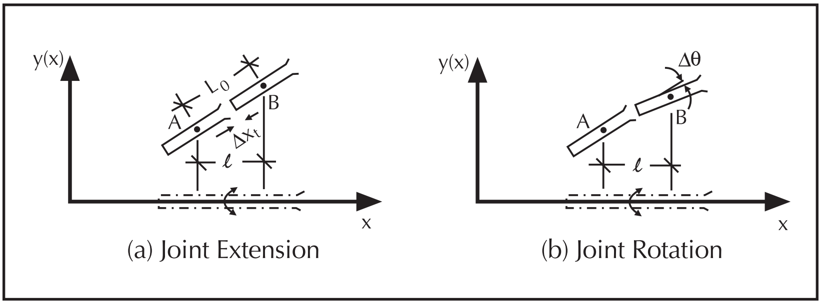

After M. O'Rourke and Nordberg, 1991

■ **Figure 9.1 Plan View of Segmented Pipeline Subject to Distributed Transverse PGD**

$$\Delta x_t = \frac{L_o}{2}\left(\frac{\pi\delta}{W}\sin\frac{2\pi x}{W}\right)^2 \tag{9.5}$$

where x is the distance from the margin of the PGD zone and L_o is the pipe segment length.

The axial displacements are largest for joints near $x = W/4$ and $3W/4$. Hence, a pure joint pull-out failure mode is most likely at the locations $W/4$ away from the center of the PGD zone. The peak axial displacement is given by:

$$\Delta x_t = \frac{L_o}{2}\left(\frac{\pi\delta}{W}\right)^2 \tag{9.6}$$

Assuming that the slope of the rigid pipe segment exactly matches the ground slope at the segment midpoint, the joint opening due to the joint rotation, Δx, is as follows:

$$\Delta x_r = \begin{cases} \dfrac{\pi^2\delta D L_o}{W^2}\cos\dfrac{2\pi x}{W} & \Delta x_t > \Delta\theta\cdot D/2 \\[2ex] \dfrac{2\pi^2\delta D L_o}{W^2}\cos\dfrac{2\pi x}{W} & \Delta x_t < \Delta\theta\cdot D/2 \end{cases} \tag{9.7}$$

where D is the pipe diameter. This function is a maximum at x = 0, $W/2$ and W. Hence, a pure joint rotation failure and/or flexural round cracks are more likely at the margins and middle point of the PGD zone.

The total maximum opening at one side of a joint, Δx due to transverse PGD, is simply the sum of axial extension plus rotation effects. However, the axial and rotational components are largest at different points as discussed previously. Combining these effects, the resulting maximum joint opening is:

$$\Delta x = \begin{cases} \dfrac{\pi^2 L_o \delta^2}{W^2}\left[\dfrac{2D}{\delta}\right] & 0.268 \le D/\delta < 3.73 \\[2ex] \dfrac{\pi^2 L_o \delta^2}{2W^2}\left[1 + (D/\delta)^2\right] & \textit{Others} \end{cases} \tag{9.8}$$

This relation for the maximum joint opening is plotted in Figure 9.2. Note that the maximum joint opening is an increasing function of both the δ/W ratio and the D/δ ratio.

The key question then is whether observed δ/W ratios and D/δ ratios are large enough to cause damage to segmented pipe. Figure 2.13 presents spatially distributed transverse PGD observed during the 1964 Niigata and 1983 Nihonkai-Chubu events. Observed values for the δ/W ratio range from 0.001 to 0.01, with 0.003 being a typical value. The amount of ground movement, δ, ranged from 0.2 to 2.0 m (0.66 to 6.6 ft), with 1.0 m (3.3 ft) being a typical value. Hence, from Figure 9.2, the corresponding maximum joint opening (i.e., using upper bound values of δ/W = 0.01 and δ = 2.0 m) would be 2.5 cm (1 in) for a pipe diameter

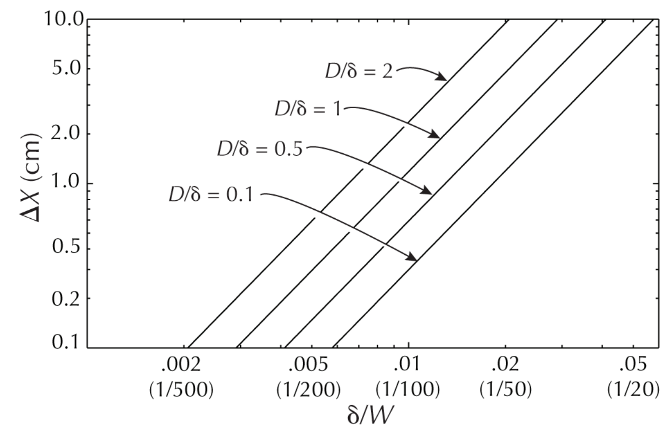

After M. O'Rourke and Nordberg, 1991

■ **Figure 9.2 Maximum Joint Opening for Segmented Pipe Subject to Distributed Transverse PGD** of 4.0 m (157 in) (i.e., $D/\delta = 2$) or less. Hence, an upper bound joint opening for transverse distributed PGD (2.5 cm) is about half the lower bound joint opening for a distributed pattern of longitudinal PGD (5.0 cm), which, in turn, is less than the lower bound for an abrupt deformation pattern of longitudinal PGD. This is all consistent with the Suzuki (1988) and the ALA (2005) observations regarding the type of PGD (longitudinal as opposed to transverse), which has led to segmented pipe damage.

Using typical values for distributed transverse PGD of $\delta/W = 0.003$, $\delta = 1.0$ m and a typical pipe diameter of $D = 0.3$ m, one calculates a maximum joint opening, Δx, of less than 0.1 cm (less than 1/16 in) using the chart in Figure 9.2. This amount of joint opening or joint closure would typically not result in damage to segment pipe joints. Some leakage is possible, however, specifically for pipelines with rigid joints. Laboratory tests by Prior (1935) suggest that the threshold for leakage in such pipelines is a joint opening of only 0.2 cm (0.08 in).

9.3 Fault Offsets

Both experimental and analytical results are available for segmented pipelines subject to fault offset (i.e., local abrupt differential ground movement transverse to the pipe axis). For example, Takada (1984) performed a laboratory test to analyze the response of segmented pipelines subject to transverse PGD. Figure 9.3 presents a sketch of the sinking soil box (dimension 10 m × 1 m × 1.5 m), in which a 169 mm (nominal 6 in) diameter Ductile Iron pipeline is surrounded by loose sand. The vertical offset is produced by decreasing the height of the six jacks, which support the movable box. Two cases were studied by Takada. In Case A, the pipeline is composed of three longer segments, while in Case B it is composed of five shorter segments.

Figure 9.4 shows the maximum pipe stress, which occurs directly over the offset, versus the ground subsidence for both cases. As shown in Figure 9.4, the stresses in the pipeline with smaller-length segments (Case B) are much less than those for large-length segments (Case A) particularly for large values of the offset.

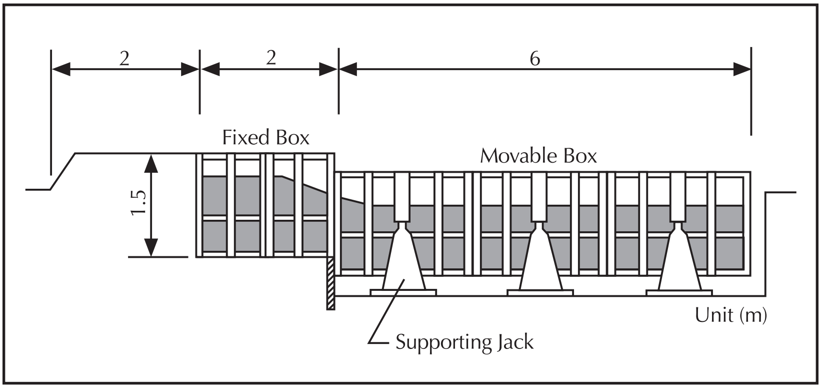

After Takada, 1984

Figure 9.3 Model Box for Segmented Pipeline Subjected to Transverse PGD

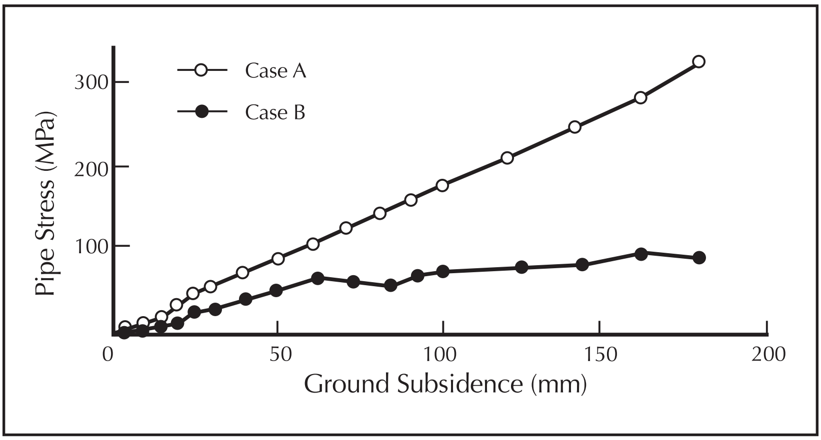

After Takada, 1984

Figure 9.4 Maximum Pipe Stress vs. Ground Subsidence for Case A and Case B

For the geometry studied by Takada, that is, a pipe at 90° with respect to the fault or offset plane, the largest stress in the pipe segments is flexural. As will be shown shortly, if one assumes rotationally flexible joints (i.e., no moment transfer across the joint), then the maximum bending moment in the pipe segment, which crosses the fault, is proportional to the pipe segment length squared. Smaller pipe stress in Case B is due, in part, to the shorter pipe segment length.

More recently, a group led by researchers from the University of Michigan subjected one-fifth scale segmented concrete pressure pipe to fault offsets using the NEES facility at Cornell University. As described in more detail by Kim et al. (2009), the individual pipe segments were roughly a meter in length (37 in), having an outside diameter of 19 cm (7.5 in) and mortar-grouted bell and spigot joints. The angle from the pipeline longitudinal axis to the fault plane (angle β in Figures 8.5(a) and 9.5) was 65°. However, unlike the right-lateral offset in Figures 8.5(a) and 9.5, the offset was left-lateral, resulting in net compression in the line. Since the joints were cement grouted they were stronger and stiffer than simple rubber gasketed, push-on bell and spigot joints, particularly when subject to axial compression. Nevertheless, the laboratory tests showed that most all the deformation occurred at the pipeline joints. That is, although the joints were stronger and stiffer than other types of joints, they proved to be weaker and more flexible than the pipe segment between the joints. The measured joint deformation in the Michigan/Cornell tests (rotation and axial compression) will be compared to simplified relations later in this chapter.

Analytical results for segmented pipes are also available. T. O'Rourke and Trautmann (1981) developed a simplified analytical method for evaluating the response of segmented pipelines subject to fault offset. They assume that the segments are rigid and the joints accommodate the ground deformation. This assumption is quite reasonable in light of the Michigan/Cornell tests mentioned above. Figure 9.5 shows the plan view of a segmented pipeline subject to fault offset. Note in this case the offset is right-lateral placing the line in net tension.

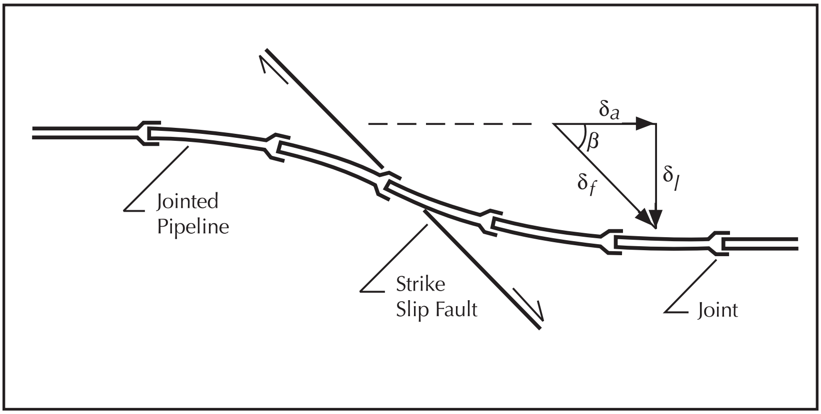

After T. O'Rourke and Trautmann, 1981

■ **Figure 9.5 Plan View of Segmented Pipeline Subject to Fault Offset**

The tolerable fault displacement can be obtained by:

$$\delta_f = \min \begin{cases} \delta_a \sec \beta \\ \delta_l \csc \beta \end{cases} \tag{9.9}$$

where δ_a is the pull-out capacity of the joint (axial deformation) near the fault offset, δ_l is the lateral deformation capacity, which depends on the joint rotation ability and is calculated by finite element simulations for typical ductile and cast iron pipelines. Note that in this formulation, all the offset is accommodated at a single joint, presumably the one closest to the fault trace.

If the intersection angle, β, is low, joint failure is due to axial effects. Conversely, if β is large lateral deformation dominates. The optimal orientation is one at which axial and lateral failures occur simultaneously. That is:

$$\beta_{optimal} = \arctan\left(\frac{\delta_1}{\delta_a}\right) \tag{9.10}$$

T. O'Rourke and Trautmann (1981) plotted the tolerable fault offset for segmented pipelines as a function of the intersection angle, as shown in Figure 9.6. Similar to the response of continuous pipelines subject to fault offset, the tolerable fault offset for pipelines with either restrained or unrestrained joints is an increasing function of β for the intersection angle less than the optimal value, and decreases thereafter. For example, the optimal intersection angle for pipe with mechanical joints is about 70°. According to T. O'Rourke and Trautmann, the decrease in capacity for $\beta > \beta_{optimal}$ is caused by the larger bending moments developed in the pipeline for large intersection angles.

Note that pipe with extra long restrained coupling are particularly effective only when the intersection angle is small. At these small intersection angles, axial effects dominant and the expansion capability of the special joints is useful. However, at large intersection angles (β > 60°) where flexural effects govern the capacity of mechanical and special joints is similar.

However, the important observation in relation to Figure 9.6 is that the tolerable offset for special pipe with long restrained joints, is less than a foot or so. For more common pipe with lead-caulked joints, the tolerable offset is about half that value. Note that these tolerable offsets are small compared to observed offsets and offsets typically specified for design. In relation to strike slip faulting, the moment magnitude corresponding to average offsets of 12 in (0.30 m) and 6 in (0.15 m) are M = 6.5 and M = 6.1, respectively, using Equation 2.1. These events are small enough that there is only a 50% chance (see Figure 2.1) that they would result in a surface offset in the first place. That is, if the event is large enough to result in a surface expression of the fault offset, the offset is typically larger than 6 to 12 in.

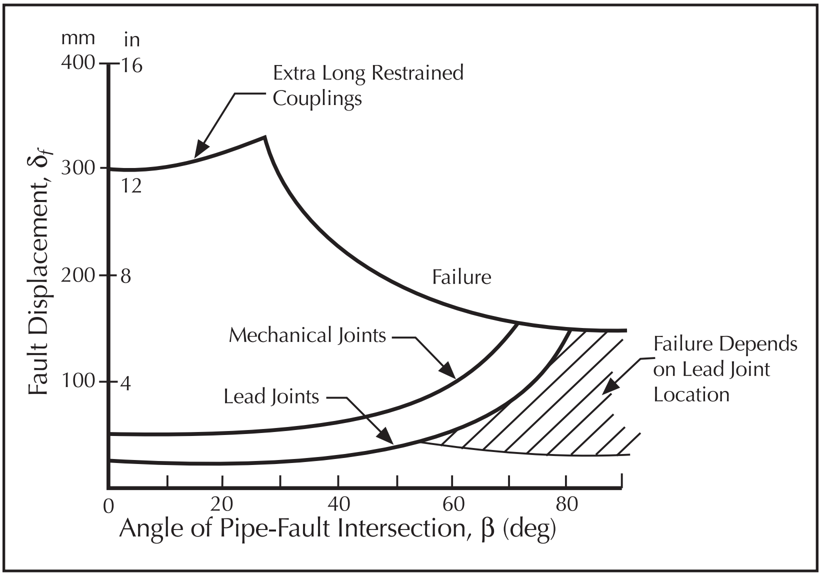

After T. O'Rourke and Trautmann, 1981

■ **Figure 9.6 Tolerable Fault Offset vs. Intersection Angle**

Similarly, in relation to localized abrupt transverse PGD such as at the margins of a lateral spread, an offset capacity of 6 to 12 in (0.15 to 0.3 m) is small compared to the observed amounts of lateral spread displacement in Figures 2.14 and 2.16. Hence, segmented pipelines are vulnerable to abrupt offsets with likely failure at the one or two joints closest to the offset location.

Other analytical relations are contained in the ALA Guidelines (2005) for segmented pipe subject to the abrupt offset hazard. Specifically, simplified relations are presented for both the bending moment in the pipe segments and the axial extension/contraction at the joints. The ALA relations envision an offset occurring exactly at the center of an individual pipe segment, as sketched in Figure 9.7. The joints are assumed flexible with respect to moment, but able to transfer shear. The offset is assumed large enough that the soil-pipe interaction force is at its maximum value, given for example in Equation 5.7 or 5.9. As such, the pipe segment is statically determinate. For the right lateral offset sketched in Figure 9.7(a) the lateral forces to the east of the fault act to the south, while those to the west act to the north. The result is a pipe segment with concave bending on one side of the fault and convex bending on the other. There is a point of counter flexure at the fault itself. The peak bending moment in the pipe is:

$$M_{max} = p_u L_o^2 / 32 \tag{9.11}$$

where p_u is the transverse force per unit length at the soil-pipe interface and L_o is the pipe segment length.

Assuming the longitudinal component of the offset is accommodated by the two joints closest to the fault, an estimate for the axial extension or contraction at each is:

$$\text{joint axial displacement} = \frac{\delta}{2} \cdot \cos \beta \tag{9.12}$$

Note that Equation 9.12 is based exclusively on the axial component of fault offset. The rotation of the pipe segment also influences the joint displacement. For an offset that results in net tension in the line, the additional joint displacement due to rotation of the center pipe segment is:

$$\text{rotation displacement} = \frac{L_o}{2} - \sqrt{\left(\frac{L_o}{2}\right)^2 - \left(\frac{\delta}{2}\sin\beta\right)^2} \tag{9.13}$$

If the offset results in net compression in the line, the increment in Equation 9.13 results in a decrease in the absolute value of the joint axial contraction. From geometry, the relative rotation at the same joint, α, is:

$$\alpha = \arcsin\left(\frac{\delta}{L_o}\sin\beta\right) \tag{9.14}$$

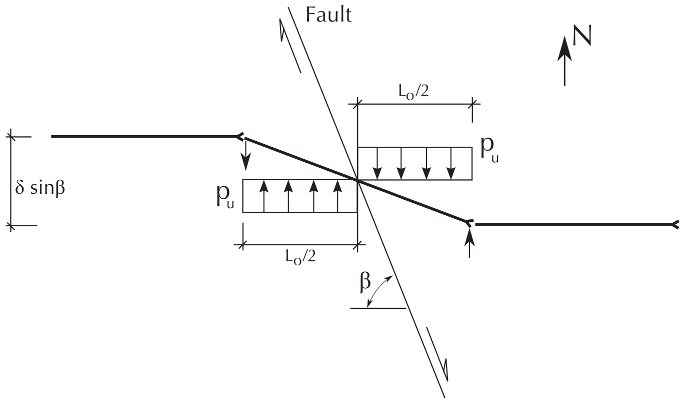

a) Plan View of Segmented Pipe with Soil-Pipe Interaction Forces

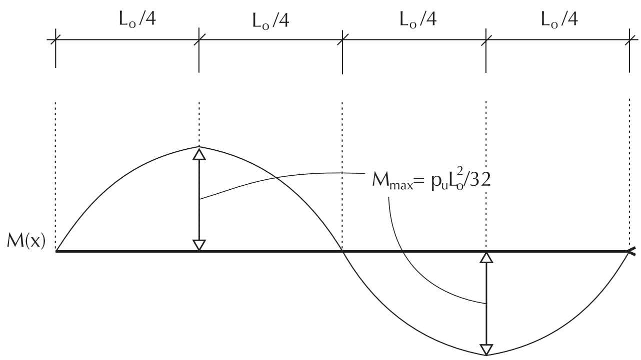

b) Bending Moment Diagram

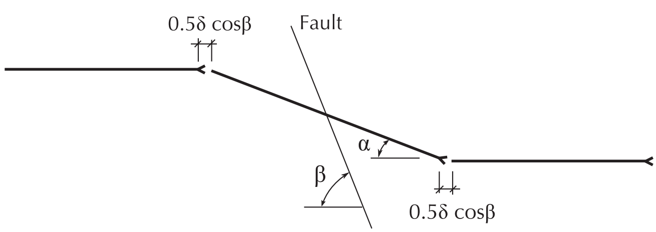

c) Joint Extension and Rotation

■ **Figure 9.7 Segmented Pipe Subject to Abrupt Offset, Offset at Segment Midpoint**

Equation 9.14 assumes that the offset, δ, is small in comparison to the pipe segment length L_o.

The offset location in Figure 9.7(a) minimizes the bending moment in the pipe segment. As the fault or offset location moves closer to the pipe joint, the bending moments increase. The worst location, in terms of pipe segment bending moment, is an offset at a pipe joint, as sketched in Figure 9.8. For that case, the whole pipe segment to the east of the fault has concave flexure while the segment to the west is in convex flexure. The point of counter flexure is at the joint itself.

The peak bending moment for the offset location in Figure 9.8 is:

$$M_{max} = {p_u L_o^2}/{8} \tag{9.15}$$

which is four times the value in Equation 9.11. Assuming the longitudinal component of the offset is accommodated by the single joint at the fault, and neglecting the influence of pipe segment rotation, the axial extension or contraction is:

$$\text{joint axial extension} = \delta \cdot \cos\beta \tag{9.16}$$

which is twice the value in Equation 9.12. From geometry, the relative rotation at the two joints adjacent to the central joint is:

$$\alpha = \arcsin\left(\frac{\delta}{2L_o}\sin\beta\right) \tag{9.17}$$

which is less than that in Equation 9.14.

Hence the offset, irrespective of its exact location with respect to the pipe segments, induces axial extension/contraction as well as rotation at the joints and flexure in the pipe segments between joints. In relation to movement at the joint, axial extension/contraction dominates for small values of the intersection angle β, while angular rotation dominates for large β. Furthermore, the joint movement demand imposed by the abrupt offset (either axial or rotational depending on the angle β) are typically much larger than the joint movement capacities discussed in Chapter 4.

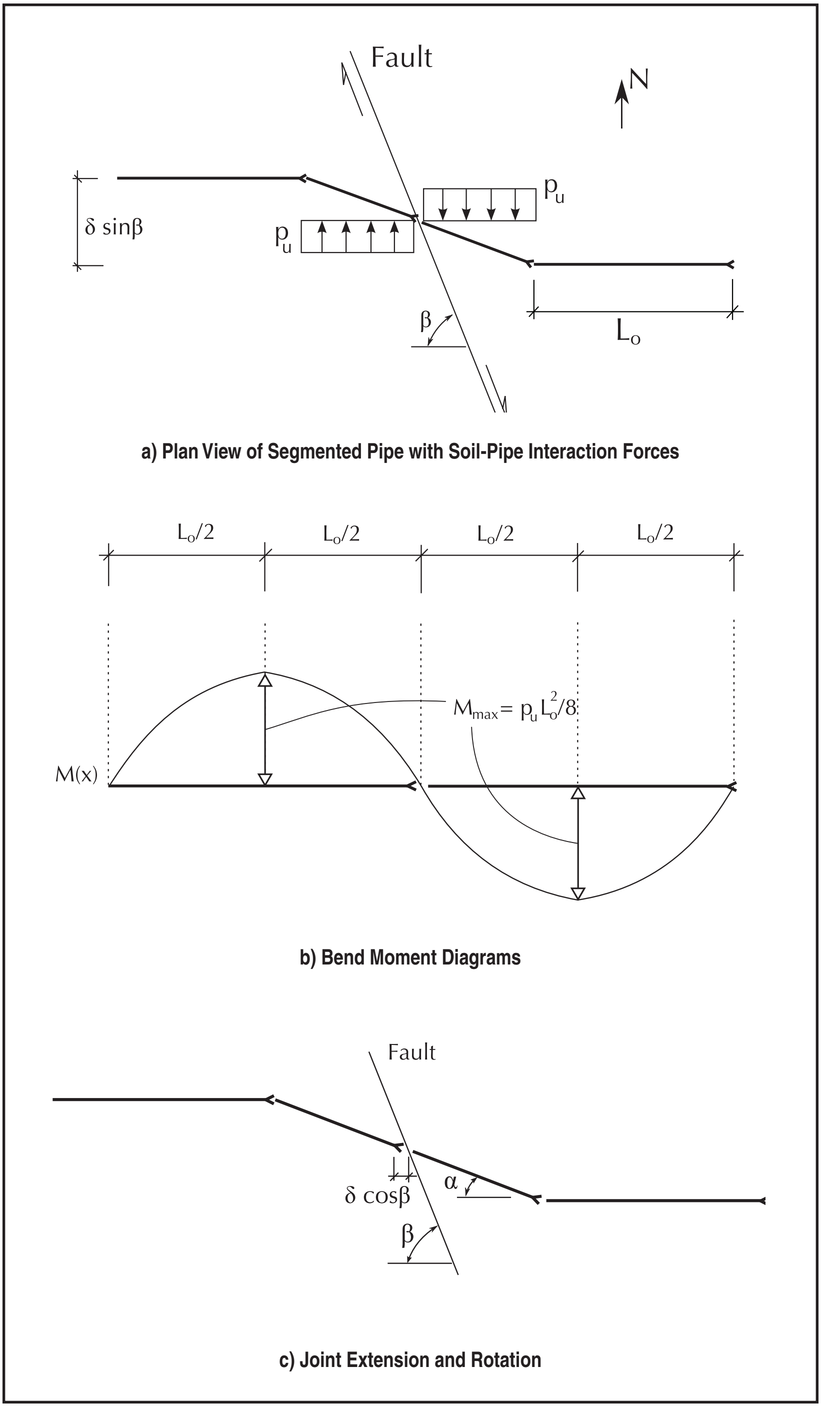

a) Plan View of Segmented Pipe with Soil-Pipe Interaction Forces

b) Bend Moment Diagrams

c) Joint Extension and Rotation

■ **Figure 9.8 Segmented Pipe Subject to Abrupt Offset, Offset at Joint**

On the other hand, the flexural capacity of typical pipe is not greatly different than the flexural demands imposed by abrupt offsets. That is, as a first approximation it seems reasonable to concentrate on the joint movement parameters as in the T. O'Rourke and Trautmann (1981) model.

The recently completed Michigan/Cornell tests allow determination of the relative accuracy of the ALA simplified relations. In these tests, the fault was located exactly at the center of the pipe segment, and as noted above the pipe segment length L_o was 94 cm and the intersection angle β was 65º (180º - 65º = 115º with respect to Figures 9.7 and 9.8). For an offset of 15.3 cm, the measured axial compression at the two joints closest to the fault were 10.8 mm and 10.2 mm. From Equation 9.12, the expected axial contraction is 32.3 mm. If one includes the rotation term in Equation 9.13, the expected value reduces to 27.2 mm. The rotation at these two joints were 11.6º and 10.5º. From Equation 9.14, the expected rotation was 8.5º.

Hence, the relation in Equation 9.12, consideration of the axial component of fault offset (or combining Equations 9.12 and 9.13) results in an overestimation of the observed joint axial contraction. It should be noted that 3.2 mm of joint compression was observed at a next joint, accounting in part for the difference between the measured joint compression (compression at three or more joints) and the expected joint compression from Equation 9.12 and/or Equations 9.12 and 9.13 (compression assumed to occur at two joints only). One expects that the relation for an axial displacement at a joint would be more accurate if the offset placed the line in net tension.

The simplified relation for joint rotation in Equation 9.14 underestimated the observed rotation by about 30%. For an offset that places the line in net compression, the joint to the west of the fault in Figure 9.7(a) would likely move a bit further to the north, while the joint to the east of the fault would move a bit further to the south. This would result in more joint rotation than envisioned in Equation 9.14. One expects that the relation for joint rotation would be more of an upper bound if the offset placed the line in net tension.

10

Response of Buried Continuous Pipelines to Wave Propagation

There have been some events, such as the 1964 Puget Sound, 1969 Santa Rosa, 1983 Coalinga and 1985 Michoacan earthquakes, for which seismic wave propagation was the predominate hazard to buried pipelines. For example, the damage ratio for the water supply system in the Lake Zone (soft soil zone) of Metropolitan Mexico City of about 0.45 repairs/km has been attributed to wave propagation effects in the 1985 Michoacan event.

As discussed in Chapter 3, when a seismic wave travels along the ground surface, any two points located along the propagation path will undergo out-of-phase motions. Those motions induce both axial and bending strains in a buried pipeline due to interaction at the pipe-soil interface. For segmented pipelines, damage usually occurs at the pipe joints. Although seismic wave propagation damage to continuous pipelines is less common, the observed failure mechanisms have been local buckling or tensile failure at weak circumferential welds.

This chapter and the next one focus on buried pipe response due to wave propagation effects. The existing methods for evaluating the response of continuous pipelines, continuous pipeline connecting buried facilities, such as tanks at treatment plants, as well as the behavior of continuous pipeline containing elbows and tees, are discussed and compared in this chapter. Chapter 11 discusses similar issues for segmented pipelines.

10.1 Straight Continuous Pipelines

Upper bound relations for axial and bending strain in continuous buried pipe were developed in Chapter 3. It was shown that the upper bound axial strain was two or three orders of magnitude larger than the upper bound bending strain. In general, the axial strain induced in a straight continuous pipeline depends on the ground strain, the wavelength of the traveling waves and the interaction forces at the pipe-soil interface. For small to moderate ground motion, one may simply assume that pipe strain is equal to ground strain. This assumption results in the aforementioned upper bound relation. However, for large ground motion, slippage typically occurs at the pipe-soil interface, resulting in pipe strain somewhat less than the ground strain.

10.1.1 Newmark's Approach

Simplified procedures for assessing pipe response due to wave propagation were first developed by Newmark (1967), and have since been used and/or extended by a number of authors (e.g., Yeh, 1974). Newmark's approach is based on three assumptions. The first assumption, which is common to most all the deterministic approaches, deals with the earthquake excitation. The ground motion (that is, the acceleration, velocity and displacement time histories) at two points along the propagation path are assumed to differ only by a time lag. That is, the excitation is modeled as a traveling wave. The second assumption is that pipeline inertia terms are small and may be neglected. Experimental evidence from Japan (Kubo, 1974), as well as analytical studies (Sakurai and Takahashi, 1969, Shinozuka and Koike, 1979), indicate that this is a reasonable engineering approximation. The third assumption is that there is no relative movement at the pipe-soil interface and, hence, the pipe strain equals the ground strain.

Figure 10.1 shows a pipeline subject to S-wave propagation in a vertical plane having an angle of incidence γ_s with respect to the vertical. For this case, the ground strain parallel to the pipe axis is:

$$\varepsilon_g = \frac{V_{max}}{V_s} \sin\gamma_s \cos\gamma_s \tag{10.1}$$

where V_{max} is the peak ground velocity and V_S is the shear wave velocity. In terms of Equation 3.5, $V_{max}\cos\gamma_S$ is the particle velocity parallel to the pipe axis and $V_S/\sin\gamma_S$ is the apparent propagation velocity with respect to the ground surface and the pipeline axis.

Similarly, for a R-wave traveling parallel to the pipe axis, the ground strain parallel to the pipe axis is:

$$\varepsilon_g = \frac{V_{max}}{C_R} \tag{10.2}$$

where C_R is the propagation or phase velocity of the R-wave.

Since, as noted above, bending strain in a pipe due to wave propagation is typically a second order effect, our attention is restricted to axial strain in the pipe. Equations 10.1 and 10.2 over-estimate pipe strain, especially when the ground strain is large. For those cases, slippage occurs at the pipe-soil interface and the pipe strain is less than the ground strain.

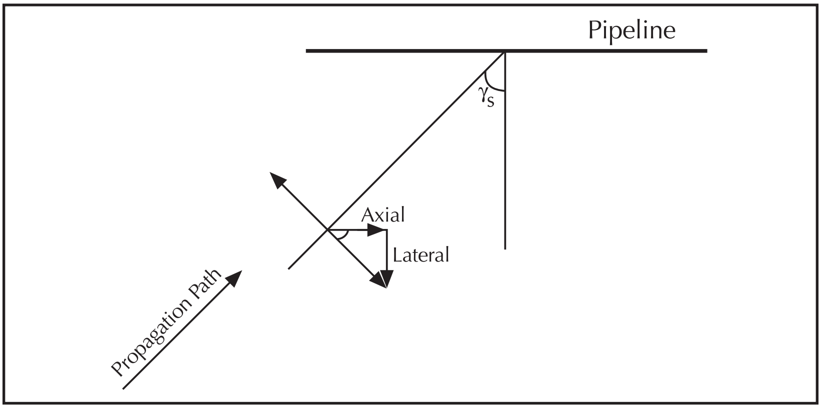

After Meyersohn, 1991

■ **Figure 10.1 Elevation View of Pipeline Subject to S-Wave Propagation**

10.1.2 Sakurai and Takahashi Approach

In relation to Newmark's assumption regarding pipeline inertia, Sakurai and Takahashi (1969) developed a simple analytical model for a straight pipeline surrounded by an infinite elastic medium (soil). They used D'Alembert's principle to handle the inertia force. For a pipeline subject to the ground displacement u_g, the equilibrium equation for a pipe element is:

$$\rho \frac{\partial^2 u_p}{\partial t^2} - E \frac{\partial^2 u_p}{\partial z^2} = K_g \left(u_g - u_p\right) \tag{10.3}$$

where u_p is the displacement of the pipeline in z direction (longitudinal direction), assumed to be the direction of wave propagation, K_g is the linear soil stiffness per unit length, as shown in Figure 5.1, and ρ is the mass density of pipe material.

The analytical results from Equation 10.3, which do not consider slippage at the pipe-soil interface, indicate that the pipe strain is about equal to free field strain and, hence, the inertia effects are negligible. This result regarding inertia terms is not surprising in light of the fact that the unit weight of a fluid filled pipe is not greatly different from that of the surrounding soil.

10.1.3 Shinozuka and Koike Approach

In relation to Newmark's assumption regarding no relative displacement at the pipe-soil interface, Shinozuka and Koike (1979) modify Equation 10.3 as follows:

$$\rho \frac{\partial^2 u_p}{\partial t^2} - E \frac{\partial^2 u_p}{\partial z^2} = \tau_s / t \tag{10.4}$$

where τ_S is the shear force at the pipe-soil interface per unit length and t is the pipe wall thickness.

Neglecting the effects of inertia, Shinozuka and Koike (1979) developed a conversion factor between ground and pipe strains. For the case of no slippage at the pipe-soil interface (i.e., the soil springs remain elastic), the conversion factor is:

$$\beta_o = \frac{1}{1 + \left(\frac{2\pi}{\lambda}\right)^2 \cdot \frac{AE}{K_g}} \tag{10.5}$$

That is, the pipe strain is β_o times the ground strain. This result holds as long as the shear strain at the pipe-soil interface, γ_o,

$$\gamma_o = \frac{2\pi}{\lambda} \frac{Et}{G} \varepsilon_g \beta_o \tag{10.6}$$

is less than the critical shear strain, γ_{cr}, beyond which slippage occurs at the pipe-soil interface. The critical shear strain as estimated by Shinozuka and Koike is:

$$\gamma_{cr} = \frac{t_u}{\pi DG} \tag{10.7}$$

In their analysis, Shinozuka and Koike (1979) assumed that the critical shear strain is 1.0×10^{-3}. That is, for $\gamma_0 \leq 1 \times 10^{-3}$, slippage will not take place, while for $\gamma_0 > 1 \times 10^{-3}$, slippage occurs at the pipe-soil interface.

For large amounts of ground movement, i.e., $\gamma_0 > \gamma_{cr}$, the ground to pipe conversion factor is:

$$\beta_c = \frac{\gamma_{cr}}{\gamma_o} q \beta_o \tag{10.8}$$

where q is a factor that ranges from 1 to $\pi/2$ and quantifies the degree of slippage at the pipe-soil interface. That is, for slippage over the whole pipe length $q = \pi/2$.

The pipe axial strain is then simply calculated by:

$$\varepsilon_p = \beta_c \cdot \varepsilon_g \tag{10.9}$$

10.1.4 M. O'Rourke and El Hmadi Approach

Also in relation to Newmark's "no relative displacement assumption," M. O'Rourke and El Hmadi (1988) use a somewhat different approach to estimate the maximum axial strain induced in a continuous pipe due to wave propagation.

Consider a model of a buried pipeline shown in Figure 10.2. The pipe has cross-sectional area A and modulus of elasticity E. The soil's resistance to axial movement of the pipe is modeled by a linear spring with stiffness K_g and a slider, which limits the soil spring force to the maximum frictional resistance t_u at the pipe-soil interface. If the system remains elastic, that is, the pipe strain remains below its yield strain and the soil spring force remains below t_u, the differential equation for the pipe axial displacement $u_p(x)$ is:

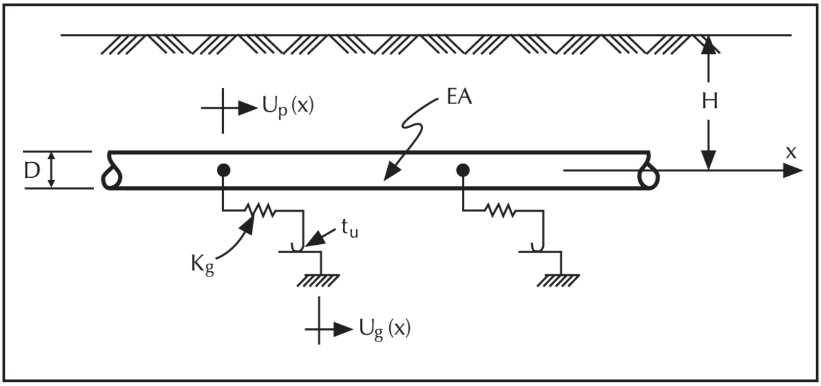

After M. O'Rourke and El Hmadi, 1988

Figure 10.2 Continuous Pipeline Model

$$\frac{d^2}{dx^2}u_p(x) - \beta^2 u_p(x) = -\beta^2 u_g(x) \tag{10.10}$$

where $\beta^2 = K_g/(AE)$ and $u_g(x)$ is the ground displacement parallel to the pipe axis.

If the ground strain between two points separated by a distance L_S is modeled by a sinusoidal wave with wavelength $\lambda = 4L_S$, the ground deformation $u_g(x)$ (i.e., displacement of the base of the soil springs) is given by:

$$u_g(x) = \varepsilon_g L_s \sin\frac{\pi x}{2L_s} \tag{10.11}$$

where ε_g is the average ground strain over a separation distance L_S.

The pipe strain is then given by:

$$\varepsilon_p = \frac{du_p}{dx} = \frac{\pi}{2}\varepsilon_g \frac{\beta^2}{\beta^2 + \left(\frac{\pi}{2L_s}\right)^2} \cos\frac{\pi x}{2L_s} \tag{10.12}$$

The elastic solution given in Equation 10.12 holds as long as the pipe strain is below its yield strain and the maximum force in the soil spring is less than the frictional resistance at the pipe-soil interface. That is:

$$\varepsilon_g\, L_s \left[1 - \frac{\beta^2}{\beta^2 + \left(\dfrac{\pi}{2L_s} \right)^2} \right] < \frac{t_u}{K_g} \tag{10.13}$$

From Equation 10.13, a slip strain ε_s is defined as:

$$\varepsilon_s = \frac{t_u}{K_g L_s} \left[\frac{\beta^2 + \left(\dfrac{\pi}{2L_s} \right)^2}{\left(\dfrac{\pi}{2L_s} \right)^2} \right] \tag{10.14}$$

For moderately dense backfill, the slip strain is plotted in Figure 10.3 as a function of separation distance L_S. In this plot, two different nominal diameters of X-60 grade pipe, D = 30 cm (12 in) and 91 cm (36 in), as well as two different burial depths, H = 0.75 m (2.5 ft) and 1.5 m (5 ft), are considered.

Since the slippage strains are less than the strains that would result in pipe damage, wave propagation damage to continuous pipe typically involves some slippage at the pipe-soil interface.

With this in mind, M. O'Rourke and El Hmadi consider the upper bound case where slippage occurs over the whole pipe length. For a wave with wavelength λ, the points of zero ground strain (Points A and B), as shown in Figure 10.4, are separated by a horizontal distance of λ/2. Assuming a uniform frictional force per unit length t_u, the maximum pipe strain at Point C due to friction is given by:

$$\varepsilon_p = \frac{t_u L_s}{AE} \tag{10.15}$$

where $L_s = \dfrac{\lambda}{4}$.

This result combined with the upper bound axial strain relation from Chapter 3 provides a simple procedure for determining axial pipe strain, ε_p, due to wave propagation:

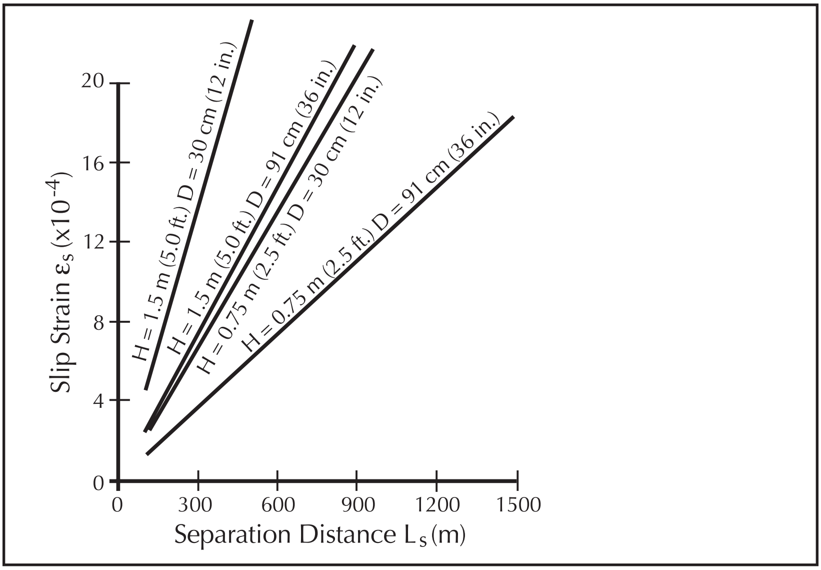

After M. O'Rourke and El Hmadi, 1988

■ **Figure 10.3 Slip Strain vs. Separation Distance for Moderately Dense Sand Backfill**

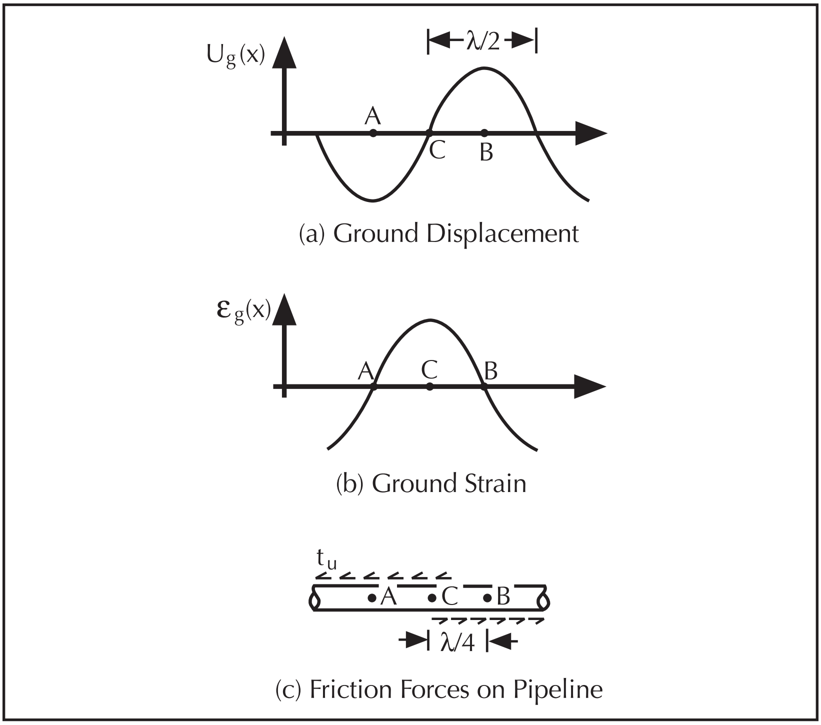

M. O'Rourke and El Hmadi, 1988

■ **Figure 10.4 Friction Strain Model for Wave Propagation Effects on Buried Pipelines**

$$\varepsilon_p = \text{smaller of} \begin{cases} \varepsilon_g \\ \dfrac{t_u \lambda}{4AE} \end{cases} \tag{10.16}$$

That is, the pipe strain equals the ground strain when the ground strain is low. However, for larger ground strains, the pipe strain is due to friction forces acting over a quarter-wavelength distance.

The relation in Equation 10.16 can be applied directly for body wave propagation since the propagation velocity and hence the ground strains are not functions of frequency or wavelength.

The situation is more complex for R-waves due to the dispersive nature of R-wave propagation (i.e., phase velocity an increasing function of wavelength). Hence, for a constant peak particle velocity the resulting soil strain is a decreasing function of separation distance or wavelength. On the other hand, the pipe strain, due to the friction at the pipe-soil interface, is an increasing function of separation distance or wavelength. At a particular separation distance (that is, for a particular wavelength), the friction strain matches the soil strain. This unique strain then becomes the peak strain which could be induced in a continuous pipeline by R-wave propagation. Figure 10.5 shows both the ground strain and the pipe strain as function of the quarter-wavelength separation distance for an elastic pipe.

As shown in Figure 10.5, for shorter quarter-wavelength separation distances, the pipeline frictional force acts over the whole length (i.e., from A to B in Figure 10.4) and, hence, the pipe strain is linearly proportional to the quarter-wavelength separation distance. However, at longer quarter-wavelength separation distances, the pipe frictional force acting only near Points A and B results in a pipe strain equal to the ground strain at Point C. Note that this procedure for R-waves conservatively assumes that the peak ground velocity, V_{max}, applies to all frequencies (wavelengths) of R-wave propagation and that all frequencies (wavelengths) are present in the record.

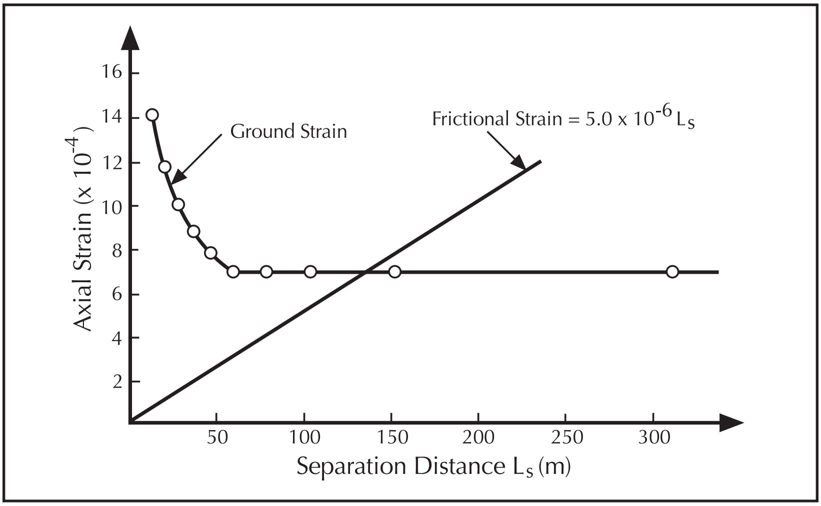

After O'Rourke and El Hmadi, 1988

■ **Figure 10.5 Frictional Strain and Ground Strain vs. Separation Distance**

10.1.5 Comparison Among Approaches

A comparison of the three approaches for a continuous pipe subject to wave propagation is presented in this subsection. The comparison is based on R-wave propagation having a dispersion curve with $\upsilon = 0.48$ shown in Figure 10.6. The peak particle velocity is taken as 0.35 m/sec. The ground strains at three frequencies, from Equation 10.2, are presented in Table 10.1 along with the estimated strain in a straight pipeline with $D = 1.07$ m (42 in) and $t = 8$ mm (5/16 in).

As shown in Table 10.1, three approaches result in essentially the same pipe strain when the ground strain is small. In this case, the pipe and soil move together and pipe strain is equal to ground strain since no slippage occurs. However, for large ground strains, the pipe strains from the Shinozuka and Koike approach as well as the M. O'Rourke and El Hmadi approach are both much less than ground strain. That is, although the ground strains are larger, the quarter-wavelength distances over which the soil friction forces act are comparatively small. Note that Shinozuka and Koike's approach for the full slippage case with $q = \pi/2$ is essentially the same as M. O'Rourke and El Hmadi's. For $q = 1$ in the Shinozuka and Koike approach, slippage occurs only over a portion of the pipe, and the corresponding pipe strains are lower bounds.

■ **Table 10.1 Comparison for Straight Continuous Pipeline**

f (Hz)	C_R (m/s)	Wavelength (m)	ε_g ($\times 10^{-3}$)	Pipe Strain ($\times 10^{-3}$)			
				Newmark	Shinozuka & Koike $q = 1$	$q = \pi/2$	O'Rourke & El Hmadi
0.2	900	4,500	0.39	0.39	0.31	0.39	0.39
0.3	137	456	2.5	2.5	0.77	1.3	1.3
0.4	92	230	3.8	3.8	0.4	0.6	0.6

10.1.6 Case Histories of Wave Propagation Damage to Continuous Pipe

Some mistakenly believe that wave propagation damage to continuous pipe does not occur. Although not common, there have been situations in the past where it has occurred. Two such case histories of wave propagation damage to continuous pipe are presented in this subsection.

10.1.6.1 1985 Michoacan Earthquake

During the 1985 Michoacan earthquake, an API 120 X-42 grade welded steel pipeline with D = 107 cm (42 in), t = 0.8 cm (5/16 in) was damaged at several locations within the Lake Zone in Mexico City. As a case study, M. O'Rourke and Ayala (1990) estimated the compressive stress in the pipe due to R-wave propagation.

Figure 10.6 shows the dispersion curve for the fundamental R-wave, corresponding to the subsoil conditions of the Lake Zone in the Mexico City (M. O'Rourke and Ayala, 1990). Note that the generalized ground profile for this site consists roughly of a 40 m layer of soft clay with a shear wave velocity of 40 m/sec. Under this layer, there are two stiffer strata with shear wave velocities of 300 and 500 m/sec, respectively. At the bottom is rock with a shear wave velocity of 1,250 m/sec.

For a pipe surrounded by loose sand with γ = 110 lb/ft^3 (17.2 kN/m^3) and a coefficient of friction μ = 0.5, the estimated compressive strain using M. O'Rourke and El Hmadi's procedure was about 0.0023 resulting from a peak velocity of about 35 cm/sec and an R-wave propagation velocity of roughly 150 m/sec. The corresponding plot of the ground strain and friction strain is shown in Figure 10.7. Note in this figure, the friction strain is proportional to the quarter wavelength (i.e., separation distance) for strains less than about 0.001 ($\lambda/4 \approx 100$ m). For larger separation distances, although the axial force is still proportional to separation distance, the strain is not since we are now in the nonlinear portion of the stress-strain diagram for the steel. The initial local buckling strain is estimated to be about 0.0026 based on D/t = 134. That is, the analytical procedure suggests that the pipeline was very close to buckling. Note that the pipeline did, in fact, suffer a local buckling failure at several locations separated by distances of 300 to 500 m (984 to 1,640 ft). This corresponds reasonably well with the 130 m (426 ft) quarter-wavelength distance in Figure 10.7. That is, high compression regions are a wavelength apart, or 520 m (1,706 ft) for the critical quarter-wavelength separation distance of 130 m (426 ft).

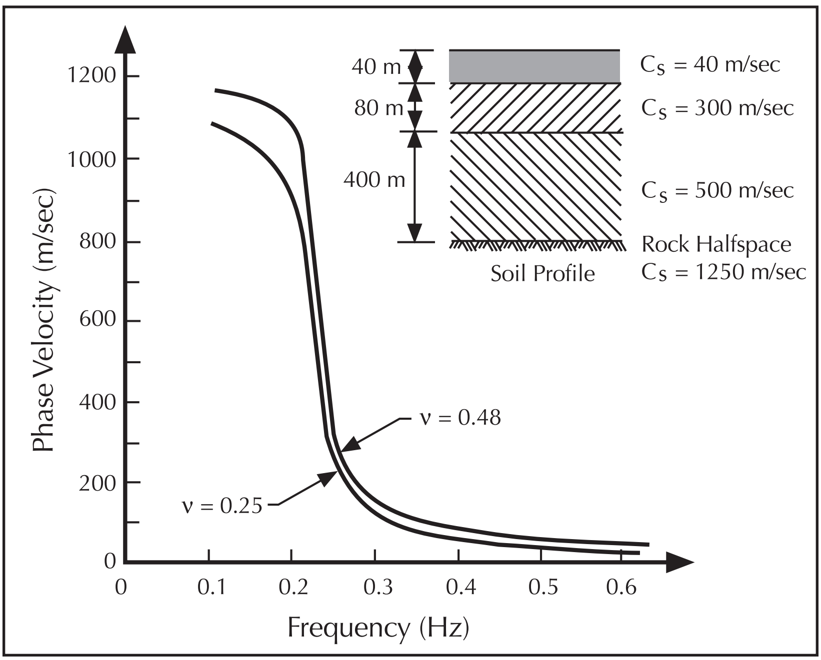

After M. O'Rourke and Ayala, 1990

■ **Figure 10.6 Dispersion Curve and Ground Profile for the 1985 Mexico Earthquake Case History**

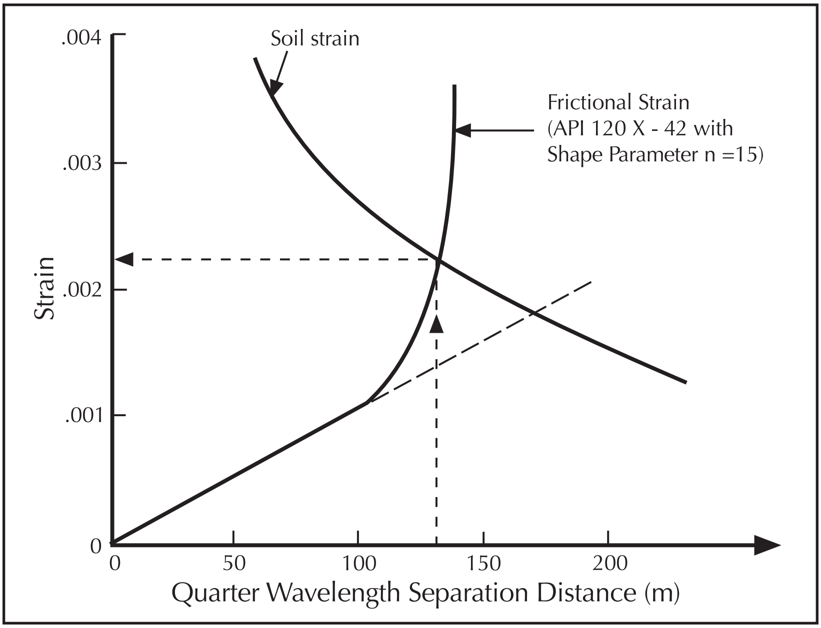

After M. O'Rourke and Ayala, 1990

■ **Figure 10.7 Soil and Friction Strain for Ciudad Nezahualcoyoti Pipeline**

10.1.6.2 1994 Northridge Earthquake

The 1994 Northridge event resulted in 21 pipe failures over a distance of 6.6 km to a 1925 gas pipeline in Potrero Canyon. Line 1001 had a nominal diameter of 12 in (30.5 cm) and a wall thickness of 0.22 in (5.6 mm) (D/t = 54). The line runs in a nominally east-west direction in the canyon. The peak ground velocity at the closest station about 5 km away (USC 56) was 1.18 m/sec. This large peak ground velocity spike occurred quite early in the record, indicating it was due to S-wave propagation. At the time of the earthquake, the operating pressure in the line was 1,690 kPa, while the most recent test pressure was 3,560 kPa.

The line had oxyacetylene girth welds which turned out to be of relatively poor quality. As described in detail by Honegger (1999, 2000), the effective ligament length (effective girth weld thickness) ranged from a low of about 1.5 mm to a high of about 7 mm, with a median value of 3.82 mm. Honegger characterized the effective ligament parameter with a lognormal cumulative distribution function. As part of the post-earthquake investigation as reported by Honegger, 30 weld specimens were tested to failure. Twenty one of the 30 specimens had a tensile strain to failure

(STF) of 0.01 or less, while nine of 30 had STF of 0.002 or less. A regression between the effective ligament length, b_{eff} in mm, and STF in microstrain resulted in:

$$\ell n(STF) = 0.468\ b_{eff} + 6.19 \tag{10.17}$$

There is a fair amount of scatter in Equation 10.17, specifically, the standard deviation of ℓn (STF) was 0.70.

The epicenter for the Northridge event was south-southeast of Potrero Canyon resulting in an angle of incidence with respect to the nominal east-west longitudinal axis of the pipeline of about 71°. However, the rupture progressed to the northeast, with the apparent center of energy release being about 12.5 km from the epicenter. From this apparent center of energy release, the angle of incidence with respect to the pipeline axis is about 36°.

As noted in relation to Equation 10.1, the angle of incidence influences the ground strain parallel to the pipe axis. Although Equation 10.1 envisions an S-wave propagating in a vertical plane with an angle of incidence with respect to the vertical axis, the same formula holds for an S-wave propagating in a horizontal plane with an angle of incidence with respect to the pipes longitudinal axis. For a given peak ground velocity V_{max} and apparent propagation velocity with respect to the ground surface C_s, an angle of incidence of 45° results in the largest ground strain parallel to the pipe axis. In that case, the ground strain is the $V_{max}/(2C_s)$. For angles of incidence of 71° and 36°, the ground strains are $V_{max}/(3.25\ C_s)$ and $V_{max}/(2.11\ C_s)$, respectively.

Based on Figure 3.9, an average value of 1,000 m/sec is used as the apparent propagation velocity S-waves with respect to the ground surface. Hence, for incidence angles of 71° and 36°, the ground strain parallel to the longitudinal axis of Line 1001 are 0.00036 and 0.00056 respectively for a peak ground velocity of 1.18 m/sec. Due to internal pressure and Poisson's ratio (taken as = 0.29), there is an additional axial strain of 0.000058. Hence, the total axial strains, wave propagation plus internal pressure, are estimated to be 0.00042 and 0.00062, respectively. These axial pipe strains are roughly four and six times larger respectively than the axial pipe strain induced by the last pressure test. Hence, one could argue that the first time the line experienced this level of axial strain was during the earthquake.

Knowing the probabilistic distribution of girth weld thickness, b_{eff}, and the relation between the b_{eff} and STF, one can calculate the probability of failure for an individual girth weld, as well as the expected number of breaks given the 1,082 girth welds over the 6.6 km length of the pipe (girth welds at 6.1 m spacing). These results are summarized in Table 10.2. Note that the expected number of failures, 17 for waves originating at the epicenter and 47 for waves originating from the apparent center of energy release, bound the observed value of 21 failures. That is, the observed numbers of failures are consistent with what one would expect from wave propagation effects on this pipeline with weak welds.

■ **Table 10.2 Pipe Strain and Probability of Failure for Potrero Canyon Case History with Peak Ground Velocity of 1.18 m/sec and Apparent Propagation Velocity of S-Waves with Respect to Ground Surface of 1,000 m/sec**

Assumed Point of Origin	Angle of Incidence in Horizontal Plane	Ground Strain Parallel to Pipe Axis	Total Pipe Strain	Probability of Individual Weld Failure	Expected Cumulative Number of Failures
Epicenter	71°	0.00036	0.00042	0.0154	17
Apparent Center of Energy Release	36°	0.00056	0.00062	0.043	47

This analysis assumes that there is enough friction at the soil pipe interface so that the axial strain induced in the buried pipe equals the ground strain. Fortunately, Honegger provides information on the adhesion factor, $\alpha \simeq 0.4$, and the undrained shear strength, $S_u \simeq 75$ kPa, for the clay soils in Potrero Canyon. Based on Equation 10.15, the distance over which the soil friction force must act to induce a ground strain of 0.00056 is only about 15 m, substantially less than the approximate 100 m minimum separation distance between observed pipe failures. That is, the soil was stiff enough to justify the $\varepsilon_p = \varepsilon_g$ assumption.

In summary, it seems clear that wave propagation has resulted in damage to continuous pipelines in past earthquakes, although it should be mentioned that Honegger (1999, 2000) has proposed an alternate overall damage mechanism for the Potrero Canyon case. However, it is not a common occurrence and requires special circumstances. For the Mexico City case history, the special circumstances were reasonably high peak ground velocity (~ 35 cm/sec), comparatively thin pipe wall (*D/t* ~134), coupled with very low R-wave propagation velocities of about 150 m/sec. In the Potrero Canyon case, the special circumstances were very high peak ground velocity (~ 1.2 m/sec) coupled with very weak girth welds.

10.2 Behavior at Treatment Plants

The general concept in Equation 10.16 can be applied to situations where a buried pipeline connects tanks, basins or other buried facilities, such as at a water treatment plant. In Equation 10.16, the pipe strain is the smaller of the ground strain or a friction strain. The ground strain controls when it is small, the wavelength is big or the pipe is relatively flexible. In that case, the pipe moves exactly with the ground. On the other hand, the friction strain controls when the ground strain is large, the wavelength is small or the pipe is relatively stiff. In that case, the soil slips past the pipe and the pipe strain is due to soil friction acting over a quarter-wavelength distance.

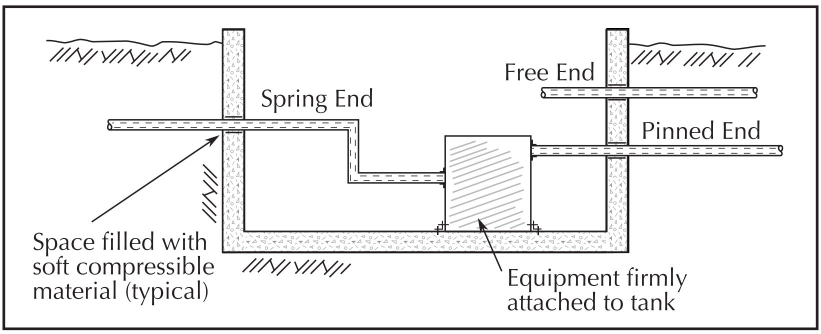

After M. O'Rourke et al., 2008

Figure 10.8 Buried Tank with Spring, Free and Pinned End Conditions at the Wall Penetration

M. O'Rourke et al. (2008) applied that concept to buried pipes at treatment plants. As sketched in Figure 10.8, they consider three idealized end conditions where the pipe intercepts the tank wall. A free end condition would occur if the buried pipe terminates upon entering the buried tank and the gap at the pipe/wall penetration is filled with soft material. This free end condition is characterized by zero pipe strain at the tank location. A pinned end condition would occur if the pipe is securely attached to equipment, such as a pump, which in turn is securely attached to the tank floor. However, the penetration of the pipe through the tank wall is still soft, allowing the pipe to rotate about a vertical or horizontal axis. Since the tank is assumed to move exactly with the ground and the end of the pipe is assumed to move with the tank, this connection is characterized by zero relative displacement between the pipe and the ground at the tank location. Finally, a spring end condition would occur if the pipe has single or multiple 90^o bends between the wall penetration and its attachment to equipment. This end condition is characterized by an axial spring between the pipe and the ground, at the tank location.

The concept of a pipe development length, L_d, is utilized to analyze response. The pipe development length equals the length over which soil friction forces must act to induce a given level of ground strain in the buried pipe:

$$L_d = \frac{AE\varepsilon_g}{t_u} \tag{10.18}$$

If L_d is greater than the "available" length, the pipe is underdeveloped and friction strain controls.

M. O'Rourke et al. (2008) present analytical relations for the peak pipe strain, the anchorage force at the tank wall for pin and spring connections, and the relative displacement at the wall for free connections. This is done for each of the six possible combinations of end conditions: free-free, free-pin, etc.

For example, Figure 10.9 shows the distribution of soil friction forces and the displacement of both the pipe and soil for an underdeveloped pipe (pipe development length L_d greater than the "available" length L_s) with free-pin end conditions. The force at the pin connection is:

$$F_p = t_u \cdot L_s \tag{10.19}$$

where L_s is the separation distance between the tanks. The peak pipe strain is:

$$\varepsilon_p = \frac{t_u L_s}{AE} \tag{10.20}$$

Figure 10.10 shows the same quantities for a fully developed pipe (i.e., $L_d \leq L_s$) with free-pin end conditions. In a fully developed pipe, the axial pipe strain equals the ground strain ε_g and the force at the pin connection is:

$$F_p = E \cdot A \varepsilon_g \tag{10.21}$$

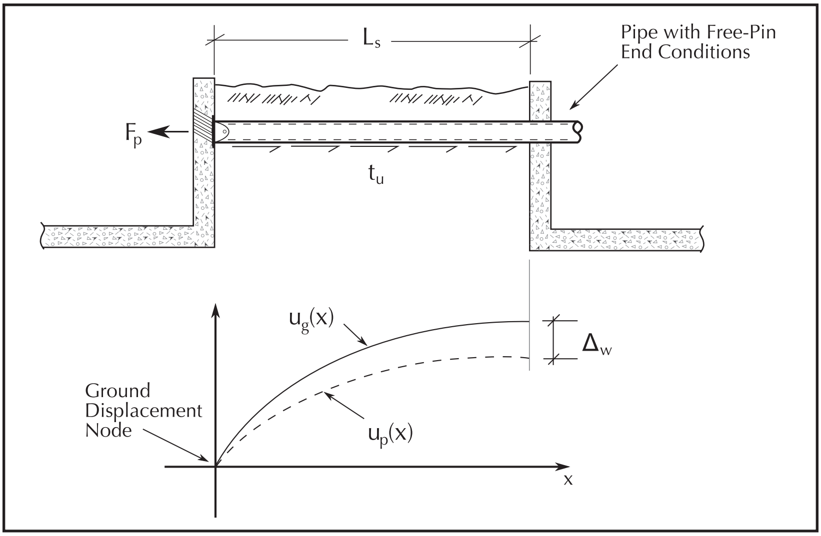

After M. O'Rourke et al., 2008

Figure 10.9 Underdeveloped Pipe with Free-Pin End Conditions

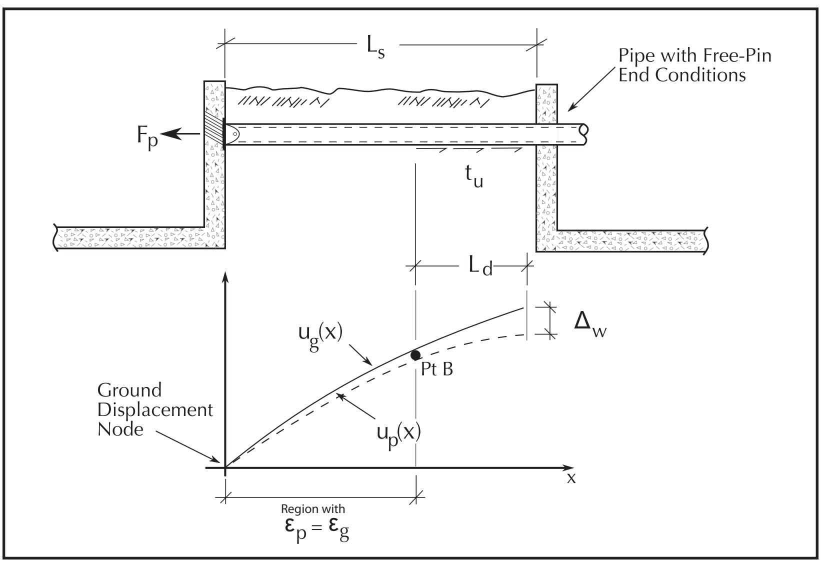

After M. O'Rourke et al., 2008

Figure 10.10 Fully Developed Pipe with Free-Pin End Conditions

10.3

Bends and Tees

A pipe network is typically composed of straight pipeline sections, and interconnecting bends, tees and crosses. The presence of these elements can produce additional bending strains at these interconnects and possibly lead to pipe damage. This section will focus on the effects of bends and tees for buried pipe subject to wave propagation effects.

10.3.1 Shah and Chu's Approach

Considering the interaction forces at the pipe-soil interface, Shah and Chu (1974), as well as Goodling (1983), developed analytical formulae for forces and moment at elbows and tees. Figure 10.11 shows the forces acting on a pipeline and pipe deformation near the bend. The traveling wave is assumed to be propagating parallel to Leg 1 with ground motion also parallel to Leg 1 (e.g., R-wave propagation parallel to Leg 1). Leg 2 is modeled as a beam on an elastic foundation with lateral soil stiffness K_g.

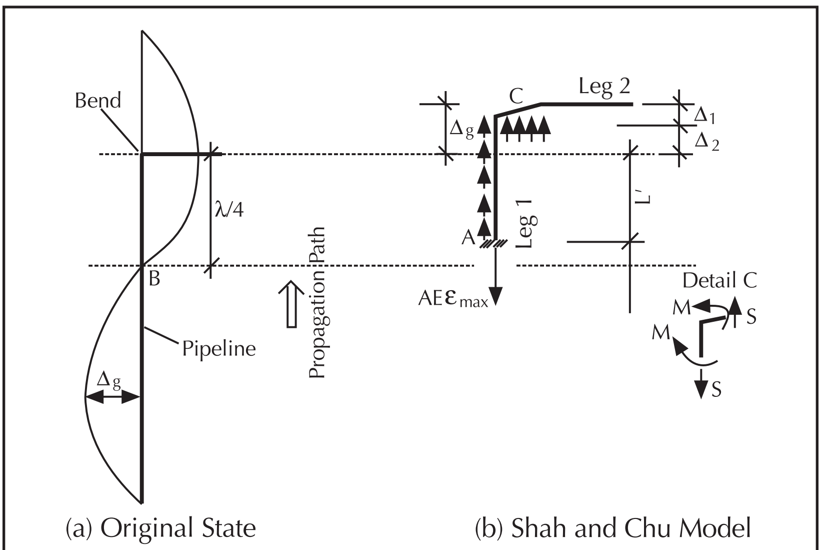

After Shah and Chu, 1974

■ **Figure 10.11 Displacement and Forces in a Pipe with an Elbow**

Shah and Chu (1974) assumed that the pipe and ground strains are equal at a location (Point A in Figure 10.11(b)) where no relative displacement occurs at the pipe-soil interface. Denoting the distance from this location to the bend, as L' shown in Figure 10.11, Shah and Chu (1974) as well as Goodling (1983) then estimated the maximum axial force in Leg 1 at the bend (shear force in Leg 2) by:

$$S = \varepsilon_{max} AE - t_u L' \tag{10.22}$$

The moment and flexural displacement at a bend can then be calculated as:

$$M = \frac{S}{3\zeta} \tag{10.23}$$

$$\Delta_1 = \frac{4\zeta S}{3K_g} \tag{10.24}$$

where $\zeta = \sqrt[4]{K_g /(4EI)}$ and L' is the effective slippage length at the bend.

The effective slippage length, L', can be calculated based on displacement compatibility at the bend. That is, within the distance L', total ground deformation (taken as $\varepsilon_{max} L'$) is accommodated by the lateral displacement of Leg 2, Δ_1, and axial deformation of Leg 1, $\frac{SL'}{AE} + \frac{t_U L'^2}{2AE}$. For a long leg case (i.e., long Leg 1), this compatibility condition yields:

$$L' = \frac{4AE\zeta}{3K_g} \left(\sqrt{1 + \frac{3\varepsilon_{max} K_g}{2t_u \zeta}} - 1 \right) \tag{10.25}$$

Similarly, Figure 10.12 shows the forces and deformation for a tee, again for a wave propagating path parallel to Leg 1.

Using the same procedure as that for bends, Shah and Chu estimate the force, moment and displacement for a tee by the following equations:

$$S = \varepsilon_{max} AE - t_u L' \tag{10.26}$$

$$M = \frac{S}{2\zeta} \tag{10.27}$$

$$\Delta_1 = \frac{\zeta S}{K_g} \tag{10.28}$$

$$L' = \frac{AE\zeta}{2K_g}\left(\sqrt{1+\frac{4\varepsilon_{max}K_g}{t_u\zeta}}-1\right) \tag{10.29}$$

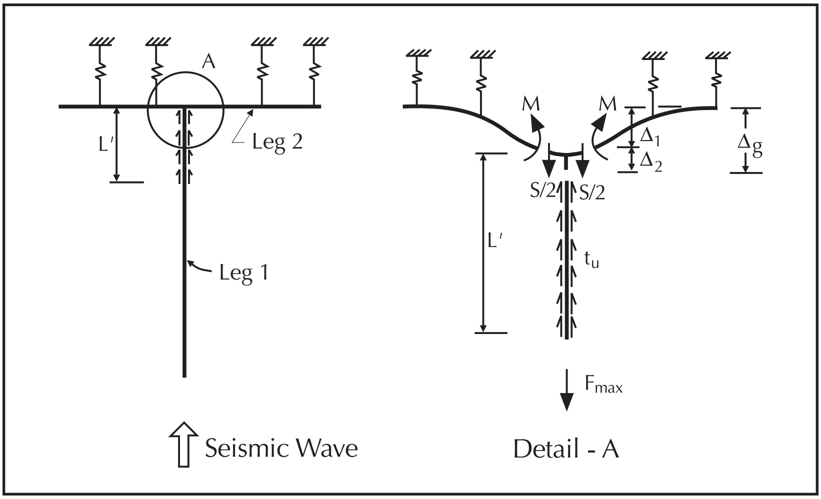

After Gooding, 1983

■ **Figure 10.12 Representation of Forces, Moments and Displacement at a Tee**

Note that Shah and Chu (1974) as well as Goodling (1983) assume pipe strain is equal to the maximum ground strain at Point A (Figure 10.11). Based upon the previous discussion of straight pipe response to wave propagation, this assumption is likely only true for small ground strains. Furthermore, they estimate the total ground displacement simply by the maximum ground strain times the effective length L'. This implies that the ground strain is constant over the length L', which only applies for a wavelength many times larger than the length L'.

10.3.2 Shinozuka and Koike's Approach

Assuming a pipe moving with the soil at the location with zero ground movement (Point B in Figure 10.13), Shinozuka and Koike (1979) developed simple equations to estimate pipe strain at bends based on structural analysis similar to that discussed above. In their analysis, the effective length, that is, the L' term, is assumed to be a quarter wavelength, and the forces are obtained, as in the previous model, by displacement compatibility at the bend. The axial force, S, can be then expressed by:

$$s = \frac{3\lambda}{8\pi} \cdot \frac{K_g}{\zeta} \cdot \frac{1}{1+Q}\left(1-\beta_c\right)\varepsilon_g \tag{10.30}$$

where $Q = \dfrac{3}{16}\dfrac{K_g\lambda}{AE\zeta}$

The moment and displacement at the bend can then be calculated by Equations 10.23 and 10.24. Note that the total ground

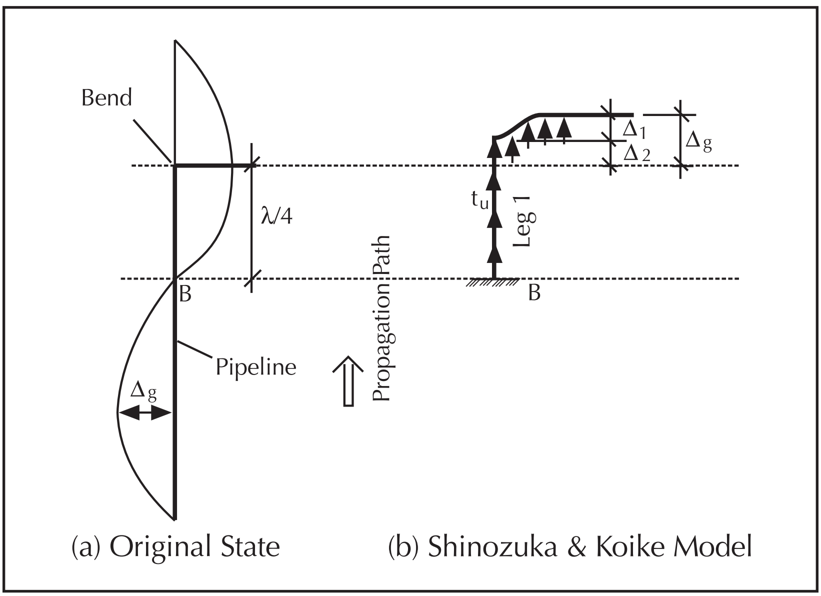

After Shinozuka and Koike, 1979

■ **Figure 10.13 Displacement and Forces in a Pipe at an Elbow** deformation within the quarter wavelength is calculated by integrating the pipe strain. That is:

$$\Delta_g = \frac{\lambda}{2\pi} \cdot \varepsilon_{max} \tag{10.31}$$

Similarly, the axial force S in Leg 1 for a tee is:

$$S = \frac{\lambda}{2\pi} \cdot \frac{K_g}{\zeta} \cdot \frac{1}{1+\frac{4}{3}Q}\left(1-\beta_c\right)\varepsilon_g \tag{10.32}$$

10.3.3 Finite Element Approach

In order to independently evaluate the assumptions which underlay the existing approaches, the finite element model shown in Figure 10.14 was used. In this numerical model, axial and lateral soil springs are used to model the interaction at the pipe-soil interface. Leg 1 is 600 m long and, hence, considered appropriate for a wavelength of roughly 600 m or less. The quasi-static seismic excitation is modeled by displacing the bases of the soil

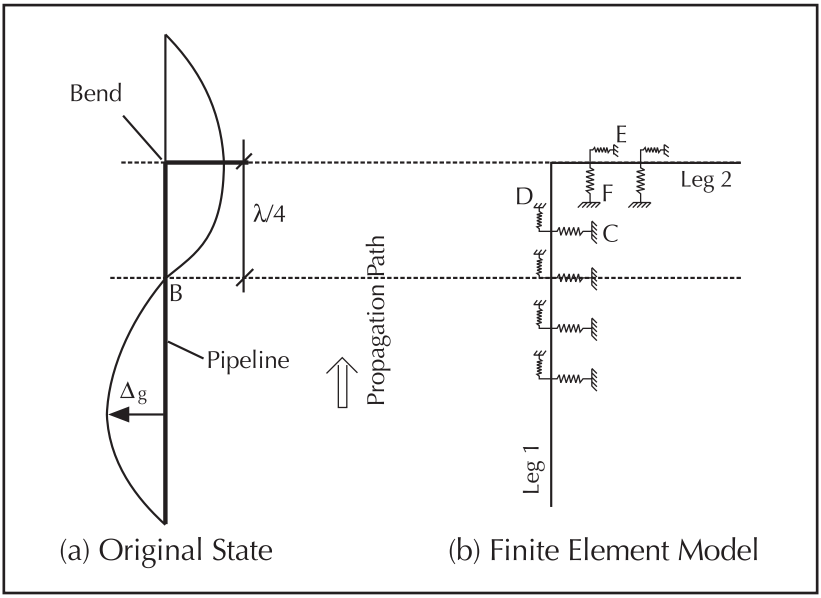

Figure 10.14 FE Model for Elbow Subject to Wave Propagation

springs. For example, Point F moves Δ_g in the direction of wave propagation, while Point E does not move. For Leg 1, the movement of the bases (e.g., Point D) of the longitudinal soil springs varies along the pipe matching the sinusoidal pattern, as shown in Figure 10.14(a).

A steel pipe with diameter D = 0.76 m (30 in), wall thickness t = 0.0095 m (3/8 in) is considered. The assumed seismic excitation is an R-wave with V_{max} = 0.36 m/sec propagating parallel to Leg 1.

10.3.4 Comparison Among Approaches

Results from the finite element approach described in Section 10.3.3 are compared to the existing analytical approaches in this section. For an elbow, the force, moment and displacement at the elbow due to traveling wave effects are listed in Table 10.3 using the Shah and Chu approach, the Shinozuka and Koike approach, as well as the finite element approach described above. Note that two cases are considered in Table 10.3. In this first case (Case I), the ground strain and wavelength are taken as 0.29×10^{-3} and 244 m, respectively. While in Case II, $\varepsilon_g = 1.8 \times 10^{-3}$ and λ = 100 m.

From Equation 10.25, the effective length for the large ground strain, small wavelength case is 233.3 m by the Gooding/Shah and Chu approach. Since this effective length is much larger than a quarter wavelength, that approach cannot be used. Note that the effective length by Shinozuka and Koike matches relatively well with the finite element results for both cases considered here.

As shown in Table 10.3, for a small ground strain case, the peak pipe strain at the elbow by Shah and Chu is larger than that by both Shinozuka and Koike and the finite element method. This is due to the fact that Shah and Chu overestimate the ground deformation, and simply assume the maximum pipe strain equal to maximum ground strain. On the other hand, Shinozuka and Koike's approach underestimates the pipe strain at the elbow. This is due to the fact that the axial soil stiffness they suggested ($K_g = 2\pi G = 2\pi\rho C_s^{\,2} = 4.1 \times 10^9$ N/m^2 (595 kips/in^2)) is much larger than that ($K_g = t_u/x_u = 8.3 \times 10^6$ N/m^2 (1.2 kips/in^2)) in the finite element model. For example, by using $K_g = 8.3 \times 10^6$ N/m^2 (1.2 kips/in^2) in Shinozuka and Koike's approach, for the small ground strain case, the peak strain at the elbow is estimated to be 4.9×10^{-5}, which matches the numerical strain (4.5×10^{-5}) very well.

■ **Table 10.3 Comparison for Bend**

Approach	Case	λ (m)	ε_g ($\times 10^{-3}$)	Effect Length (m)	Δ_g (cm)	Δ_1 (cm)	S (*N*)	M ($N \cdot m$)	Peak Strain
Goodling, Shah & Chu	II	244	0.29	42.8	1.24	0.61	4.2×10^4	5.9×10^4	1.4×10^{-4}
	I	100	1.8	233.3	-	-	-	-	-
Shinozuka & Koike	II	244	0.29	$61(\frac{\lambda}{4})$	1.1	.001	71.8	100.6	0
	I	100	1.8	$25(\frac{\lambda}{4})$	2.9	2.4	1.64×10^5	2.3×10^5	5.5×10^{-4}
Finite Element	II	244	0.29	60	1.1	0.3	3.2×10^4	3.7×10^4	4.5×10^{-5}
	I	100	1.8	23.6	2.9	2.4	1.9×10^5	2.9×10^5	5.9×10^{-4}

10.3.5 Generalized Behavior at an Elbow

Table 10.3 suggests that the Shinozuka and Koike approach, with the appropriate soil spring stiffness, K_g, yields apparently reasonable results. However, that approach, as well as those of Shah and Chu, and Gooding, assumes elastic behavior of the transverse soil springs (e.g., soil spring *F* in Figure 10.14 (b)). McLaughlin (2003) investigated the overall behavior and determined that the introduction of inelastic behavior in the transverse soil springs did not markedly change the resulting pipe strains. This again verifies the Shinozuka and Koike model.

McLaughlin (2003) and McLaughlin and M. O'Rourke (2009) presented results in a manner which clarified the overall behavior. For example, Figure 10.15 shows pipe strain at an elbow (primarily bending strain) and peak pipe strain away from the elbow (primarily axial strain) plotted versus ground strain. Figure 10.15 shows results for a 0.61 m (24 in) diameter pipe with 1.27 cm (0.5 inch) wall thickness subject to R-Wave propagation with a peak particle velocity of 36 cm/sec (14.5 in/sec), a wavelength of 500 m (1,650 ft), and a period of 1.0 second.

Notice that the peak pipe strain away from the elbow follows the behavior in Equation 10.16. That is, at low ground strains, ε_g less than about 0.5×10^{-3} in this case, the pipe strain matches the ground strain. While at higher ground strain $\varepsilon_g > 0.5 \times 10^{-3}$ in this case, axial slippage at the soil pipe interface occurs and the pipe strain away from the elbow has reached the friction strain limit (constant with increasing ground strain).

As one might expect, the pipe strain at the elbow is quite low prior to slip at the soil-pipe interface ($\varepsilon_g < 0.50 \times 10^{-3}$ in this

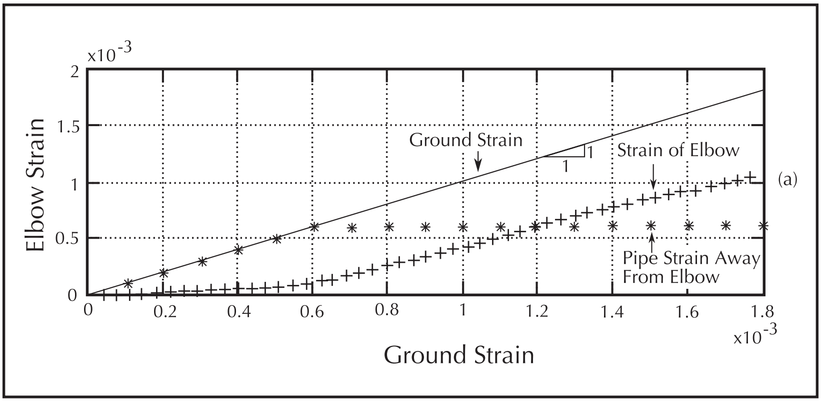

After McLaughlin and M. O'Rourke et al., 2009

■ **Figure 10.15 Pipe Strain at an Elbow and Pipe Strain Away From an Elbow for Increasing Ground Strain**

case). After slip, the elbow strain increases at a rate slightly less than the ground strain. As a result, the elbow strain matches the pipe strain away from the elbow ($\varepsilon_p \simeq 0.6 \times 10^{-3}$) at a ground strain of about 1.2×10^{-3} (slightly more than twice the slippage strain). Hence, for the pipe properties in Figure 10.15, the friction strain is an upper bound for wave propagation induced elbow strain. At larger ground strains (due in all likelihood to some sort of PGD), the elbow strain keeps increasing, but, at least for this case, is always less than the ground strain. McLaughlin and M. O'Rourke (2009) determined the elbow strain for buried pipeline models with pipe diameter ranging from 0.3 to 0.9 m (12 to 36 in), burial depths ranging from 0.9 to 1.35 m (3 to 4.5 ft), pipe wall thickness ranging from 6.3 to 12.7 mm (0.25 to 0.50 in) and wavelength ranging from 460 to 3,050 m (1,500 to 10,000 ft). For ground strains up to 0.2% (expected upper bound range for ground strains due to wave propagation), the elbow strain in almost all cases was less than the ground strain. In the worst case, (thick pipe wall, shallow burial depth and short wavelength) the elbow strain was at most 1.25 ε_g.

This suggests the following simple rules of thumb. For continuous pipe subject to wave propagation, the peak pipe strain away from an elbow is the lesser of the ground strain and the friction strain. At an elbow, the induced strain is less than 1.25 ε_g.

11

Response of Segmented Pipelines to Wave Propagation

As noted previously, seismic wave propagation has caused damage to segmented pipelines. Damage, particularly for larger pipe diameters, most frequently occurs at joints. The corresponding failure modes include pull-out at joints and crushing of bell-spigot joints. For smaller diameter pipe, circumferential cracking due to bending is also a frequent failure mode. In this chapter, analytical approaches for estimating the behavior of joints in straight segmented pipelines are reviewed. Observed expansion/contraction behavior of joints at elbows and connections is also presented.

11.1 Straight Pipelines/Tension

For a long straight run of segmented pipe, the ground strain is accommodated by a combination of axial strain in the pipe segments themselves and relative axial displacement (expansion/contraction) at pipe joints. As noted by Iwamoto et al. (1984), since the overall axial stiffness for segments is typically much larger than that for the joints, ground strain results primarily in relative displacement at the joints. As a first approximation, assuming that the pipe segment axial strain can be neglected (i.e., rigid segment) and that all joints experience the same movement, the maximum relative movement Δu at a typical joint is:

$$\Delta u = \varepsilon_g \cdot L_o \tag{11.1}$$

where L_o is the pipe segment length and ε_g is the maximum ground strain parallel to the pipe axis given, for example, by Equation 3.5 or 3.7.

For ground motion perpendicular to the pipe axis, the maximum relative rotation at pipe joints can be estimated by:

$$\Delta\theta = K_g \cdot L_o \tag{11.2}$$

where K_g is the maximum ground curvature given, for example, by Equation 3.6. Equation 11.2 assumes that the bending strain in the pipe segments is small and that all joints experience the same relative joint rotation.

In relation to the rigid segment assumption, Wang (1979) determined the joint deformation and pipe strain using an analytical model shown in Figure 11.1 in which the joint is modeled as a linear spring with axial stiffness K_j.

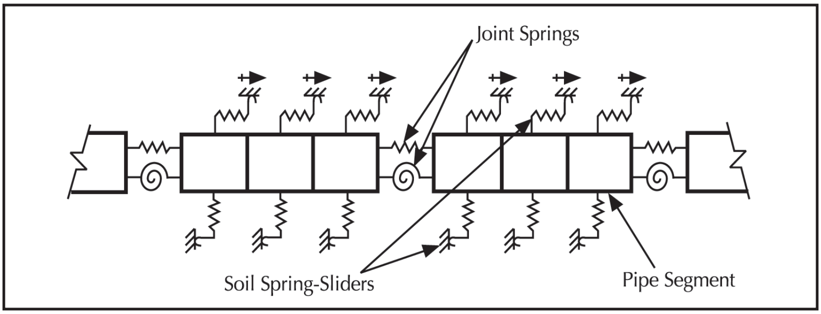

After Wang, 1979

Figure 11.1 Model of Segmented Pipelines

Figures 11.2 and 11.3 present the joint opening and maximum axial strain at pipe segments respectively, as a function of joint stiffness for the east-west component of the 1940 El Centro event. The assumed pipe diameter is 45.7 cm (18 in), the pipe segment length is 6.1 m (20 ft), the axial soil spring has a stiffness of 23.4 MPa (3,400 lbs/in^2) and the propagation velocity is taken as 244 m/sec (800 ft/sec). As one expects, the joint opening is a decreasing function of the joint stiffness while the pipe strain is an increasing function of joint stiffness. That is, for a small joint stiffness, the ground deformation is accommodated primarily by joint opening.

The peak ground velocity for the record used by Wang is 0.37 m/sec, and the value given by Equation 11.1 is close to the upper bound joint opening of 0.85 cm (0.32 in) in Figure 11.2.

The Wang model correctly captures the trend of decreasing joint opening with increasing joint stiffness. However, it assumes an equivalent linear joint stiffness while laboratory tests suggest

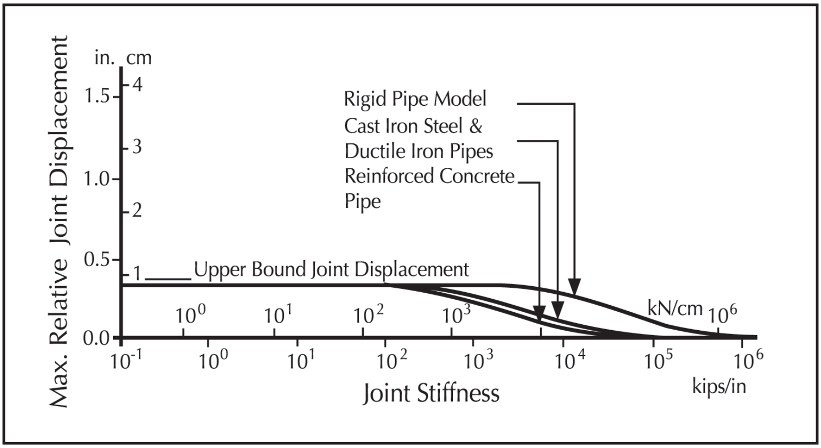

After Wang, 1979

Figure 11.2 Joint Opening Due to Wave Propogation vs. Joint Stiffness

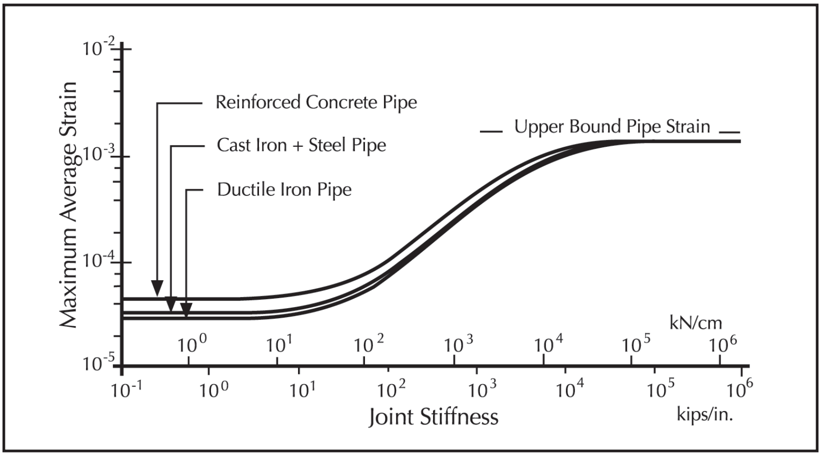

After Wang, 1979

Figure 11.3 Maximum Axial Strain at Pipe Segments vs. Joint Stiffness

that joint axial behavior is non-linear. More importantly, for a given stiffness, the relative displacement at each joint in the model is the same. That is, it does not capture the variation in displacement from joint to joint. This variation from joint to joint is considered important since, as will be discussed in greater detail in Chapter 12, even for relatively large amounts of wave propagation damage, only a few joints require repair. That is, since it is reasonable to assume some variation in response from joint to joint, the few joints with the largest response control the damage as opposed to the many joints with "average" response.

Consider the model in Figure 11.4 in which a segmented pipeline is subject to uniform tensile ground strain along the pipeline axis. The ground and pipe displacements are shown as a function of distance along the pipeline axis. Since the ground strain is uniform, the ground displacement is a straight line with slope ε_g. As a simplifying assumption, the pipe segments between the joints are considered rigid. Therefore, all the ground strain is accommodated by relative displacement (expansion) at the joints.

Figure 11.4(a) shows the condition where the strength and stiffness are exactly the same at each joint. The relative displacement Δu at each joint is the same as given Equation 11.1, and hence the tensile force at each joint, F_j, is also the same, corresponding to Δu.

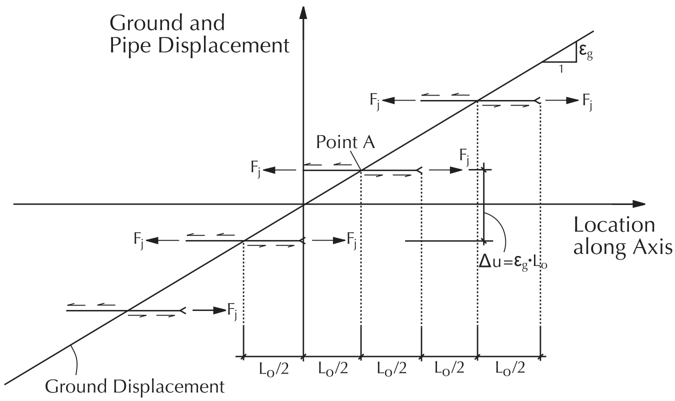

a) Pipeline Model with Identical Joint Properties

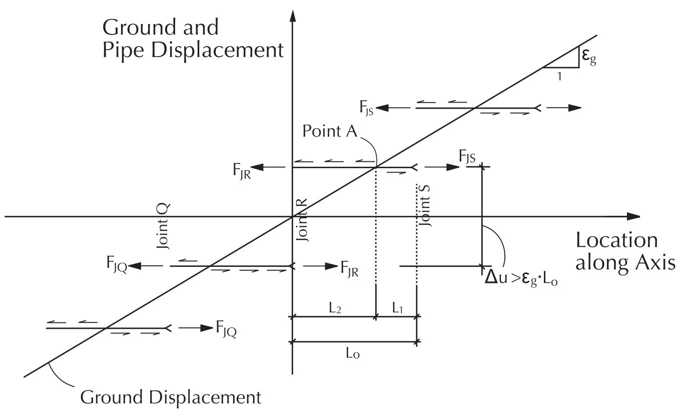

b) Pipeline Model with Flexible Joint R at Origin

Figure 11.4 Model with Rigid Pipe Segments Subject to Uniform Ground Strain

The rigid pipe segment displacement matches the ground displacement at the middle of the pipe segment (e.g., at Point A). Hence, for that segment the ground displacement is larger than the pipe displacement for points to the right of Point A. This results in soil pipe interaction forces tending to pull the pipe segment to the right. Conversely, for that same pipe segment the ground displacement to the left of Point A is smaller than the pipe displacement, resulting in soil friction forces tending to pull the pipe to the left. Herein we assume the soil friction force per unit length is t_u as given, for example in Equation 5.1 or 5.3. Hence, each pipe segment is in equilibrium with axial tensile force F_j at the end (i.e., at the joint) and an axial tension force $F_j + L_o \cdot t_u/2$ at the center.

As one increases the ground strain, each joint experiences the same increasing joint displacement and joint force. At a specific level of ground strain, the force reaches its maximum value. At that point, all the joints would fail simultaneously. That is, with a uniform joint properties model, all joints are undamaged up to a specific level of ground strain, and all joints fail beyond that ground strain level.

Now consider the model in Figure 11.4(b) in which Joint R is substantially more flexible (less stiff) than the others. Being less stiff, the axial force at the joint F_R, would be somewhat less than those at Joints Q and S. Since the pipe segment still needs to be in the equilibrium, the location along the pipe segment where the rigid pipe segment displacement matches the ground displacement would no longer be at the center of the segment. Considering the pipe segment between Joints R and S, Point A is now somewhat to the right of the middle. Hence, the soil friction forces tending to pull the pipe segment to the right act over a shorter distance ℓ_1 ($\ell_1 < L_o/2$) while those tending to pull the pipe to the left act over a larger distance $\ell_2 = L_o - \ell_1$ ($\ell_2 > L_o/2$), resulting in equilibrium of the pipe segment in the axial direction.

$$F_R + \ell_2 t_u = \ell_1 t_u + F_S \tag{11.3}$$

Note that, as a result, the joint opening at the flexible joint is larger than average:

$$\Delta u_R = 2 \cdot \ell_2 \cdot \varepsilon_g > L_o \cdot \varepsilon_g \tag{11.4}$$

while the joint displacement at Q and S are a bit smaller than average.

For the non-uniform joint model in Figure 11.4(b), eventually the ground strain, which varies with time and location, will be large enough to cause a failure at the flexible joint. However, unlike the uniform joint model, in this case the neighboring joints survive. Once the weak joint fails, that joint may be regarded as a completely flexible joint (incapable of transmitting axial tension force). As such, joint displacements tend to accumulate at the failed joint and there is less axial force at the neighboring joints.

With this in mind, El Hmadi and M. O'Rourke (1990) considered a model somewhat similar to that in Figure 11.4(b), in which the joint properties vary from joint to joint and the soil properties vary from pipe segment to pipe segment. Specifically, a cast iron pipe with lead-caulked joints subject to tensile ground strain was considered. The assumed force-deformation relation for the joint in tension is shown in Figure 11.5. The expected variation in the joint slippage force, F_S, was based upon results by T. O'Rourke and Trautmann (1980).

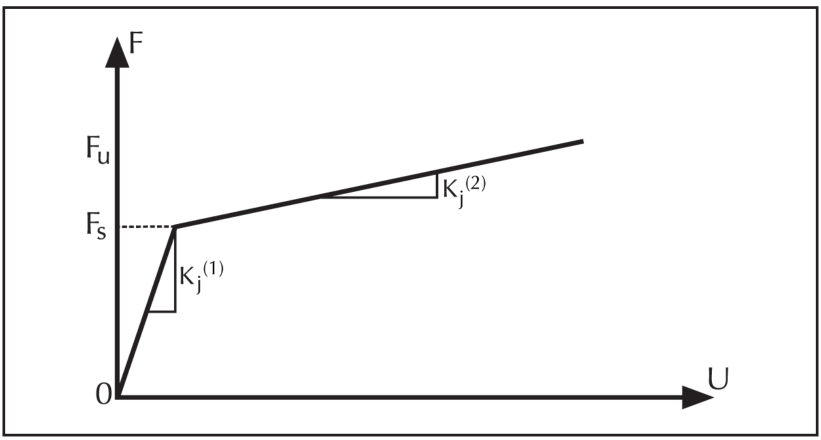

After El Hmadi and M. O'Rourke, 1990

■ **Figure 11.5 Axial Force-Displacement Curve for a Lead-Caulked Joint**

A quasi-static approximation to the seismic wave propagation environment is modeled by displacing the base of the soil spring sliders in the longitudinal direction. The tensile ground strain, ranging from 0.01 to 0.7%, accounts for variations in the earthquake magnitudes and site conditions. A simplified Monte Carlo simulation technique is used to establish the characteristics of the force-displacement relationships at each joint and soil restraint along each pipe segment. Figure 11.6 shows the joint deformation as a function of ground strain for a segmented pipe with a diameter of 0.41 m (16 in).

As shown in Figure 11.6, the average joint displacement is approximately equal to the product of the ground strain times the pipe segment length. However, for the data in Figure 11.6, one in a 100 joints (1% probability of exceedance) have joint displacement about three times the average value, while for the 0.1% exceedance probability (one in a 1,000), the joint opening is about five times the average. Based upon these results, the ALA *Guidelines for Seismic Resistant Water Pipeline Installations* (2005) requires that segmented pipeline joints be able to accommodate seven times the average joint displacement given in Equation 11.1. The ALA expectation is that this would result in damage to no more than one in 10,000 joints.

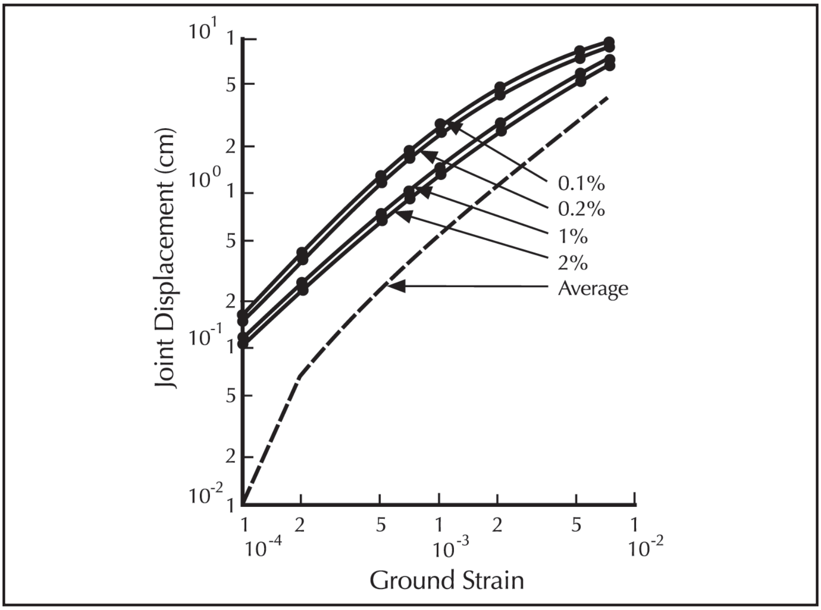

After El Hmadi and M. O'Rourke, 1990

■ **Figure 11.6 Relative Joint Displacement vs. Ground Strain for 41-cm Diameter Cast Iron Pipe with Lead-Caulked Joints**

Theoretically, this information, coupled with the probability of leakage as a function of the normalized joint opening, as shown in Figure 4.12, would allow one to estimate joint pull-out damage (repair per kilometer) as a function of ground strain. However, such an approach requires joint information, typically derived from laboratory tests, on the expected variability of joint properties.

El Hmadi and M. O'Rourke found that the variability of joint displacement was a decreasing function of pipe diameter. That is, at larger diameters, the joint displacements with 1% and 0.1% probability of exceedance were closer to the average value. This suggests that the damage ratio (repair/km) for joint pull-out in a cast iron pipe with lead-caulked joints is a decreasing function of pipe diameter. As such, this is consistent with a trend observed by Honegger (1995). The topic of diameter effects is discussed in more detail in Section 12.4.

11.2 Straight Pipelines/Compression

Extensive damage to concrete pipelines has occurred when these elements are subject to compressive ground strain. For wave propagation resulting in compressive ground strain, the failure mode of interest is crushing (i.e., telescoping) at pipe joints. For concrete pipelines, the pipe wall thickness, diameter and concrete strength were used to establish the joint crushing force, as discussed in Section 4.3.2. Figure 11.7 presents the force-displacement relationship for a 30-in-diameter reinforced concrete cylinder (RCC) pipe joints subject to compressive load. This relation is based upon a series of laboratory tests on RCC pipe with rubber gasketed joints by Bouabid (1995).

These tests indicate that the joint behaves in a sigmoidal fashion before "lock-up" (at about 0.3 inches, as shown in Figure 11.7). The joint compressive displacement, Δu_{ult}, at lock-up typically ranges from 0.125 to 0.375 in (0.32-0.95 cm), with corresponding loads of 3.5 to 4.5 kips (16-20 kN).

When subject to compressive ground strain ε_g, the response of a segmented pipe is complicated by this "lock-up" behavior. That is, before lock-up, the average joint contraction is given by Equation 11.1. If a particular joint has somewhat less stiffness than the others, its contraction will be somewhat larger than the average, as demonstrated for tensile ground strain by Figure 11.4(b).

However, unlike tensile behavior, a joint under compression does not experience significant contraction beyond "lock-up." That is, as shown in Figure 11.7, when a joint is fully closed we

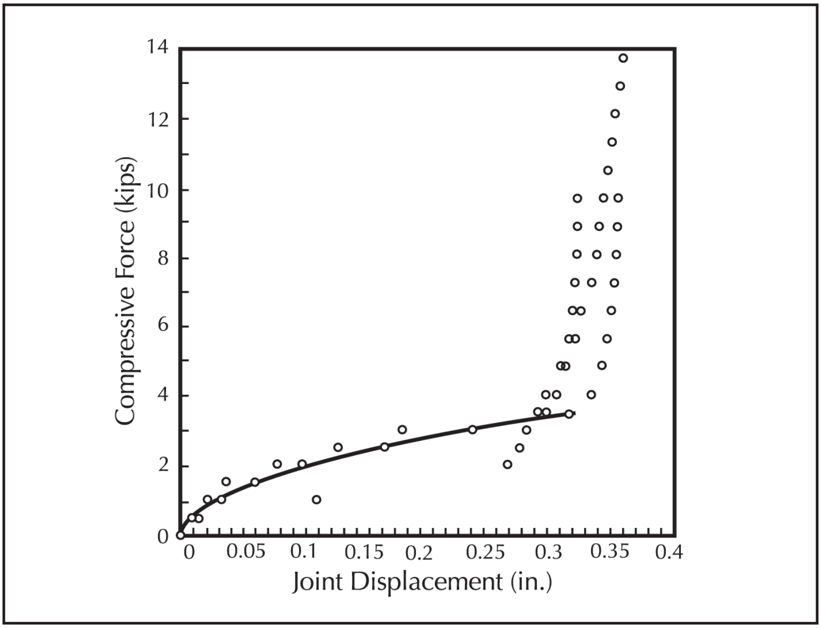

After Bouabid, 1995

■ **Figure 11.7 Force-Displacement Relationship for Reinforced Concrete Cylinder Pipe Joints**

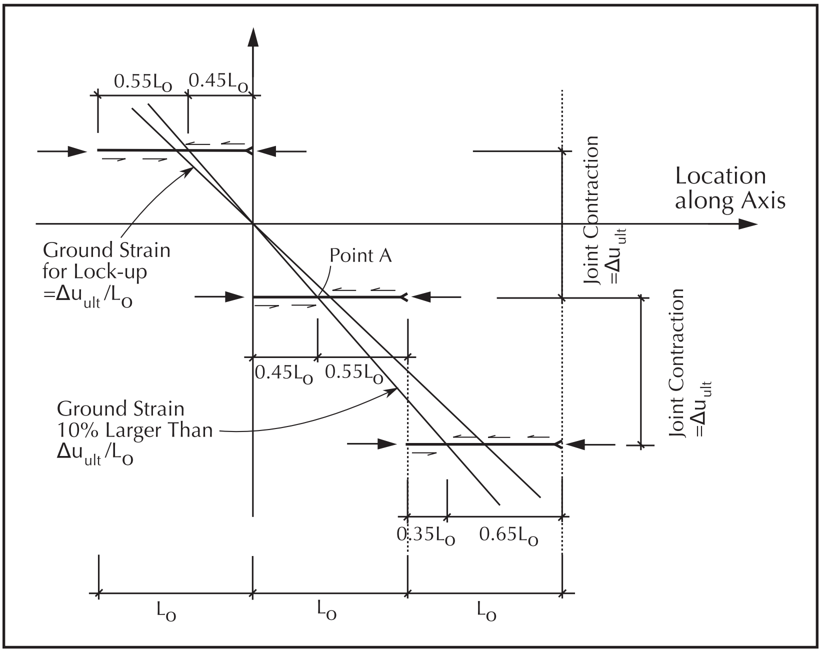

■ **Figure 11.8 Model with Rigid Pipe Segments Subject to Uniform Compressive Ground Strain Beyond Joint Lock-up** get large increases in compressive joint force with little or no increase in relative joint displacement. This results in a non-uniform distribution of compressive joint force after lock-up, even for a model with uniform properties (stiffness and lock-up displacement) from joint to joint.

Consider a model shown in Figure 11.8 of a segmented pipeline, with rigid segments and uniform joint properties, subject to compressive ground strain. For a pipe segment length of about 5.5 m (18 ft), one expects lock-up at each joint for a ground strain of:

$$\varepsilon_g = \Delta u_{ult} / L_o \tag{11.5}$$

or about 0.139% using Δu_{ult} = 0.3 in, as given in Figure 11.7. The force at each joint would be about 3.5 kips, again from Figure 11.7. For a 30-in-diameter pipe with a depth to the centerline of the pipe (H) of 4 ft, buried in sand with effective unit weight (γ) of 110 pcf and an angle of shear resistance (ϕ) of 40°, the friction force per unit length t_u from Equation 5.1 is 2.9 kips/ft for $k_o = k = 1.0$. Note that at initial lock-up, the ground displacement at the segment midpoint matches the rigid pipe displacement. Hence, there are soil friction forces to the right of the midpoint tending to push the pipe segment to the left, and soil friction forces to the left of the midpoint tending to push the rigid pipe segment to the right. These soil friction forces balance, the pipe segment is in equilibrium and the peak compressive force at the middle of each pipe segment is 3.5 kips + 2.9 kips/ft (18′/2) = 29.6 kips.

In this condition a modest increase in ground strain results in a very large increase in compressive force in the pipe. Assume the ground strain increases only 10% above that for lock-up ($\varepsilon_g \simeq$ 0.153%). Due to lock-up, the pipe segments do not displace since all the joints are fully closed. Hence, the ground displacement line no longer intersects each pipe segment at its midpoint. As sketched in Figure 11.8, for the two pipe segments closest to the center of the ground compression zone, the ground displacement intersection (Point A) is now at 0.45 L_o from the left end. Due to the unbalanced soil friction forces, the axial force at the left joint is 0.10 (18′)(2.9 k/ft) = 5.2 kips larger than that at the right joint. The intersection point for the next pipe segment is 0.35 L_o from the left end, leading to more unbalanced of the soil friction forces, and a larger difference between the joint force at the left (higher) and right (lower) ends. At the sixth segment from the center and all those further, the ground displacement line no longer intersects the pipe segment and those segments have soil friction forces all pushing in the same direction. The axial force in the sixth pipe segment is therefore due to soil friction acting on all pipe segments between it and the end of the compressive ground strain zone.

For the wave propagation hazard, the distance from the center of the ground strain zone to the end of the zone is a quarter wavelength. Assuming the wavelength is 2,000 ft, the quarter wavelength distance is 500 ft and the distance from the sixth segment to the end of the zone is 500 - 6 (18) = 392 ft. Again, for a soil friction force of 2.9 kips/ft, the axial compression force at the sixth segment is 1,140 kips and somewhat larger and closer to the center of the zone. That is, in this example, with uniform properties from joint to joint, the axial compressive force in the pipe segment increased from 29.6 kips to over 1,140 kips, for an increase of 10% in ground strain (ε_g increase from 0.139% to 0.155%).

This behavior is illustrated by fragility relations developed by M. O'Rourke and Bouabid (1996) using Monte Carlo techniques. Figure 11.9 shows the relations for three types of concrete pipe subject to axial compression. These three pipes are a 30-in-diameter reinforced concrete cylinder pipe (30″ RCC), a 48-in-diameter prestressed lined cylinder pipe (48″ LCP) and a 60-in-diameter prestressed embedded cylinder pipe (60″ ECP).

In this case, the variation in joint crushing thresholds was based upon the cross-sectional area near the joint and an assumed normal distribution of concrete strength (mean strength of 5 ksi (34.5 MPa) and 7% coefficient of variation).

Notice that the larger diameter pipe is the least vulnerable, possibly reflecting the larger ground strain for lock-up of these pipes with deeper joints. For all three pipes there is a dramatic increase in estimated damage ratio for modest increases in compressive ground strain. For the 48″ LCP line, there is roughly a three order of magnitude increase in simulated damage ratio for roughly a 25% increase in ground strain (from 0.20% to 0.25%). Hence, these simulated damage ratios mirror what one theoretically expects for lock-up behavior of pipe with the same properties from joint to joint, that is, the behavior in Figure 11.8. However, as will be establish in Chapter 12, observed damage to buried pipe does not show this step behavior—little or no damage below a threshold ground strain, essentially complete damage for ground strain somewhat above the threshold. On the contrary, observed

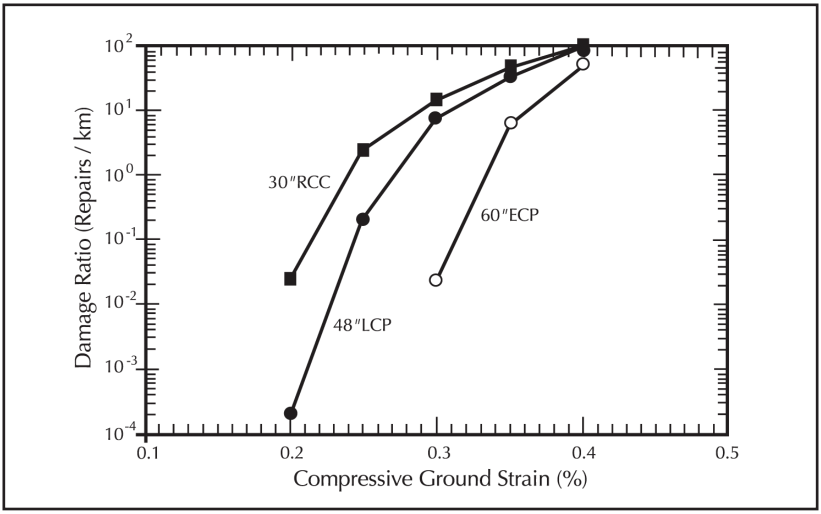

After M. O'Rourke and Bouabid, 1996

Figure 11.9 Analytical Fragility Curves for Concrete Pipe Subject to Compressive Ground Strain

damage to buried pipe is essentially a linear function of ground strain. That is, it seems that a pipeline model with variability in properties from site to site and from joint to joint is more likely to simulate observed behavior. In that model damage occurs at locations with ground high strains, particularly at weak or flexible joints, with no damage at nearby joints. Note in this regard, that in the M. O'Rourke and Bouabid model, the failure force varied from joint to joint but not the lock-up displacement. It is expected that a Monte Carlo simulation with the lock-up displacement varying from joint to joint would result in more realistic fragility relations.

11.3 Elbows and Connections

There appears to have been relatively little analytical research on the wave propagation behavior of bends and elbows in segment pipe systems. However, measurements by Iwamoto et al. (1985) suggest that joint openings at bends and elbows are, in fact, different from those in long straight runs of pipe. For example, Figure 11.10 shows observations at three sites (Kansen, Hakusan and Shimonaga) in Japan.

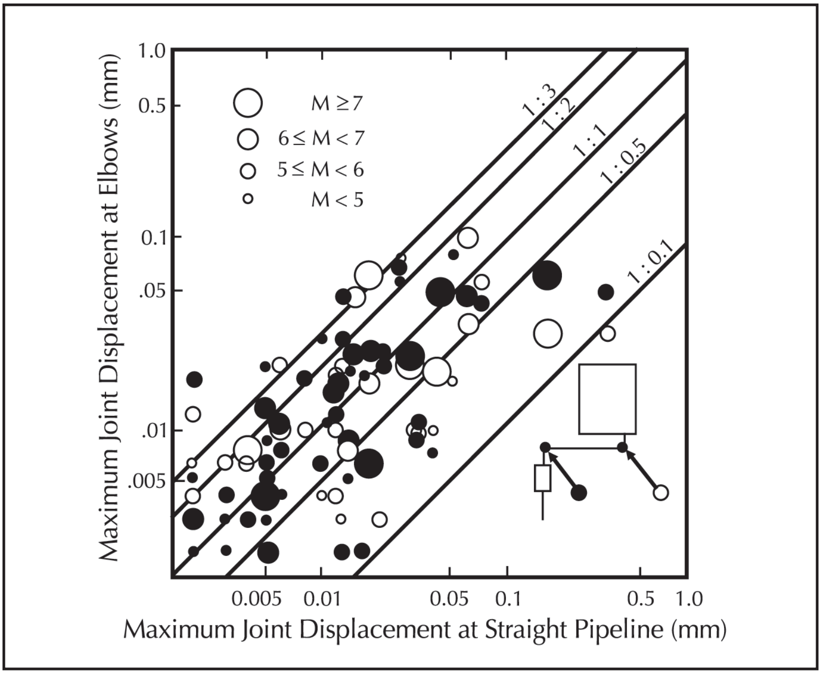

After Iwamoto et al., 1985

■ **Figure 11.10 Observed Joint Displacement and Amplification Factor for Elbows**

For various events, the maximum expansion/contraction at an elbow is plotted versus the corresponding expansion/contraction for joints in a straight run. In some cases, the response on the elbow joint was only a tenth of that for a straight pipe joint. However, in other cases, presumably for other angles of incidence, the elbow joint response was three times larger than the straight joint response.

For pipe design purposes, it seems reasonable to use three as the amplification factor for joint openings at bends, relative to the maximum joint opening induced in corresponding straight pipelines. Iwamoto et al. (1985) also measured expansion/contraction for joints adjacent to valve boxes. As shown in Figure 11.11, the behavior is similar to that at elbows in that an amplification factor of three seems appropriate, particularly for large ground strains (i.e., when the corresponding straight pipe response is larger).

Similar information from Iwamoto et al. (1985) is presented in Figure 11.12 for joints adjacent to buildings. However, in this case, the amplification factor is as large as 10.

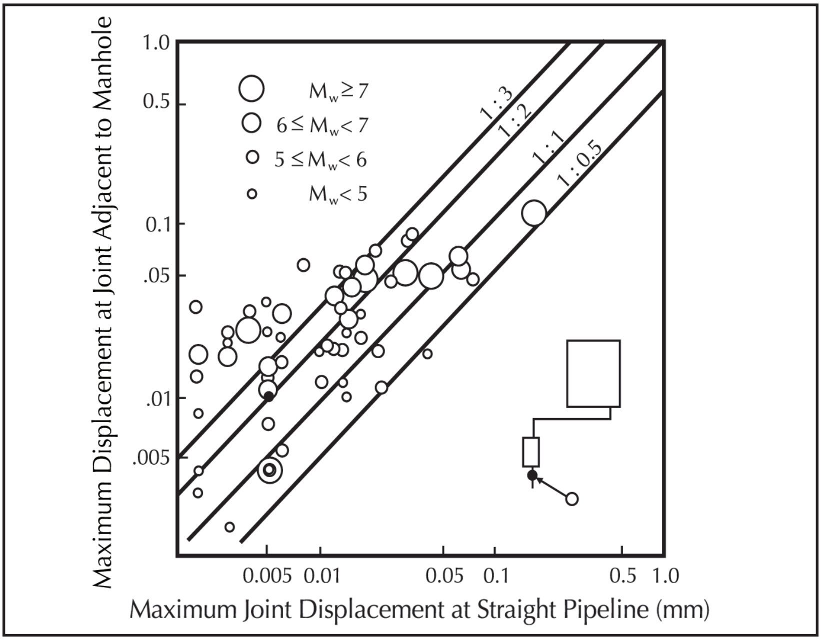

After Iwamoto et al., 1985

■ **Figure 11.11 Observed Joint Displacement and Amplification Factor at Joint Adjacent to Manhole**

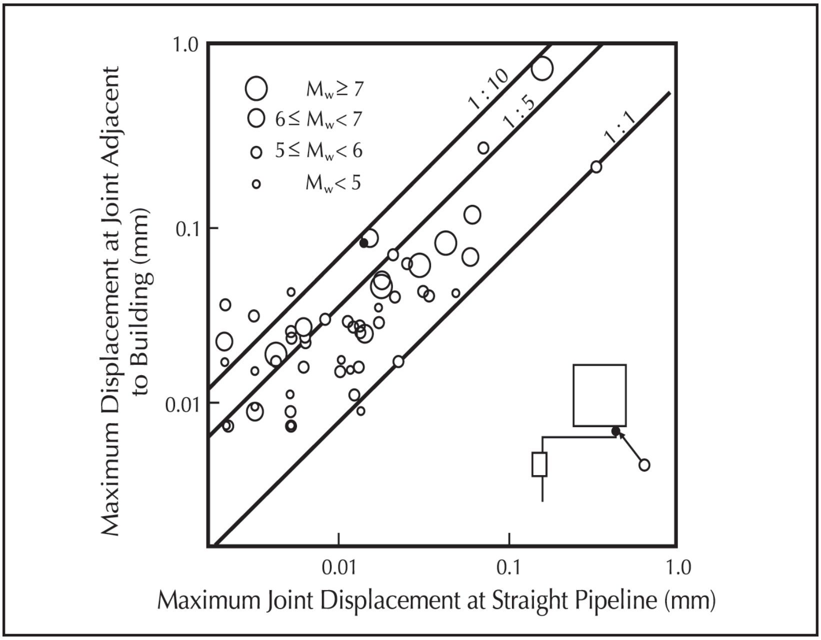

After Iwamoto et al., 1985

■ **Figure 11.12 Observed Joint Displacement and Amplification Factor at Joint Adjacent to Buildings**

11.4

Comparison Among Approaches

This section presents a comparison of three approaches for estimating joint expansion/contraction in a straight run of pipe subject to wave propagation. For the comparison presented in Table 11.1, the peak ground velocity is taken as 0.37 m/sec and the propagation velocity near the ground surface is taken as 240 m/sec, which results in a ground strain of 0.00154. The CI pipe has a diameter of about 0.44 m (specifically, 0.46 m (18 in) for the Wang model, and 0.41 m (16 in) for the El Hmadi and M. O'Rourke model) and a segment length of 6.1 m. In the Wang approach, the joint axial stiffness is modeled as a linear spring, while in the El Hmadi and M. O'Rourke approach a bi-linear model is used. Specifically, for a 16-in diameter with lead-caulked joints, the joint stiffness $K_j^{(1)}$ and $K_j^{(2)}$ are 3.6×10^5 kN/cm (20.6 kips/in) and 26.5 kN/cm (1.5 lbs/in), respectively. For comparison purposes, the joint opening from the Wang approach is evaluated separately assuming linear stiffness of 3.6×10^5 kN/cm and 26.5 kN/cm, respectively.

The average joint opening from the El Hmadi and M. O'Rourke approach matches reasonably well with the results from Equation 11.1 and with the Wang approach for K_j = 26.5 kN/cm. However, when the initial joint stiffness of 3.6×10^5 kN/cm is used in Wang's approach, the joint opening is much smaller and the axial strain in the pipe segments is much larger, as shown in Table 11.1. This illustrates that care must be taken when attempting to model bi-linear behavior (in this case, the axial stiffness of CI pipe joints) with a linear model.

Based upon a joint depth (d_p in Figure 4.12) of 10.2 cm (4 in) for a 16- to 18-in-diameter pipe, one would not expect damage due to joint pull-out for a joint opening in the range of 0.8 to 0.92 cm since, as mentioned in Section 4.3.1, the normalized joint displacement is less than 0.1 (0.92/10.2 = 0.09) and from Figure 4.12, the probability of leakage for a normalized joint opening of 10% is zero. However, using the El Hmadi and M. O'Rourke approach, the displacement of one in a 100 joints and one in a 1,000 joints are 2.0 cm and 3.4 cm, respectively. The normal-

■ **Table 11.1 Comparison of Wave Propogation Response of Straight Segmented Pipelines**

Item	Eqn. 11.1 (Max.)	Wang (Max.)		El Hmadi & O'Rourke (Average)
		$K_j = 3.6 \times 10^5$ kN/cm	$K_j = 26.5$ kN/cm	
Ground Strain	0.00154	0.00154		0.00154
Pipe Strain	-	1.2×10^{-3}	4.0×10^{-5}	-
Joint Opening (cm)	0.92	0.21	0.8	0.83 Average 2.0 1% Exceedance 3.4 0.1% Exceedance

ized joint openings are 20% and 33%, respectively, for which the probability of leakage (again from Figure 4.12) are 1% and 15%, respectively. A rough approximation for the damage ratio can be determined by simply adding the probabilities—1% of one in a 100 and 15% of one in a 1,000—or a damage rate of one in 4,000. As will be established in Chapter 12, the damage rate based upon observation for a ground strain of 0.15% is about two repairs per kilometer or damage to about one in 100 joints. Hence, it seems that El Hmadi and M. O'Rourke were on the right track in that their model at least predicts some damage, which is more consistent with observation than a model with no variation in ground strains and joint properties. However, the variation in joint properties and the interaction between joint stiffness and strength they assume results in lower estimates of damage than post-event observation.

An advantage of the Wang approach is that an estimate of the pipe strain is provided. However, based upon the above discussion, the expected tensile strain in the segments (4.0×10^{-5} strain corresponding to 0.8 cm joint opening) is less than the yield strain for a CI pipe of about 2.0×10^{-3} from Chapter 4. Hence, although pipe strain is provided, it is unlikely that a pipe segment axial failure mode governs, since the pipe strain is more than two orders of magnitude lower than the yield strain.

12

Seismic Fragility Relations for Buried Pipe

In this chapter, fragility relations for buried pipe subject to either the wave propagation or permanent ground deformation (PGD) hazards are developed. Available information on the influence of pipe material and diameter is also presented.

Often the first step in the seismic upgrade of an existing pipeline system is an evaluation of the likely amounts of damage in the system due to the potential earthquakes. For buried pipelines, empirical correlations between observed seismic damage and some measure of ground motion have typically been used.

Most commonly these empirical relations are for various type of segmented pipe. This is due to two factors. First of all, segmented pipelines are arguably more common than continuous pipelines. Secondly, segmented pipelines are much more susceptible to seismic damage than continuous pipelines. For example, EDM Services (1993) prepared a hazardous liquid pipeline risk assessment for the California State Fire Marshall. Over a 10-year period (1981-1990), there were a total of over 500 leaks in the 7,800 miles of hazardous liquid (continuous steel) pipeline. Of the 500+ leaks, only three were judged to be due directly to seismic effects. The resulting seismic "incident rate" for a Modified Metallic Intensity of VIII was only 0.022 leaks per kilometer of pipeline. As will be demonstrated shortly, this damage rate is quite low compared to that typically observed for segment pipeline subject only to the wave propagation hazard, and extraordinary low compared to damage rates for segmented pipeline subject to PGD.

Wave Propagation Relations

It appears that Eguchi was the first to separate wave propagation damage and PGD damage. For wave propagation, Eguchi (1983) summarized pipe break rate versus Modified Mercalli Intensity (MMI) for several earthquakes in the United States, and developed fragility relations for six different pipe materials subject to wave propagation only. Subsequently, Eguchi (1991) modified his relationship and obtained a bilinear curve.

Based on data from three U.S. earthquakes, Barenberg (1988) established an empirical relation between seismic wave propagation damage to cast iron pipe and peak horizontal ground or particle velocity V_{max}. The choice of V_{max} is an outgrowth of the fact that

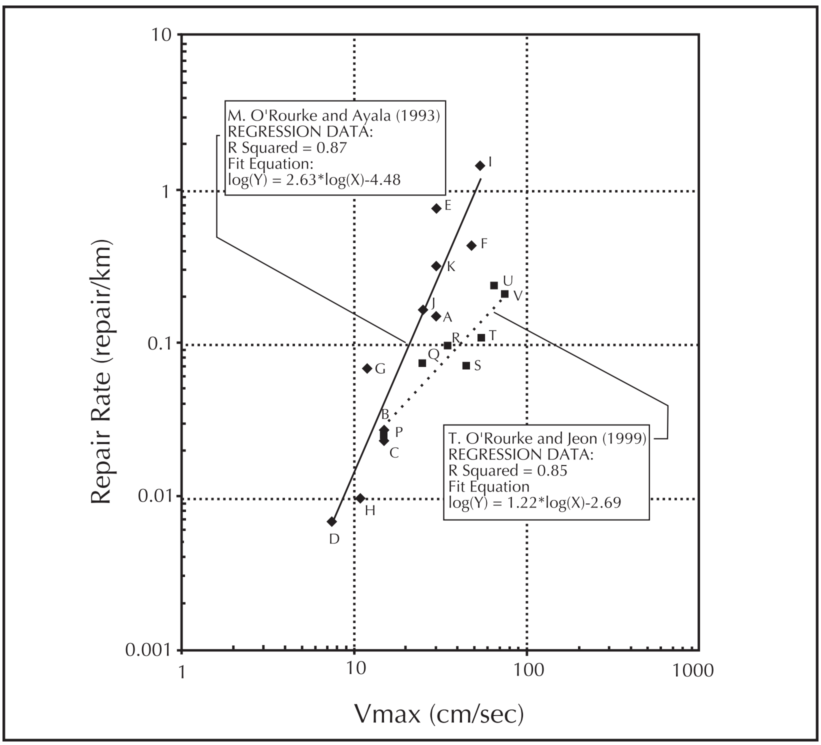

After M. O'Rourke and Deyoe, 2004

■ **Figure 12.1 Wave Propagation Repair Rate vs. Peak Particle Velocity (M. O'Rourke and Ayala Relation Solid Line; T. O'Rourke and Jeon Relation Dashed Line)** wave propagation ground strain, and hence presumably pipe damage, are linear functions of V_{max}, as demonstrated in Chapter 3.

Including additional data from three other earthquakes, M. O'Rourke and Ayala (1993) prepared a plot of wave propagation repair rates versus peak ground velocity for common segmented water pipe materials—specifically cast iron, concrete pipe, prestressed concrete pipe and asbestos cement pipe. The M. O'Rourke and Ayala relation is shown as the solid line in Figure 12.1. It is based upon data points from the 1971 San Fernando and 1983 Coalinga events, among others, and four data points from the 1985 Michoacan event in Mexico. These M. O'Rourke and Ayala data points are labeled A through K in Figure 12.1.

The specific functional form of the M. O'Rourke and Ayala relation is:

$$RR = \left(\frac{V_{max}}{50}\right)^{2.63} \tag{12.1}$$

where RR is the repair rate in repairs per kilometer and V_{max} is the peak horizontal velocity in cm/sec. It is the basis for pipe fragility relations in HAZUS and suggests that a peak particle velocity of 50 cm/sec results in about 1 repair per kilometer of pipe, while V_{max} of 10 cm/sec results in about 0.015 repairs per kilometer.

Somewhat more recently, T. O'Rourke and Jeon (1999) developed an empirical wave propagation fragility relation for buried segmented pipe using information from the 1994 Northridge event. This Northridge relation is shown as the dashed line in Figure 12.1 and is based on data points labeled P through V. The specific functional form is:

$$RR = \left(\frac{V_{max}}{266}\right)^{1.22} \tag{12.2}$$

Based upon Equation 12.2, one expects about 0.13 repairs per kilometer for a V_{max} of 50 cm/sec and a repair rate of about 0.018 for V_{max} for 10 cm/sec. That is, both relations predict similar levels of pipe damage for peak particle velocities of about 10 cm/sec. However, as the level of ground shaking increases, the older M. O'Rourke and Ayala relation predicts much more damage than the newer T. O'Rourke and Jeon relation, the difference being almost an order of magnitude (1.0 versus 0.13) for V_{max} of 50 cm/sec.

Subsequently, Trifunac and Todorovska (1997) developed empirical relations between the density of water pipe breaks in urban areas (quantified by breaks per square kilometer of land area) and the peak soil shear strain in a vertical plane. Unfortunately, a direct comparison between the Trifunac and Todorovska relations and Equations 12.1 and 12.2 is not possible due to differences in the damage measures (i.e., repairs per square kilometer of land versus repairs per kilometer of pipe). Damage relations will be developed herein between pipe damage and ground strain. However, herein the peak axial strain in the horizontal plane is used to quantify the intensity of shaking, as opposed to peak shear strain in a vertical plane as used by Trifunac and Todorovska.

Finally, an American Lifeline Alliance (ALA, 2002) project developed the following wave propagation damage relation:

$$RR = 0.0024\ V_{max} \tag{12.3}$$

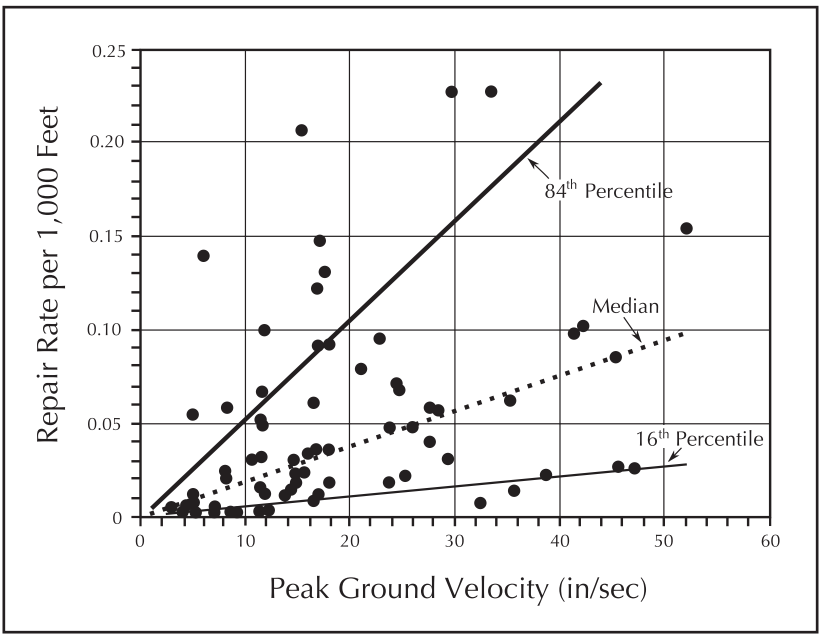

After American Lifeline Alliance, 2002

■ **Figure 12.2 ALA Wave Propagation Fragility Relation (Medium, 84th Percentile and 16th Percentile Lines Shown)**

The ALA relation is based upon an analysis of 81 data points from 12 earthquakes shown in Figure 12.2. This database contains most all the data points shown in Figure 12.1, as well as additional data points from the 1995 Hyogoken-Nanbu (Kobe) event among others. It yields about 0.12 repairs per kilometer for V_{max} of 50 cm/sec and a repair rate of about 0.02 for V_{max} at 10 cm/sec. Hence, for this range of peak horizontal velocities, it provides damage rates similar to the Northridge relation in Equation 12.2. However, since it is based, at least in part, on the data points in Figure 12.1 there is a large amount of scatter of the 81 data points about the median given in Equation 12.3. As noted in the ALA report, the 84th percentile function (damage relation which provides an upper bound for the 84% of the data) is 2.8 times the median line given in Equation 12.3, while the 16th percentile function is 0.28 times the median. As a result, there is an order of magnitude (2.8/0.28 = 10.0) between the 84th percentile estimate and the 16th percentile estimate.

12.2 PGD Relations

In the past, fragility relations for buried segmented pipe subject to PGD have used the amount of permanent ground movement to quantify the hazard. The ALA (2002) relation shown in Figure 12.3 is typical. The median repair rate, in repairs per kilometer, is given by:

$$RR = 2.58\,(D_{max})^{0.319} \tag{12.4}$$

where D_{max} is the amount of permanent ground displacement in cm. However, as with the ALA wave propagation relation, there is a significant amount of scatter of observed data points about the median relation given in Equation 12.4. Specifically, the 84th percentile value is more than four times the 16th percentile value. As will be shown later, the scatter in such PGD relations is significantly reduced when the hazard is characterized by ground strain as opposed to D_{max}.

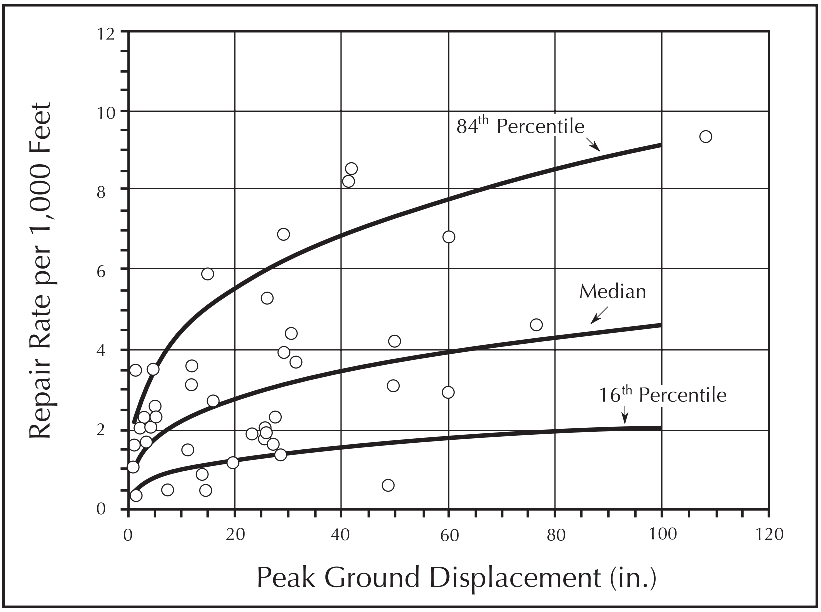

After American Lifeline Alliance, 2002

Figure 12.3 ALA Permanent Ground Deformation Fragility Relation (Median, 84th Percentile and 16th Percentile Lines Shown)

12.3

Ground Strain Relations

As noted above, the choice of V_{max} as the ground motion parameter in wave propagation fragility curves is due to its direct relationship to ground strain. That is, as shown in Equation 3.5 for R-Waves and in Equation 3.7 for S-waves, the ground strain is linearly proportional to the peak particle velocity V_{max}. However, as shown by those same equations, the ground strain is inversely proportional to a propagation velocity. For the simplest case of a half space, the R-wave phase or propagation velocity is slightly less than (seven eighths of) the shear wave velocity of the half space. Hence, for a half space model of the near surface soils, the apparent propagation velocities for both S and R-waves are related to the shear wave velocity, V_s, of the near surface soils. For R-waves, it is about 90% of V_s. From Equation 3.1, the apparent propagation velocity for S-waves is V_s divided by the sine of a small angle, a much larger value than for R-waves.

Hence, ground strain and presumably segmented pipe damage is strongly influenced by wave type. Recognizing this, M. O'Rourke and Deyoe (2004) established fragility curves wherein pipe damage is presumed to be a function of ground strain. Following the 1984 ASCE guidelines, they assume R-wave propagation for sites with an epicentral distance at least five times the focal depth, and S-wave propagation for closer sites. In addition, for R-wave sites they use C_R = 500 m/sec in Equation 3.5 to determine ground strain. For S-wave sites, they use C_S = 3,000 m/sec in Equation 3.7 to determine ground strain. Finally, they only consider statistically significant data points, those for which the sample size (number of kilometers of pipe) are large enough so that there is a 95% probability that the sampled repair rate is within 50% of the true value. Using this criterion, one needs at least 1,521 km of pipe in the sample if the damage rate is 0.01 repairs/km. If the damage rate is 0.1 repairs/km, one needs at least 138 km of pipe for the observed damage rate to be statistically reliable.

Figure 12.4 shows the resulting plot of repair rate (repairs per kilometer) versus ground strain. This figure includes many of the data points from Figure 12.1 (those that satisfy the sample size criterion), as well as PGD data points from earthquakes in the U.S. and Japan that can be characterized by ground strain. The single letter data points (A, C, etc.), as well as EK, are for wave propagation damage, while the double letter data points (AA, BB, etc.) are for PGD damage. Note the remarkable consistency over roughly four orders of magnitude when segmented pipe damage is plotted versus ground strain.

The best fit line for the combined (wave propagation and PGD) data set is:

$$RR = 724\ \varepsilon_g^{0.92} \tag{12.5}$$

The R^2 value for Equation 12.5 is 0.92, which is a better fit to the combined wave propagation and PGD data set than either Equation 12.1 or 12.2 are to their individual wave propagation only data sets.

As noted above, for nearby sites where S-waves are expected to control, M. O'Rourke and Deyoe (2004) used Equation 3.7 and C_S = 3,000 m/sec to calculate ground strain. This value for C_S is reasonably consistent with values listed in Table 3.2. Note in this regard that Equation 3.7 assumes traveling waves with per-

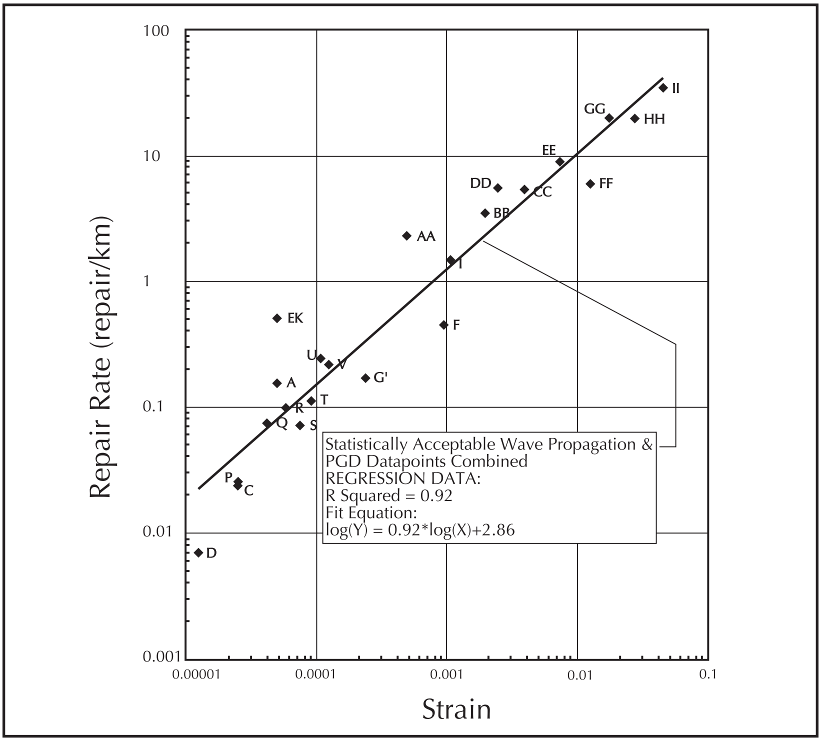

After M. O'Rourke and Deyoe, 2004

■ **Figure 12.4 Wave Propagation and PGD Repair Rates vs. Ground Strain**

fect coherence (exactly the same wave shape along the propagation path). However, as shown recently by Paolucci and Smerzini (2008), when one back-calculates the effective propagation velocity from real records which by nature have some incoherence, the C_S value is substantially smaller. Using a value of C_S = 1,000 m/sec (C = 2,000 m/sec) from Figure 3.9, M. O'Rourke (2009) developed a revised fragility relation:

$$RR = 1905\ \varepsilon_g^{1.12} \tag{12.6}$$

This revised relation is shown in Figure 12.5 along with that from Equation 12.5.

Combining Equation 12.6 with ground strain relations in Equations 3.5 and 3.7 and the assumed propagation velocities results in damage relations in terms of the peak particle velocity V_{max}. If the ground strain is due to surface wave propagation (i.e., R-waves) then the damage relation becomes:

$$RR_R = 0.0104\ V_{max}^{1.12} \tag{12.7}$$

where RR_R is the surface wave repair rate in repairs per kilometer and V_{max} again has units of cm/sec. If the ground strain is due to body wave propagation (i.e., S-waves) then the damage relation becomes:

$$RR_S = 0.0022\ V_{max}^{1.12} \tag{12.8}$$

where RR_S is the body wave repair rate. That is, for a given value of V_{max}, there is a factor of five times difference in expected repair rates depending upon the controlling wave type. Note further that this relation for damage due to body wave propagation is similar to the ALA relation in Equation 12.3.

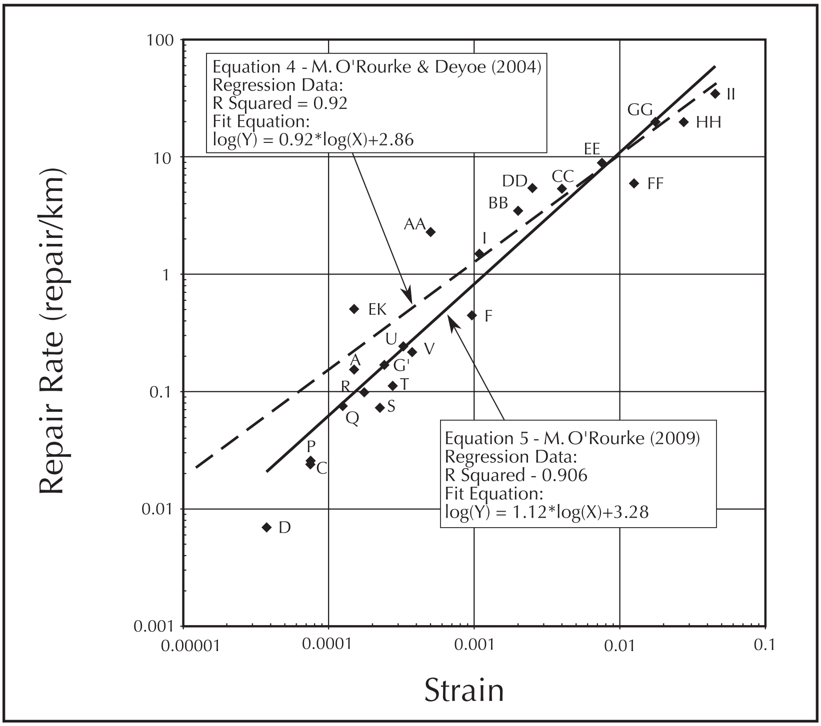

After M. O'Rourke, 2009

Figure 12.5 Revised Fragility Relation for Segmented Pipelines from M. O'Rourke (2009)

The relations in Equations 3.5 and 3.7 provide the maximum ground strain due to wave passage. That is, for an R-wave propagating in a particular direction, Equation 3.5 provides the ground strain in that direction. The ground strain in other directions would be less, with zero ground strain in the direction perpendicular to the direction of propagation. However, for a grid or network of pipelines with comparable lengths in the project north-south and project east-west directions (such as the wave propagation data analyzed herein), the direction of R-wave propagation does not have a significant influence. Consider an R-wave propagating north-south. The north-south pipes would experience the full ground strain while the east-west pipes would experience none. For an R-wave propagating northeast-southwest, Mohr's Circle for plane strain shows that both the north-south as well as east-west pipes would experience half the full ground strain. Since the repair rate is essentially a linear function of ground strain, the total number of repairs would be essentially the same. That is, for pipes in a distribution network, pipeline orientation with respect to propagation direction is not a major concern for R-waves. However, for a single transmission line subject to R-wave propagation, one expects that the repair rate, all other things being equal, would vary from zero to twice the value given by Equation 12.7, depending upon pipeline orientation.

The situation for S-wave propagation is more complex. The ground strain for S-wave propagation is a maximum in the direction 45° to the direction of wave propagation. It is zero in the direction of propagation, hence for an S-wave propagating north-south, north-south and east-west pipes would experience zero ground strain, while northeast-southwest and northwest-southeast pipes would experience the full ground strain given by Equation 3.7. Hence, unlike R-wave propagation, pipeline orientation with respect to the direction of wave propagation plays an important role for both a network of pipelines, as well as single transmission pipeline subject to S-wave propagation.

The remarkable consistency of segmented pipe damage from both wave propagation and PGD leads to the following important observations:

1) Since the independent variable in Figure 12.5 is ground strain, one is led to the conclusion that the seismic behavior of segmented pipe is controlled by axial effects. That is, bending of the pipe segments and angular rotation of pipeline joints appear to be of secondary importance. Whereas axial tension and compression in the pipe segments and axial expansion and contraction at pipeline joints appear to be of primary importance.

2) Wave propagation ground strains (i.e., single letter data point and EK) range from about 0.004 to 0.1%, with a typical value of roughly 0.02%. PGD ground strains (i.e., double letter data points excluding EK) range from about 0.1 to 5%, with a typical value of roughly 1%. That is, for the events captured in Figure 12.5, the PGD ground strains are roughly 50 times larger than the wave propagation ground strains. Since the relation in Equation 12.6 is close to linear, PGD—when and if it occurs—is about 50 times more damaging to segmented pipe than wave propagation. Of course, PGD typically occurs over a small fraction of a pipeline network while wave propagation can arguably affect the whole network.

3) Even at comparatively high damage rates only a small fraction of the pipe segments actually experience damage. For example, at a ground strain of 1%, presumably due to PGD, the corresponding damage rate is 10 repairs per kilometer. For a pipe segment length of 5.5 m (18 ft), this corresponds to one repair every 18.2 pipe segments or a repair to about 5% of the pipe segments. At a ground strain of 0.1% (corresponding to either a high amount of wave propagation or a low to moderate amount of PGD) one expects repairs at roughly one in 182 pipe segments (0.5%). Hence, the overall behavior is likely controlled by a particularly weak joint or pipe segment, as opposed to being controlled by the typical joint or pipe segment. That is, for larger pipe diameters where damage is more likely due to expansion/ contraction at the joints, appropriate characterization of the particularly weak (e.g., easy to pull-out) joints are crucial. Finally, analytical models intended to replicate segmented pipe response to ground strain must incorporate variability in joint properties. An analytical model with all joints having exactly the same characteristics will not yield realistic results.

12.4

Influence of Modifying Factors

Although Figure 12.5 and Equations 12.6 through 12.8 are based on a mix of pipe materials and diameters, the most common material is cast iron typically with lead-caulked joints, and the most common diameter is 15 cm (6 in). The questions then arise as to the influence of pipe material, diameter and other factors on seismic fragility of buried pipe. Over the years, a number of authors—Eguchi (1983, 1991), Eidinger et al. (1995), Honegger (1995), Heubach (1995) and Porter et al. (1991)—have suggested different relationships. It seems that in most cases the postulated inter-relationships are based on a comparatively small amount of data combined with a large dose of engineering judgment. The ALA (2002) project reviewed the available information and provides arguably reasonable modification factors. Note that the ALA report provides two tables of modification factors, one for wave propagation damage and another for PGD damage. However, the factors are not greatly different, as one would expect in light of the commonality of behavior exhibited in Figure 12.5.

Material: According to the ALA tables, Cast Iron (CI), Asbestos Cement (AC) and Concrete Cylinder (CC) pipe with stiff joints ("cement" joint type) have nominally the same behavior, that is, a modification factor of 1.0. Somewhat less damage is expected for CI, AC, CC, Ductile Iron (DI) and PVC pipe with flexible ("rubber gasket" joint type), with modification factors ranging from 0.5 to 0.8. One could argue that the modification factors for flexible joints may in fact be a bit lower, based on data presented in the ALA report. Specifically, in the 1995 Kobe event, the ratio of repair rates for DI pipe compared to CI pipe ranged from 0.26 to 0.56 for the most common pipe diameter (10 to 45 cm, 4 to 18 in).

Diameter: The influence of diameter is considered particularly important since most of the data is for small diameter pipe while arguably the most critical lines have large diameters. Fortunately, most authors agree that the damage rate for large diameter pipe is less than that for smaller diameters. Hence, using the smaller diameter fragility relations would conservatively overestimate the expected amount of damage for the larger diameter (more critical) lines.

In the ALA report, diameter related modification factors are provided for only one material: steel pipe with arc welded lap joints. For small (4 to 12 in) diameter steel pipe, the modification factor is 0.6 while for larger (16 in and above) diameters the factor is 0.15, suggesting a large diameter modification factor of 0.25. One could argue that the diameter modification factor may not be that low, based on data for the 1995 Kobe event presented in the ALA report. The Kobe data suggests a diameter modification factor of 1.0 for pipe in the 10 to 25 cm (4 to 10 in) range, a factor of 0.8 for pipe with diameters in the 30 to 45 cm (12 to 18 in) range, and a factor of 0.55 for diameters of 50 cm (20 in) and larger.

Intuitively, it seems likely that the diameter effect is related to the joints embedment distance discussed in Chapter 4. For a model where the pipe segments themselves are assumed to be rigid in comparison to the joints, ground strain is accommodated by axial extension or compression at individual joints. Since a joints embedment depth, and presumably its capacity to accommodate axial expansion or contraction, are increasing functions of diameter, one expects less damage for larger pipe diameters.

Other Factors: The ALA report presents different modification factors for iron-based pipe materials (CI and WS) in corrosive and non-corrosive soils. Based upon the ALA soil factors, in corrosive soils one expects 40 to 50% more damage than in “normal” soil. In non-corrosive soil, one expects 30 to 50% less damage than normal. A difficulty with the ALA values is that definitions of corrosive and non-corrosive soil are not provided. Nevertheless, the effect of corrosive soil is significant and the ALA report identifies the correct trend. As noted by Isenberg and Taylor (1984), the higher than expected damage rate for pipe in the 1983 Coalinga event (data point EK in Figure 12.4) was apparently due to corrosive soil.

12.5 System Performance

There has been a large amount of research work over the past two decades on pipeline system performance. Notable contributions have been made by Isoyama and Katayama (1982), Liu and Hou (1991), Sato and Shinozuka (1991), Honegger and Eguchi (1992), and Markov et al. (1994). A detailed discussion of overall system modeling and performance is beyond the scope of this state-of-the-art review, which focuses primarily on component performance, behavior and design. However, a summary of the results of system performance evaluations as a function of buried pipeline component performance (specifically, breaks per unit length) will be discussed briefly.

Isoyama and Katayama (1982) evaluated water system performance following an earthquake for two supply strategies: supply priority to nodes with larger demands, and supply priority to nodes with lowest demands. These two strategies correspond to the best and worst system performance, which is shown in Figure 12.6. Somewhat more recently, Markov et al. (1994) evaluated the performance of the San Francisco auxiliary water supply system (AWSS), while G & E (1994) did a similar study for the water supply system in the East Bay Municipal Utility District (EBMUD). Their results are also shown in Figure 12.6. Based on these results, the National Institute of Building Sciences (NIBS) (1996) proposed a damage algorithm, in which the system serviceability index is a lognormal function of the average break rate. Note that in this figure, the serviceability index is considered to be a measure of reduced flow.

Although there is considerable variation from hydraulic model to hydraulic model, the serviceability index is 60% or better for average rates of 0.05 breaks/km or less. On the other hand, the serviceability index is 50% or lower for average break rates of 0.2 breaks/km or higher. Hence, one could argue that the tipping point for system serviceability, the boundary between acceptable and unacceptable levels of pipe damage, is somewhere around 0.1 breaks/km. Note, that the relations between damage and ground strain in Figure 12.5 characterize pipe damage as repairs per kilometer, not breaks per kilometer. According to Bal-

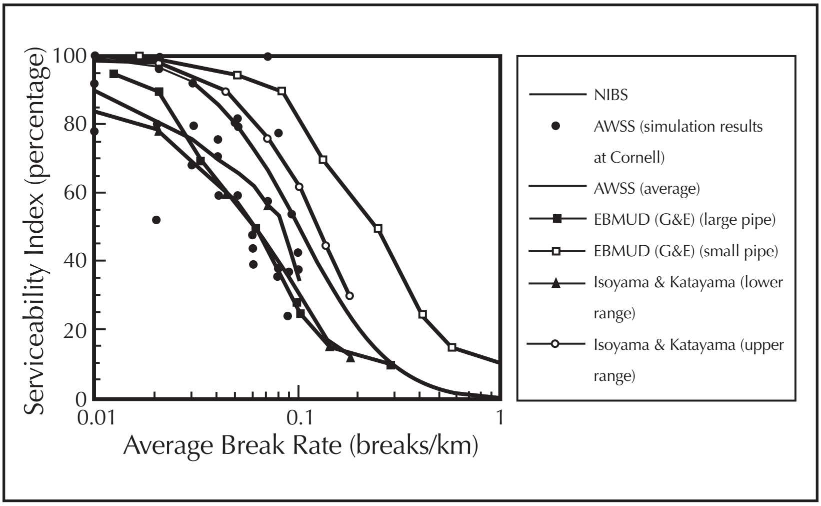

After NIBS, 1996

■ **Figure 12.6 Serviceability Index vs. Average Break Rate for Post-Earthquake System Performance**

lantyne et al. (1990), for two events in the Puget Sound area, about 15% of the repairs were breaks, with the remaining 85% being leaks. According to Romero et al. (2009), LADWP experienced 5% breaks and 95% leaks in the Northridge event. If one splits the difference, we have one break for every 10 repairs. If system serviceability is due solely to breaks (leaks have no influence), a break rate of 0.1 breaks/km would correspond to a repair rate of 1.0 repairs/km. However, if one assumes that five leaks are hydraulically equivalent to one break, the tipping point becomes 0.36 repairs/km. Hence, the apparent tipping point between arguably acceptable and unacceptable system behavior is around 0.36 to 1.0 repairs/km. In Figure 12.5, this tipping point corresponds to ground strain in the 0.05 to 0.12% range.

Notice that the ground strain level of 0.05 to 0.12% nominally separates the wave propagation ground strains from the PGD ground strains. This is consistent with the commonly held view that wave propagation, of and by itself, does not result in unacceptable water system behavior. The exception is Mexico City in 1985 where wave propagation itself led to repair rates of 0.45 and 1.5 repairs/km and ground strain of roughly 0.1% in the Lake Zone and Tlahuac, both above the apparent tipping point. Water supply was, in fact, unavailable for many parts of the city after the 1985 Michoacan earthquakes.

The ALA Guideline (2005) establishes target break rates for various functional classes of pipe. For ordinary pipe (functional class II) the target break rate for a 475-year event is 0.10 to 0.20 breaks/km or less. That is, in relation to Figure 12.6 and the tipping point of about 0.1 breaks/km discussed above, the ALA target arguably ensures something close to acceptable behavior (serviceability index of 50% or more) for the 475-year event. The target rates for critical (function class III) and essential (function class IV) pipe are 0.02 to 0.033 and 0.01 to 0.02 breaks/km, respectively. The repair rates corresponding to a break rate of 0.033 breaks/km are 0.33 repairs/km (leaks have no influence) and 0.12 repairs/km (five leaks equivalent to one break). In relation to Figure 12.5, these repair rates correspond to ground strain in the 0.02% to 0.05% range. This suggests that, following the ALA Guidelines, all critical or essential segmented pipes subject to either PGD or wave propagation in the 475-year event with ground strains of about 0.03% would need to be upgraded in some fashion.

13

Countermeasures to Mitigate Seismic Damage

As indicated previously, seismic damage to buried pipeline is due to either PGD and/or wave propagation. Prior studies have suggested various methods to mitigate against seismic damage to pipelines. These methods include the use of high strength or high ductility materials for the pipelines themselves, the use of joints with enhanced expansion/contraction or rotation capability, various methods to isolate the pipeline from ground movements, various methods to reduce the amount of ground movement, and finally, routing of new pipelines or rerouting existing pipeline around areas particularly susceptible to damaging ground movements.

This chapter will briefly describe each of these techniques and identify situations in which they may be particularly effective.

13.1 Routing and Rerouting

This technique involves simply avoiding areas that are susceptible to large ground movements. It is comparatively easy to implement during the initial design stage (i.e., route selection) for a new pipeline, but can also be used for an existing line. For example, Bukovansky et al. (1985) report on the relocation of a 66 cm (26 in) natural gas pipeline that was subject to a landslide hazard. About 365 m (1,200 ft) of line was relocated at a direct cost of roughly $1 million. As one might expect, relocation of an existing line typically requires temporary suspension of service.

This method would typically be more effective for the PGD hazard, such as landslides or areas susceptible to liquefaction. It could also be used for the fault crossing hazard if the end points for the line are both on the same side of the active fault. That is, routing and rerouting tend to be more effective when the hazard exists only in an isolated area that can be avoided. Routing and rerouting tends to be less effective for wave propagation damage, since this hazard typically exists over much larger areas. Finally, routing and rerouting would typically be easier to implement for transmission pipe, for which there may be a number of options in terms of route selection, but more difficult for distribution pipe. For example, if natural gas service is needed along a given street, alternate locations may be severely limited.

13.2 Optimal Orientation in the Horizontal Plane

Optimal orientation approaches are more frequently considered for continuous pipe subject to the PGD hazard. First of all, segmented pipelines are likely to be damage by PGD irrespective of the pipelines orientation in the horizontal plane. Secondly, unlike PGD where the expected direction of ground movement is typically known, the “direction” of wave propagation and corresponding ground strain are variable due to the various possible locations for the earthquake epicenter. Hence, an optimal orientation of the pipe with respect to the direction of wave propagation is typically difficult or impossible. Another common feature of optimal orientation approaches is the elimination of pipeline bends or elbows from the PGD zone. As noted in Chapter 6, bends and elbows act as net stress or strain risers and hence should be located well away from the PGD zone.

For the **fault crossing hazard**, optimal orientation in the horizontal plane involves selection of the best pipe crossing angle. As noted in Chapter 8, fault crossing induces bending in the pipe as well as either axial tension or axial compression. Since the allowable axial tension strains are larger than those for axial compression, any angle that results in net axial compression should be avoided if possible. That is, for a north-south fault with right lateral offset a pipeline orientation NW to SE is recommended. A 90° crossing angle (east-west for north-south fault trace) results in minimal axial strain. However, due to the sensitivity of results to crossing angle, Kennedy et al. (1977) suggest a crossing angle of no more than 60° for buried onshore pipelines, as sketched in Figure 13.1.

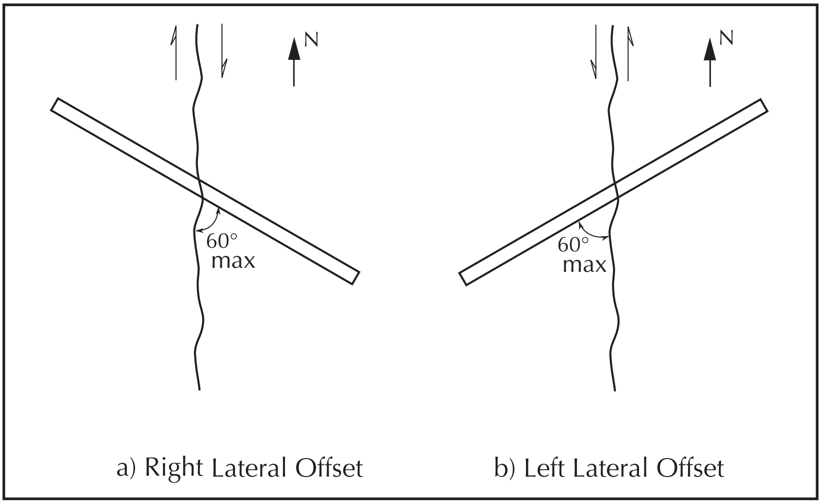

Figure 13.1 Recommended Crossing Angles for North-South Faults

For an **isolated area of PGD**, the optimal pipeline orientation in the horizontal plane is a function of the geometric characteristics of the PGD zone. Consider an area of PGD sketched in Figure 13.2 where the ground movement is to the south. For a pipeline running nominally, north-south, the pipe strain is typically controlled by the length of the PGD zone, *L*. For a pipeline running nominally east-west, the pipe strain is typically controlled by the amount of ground movement, δ, at both margins of the zone. Hence, for a PGD zone with a "large" *L* and "small" δ, an east-west pipe orientation is preferred. For any particular combination of *L* and δ, the relations in Chapter 6 for longitudinal PGD (N-S pipeline) and Chapter 8 for fault crossing (E-W pipeline) allow calculation of pipe strain for each scenario. If a longitudinal crossing of the PGD zone is chosen as a result of strain calculation or right-of-way constraints, a pipe orientation exactly parallel to the direction of ground movement (N-S pipeline for ground movement to south, as shown in Figure 13.2(a)) is preferred. Other similar orientations (e.g., NNE-SSW or NNW-SSE) result in a longer length of pipeline being exposed to longitudinal soil friction forces and hence larger pipe axial strains.

If a transverse crossing of the PGD zone is chosen, the pipe is more or less subject to a "fault crossing" like hazard at each margin. Assuming the margins are nominally parallel to each other and to the direction of ground movement, the preferred pipeline orientation is exactly perpendicular to the margin (E-W pipeline

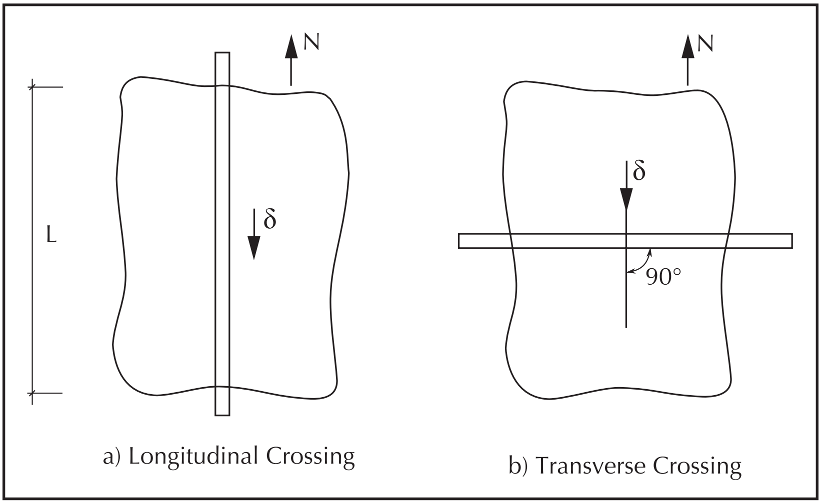

Figure 13.2 Recommended Pipe Orientation for Isolated PGD Zone

for ground movement to south), as shown in Figure 13.2(b). Other similar orientations (e.g., ENE-WSW or ESE-WNW) result in net tension at one margin but net compression at the other. That is, for the ground movement in Figure 13.2, we have a left-lateral offset at the east margin. The perpendicular crossing (with respect to the direction of ground movement) avoids net compression at either margin.

Offshore landslides typically have large sliding displacements as well as large lengths and widths. As such, their spatial extent tends to control pipeline behavior. The lateral pipe-soil interaction force is often many times larger than the axial pipe-soil interaction force, and a longitudinal crossing is preferred. Similar conclusions were reached by Demars (1978) based on damage information from 1971-75 for buried pipelines in the Gulf of Mexico.

Compared to onshore pipelines, offshore pipelines have low D/t ratios and, hence, high compressive strain capacity. At a compressive margin of PGD, lateral buckling is likely under small pipe compressive force. When subjected to landslides, offshore pipelines are likely to fail in tension. An oblique crossing tends to increase tension at the head of the landslide, and hence should be avoided.

The final PGD hazard considered is **lateral spreading at a river crossing** (ground movement of the bank nominally towards the river). For this case, a transverse crossing, as sketched in Figure 13.2(b), is impractical since presumably the pipeline eventually needs to cross the river. Hence, a straight longitudinal crossing with the pipeline orientated perpendicular to the river bank is recommended. Honegger et al. (2006) further recommended that any pipe bends or elbows in the horizontal plane be located no less than a 100 to 200 m set back distance from the bank.

13.3 Optimal Location in the Vertical Direction

Besides routing, rerouting and orientation in the horizontal plane, other techniques can be used to mitigate against seismic damage to pipelines. In this case, the pipeline traverses the hazardous area but is isolated from the effects of large ground movements by realignment in the **vertical** direction. A classic example is the placement of the Trans-Alaskan pipeline on above ground "goal post" type supports at fault crossing locations. That is, for strike-slip faults there needs to be enough "rattle-space" between the goal post uprights that the potential fault movement can be accommodated without overstressing the pipe. This method can be used for most types of PGD hazards, however, proper implementation often requires a low-friction sliding surface between the pipe and its horizontal supporting member.

When exposing the pipeline is not acceptable, placing the pipeline in a large sacrificial culvert is an option. As with the above ground goal posts, the rattle-space between the pipeline and the inside wall of the culvert needs to be large enough to accommodate the design offset. Also, since the pipeline is no longer immediately surrounded by soil, it is subject to seismic shaking due to ground acceleration and pipe inertia. This general approach using segmented culverts in combination with ball and slip (contraction) joints is currently being proposed for two large diameter water pipelines that cross the Hayward Fault in the San Francisco Bay area.

For certain PGD hazards, the same objectives can be obtained by directional drilling technology. In this case, the pipe is isolated from potential damage by being located below the hazardous area. Directional drilling can be used for the landslide hazard as well as the liquefaction hazard. It is particularly attractive at river crossings, which may be susceptible to liquefaction induced PGD of the bank. Obviously, this technique cannot be used effectively at faults, since it is not possible to place the pipe "below" the fault.

Honegger et al. (2006) present a detailed recommendation for a river crossing geometry intended to minimize **onshore** pipeline exposure to PGD. Specifically, they recommend that immediately below the river, the pipeline be located at the top of the liquefiable layer. In this way the pipeline would be below the "cap layer," within which significant ground/movement is expected. This "bottom of the cap layer" pipe elevation is maintained for three to eight channel depths back from the banks. In this manner, the pipe is only allowed to rise back towards the ground surface (1:10 rise to run recommended) at locations where lateral spreads are not expected.

13.4 Ground Remediation

These mitigation techniques involve various types of field treatments to reduce the potential for lateral spreading. The methods include increasing the density of sand, lowering the ground water level and increasing the dissipation of pore water pressure. For example, Miyajima et al. (1992) proposed a vertical gravel drain system along the pipeline right-of-way, which reduces the maximum pore water pressures. Fujii et al. (1992) suggest sand compaction as a technique to increase soil density, and thereby reduce the potential for liquefaction. Iwatate et al. (1988) performed experiments on buried culverts that drain ground water away from the pipeline. Finally, one could replace liquefaction soils in the vicinity of the pipe with non-liquefiable materials, such as gravel, to reduce the potential for liquefaction.

These field treatment methods tend to be practical only when the spatial extent of the liquefied soil deposits is limited and the liquefiable soil layer is relatively close to the ground surface. They are less practical and cost effective for the typical landslide hazard. In a retrofit situation, they would not necessarily result in service disruption if done carefully.

13.5 Stronger Pipe

As one might expect, improved seismic performance for continuous pipe results from the use of stronger pipe (i.e., higher nominal yield stress) and larger pipe wall thickness. For example, Table 6.3 shows that the higher strength X-70 pipe can accommodate more longitudinal PGD than a corresponding Grade B pipe. Similar improved performance for higher strength pipe subject to transverse PGD is shown in Figure 7.18 (reduced tensile strain). Similarly, Table 6.3, Figure 7.15 and Figure 8.8 show improved performance for thicker wall pipe subject to longitudinal PGD, transverse PGD and fault crossing, respectively.

Note that this improved performance is for pipe with electric arc welded butt joints and steel grades of X-42 through X-70. These steels have reasonably large minimum elongation as well as low to moderate yields to ultimate stress ratios. Both these qualities are desirable when allowable strains are above the yield strain. Newer, higher strength pipe with steel grades of X-80 through X-100 have recently become available. These pipes have yield to ultimate ratios of roughly 0.9, lower minimum elongations and difficulty achieving weld strength greater than actual pipe strength. As such, they are not particularly well suited for seismic hazards where significant excursion beyond yield strain is envisioned.

Finally, as discussed in more detail in Section 9.1.1, the use of "chained" joints can improve the seismic resistance of segmented pipelines.

13.6 Load Reduction

Another mitigation option involves reducing the load on the pipe as opposed to increasing the strength of the pipe. As shown in Chapter 6, the axial strain induced in a continuous pipe by longitudinal PGD is an increasing function of the pipe burial parameter β_p, as defined in Equation 6.5.

$$\beta_p = \frac{\mu \gamma H}{t} \tag{13.1}$$

Hence, axial strain can be reduced by using the smallest possible burial depth (H), using low density backfill (γ), and/or using smooth coatings, which reduce the coefficient of friction at the soil-pipe interface (μ). **Offshore** pipelines in suitable locations (e.g., deep water not susceptible to third party damage) can be simply laid on the seabed. This will significantly reduce pipe-soil interaction forces and hence strain induced by PGD.

For onshore pipelines, the use of light weight backfill can similarly reduce pipe strain. For example, Choo et al. (2007) use centrifuge testing to evaluate the benefit of low density expanded polystyrene (EP) blocks as backfill. For the fault crossing hazard wherein the pipe is placed in net tension, the low density backfill resulted in a 30 to 60% reduction in pipe flexural strain and a 5 to 30% reduction in pipe axial strain depending on the extent of the EP backfill. Unfortunately, for a fault offset which places the pipe in net compression, low density EP backfill resulted in an earlier onset of buckling of the HDPE pipeline.

The use of smooth coatings has similar effects. From Table 5.1, the friction factor, k, for a smooth polyethylene coating is 0.60 compared to k = 1 for a concrete coating. From Equation 5.1, the longitudinal resistance for sand with a friction angle of 35° and pipe with polyethylene coating is about half of that for a concrete coating and the same soil. Similarly, multiple layers of geotextile fabric are expected to reduce axial friction forces.

These mitigation options can be easily used for design of new pipelines and also for retrofit of key sections of existing pipe. Of course, in the retrofit situation, replacement would in all likelihood result in disruption of service.

13.7

Flexible Material, Slip and Ball Joints

It has long been argued that the use of more flexible materials tends to improve the seismic performance of buried pipeline. The purported benefits of flexible materials are shown in Figure 13.3, which is an older fragility relation from Eguchi (1991). Note that the relation suggests fewer repairs per unit length for ductible iron (DI) and polyethylene (PE) pipe, at a given MMI level, than for more brittle materials such as asbestos cement (AC), cast iron (CI), concrete (Conc), and polyvinyl chloride (PVC). Figures 13.4 and 13.5 are older PGD fragility relations from Porter et al. (1991) and Eguchi (1983), respectively. According to these relations, one similarly expects improved seismic performance for flexible pipe materials, such as arc-welded steel and ductile iron pipe, when subject to various PGD hazards. Unfortunately, since none of the three fragility relations show the underlying data points, it is difficult to judge whether the purported behavior is based upon engineering judgment or rigorous analysis of observed behavior.

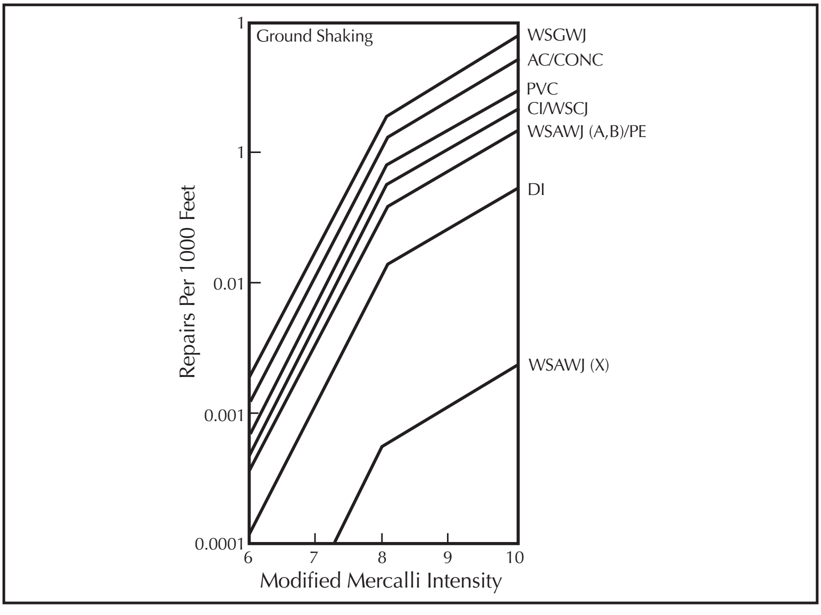

After Eguchi, 1991

Figure 13.3 Wave Propagation Pipe Damage vs. Modified Mercalli Intensity

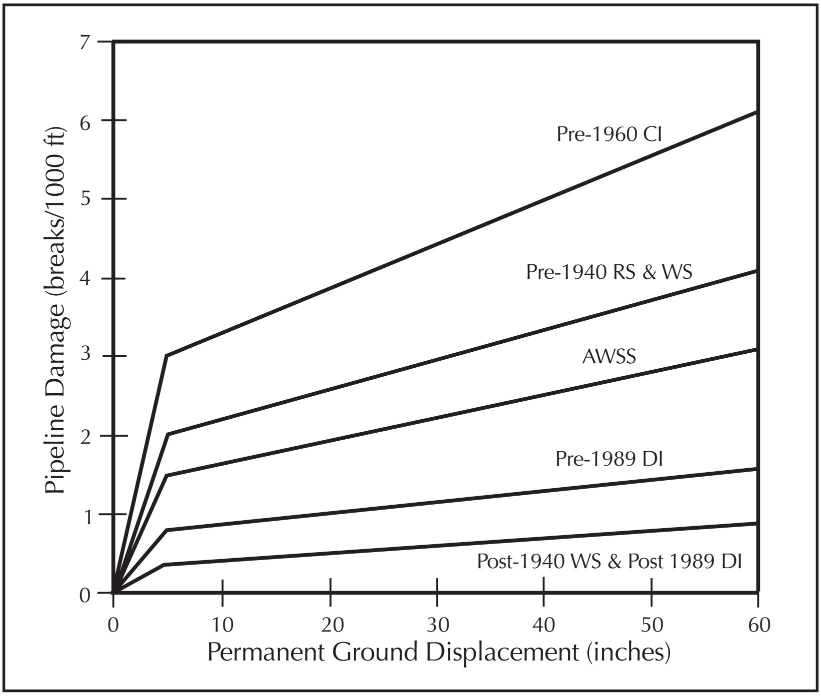

After Porter et al., 1991

■ **Figure 13.4 Pipe Breaks vs. Permanent Ground Displacement**

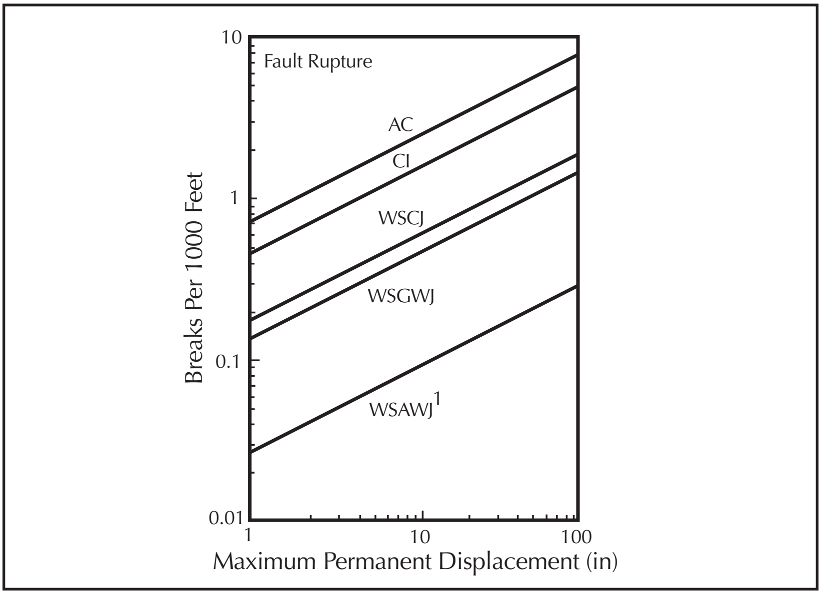

After Eguchi, 1983

■ **Figure 13.5 Vulnerability Relationships for Buried Pipelines in Fault Rupture Areas**

For segmented pipe, Isenberg and Richardson (1989), Ballantyne (1992) and Wang (1994) have suggested the use of flexible joints for pipeline subject to the PGD hazard. Figure 13.6 presents sketches of various joint types while Table 13.1 lists the expected deformation capacity, based upon information provided by Singhal (1984), Isenberg and Richardson and Akiyoshi et al. (1994). However, as explained in Chapter 6, expansion joints need to be used with caution. For example, if an expansion joint is placed at only one end of a lateral spread zone, the strain in a continuous pipe induced by longitudinal PGD would actually be larger than that for a pipe with no expansion joints.

Table 13.1 Deformation Capacity of Flexible Joints

Item	Pull-Out	Rotation	Note
Mechanical Joint	3 cm	5°	
Locked Mechanical Joint	<1 cm	5°	Slight Expansion
Restrained Mechanical Joint	5 cm	5°	S-Type Joint (Japan)
Tyton Joint	3 cm	3° - 5°	Vary with Pipe Diameter
Flange-locked Joint	3 cm	5°	
TR FLEX Telescoping Sleeve	2 D		D–Pipe Diameter
Restrained Expansion Joint	25 cm	5°	
XTRA FLEX Coupling		20°	
Ball Joint		15°	

For localized abrupt PGD offsets, such as at a fault crossing, Ford (1983) suggests, the use of rotationally flexible ball joints in combination with an expansion joint, as shown in Figure 13.7. As noted above, ball (rotation) and slip (axial contraction) joints in combination with a segmented sacrificial culvert are currently envisioned for the Hayward Fault crossing. This combined rotation and extension/contraction flexibility could also be useful at other locations when differential movements are expected. Examples of such locations include the margins of areas with variable subsurface conditions and inlet/outlet to stiff structures, such as tanks and buildings. In the offshore environment, an expansion loop or "dogleg" is often used to connect the horizontal seafloor pipe with a fixed riser, such as at a platform. The expansion loop/ dogleg serves to isolate the riser pipe from seabed pipe displacement caused by operating pressure and temperature loads. Similarly, the loop isolates the riser from PGD induced movement of the seafloor pipe.

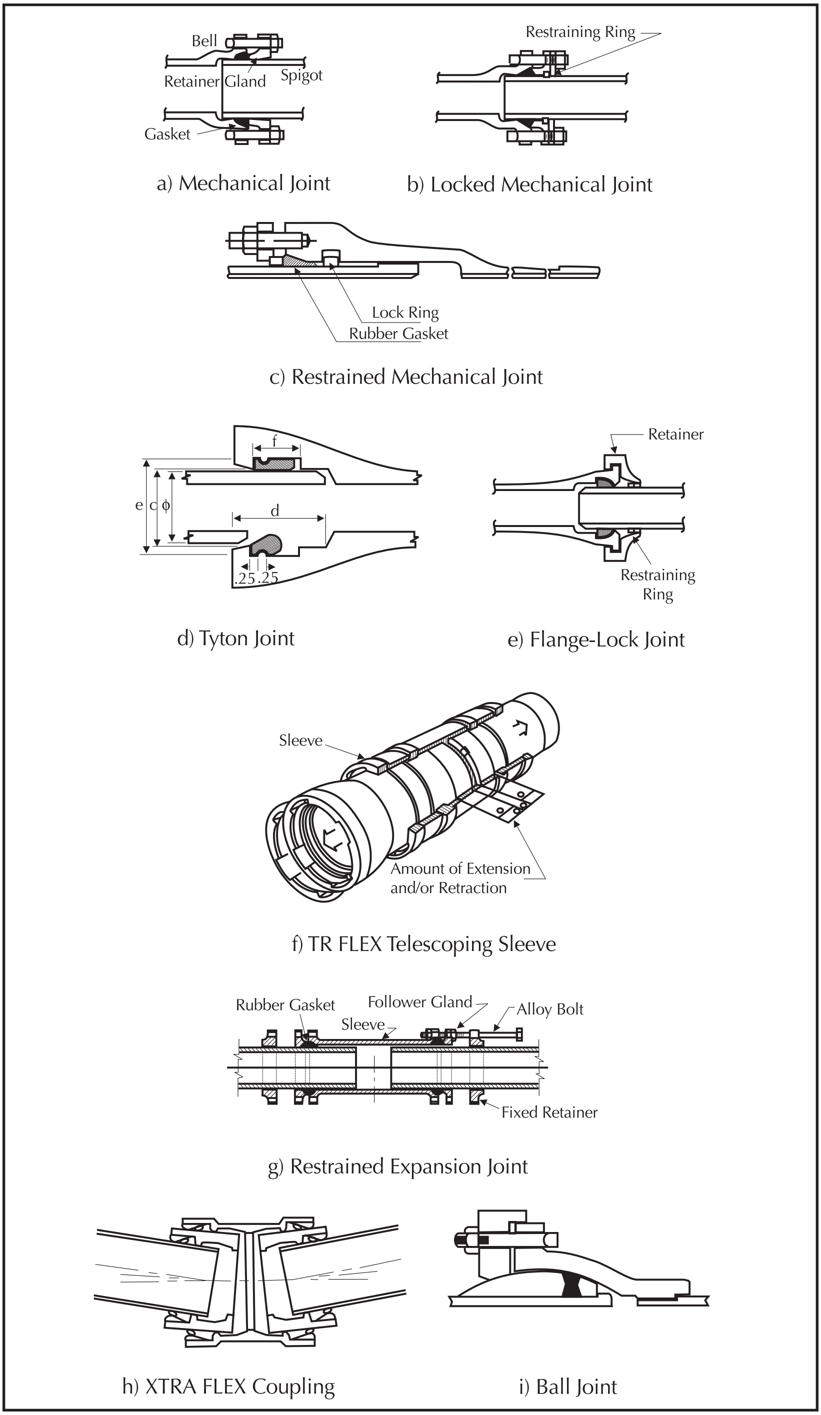

■ **Figure 13.6 Various Joint Types**

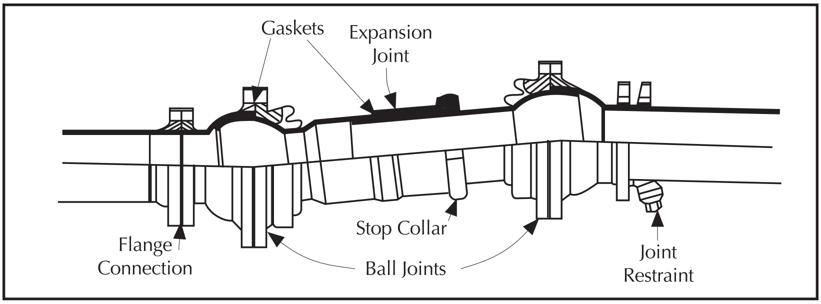

After Ford, 1983

■ **Figure 13.7 Combined Ball and Expansion Joint**

13.8 Anchor Points and Soft Joint Springs

For the longitudinal PGD hazard discussed in Chapter 6, the axial friction forces over the length of the PGD zone are equilibrated by axial tension at the head and axial compression at the toe of the zone. All things being equal (i.e., uniform soil, uniform burial depth, etc.), the pipe tensile strain at the head exactly matches the pipe compressive strain at the toe. However, as noted in Chapter 4, the allowable axial tension strain is usually significantly larger than the allowable axial compression strain. Hence, it would be beneficial to redistribute the soil friction force such that a larger percentage was taken by axial tension at the head.

One way to accomplish this redistribution is by installing a fixed **anchor point** immediately upslope of the head of the PGD zone. Figure 13.8 shows such an anchor point a bit upslope of a longitudinal PGD zone having length L and ground movement δ. Figure 13.8(a) shows the ground displacement $u_g(x)$, as well as the pipe displacement $u_p(x)$, while Figure 13.8(b) shows the axial force in the pipe. The pipe displacement is zero at Point A due to the presence of the pipe anchor. The displacement is maximum at Point B where the axial force in the pipe is zero. The peak pipe displacement is:

$$\delta_{max} = \frac{1}{2}\frac{t_u \ell_t^{\,2}}{AE} \qquad (13.2)$$

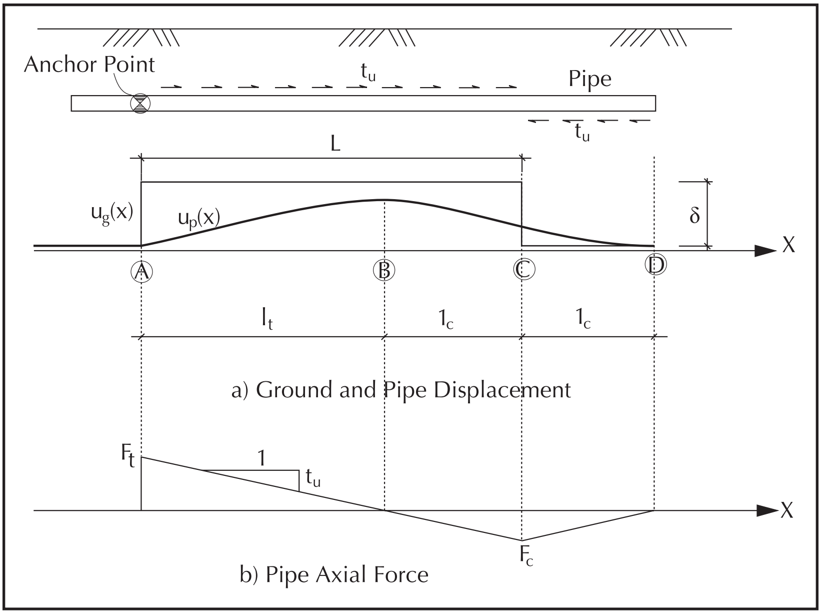

■ **Figure 13.8 Pipe Displacement and Axial Force for an Anchor Point Upslope of a Longitudinal PGD Zone**

where as before t_u is the axial friction force per unit length at the soil pipe interface, *AE* is the pipe axial rigidly and ℓ_t is the length over which the pipe is stretching (distance from A to B).

The pipe is in axial compression between Points B and D, resulting in zero pipe displacement of Point D. Hence:

$$\delta_{max} - 2\left[\frac{1}{2}\frac{t_u \ell_c^{\ 2}}{AE}\right] = 0 \tag{13.3}$$

where ℓ_c is the distance from Point B to Point C, as well as the distance from Point C to Point D. Noting that $\ell_t + \ell_c$ equals the length of the PGD zone, Equation 13.3 can be solved for the length ℓ_t and ℓ_c:

$$\ell_{\mathrm{t}} = 0.59L \tag{13.4}$$

and

$$\ell_{\mathrm{c}} = 0.41L \tag{13.5}$$

Hence, an anchor point just beyond the head of the PGD zone is effective in redistributing the axial forces in the pipeline. The peak axial tension force F_t increases from 0.5L t_u to 0.59L t_u, while the peak compressive force F_c reduces from 0.5L t_u to 0.41L t_u, about an 18% reduction.

Notice for the anchor point approach to work, the peak displacement δ_{max} needs to be less than the ground movement δ.

Although an anchor point results in a reduction in the peak compression force, the reduction is only 18%. Larger reductions are possible by placing a **soft spring** just beyond the toe of the PGD zone. Figure 13.9 shows such as soft spring downslope of a longitudinal PGD zone again having length L and ground movement δ. Figure 13.9(a) shows the ground $u_g(x)$ and pipe $u_p(x)$ displacements, while Figure 13.9(b) shows the axial forces in the pipe. The peak pipe displacement δ_{max} occurs at Point C where the pipe axial force is zero. The peak displacement is due to tensile stretching from Point A to Point C. As such:

$$\delta_{max} = 2\left[\frac{1}{2}\frac{t_u \ell_t^{\,2}}{AE}\right] = \frac{t_u \ell_t^{\,2}}{AE} \tag{13.6}$$

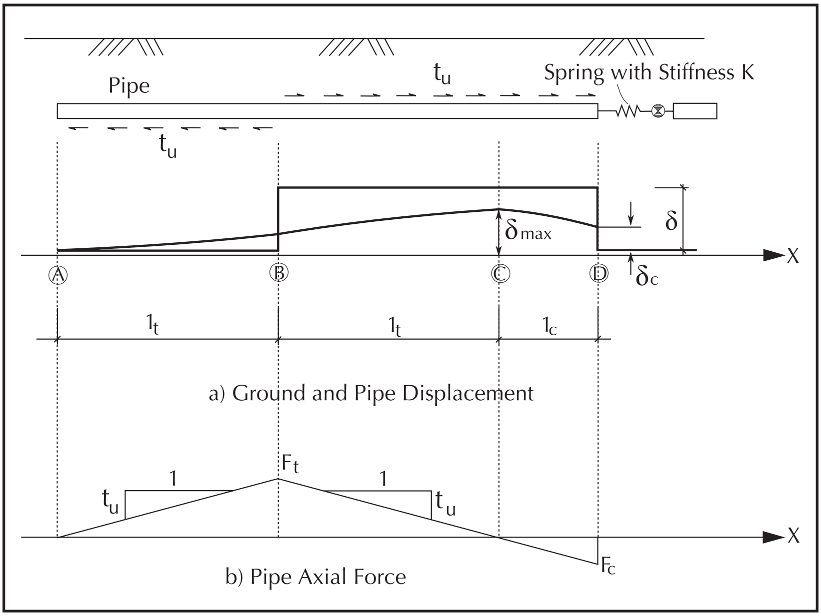

■ **Figure 13.9 Pipe Displacement and Axial Force for a Soft Spring Downslope of a Longitudinal PGD Zone**

The pipe displacement at the toe of the PGD zone, δ_c, is the peak displacement reduced by the axial compression between Points C and D, or:

$$\delta_c = \delta_{max} - \frac{1}{2}\frac{t_u \ell_c}{AE} \qquad (13.7)$$

If the soft spring at Point D (just beyond the toe) has stiffness *K*, then the axial force at the toe:

$$F_c = K \cdot \delta_c \qquad (13.8)$$

which, from equilibrium, matches the friction force per unit length acting over the distance ℓ_c (distance from C to D) or:

$$K \cdot \delta_c = t_u \cdot \ell_c \qquad (13.9)$$

Again, nothing that $\ell_t + \ell_c$ equals the length of the zone *L* results in the following relation for the normalized length of the axial compression region:

$$\frac{\ell_c}{L} = 2 + \beta - \sqrt{2 + 4\beta + \beta^2} \qquad (13.10)$$

where β is a ratio of pipe to spring stiffness $\beta = AE/LK$.

Table 13.2 presents the resulting normalized length of the compression region for various values of β. Note β = 0 corresponds to an anchor point at the base or toe of the PGD zone. This results in the undesirable condition where there is an increase in the peak compressive force ($\ell_c = 0.59L$ compared to $\ell_c = 0.5L$). However, for β larger than roughly 0.5 the desired reduction in the peak compressive force occurs. Also, note that unlike the anchor point approach (fixed reduction of 18%) one can achieve any desired reduction in the peak compressive force by decreasing the spring stiffness. Chapter 14 contains an example of the application of these concepts.

Note that the anchor point and soft joint spring concepts are only effective when the pipe compressive strain limit is significantly less than the tensile strain limit (pipe with high *D/t* ratios).

Furthermore, there concepts require fairly accurate information on the location of the head and toe of the PGD zone. For example, the situation could well be worse if the anchor point happens to be located within the PGD zone.

Table 13.2 Variation of Normalized Length of Compression Region for Various Stiffness Ratios

Stiffness Ratio $\beta = AE/KL$	Normalized Compression Zone Length ℓ_c/L
0	0.59
0.5	0.43
1.0	0.35
2.0	0.258
5.0	0.144
10.0	0.084
20.0	0.045
50.0	0.019
100.0	0.010

14

Design Examples

This final chapter presents three design examples which illustrate the application of relations and procedures introduced in earlier chapters.

14.1 Retrofit: Water Pipeline Crossing Lateral Spread Zone

An 18-inch-diameter water pipe with Welded Slip Joints (WSJs) crosses a lateral spread zone (longitudinal PGD). The pipe wall thickness is ¼ in and the external welds are nominal ¼ in with E70 electrodes. The pipe is Grade B steel with a yield stress of 35 ksi. The length of the curved bell for the slip joints is 2 in.

The top of the pipe is buried 4 ft below the ground surface in soil with an effective unit weight $\bar{\gamma}$ = 105 pcf and ϕ =33°. The project geotechnical engineer estimates the length of the PGD zone to be L = 600 ft, while the expected ground displacement is δ = 2.5 ft.

The problem is to evaluate the vulnerability of the existing line and propose retrofit options as appropriate.

Evaluate Existing Line

The force per unit at the soil-pipe interface is given by Equation 5.1:

$$t_u = \pi D\bar{\gamma}H\left(\frac{1+k_o}{2}\right)\tan k\phi$$

The existing condition at the soil-pipe interface (i.e., smooth or rough) is unknown. Herein, we use the upper bound value of k = 0.8 from Table 5.1, which is conservative. As per suggestions in Chapter 5, we use k_o = 1.0.

$$t_u = \frac{\pi}{2}\left(\frac{18\text{ in}}{12\text{ in/ft}}\right)(105\text{ pcf})(4.75\text{ ft})(1+1)\cdot\tan\left(0.8\times 33^\circ\right)$$

$$= 1{,}176\text{ plf}$$

For uniform soil properties and burial depth for the whole PGD zone, we have the same axial tension at the head of the lateral spread zone as the axial compression at the toe.

As noted in Chapter 6, there are two possible scenarios for a continuous buried pipe subject to longitudinal PGD. If the peak pipe displacement is less than the ground displacement δ, we have Case I, as sketched in Figure 6.5.

For our case:

$$\text{Peak pipe displacement} = 2\left[\frac{1}{2}\cdot\frac{t_u\left(L/2\right)^2}{AE}\right]$$

$$= \frac{1{,}176\text{ plf}\left(\frac{600\text{ ft}}{2}\right)^2}{\pi(18)\left(\frac{1}{4}\right)\cdot 29{,}000{,}000\text{ psi}}$$

$$= 0.258\text{ ft}$$

which is less than the expected ground movement (δ = 2.5 ft). Hence, we have Case I with:

$$T_{max} = C_{max} = t_u\cdot L/2 = 1{,}176\,\text{lb}/\text{ft}\left(\frac{600\text{ ft}}{2}\right)$$

$$= 353\text{ kips}$$

Tensile Capacity at Head

The capacity is given by Equation 4.16 for a WSJ with a ¼-inch fillet weld:

$$\begin{aligned}\text{Capacity} &= 1.33\left(0.6F_{exx}\right)\left(0.707t_w\right)\cdot\pi D\\ &= 1.33\left(0.6\cdot 70\text{ksi}\right)\left(0.707\cdot 1/4\right)\cdot\pi\cdot 18''\\ &= 558\text{kips}\end{aligned}$$

Hence, the WSJ pipe in tension can carry its share of the friction force along the PGD zone. As a matter of fact, the pipe in axial tension can carry:

$$\frac{558^k}{1.175\,\text{klf}\,(600\,\text{ft})} = 0.79$$

or about 80% of the total friction force.

Compressive Capacity at Toe

The capacity is a function of the *D/t* ratio and the *l/t* ratio at the WSJ. For our case, with an exterior weld and:

$$D/t = \frac{18}{1/4} = 72$$

$$\ell/t = \frac{2}{1/4} = 8$$

Figure 4.9 indicates that the joint efficiency is about 0.55. Hence, the axial compression capacity is:

$$\begin{aligned} \text{Capacity} &= \text{Joint Efficiency} \times \pi \cdot D \cdot t \cdot F_y \\ &= 0.55\left(\pi \cdot 18 \cdot \tfrac{1}{4} \cdot 35\,\text{ksi}\right) \\ &= 272\,\text{kips} \end{aligned}$$

Since the axial compression capacity of the WSJ line (272 kips) is less than the peak compressive force for the unretrofitted WSJ pipe (353 kips), the line needs to be retrofitted.

Retrofit Approach #1

The axial tension and axial compression force induced in the pipe by the lateral spread can be reduced by lowering the force per unit length at the soil-pipe interface. This can be accomplished by replacing the backfill with low-density expanded polystyrene (EP) blocks. Using this approach, the effective unit weight over the 600-ft length of the PGD zone needs to be less than:

$$\bar{\gamma} \le 105\,\text{pcf} \cdot \frac{272^k}{353^k} = 81\,\text{pcf}$$

so that the axial compressive capacity of the WSJ pipe is not exceeded. A geotechnical engineer would need to determine the placement of EP blocks to effectuate this reduction in soil friction force.

Retrofit Approach #2

The axial compression capacity of existing WSJ pipeline can be improved by replacing a portion of the line with butt welded pipe with the same diameter and wall thickness. Consider a replacement with X-42 steel pipe with a yield stress of 42 ksi and Ramberg-Osgood parameters n = 15 and r = 32, as given in Table 4.1. From Figure 6.5 the peak compressive strain is:

$$\varepsilon_{peak} = \frac{\beta_p L}{2E}\left[1 + \frac{n}{1+r}\left(\frac{\beta_p L}{2\sigma_y}\right)^r\right]$$

where the pipe burial parameter is:

$$\beta_p = \frac{\mu\gamma H}{t} = \frac{\tan k\phi(105\,\text{pcf})(4.75\,\text{ft})}{0.25\,\text{in}}\left(\frac{1\text{ft}}{12\,\text{in}}\right)^2$$
$$= 6.91\,\text{pci}$$

For our lateral spread with L = 600 ft:

$$\varepsilon_{peak} = \frac{(6.91\,\text{pci})(600\,\text{ft} \times 12\,\text{in/ft})}{2(29{,}000{,}000\,\text{psi})}\left[1 + \frac{15}{33}\cdot\left(\frac{6.91 \times 600 \times 12}{2 \cdot 42{,}000}\right)^{32}\right]$$
$$= 0.00086$$

Alternately, since the pipe strains are well below yield, the peak strain is simply the stress divided by the modulus of elasticity:

$$\varepsilon_{peak} = \frac{t_u \cdot L/2}{AE} = \frac{353^k}{\pi(18)(.25)(29{,}000\,\text{ksi})}$$
$$= 0.00086$$

This peak compressive strain now needs to be compared to the allowables in Table 4.3. Using the lower bound in the 1984 ASCE guidelines:

$$\varepsilon_{allow} = 0.3t/D = \frac{0.3\left(\frac{1}{4}\right)}{18} = 0.0041$$

That is, the compressive strain capacity is roughly five times the demand. Hence, the replacement with X-42 butt-welded pipe is feasible. If the capacity were closer to the demand, one might consider the other more complex capacity relations in Table 4.3.

The replacement is needed only in the toe region where the WSJ pipe is inadequate. That is, the existing WSJ pipe is okay where the compressive force is 272 k or less. Since the soil friction force is 1.176 k/ft, the replacement X-42 pipe is needed within:

$$\frac{353^k - 272^k}{1.176\ \text{k/ft}} = 69\ \text{ft}$$

each side of the toe of the PGD zone. That is, the X-42 replacement pipe needs to be at least 138 ft in length and centered at the toe of the PGD zone.

Retrofit Approach #3

As noted in Chapter 13, the peak axial compression in the pipeline can be reduced by installation of an anchor point at the head of the PGD zone. The peak tensile force increases to 0.59 $t_u L$, while the peak compressive force decreases to 0.41 $t_u L$ or:

$$\begin{aligned} C_{max} &= 0.41\, t_u L = 0.41(1.17k\ell f)(600\,\text{ft}) \\ &= 287^K \end{aligned}$$

Unfortunately, this peak compressive force is still larger than the axial capacity of the WSJ pipe. Hence, an anchor at the head of the zone is not a viable option.

Retrofit Approach #4

A soft spring at the toe of the PGD zone is another way to reduce the peak compressive force in the pipeline. For our case, the spring needs to be soft enough that the axial compression is limited to 272^K. Hence, the desired maximum normalized length of the compression zone is the WSJ capacity divided by the total friction force over the PGD Zone.

$$\frac{\ell_c}{L} \le \frac{272^k}{600\,\text{ft}(1.17k\ell f)} = 0.39 \text{ or } 39\%$$

This results in the normalized length of the tension zone being:

$$\frac{\ell_t}{L} = 1 - 0.39 = 0.61 \text{ or } 61\%$$

As demonstrated above, the existing WSJ pipe is capable of taking 79% of the total friction force. Hence, the soft spring approach is feasible. A design in which the tension zone takes 67% and the compression zone takes 33% results in comparable factors of safety at both the head (0.79/0.67 = 1.18) and toe (.39/.33 = 1.18).

From Table 13.2, the stiffness ratio needs to be somewhat larger than 1.0 for the normalized compression zone $l_c/L = 0.33$. Iterating with Equation 13.10 gives β = 1.20, hence, the stiffness of the soft spring at the toe should be:

$$K = \frac{AE}{L\beta} = \frac{\pi(18)(.25)(29{,}000 \text{ ksi})}{600 \text{ ft}\left(\frac{12 \text{in}}{\text{ft}}\right)(1.2)}$$
$$= 47.4 \text{ k/in}$$

The soft spring would likely consist of an expansion loop within a vault, as sketched in Figure 14.1. The vault penetration for the entering pipe (PGD side of vault) needs to allow axial movement of the pipe. Beyond the expansion loop, the outgoing pipe needs to be rigidly attached to the vault allowing no transfer of axial compression beyond the vault.

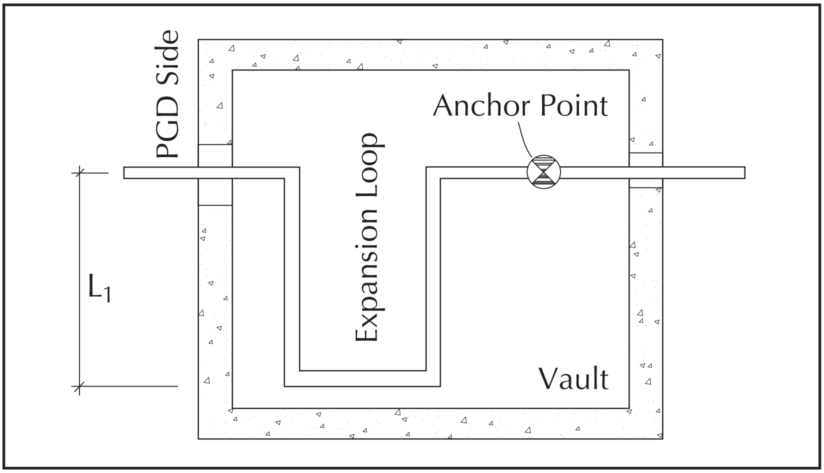

Figure 14.1 Plan View of Expansion Loop Vault for Soft Spring Retrofit

A detailed analysis of the effective stiffness of the expansion loop needs to be undertaken. However, the feasibility of the soft spring/expansion loop retrofit can be determined by investigating a simple upper bound case.

The effective stiffness of the loop (18-inch-diameter pipes, ¼-inch wall thickness, full penetration butt welds) will be somewhat less than that for two built-in beams where the loaded end can translate but not rotate. For such a beam, the deflection at the end for a unit load is $L^3/12EI$. The total deflection is twice that for one leg of the loop, hence, the effective stiffness is:

$$K = \frac{12EI}{2L_\ell^{\,3}}$$

where L_ℓ is the length of each leg in Figure 14.1. Hence, an upper bound for L_ℓ is given by:

$$47.4\ {}^{\mathrm{k}}\!/_{\mathrm{in}} = \frac{12(29{,}000)\left(\pi \cdot 18^3 \cdot 0.25/8\right)}{2L_\ell^{\,3}}$$

or

$$L_\ell = 126.9 \text{ in} = 10.6 \text{ ft}$$

This upper bound leg length seems feasible.

14.2 Risk Assessment: Water Supply Network Subject to Wave Propagation

The Seismic City Water District (SCWD) is interested in an estimate of likely earthquake damage to its system. There are two specific issues. First, SCWD would like an estimate of the expected number of repairs to the 400 km of segmented water pipe in its system, the majority of which is 6-inch-diameter, lead-caulked Cast Iron (CI) pipe. Secondly, SCWD would like a probabilistic estimate of damage to the 3.2 km of 24-in CI pipe, which connects BK & M Industries (Seismic City's main employer) to its water source located directly to the west of the BK & M plant.

The only seismic source in the area is the XYZ fault shown in Figure 14.2. According to the project seismologists, the epicenter of the design event is equally likely to be located anywhere along the 87 km length of the active portion of the fault. As shown in Figure 14.2, the XYZ fault runs north-south. The starting point for the active portion of the fault is located 18 km east and 10 km south of the center of Seismic City.

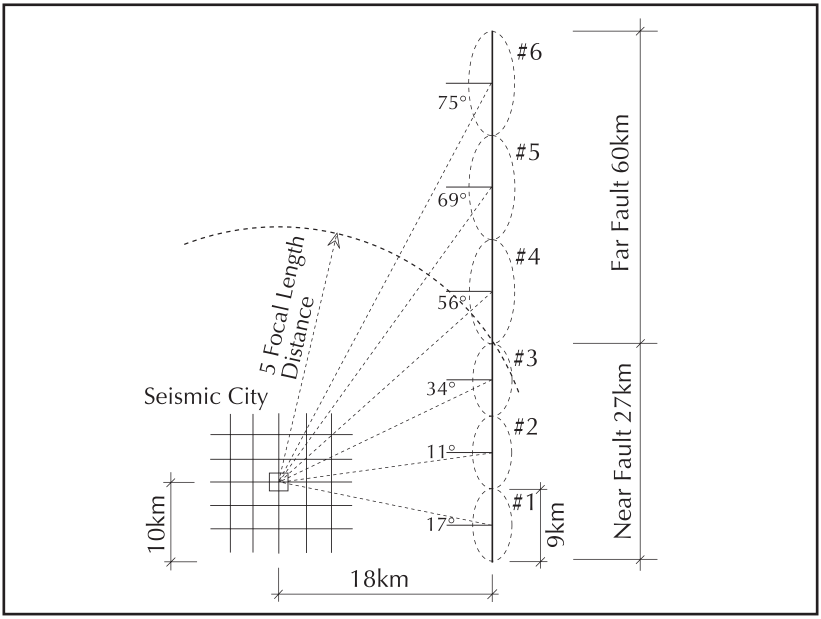

■ **Figure 14.2 Seismic City and XYZ Fault**

Seismic City is fairly flat and, hence, seismically induced landslides are unlikely. Also since the surfacial soils are clay, liquefaction and lateral spreading are not expected. Hence, the only seismic hazard of interest is wave propagation.

Since one expects differences in propagation velocity for seismic waves from "near" and "far" sources, peak ground velocity from the USGS Probablistic Seismic Hazard Analysis (PSHA) cannot be used directly. The PSHA peak ground velocity is due to both near and far sources and cannot be disaggregated based upon distance.

The boundary between the "near" and "far" sources is based upon the 1984 ASCE Guidelines, which suggest that body waves are expected for seismic sources within five focal depths of the site (i.e., within 25 km of Seismic City for the 5 km expected focal depth associated with events on the XYZ fault). The project geotechnical earthquake engineer estimates a PGV (V_{max}) of 28 cm/sec for near (body wave) sources and 18 cm/sec for far (surface wave) sources.

Finally, the project geotechnical estimates the average shear wave velocity in the top 50 m of soil between the fault and Seismic City to be 350 m/sec.

Expected Repairs in SCWD

The ground strains due to the "near" fault segment (assumed body waves) and the "far" fault segment (assumed surface waves) need to be evaluated.

As noted in Chapter 3, the peak ground strain for body wave propagation (assumed 45° angle of attack) can be estimated using Equation 3.7 with C_s = 1,000 m/sec:

$$\varepsilon_{body} = \frac{V_{max}}{2C_s} = \frac{0.28\text{ m/sec}}{2(1{,}000\text{ m/sec})}$$
$$= 1.4 \times 10^{-4}$$

Again from Chapter 3, ground strain due to surface wave (specifically, R-waves) can be estimated using Equation 3.5 with the propagation velocity C_R taken as twice the shear wave velocity of the top 50 m of soil:

$$\varepsilon_{surface} = \frac{V_{max}}{C_R} = \frac{0.18\text{ m/sec}}{2(350\text{ m/sec})}$$
$$= 2.6 \times 10^{-4}$$

From Figure 12.5, the relation between repairs per kilometer (*RR*) and ground strain is:

$$\log(RR) = 1.12\ \log(\varepsilon) + 3.28$$

For a ground strain ε of 1.4×10^{-4}, we get:

$$\log(RR) = 1.12\ \log(1.4 \times 10^{-4}) + 3.28$$

$$= -1.036$$

or

$$RR = 0.092 \text{ repairs per km}$$

For a ground strain of 2.6×10^{-4}, the repair rate is 0.18 repairs per km. For the 400 km SCWD network, this results in 37 and 74 repairs, respectively.

Hence, SCWD can expect roughly 40 to 80 repairs to their system (one repair for every 5 to 10 km of pipeline) given the occurrence of the design event in the near or far fault regions, respectively.

BK & M Industries Water Line

For the SCWD network, the direction of the traveling waves was not a major concern since, presumably, there were comparable amounts of east-west pipe and north-south pipe. However, the BK & M Industries line runs in one specific direction (east-west) and, hence, the direction of wave travel can strongly impact the resulting ground strain.

The 27 km length of the "near" fault segment is subdivided into three 9 km subsegments. The center of the southern most subsegment (Subsegment #1) is 18 km east and 5.5 km south of Seismic City. That is, the southern subsegment is located ESE of Seismic City and the body wave angle of attack would be at 17° with respect to the east-west axis of the BK & M pipeline. The angles between the BK & M pipeline and the propagation directions for the other two near fault subsegments are presented in Table 14.1. As noted in Chapter 10 (Section 10.1.1), Equation 10.1 provides the body wave ground strain for an arbitrary angle of attack:

$$\varepsilon_{body} = \frac{V_{\max} \sin\gamma \cos\gamma}{C_s}$$

For V_{max} = 0.28 m/sec and C_s = 1,000 m/sec the body wave ground strain parallel to the pipe axis for a 17° angle of attack is:

$$\varepsilon_{body} = \frac{(0.28\,\text{m/sec}) \cdot \sin 17° \cdot \cos 17°}{1{,}000\,\text{m/sec}} = 7.8 \times 10^{-5}$$

The body wave ground strains for the other two near fault subsegments are presented in Table 14.1. The resulting number of repairs per kilometer from Figure 12.5 are 0.0477, 0.030 and 0.0839, respectively.

Table 14.1 Ground Strain and Repair Rates for BK & M Industries Pipeline

	Subsegment	Peak Ground Strain ε_g	Attack Angle	Ground Strain II to pipe ε_p	Repair Rate Figure 12.5 (rep/km)
Near Fault	1	1.4×10^{-4}	17°	7.8×10^{-5}	0.0477
	2	1.4×10^{-4}	11°	5.2×10^{-5}	0.0303
	3	1.4×10^{-4}	34°	1.29×10^{-5}	0.0834
Far Fault	4	2.6×10^{-4}	56°	8.1×10^{-5}	0.049
	5	2.6×10^{-4}	69°	3.3×10^{-5}	0.018
	6	2.6×10^{-4}	75°	1.7×10^{-5}	0.009

A similar analysis is undertaken for the far fault segment. The northern most of the three far fault subsegments has its midpoint at 18 km east and 67 km north of Seismic City, and thus has an angle of attack of 75° with respect to the BK & M pipeline.

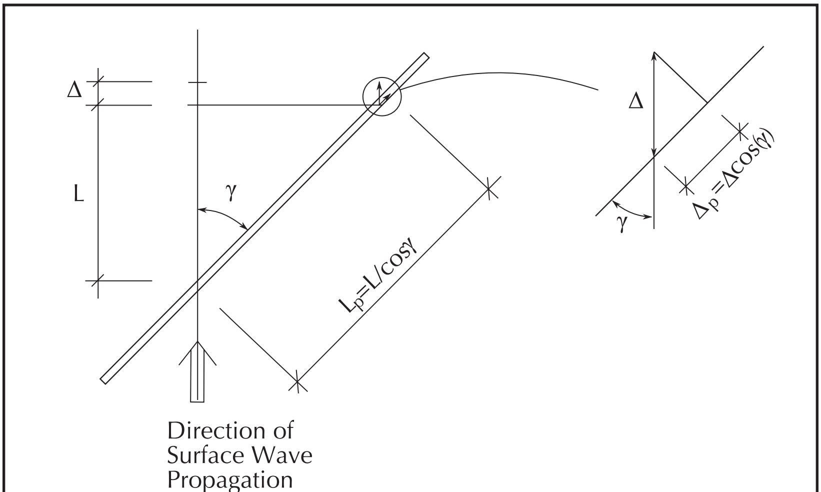

Figure 14.3 Surface Wave Ground Strain Along Pipeline Axis

The relation for the ground strain along a pipe axis for surface waves traveling at an angle of attack γ is developed in Figure 14.3. The peak ground strain is along the direction of wave propagation. The displacement at a distance L is $\Delta = \varepsilon \cdot L$. The corresponding length along the pipeline, is $L_p = L/\cos\gamma$. The component of ground displacement parallel to the pipe is:

$$\Delta_p = \Delta \cdot \cos\gamma$$

Hence, the ground strain parallel to the pipeline axis is:

$$\varepsilon_p = \frac{\Delta_p}{L_p} = \frac{\Delta \cdot \cos\gamma}{L/\cos\gamma}$$

or

$$\varepsilon_p = \varepsilon \cdot \cos^2\gamma$$

Hence, for a surface wave ground strain parallel to the direction of propagation of 2.6×10^{-4}, the ground strain along the pipeline of a 75° angle of attack is:

$$\varepsilon_p = 2.6 \times 10^{-4} \left(\cos 75°\right)^2$$
$$= 1.7 \times 10^{-5}$$

The parallel to the pipe ground strains for the other two far fault subsegments are presented in Table 14.1. From Figure 12.5, the resulting expected repair rates for a ground strain of 1.7×10^{-5} is 0.0091 repairs per km. Expected repair rates for other far fault subsegments are presented in Table 14.1.

From Table 14.1, the average expected rate for sources in the near fault region is 0.054, while rate in the far fault region is 0.0252. Since the probability is the same for the design event originating from any given point along the whole fault, the weight average expected repair rate from Figure 12.5 is:

$$RR = \frac{60\,\text{km}(0.0252) + 27\,\text{km}(0.054)}{87\,\text{km}}$$
$$= 0.034$$

This expected repair rate specifically applies to the pipe diameter database upon which Figure 12.5 is based. The most common pipe in that database was 6-inch-diameter CI pipe. Since this happens to be the same pipe as the majority of the SCWD system, no correction was applied when determining expected repair rates for the SCWD system as a whole. However, the BK & M Industries pipe has a larger diameter (24 in) and joint embedment distance than the typical 6-inch-diameter pipe upon which Figure 12.5 was based. According to Table 4.7, the embedment distance for 24-inch CI pipe is 4.0 in, while the corresponding value for 6-inch CI pipe is 3.5 in. A larger embedment distance requires a larger ground strain for a joint pull-out or a joint crushing failure. Given the near linear relation between repair rate and ground strain, it is reasonable to reduce the 6-inch pipe expected repair rate by the ratio of embedment distances. Hence, the expected number of repairs along the 3.2 km length of the BK & M pipeline is:

$$\begin{aligned}\text{Expected \# repairs} &= \frac{0.034\,\text{rep}}{\text{km}} \cdot 3.2\,\text{km} \cdot \frac{3.5\,\text{in}}{4.0\,\text{in}} \\ &= 0.095\end{aligned}$$

That is there is roughly a 10% probability of damage to the BK & M line given the design event.

14.3 Orientation for Offshore Pipeline in Mississippi River Delta

A 10-inch-diameter (10.75 O.D.) offshore pipeline will be used to transport crude oil across the Mississippi River Delta (MRD) where landslides are frequently triggered by hurricanes or earthquakes. X-60 grade steel pipe with a 0.5-inch (0.0127-m) wall thickness are selected based upon the internal design pressure and external hydro-static pressure. A 1-meter burial depth is required for the pipeline since water depth is less than 200 ft (61 m). The shear strength of the frictionless soil at the seabed is 50 psf (2.4 kN/m^2) with an 8.0 psf per ft (1.26 kN/m^2 per m) increase with depth. The deposition rate for soil is estimated to be 1 to 2 ft/year (0.3 to 0.6 m/year). The length (or drag length) of the block of soil, which moves downslope (spatial extent of the design landslide parallel to the direction of movement), is expected to be 820 ft (250 m), while the width (i.e., spatial extent perpendicular to the direction of movement) is expected to be 1,000 ft (310 m). Finally, the expected amount of ground movement is 80 ft (18 m). Hence, the run-out distance (distances from the head of the sliding block before movement to the toe of the sliding block after movement) is 900 ft (820 + 80). The problem is to determine the most favorable pipeline orientation with respect to the direction of landslide movement.

Design Data

Due to the high deposition rate, the burial depth of the pipe increases significantly over the course of its 30-year design life. Since the soil shear strength increases with depth, the strength of the soil immediately surrounding the pipe, as well as the force induced in the pipe by a given landslide, similarly increases with age.

The design engineer has recommended and the pipeline owners have approved a design based upon deposition rate of 2 ft per year (high end of expected range) and a landslide occurring at 15 years (the midpoint of the 30-year design life).

Hence, the burial depth at the time of the landslide is estimated to be the initial 3.2-foot burial depth plus 15 years worth of 2 ft per year of new seabed deposition, or a total of 33.2 ft (10 m). Note that according to Gilbert et al. (2007), the thickness of the sliding block (depth to sliding interface) is 50 to 100 ft (15 to 30 m) for landslides in the MRD. Hence, the pipeline is expected to still be within the moving soil mass. The shear soil strength at this 33.2-foot depth is:

$$S_u = 50\,\text{psf} + 8.0\,\frac{\text{psf}}{\text{ft}}(33.2\text{ ft}) = 315\,\text{psf}$$

The peak soil resistance to axial movement of the pipe is given in Equation 5.3:

$$t_u = \pi \cdot D \cdot \alpha \cdot S_u$$

where the adhesion factor α from Figure 5.2 is about 1.0 for such a low shear strength. Hence, the resistance to axial movement is:

$$t_u = \frac{\pi(10.75\text{ in})(1.0)(315\text{ psf})}{12\text{ in/ft}} = 888\text{ lbs/ft}$$

The peak resistance to transverse movement is given in Equation 5.9:

$$p_u = S_u \cdot N_{ch} \cdot D$$

where the horizontal bearing capacity factor for clay from Figure 5.6(b) is $N_{ch} = 7$ for H/D greater than ten. Hence:

$$p_u = P_{u1} = P_{u2} = (315\,\text{psf})(7)\frac{10.75\,\text{in}}{12\,\frac{\text{in}}{\text{ft}}} = 1{,}980\,\frac{\text{lbs}}{\text{ft}}$$

For the X-60 steel pipe, the Ramberg-Osgood parameters are σ_y = 60 ksi (414 MPa), n = 10, r = 12 from Table 4.1.

Parallel Orientation

The ground movements associated with offshore landslides are typically large, and pipe behavior is controlled by the spatial extent of the landslide zone (plan dimension parallel to the direction of ground movement). Assuming the soil drag force is shared equally between tension at the head and compression at the toe, peak tensile and peak compressive pipe strains ε_a and displacement for Case I in Figure 6.5 are calculated from Equations 6.3 and 6.4 with $x = L/2$.

For the offshore pipe in question with D/t = 21.5, the tensile capacity (taken to be 2.0% strain) is comparable to the compressive capacity (taken to be 0.5 t/D – 0.0025 or 2.1% from Equation 4.10).

The pipe burial parameter is calculated using Equation 6.7:

$$\beta_p = \alpha \cdot \frac{S_u}{t}$$

or

$$\beta_p = 1.0(315\,\text{psf})\left(12\,\tfrac{\text{in}}{\text{ft}}\right)/\,0.5\,\text{in} = 7.6\,\text{kips per ft}^3$$

The critical landslide length, which causes a peak pipe strain of 2%, is calculated from Equation 6.3. That is:

$$\varepsilon(L/2) = \frac{\beta_p L}{2E}\left\{1 + \frac{n}{1+r}\left(\frac{\beta_p \cdot L}{2\sigma_y}\right)^r\right\}$$

or

$$0.02 = \frac{7.6\,\text{k/ft}^3\left(\frac{L_{cr}}{2}\right)}{29.000\,\text{ksi}\cdot(12\,\text{in/ft})^2}\left\{1 + \frac{10}{1+12}\left(\frac{7.6\,\text{k/ft}^3\,(L_{cr})}{2\,\text{x}\,60\,\text{ksi}\cdot(12\,\text{in/ft})^2}\right)^{12}\right\}$$

The critical landslide length is 2,749 ft (838 m), beyond which the peak pipe strain would exceed the design strain limit of 2%.

At the critical landslide length, the peak pipe displacement is calculated from Equation 6.4, again with $x = L/2$:

$$\delta_p = \frac{\beta_p \left(\frac{L}{2}\right)^2}{E}\left\{1 + \frac{2}{2+r}\cdot\frac{n}{1+r}\left(\frac{\beta_p L}{2\sigma_y}\right)^r\right\}$$

or

$$\delta_p = \frac{7.6\ \text{k/ft}^3\left(1{,}374\ \text{ft}\right)^2}{29{,}000\ \text{ksi}\left(144\ \text{in}^2/\text{ft}^2\right)}\left\{1 + \frac{2}{2+12}\cdot\frac{10}{1+12}\left(\frac{7.6\ \text{k/ft}^3(1{,}374\ \text{ft})}{60\ \text{ksi}(144)}\right)^{12}\right\}$$

$$\delta_p = 6.94\ \text{ft}$$

which is less than the expected amount of ground movement. That is, the assumption of Case I behavior is confirmed. Hence, in a parallel orientation, the pipe can accommodate an offshore landslide with a length of 2,750 ft.

For offshore pipe with shallow burial, one expects the landslide behavior to be controlled by tension at the head of the slide with Euler or beam buckling (but no local buckling and potential tearing of the pipe wall) at the toe of the slide.

Perpendicular Orientation

When subjected to transverse PGD as shown in Figure 7.32, the pipe will experience both bending and axial strain. The axial strain from Equation 7.28 is:

$$\varepsilon_a = \frac{T_o}{AE}\left\{1 + \frac{n}{1+r}\left(\frac{T_o}{A\cdot\sigma_y}\right)^r\right\}$$

or

$$\varepsilon_a = \frac{T_o}{\pi\,(10.75\ \text{in})(0.5\ \text{in})(29{,}000\ \text{ksi})}\left\{1 + \frac{10}{1+12}\left(\frac{T_o}{\pi\,(10.75)(0.5)(60\ \text{ksi})}\right)^{12}\right\}$$

The pipe bending strain from Equation 7.29 is:

$$\varepsilon_b = \frac{D}{2}\cdot\frac{P_{u1}}{T_o}$$

or

$$\varepsilon_b = \frac{(10.75\text{ in})}{2(12\text{ in/ft})} \cdot \frac{198\text{ k/ft}}{T_o}$$

The critical value of the peak tensile force within the PGD zone, T_o, for which the combine strain is 2.0%,

$$\varepsilon_a + \varepsilon_b = 0.02$$

can be determined by iteration to be T_o = 1,217 kips (5,520 kN). The critical width—that is, the value for $2W_1$ for which T_o = 1,217 kips (total strain = 2%)—can be determined by equating the change in length from Equation 7.25:

$$\Delta L = \frac{1}{3} P_{u1}{}^2 \cdot W_1^3 \left(1 + \frac{P_{u1}}{P_{u2}}\right) / T_o{}^2$$

or

$$\Delta L = \frac{1}{3}(1.98\,{}^{\text{k}}\!/\!_{\text{ft}})^2 \cdot W_1^3 \left(1 + \frac{1.98\,{}^{\text{k}}\!/\!_{\text{ft}}}{1.98\,{}^{\text{k}}\!/\!_{\text{ft}}}\right) / (1217\text{ k})^2$$

with the corresponding value from Equation 7.26:

$$\Delta L = \frac{2W_1 T_o}{AE}(1+\chi) + \frac{T_o{}^2}{AEt_u}\left(1 + \frac{2}{2+r}\chi\right)$$

where

$$\chi = \frac{n}{1+r}\left(\frac{T_o}{A\sigma_y}\right)^r$$

or

$$\Delta L = \frac{1217\text{ k}}{\pi(10.75\text{ in})(0.5\text{ in})(29{,}000\text{ ksi})}\left[2W_1(1+\chi) + \frac{1217\text{ k}}{0.89\,\frac{\text{k}}{\text{ft}}}\left(1 + \frac{2}{2+12}\chi\right)\right]$$

and

$$\chi = \frac{10}{1+12}\left[\frac{1217\text{ k}}{\pi(10.75\text{ in})(0.5\text{ in})(60\text{ ksi})}\right]^{12} = 6.95$$

Iteration results in W_1 = 201 ft. Hence, the maximum width of the landslide zone, for which the pipe strain is no more than 2.0%, is 2 W_1 = 402 ft.

The corresponding peak lateral displacement of the pipe (at center of landslide) is given by Equations 7.20 and 7.21:

$$\delta_T = \delta_1 + \delta_2 = \frac{P_{u1} W_1^{\ 2}}{2T_o} + \frac{P_{u1} W_2^{\ 2}}{2T_o}$$

or

$$\delta_T = 2\left(\frac{\frac{1.98^{\mathrm{k}}}{\mathrm{ft}}\left(201\,\mathrm{ft}\right)^2}{2\left(1{,}217\,\mathrm{k}\right)} \right) = 65.6\ \mathrm{ft}$$

Since this pipe displacement is less than the expected landslide movement of 80 ft, the result is consistent with the assumption of the model.

In summary, since the expected drag length (820 ft) of the design landslide (plan dimension parallel to the direction of ground movement) is less than the 2,749 ft length, which results in 2% pipe strain, the parallel crossing is feasible. However, since the expected width (1,000 ft) of the design landslide (plan dimension perpendicular to the direction of ground movement) is more than the 402 ft width, which results in 2% pipe strain, the perpendicular crossing is not feasible. An oblique crossing (neither parallel nor perpendicular) would be worse. Hence, the parallel orientation is preferred.

References

Abdoun, T., Ha, D., O'Rourke, M., Symans, M., O'Rourke, T., Palmer, M., and Stewart, H., (2008), "Buried HDPE Pipeline Subjected to Normal Faulting – A Centrifuge Investigation," *Canadian Journal Goetechnical Engineering*, Vol. 45, pp. 1733-1742.

Abdoun, T., Ha, D., O'Rourke, M., Symans, M., O'Rourke, T., Palmer, M., and Stewart, H., (2009), "Factors Influencing the Behavior of Buried Pipelines Subject to Earthquake Faulting," *Soil Dynamics and Earthquake Engineering*, Vol. 29, pp. 415-427.

Akiyoshi, T., Fuchida, K., Shirinashihama, S., and Tsutsumi, T., (1994), "Effectiveness of Anti-Liquefaction Techniques for Buried Pipelines," *Journal of Pressure Vessel Technology*, Vol. 116, August, pp. 261-266.

American Lifeline Alliance (ALA), (2001), "Guidelines for the Design of Buried Steel Pipe," FEMA, 75p.

American Lifeline Alliance (ALA), (2002), "Seismic Fragility Formulations for Water Systems," www.americanlifelinealliance.org.

American Lifeline Alliance (ALA), (2005), "Design Guidelines for Seismic Resistant Water Pipeline Installations," FEMA, 255p.

American Society of Civil Engineers (ASCE), (1984), Guidelines for the Seismic Design of Oil and Gas Pipeline Systems, Committee on Gas and Liquid Fuel Lifelines, ASCE.

Ando, H. Sato, S., and Takagi, N., (1992), "Seismic Observation of a Pipeline Buried at the Heterogeneous Ground," *Proceedings of the Tenth World Conference on Earthquake Engineering*, Balkema, Rotterdam, pp. 5563-5567.

Applied Technology Council (ATC), (1985), Earthquake Damage Evaluation Data for California, ATC-13, Redwood City, California.

Ariman, T. and Lee, B.J., (1989), "On Beam Mode of Buckling of Buried Pipelines," *Proceedings of the Second U.S.-Japan Workshop on Liquefaction, Large Ground Deformation and Their Effects on Lifelines*, Buffalo, New York, Technical Report NCEER-89-0032, Multidisciplinary Center for Earthquake Engineering Research, Buffalo, New York, pp. 401-412.

Ariman, T. and Lee, B.J., (1991), "Tension/Bending Behavior of Buried Pipelines Under Large Ground Deformation in Active Faults," *Proceedings of the Third U.S. Conference on Lifeline Earthquake Engineering*, Technical Council on Lifeline Earthquake Engineering, Monograph No. 4, ASCE, pp. 226-233.

Audibert, J.M.E. and Nyman, K.J., (1977), "Soil Restraint Against Horizontal Motion of Pipes," *Journal of Geotechnical Engineering Division*, ASCE, Vol. 103, No. GT10, pp. 1119-1142.

Ayala, G. and O'Rourke, M., (1989), "Effects of the 1985 Michoacan Earthquake on Water Systems and Other Buried Lifelines in Mexico," Technical Report NCEER-89-0009, Multidisciplinary Center for Earthquake Engineering Research, Buffalo, New York.

Ballantyne, D.B., Berg, E., Kennedy, J., Reneau, R., and Wu, D., (1990), "Earthquake Loss Estimation Modeling of the Seattle Water System," Report to U.S. Geological Survey, Grant 14-08-0001-G1526, October 1990.

Ballantyne, D.B., (1992), "Thoughts on a Pipeline Design Standard Incorporating Countermeasure for Permanent Ground Deformation," *Proceedings of the Fourth Japan-U.S. Workshop on Earthquake Resistant Design of Lifeline Facilities and Countermeasures for Soil Liquefaction*, Honolulu, Hawaii, Technical Report NCEER-92-0019, Multidisciplinary Center for Earthquake Engineering Research, Buffalo, New York, pp. 875-887.

Bardet, J.P., Tobita, T., Mace, N., and Hu, J., (2002), "Regional Modeling of Liquefaction – Induced Ground Displacement," *Earthquake Spectra*, Vol. 18, No.1, pp. 19-46.

Barenberg, M.E., (1988), "Correlation of Pipeline Damage with Ground Motions," *Journal of Geotechnical Engineering*, ASCE, June, Vol. 114, No. 6, pp. 706-711.

Bartlett, S.F. and Youd, T.L., (1992), "Empirical Analysis of Horizontal Ground Displacement Generated by Liquefaction-induced Lateral Spreads," Technical Report NCEER-92-0021, Multidisciplinary Center for Earthquake Engineering Research, Buffalo, New York.

Bouabid, J. and O'Rourke, M.J., (1994), "Seismic Vulnerability of Concrete Pipelines," *Proceedings of the Fifth U.S. National Conference on Earthquake Engineering*, Chicago, Illinois, EERI, July, Vol. IV, pp. 789-798.

Bouabid, J.(1995), "Behavior of Rubber Gasketed Concrete Pipe Joints During Earthquake," Ph.D. Thesis, Rensselaer Polytechnic Institute, December.

Brockenbrough, R.L., (1990), "Strength of Bell-and-Spigot Joints," *Journal of Structural Engineering*, Vol. 116, No. 7, pp. 1983-1991.

Brown, R.W., (1995), *Practical Foundation Engineering Handbook*, McGraw-Hill.

Bruton, D., White, D., Cheuk, J., Bolton, M., and Carr, M., (2006), "Pipe-Soil Interaction Behavior During Lateral Buckling, Including Large-Amplitude Cyclic Displacement Tests by the Safebuck JIP," Offshore Technology Conference, OTC-17944, Houston, Texas, May.

Bruton, D., White, D., Carr, M., and Cheuk, J., (2008), "Pipe-Soil Interaction During Lateral Buckling and Pipeline Walking – The Safebuck JIP," Offshore Technology Conference, OTC-19589, Houston, Texas, May.

Bukovansky, M., Greenwood, J.H., and Major, G., (1985), "Maintaining Natural Gas Pipeline in Active Landslides," *Advances in Underground Pipe Engineering*, ASCE, (J.K. Jeyapalan, Editor), pp. 438-448.

Cai, J., Liu, X., Hou, Z., and Chen, G., (1992), "Experimental Research on the Liquefaction Response of Oil Supply Pipeline," *Proceedings of the Second International Symposium on Structural Technique of Pipeline Engineering*, Beijing, China, pp. 284-291.

Campbell, K.W. and Bozorgnia, Y., (2008), “NGA Ground Motion Model for the Geometric Mean Horizontal Component of PGA, PGV, PGD and 5% Damped Linear Elastic Response Spectra for Periods Ranging from 0.01 to 10s,” *Earthquake Spectra*, Vol. 24, No. 1, February, pp. 139-171.

Canadian Standards Association (CSA) (2003), Oil and Gas Pipeline Systems, Z662-03, Annex C-Limit States Design, Ontario, Canada.

Choo, Y., Abdoun, T., O’Rourke, M., and Ha, D., (2007), “Remediation for Buried Pipeline Systems Under Permanent Ground Deformation,” *Soil Dynamics and Earthquake Engineering,* Vol. 27, pp. 1043-1055.

Das, S., Cheng, J., Murray, D., Wilkie, S., and Zhou, Z., (2000), “Laboratory Study of Local Buckling, Wrinkle Development, and Strains for NPS12 Linepipe,” *Proceedings of the 2000 International Pipeline Conference*, ASME 2000, Vol. 2, pp. 909-915.

Das, S., Cheng, J., Murray, D., and Nazemi, N., (2008), “Effects of Monotonic and Cyclic Bending Deformations on NPS12 Wrinkled Steel Pipe,” *Journal of Structural Engineering*, ASCE, Vol. 134, No. 12, December, pp. 1810-1817.

Demars, K.R., (1978), “Design of Marine Pipelines for Areas of Unstable Sediment,” *Transportation Journal*, Vol. 104 (1), pp. 109-112.

Dingle, H., White, D., and Gaudin, C., (2008), “Mechanisms of Pipe Embedment and Lateral Breakout on Soft Clay,” *Canadian Geotechnical Journal*, Vol. 45, pp. 636-652.

DNV (2000), Offshore Standard OS-F101, Submarine Pipeline Systems, DNV, Norway.

Dobry, R. and Baziar, M.H., (1990), “Evaluation of Ground Deformation Caused by Lateral Spreading,” *Proceedings of the Third Japan-U.S. Workshop on Earthquake Resistant Design of Lifeline Facilities and Countermeasures for Soil Liquefaction*, San Francisco, California, December 17-19, Technical Report NCEER-91-0001, Multidisciplinary Center for Earthquake Engineering Research, Buffalo, New York, pp. 209-224.

Dorey, B., Murray, D., and Cheng, J., (2000), “An Experimental Evaluation of Critical Buckling Strain Criteria,” *Proceedings of 2000 International Pipeline Conference*, Vol. 1, pp. 71-80, IPC00-0157.

Dorey, B., Murray, D., and Cheng, J., (2006), “Critical Buckling Strain Equation for Energy Pipelines-A Parametric Study,” *Journal of Offshore Mechanics and Arctic Engineering*, Vol. 128, No. 3, pp. 248-255.

EDM Services (1993), “Hazardous Liquid Pipeline Risk Assessment,” prepared for California State Fire Marshall, Semi Valley, California, 187p.

Eguchi, R.T., (1983), “Seismic Vulnerability Models for Underground Pipes,” Earthquake Behavior and Safety of Oil and Gas Storage Facilities, Buried Pipelines and Equipment, PVP-77, ASME, New York, New York, June, pp. 368-373.

Eguchi, R.T., (1991), “Early Post-Earthquake Damage Detection for Underground Lifelines,” Final Report to the National Science Foundation, Dames and Moore P.C., Los Angeles, California.

Eidinger, J.M., Maison, B., Lee, D., and Lau, B., (1995), “East Bay Municipal Utility District Water Distribution Damage in 1989 Loma Prieta Earthquake,” *Proceedings of the Fourth U.S. Conference on Lifeline Earthquake Engineering*, ASCE, TCLEE, Monograph No. 6, ASCE, August, pp. 240-247.

Eidinger, J.M., (1999), "Girth Joints in Steel Pipelines Subjected to Wrinkling and Ovaling," *Proceedings of the Fifth U.S. Conference on Lifeline Earthquake Engineering*, TCLEE Monograph No. 16 Optimizing Post Earthquake Lifeline System Reliability.

Eidinger, J.M., Bachhuber, J., and O'Rourke, M., (2002), "Performance of a Pipeline at a Faulty Crossing," *Proceedings of the Seventh U.S. National Conference on Earthquake Engineering*, Boston, Massachusetts.

El Hmadi, K. and O'Rourke, M.J., (1989), "Seismic Wave Effects on Straight Jointed Buried Pipeline," Technical Report NCEER-89-0022, Multidisciplinary Center for Earthquake Engineering Research, Buffalo, New York.

El Hmadi, K. and O'Rourke, M.J., (1990), "Seismic Damage to Segmented Buried Pipelines," *Earthquake Engineering and Structural Dynamics*, May, Vol. 19, No. 4, pp. 529-539.

Flores-Berrones, R. and O'Rourke, M., (1992), "Seismic Effects on Underground Pipelines Due to Permanent Longitudinal Ground Deformations," *Proceedings of the Fourth Japan-U.S. Workshop on Earthquake Resistant Design of Lifeline Facilities and Countermeasures for Soil Liquefaction*, Honolulu, Hawaii, Technical Report NCEER-92-0019, Multidisciplinary Center for Earthquake Engineering Research, Buffalo, New York, pp. 465-480.

Ford, D.B., (1983), "Joint Design for Pipelines Subjected to Large Ground Deformations," Earthquake Behavior and Safety of Oil and Gas Storage Facilities, Buried Pipelines and Equipment, PVP-77, ASME, New York, New York, June, pp. 160-165.

Fujii, Y., Ohtomo, K., Arai, H., and Hasegawa, H., (1992), "The State of the Art in Mitigation of Liquefaction for Lifeline Facilities in Japan," *Proceedings of the Fourth Japan-U.S. Workshop on Earthquake Restraint Design of Lifeline Facilities and Countermeasures for Soil Liquefaction*, Honolulu, Hawaii, Technical Report NCEER-92-0019, Multidisciplinary Center for Earthquake Engineering Research, Buffalo, New York, pp. 889-909.

G&E, (1994), NIBS Earthquake Loss Estimation Methods, Technical Manual, (Water Systems), May.

Gilbert, R., Nodine, M., Wright, S., Cheon, J., Wrzyszczynski, M., Coyne, M., and Ward, E., (2007), "Impact of Hurricane-Induced Mudslides on Pipelines," OTC 18983, Offshore Technology Conference, Houston, Texas, April-May.

Goodling, E.C., (1983), "Buried Piping — An Analysis Procedure Update," Earthquake Behavior and Safety of Oil and Gas Storage Facilities, Buried Pipelines and Equipment, PVP-77, ASME, New York, New York, June, pp. 225-237.

Gresnigt, A.M., (1986), "Plastic Design of Buried Steel Pipelines in Settlement Areas," *HERON*, Vol. 31, No. 4.

Guo, P. and Stolle, D., (2005), "Lateral Pipe-Soil Interaction in Sand with Reference to Scale Effects," *Journal of Geotechnical and Geoenvironmental Engineering*, ASCE, Vol. 131, No. 3, pp. 338-349.

Ha, D., Abdoun, T., O'Rourke, M., Symans, M., O'Rourke, T., Palmer, M., and Stewart, H., (2008), "Centrifuge Modeling of Earthquake Effects on Buried High-Density Polyethylene (HDPE) Pipelines Crossing Fault Zones," *Journal of Geotechnical and Geoenvironmental Engineering*, ASCE, Vol. 134, No. 10, pp. 1501-1515.

Ha, D., Abdoun T., O'Rourke, M., Symans, M., O'Rourke, T., Palmer, M., and Stewart, H., (2010), "Earthquake Faulting Effects on Buried Pipelines – Case History and Centrifuge Study," *Journal of Earthquake Engineering*, Vol. 14, No. 5, pp. 646-669.

Hall, J.F., (1995), "Northridge Earthquake of January 17, 1994, Reconnaissance Report," *Earthquake Spectra*, EERI, April.

Hamada, M., Yasuda, S., Isoyama, R., and Emoto, K., (1986), "Study on Liquefaction Induced Permanent Ground Displacements," Association for the Development of Earthquake Prediction, Japan, 87p.

Hamada, M., Towhata, T., Yasuda, S., and Isoyama, R., (1987), "Study of Permanent Ground Displacement Induced by Seismic Liquefaction," *Computers and Geotechnics*, Elsevier Applied Science Publishers, Vol. 4, No. 4, pp. 197-220.

Hamada, M. and O'Rourke, T.D., (1992), "Large Ground Deformations and Their Effects on Lifelines," *Japanese Case Studies of Liquefaction and Lifeline Performance During Past Earthquakes*, Technical Report NCEER-92-0001, Multidisciplinary Center for Earthquake Engineering Research, Buffalo, New York.

Hance, J.J. and Wright, S., (2003), "Development of a Database and Assessment of Seafloor Slope Stability Based on Published Literature," Project Report Prepared for the Minerals Management Service Under the MMS/OTRC Cooperative Research Agreement, MMS Project 421, August.

Hansen, J.B. (1961), "The Ultimate Resistance of Rigid Piles Against Transversal Forces," Bulletin 12, Danish Geotechnical Institute, Copenhage, Denmark.

Harris, L., Sver, H., Skene, W., and Benjamin, R., (1957), "Stability of Thin-Walled Unstiffened Circular Cylinders Under Axial Compression Including the Effects of Internal Pressure," *Journal of Aeronautical Sciences*, Vol. 24, No. 8, pp. 587-596.

Haskell, N.A., (1953), "The Dispersion of Surface Waves in Multilayered Media," *Bulletin of the Seismological Society of America*, Vol. 43, No. 1, pp. 17-34.

Heubach, W.F., (1995), "Seismic Damage Estimation for Buried Pipeline Systems," *Proceedings of the Fourth U.S. Conference on Lifeline Earthquake Engineering*, Technical Council on Lifeline Earthquake Engineering, Monograph No. 6, ASCE, pp. 312-319.

Hobbs, R.E., (1981), "Pipeline Buckling Caused by Axial Loads," *Journal of Constructional Steel Research*, January, Vol. 1, No. 2, pp. 2-10.

Honegger, D.G. and Eguchi, R.T., (1992), "Determination of Relative Vulnerabilities to Seismic Damage for San Diego County Water Authority (SDCWA) Water Transmission Pipelines," October.

Honegger, D.G., (1994), "Assessing Vulnerability of BC Gas Pipelines to Lateral Spread Hazards," *Proceedings of the Fifth U.S.-Japan Workshop on Earthquake Design of Lifeline Facilities and Countermeasures Against Soil Liquefaction*, MCEER-94-0026, pp. 515-530.

Honegger, D.G., (1995), "An Approach to Extend Seismic Vulnerability Relationships for Large Diameter Pipelines," *Proceedings of the Fourth U.S. Conference on Lifeline Earthquake Engineering*, Technical Council on Lifeline Earthquake Engineering, Monograph No. 6, ASCE, pp. 320-327.

Honegger, D.G., (1999), "Assessment of Wave Propagation Effects on a 1925 Pipeline with Oxyacetylene Girth Welds," Optimizing Post Earthquake Lifeline System Reliability, *Proceedings of the Fifth U.S. Conference on Lifeline Earthquake Engineering*, ASCE, TCLEE, Monograph No. 16, pp. 414-423.

Honegger, D.G., (2000), "Wave Propagation Versus Transient Ground Displacement as a Credible Threat to Buried Oil and Gas Pipelines," *Proceedings of the 2000 International Pipeline Conference*, Calgary, Alberta, ASCE, pp. 363-372.

Honegger, D.G., and Nyman, D., (2004), "PRCI Guidelines for the Seismic Design and Assessment of Natural Gas and Liquid Hydrocarbon Pipelines," Pipeline Research Council International, published by Technical Toolboxes, Houston, Texas.

Honegger, D.G., Nyman, D., and Youd, T., (2006), "Liquefaction Hazard Mitigation for Oil and Gas Pipelines," *Proceedings of the Eighth U.S. National Conference on Earthquake Engineering*, EERI, Paper No. 1035.

Hou, Z., Cai, J., and Liu, X., (1990), "Response Calculation of Oil Pipeline Subjected to Permanent Ground Movement Induced by Soil Liquefaction," *Proceedings of the China-Japan Symposium on Lifeline Earthquake Engineering*, Beijing, China, pp. 107-114.

Howard, J.H., (1968), "Recent Deformation at Buena Vista Hills, California," *American Journal of Science*, November, Vol. 266, pp. 737-757.

Isenberg, J. and Taylor, C., (1984), "Performance of Water and Sewer Lifelines in the May 2, 1983 Coalinga California Earthquakes," *Lifeline Earthquake Engineering: Performance Design and Construction*, ASCE, pp.176-189.

Isenberg, J. and Richardson, E., (1989), "Countermeasures to Mitigate Damage to Pipelines," *Proceedings of the Second U.S.-Japan Workshop on Liquefaction, Large Ground Deformation and Their Effects on Lifelines*, Buffalo, New York, Technical Report NCEER-89-0032, Multidisciplinary Center for Earthquake Engineering Research, Buffalo, New York, pp. 468-482.

Isoyama, R. and Katayama, T., (1982), Reliability Evaluation of Water Supply Systems During Earthquakes, *Report of the Institute of Industrial Science*, University at Tokyo, February, Vol. 30, No. 1.

Iwamoto, T., Wakai, N., and Yamaji, T., (1984), "Observation of Dynamic Behavior of Buried Ductile-Iron Pipelines During Earthquakes," *Eighth World Conference on Earthquake Engineering*, San Francisco, California, Vol. VII, pp. 231-238.

Iwamoto, T., Yamamura, Y., and Hojo, S., (1985), "Observations and Analyses at the Bend and Tee Portions of Buried Ductile Pipelines During Earthquakes," Seismic Performance of Pipelines and Storage Tanks, PVP-98-4, ASME, pp. 69-79.

Iwamoto, T., Yamamura, Y., and Miyamoto, H., (1988), "Observation on Behavior of Buried Pipelines and Ground Strains During Earthquakes," *Proceedings of the Ninth World Conference on Earthquake Engineering*, Vol. VII, pp. 35-40.

Iwatate, T., Ohtomo, K., Tohma, J., and Nozawa, Y., (1988), "Liquefaction Disaster Mitigation for Underground Structures," *Proceedings of the First Japan-U.S. Workshop on Liquefaction*, Large Ground Deformation and Their Effects on Lifeline Facilities, Tokyo, Japan, November, pp. 143-151.

Japan Gas Association, (1982), Specifications for Seismic Design of High Pressure Gas Pipelines.

Japan Road Association, (1990), *Japan Road Association Specifications for Highway Briges, Part V, Earthquake Resistant Design*, Tokyo, Japan.

Jibson, R.W. and Keefer, D.K., (1993), "Analysis of the Seismic Origin of Landslides: Examples from the New Madrid Seismic Zone," *Geological Society of America Bulletin*, April, Vol. 105, pp. 521-536.

Kachadoorian, R., (1976), "Earthquake: Correlation Between Pipeline Damage and Geologic Environment," *Journal of the American Water Works Association*, March, pp. 165-167.

Karamitros, D., Bouckovalas, G., and Kouretzis, G., (2007), "Stress Analysis of Buried Steel Pipelines at Strike-Slip Fault Crossings," *Soil Dynamics and Earthquake Engineering*, Vol. 27, pp. 200-211.

Kennedy, R.P., Chow, A.W., and Williamson, R.A., (1977), "Fault Movement Effects on Buried Oil Pipeline," *Journal of the Transportation Engineering Division*, ASCE, May, Vol. 103, No. TE5, pp. 617-633.

Kim, J. Lynch, J.P., Michalowski, R.L., Green, R.A., Pour-Ghaz, M., Weiss, W.J., and Bradshaw, A., (2009), "Experimental Study on the Behavior of Segmented Buried Concrete Pipelines Subject to Ground Movements," *Proceedings of the SPIE – The International Society for Optical Engineering*, Vol. 7294, pp. 729419.

Kobayashi, T., Nakane, H., Suzuki, N., and Ishikawa, M., (1989), "Parametric Study on Flexibility of Buried Pipeline Subject to Large Ground Displacement," *Proceedings of the Second U.S.-Japan Workshop on Liquefaction, Large Ground Deformation and Their Effects on Lifelines*, Buffalo, New York, Technical Report NCEER-89-0032, Multidisciplinary Center for Earthquake Engineering Research, Buffalo, New York, pp. 348-362.

Krathy, R.G. and Salvadori, M.G., (1978), "Strength and Dynamic Characteristics of Gasket-Jointed Concrete Water Pipelines," Weidlinger Associates, Grant Report, No. 5.

Kubo, K., (1974), "Behavior of Underground Water Pipes During an Earthquake," *Proceedings of the Fifth World Conference on Earthquake Engineering*, Rome, Italy, pp. 569-578.

Kyriakides, S., Yun, H.D., and Yew, C.H., (1983), "Buckling of Buried Pipelines Due to Large Ground Movements," Earthquake Behavior and Safety of Oil and Gas Storage Facilities, Buried Pipelines and Equipment, PVP-77, ASME, New York, New York, June, pp. 140-150.

Liu, X. and Hou, Z., (1991), "Seismic Risk of Water Supply Network," *Proceedings of the Third U.S. Conference on Lifeline Earthquake Engineering*, Technical Council on Lifeline Earthquake Engineering, Monograph No. 4, ASCE, pp. 552-561.

Liu, X. and O'Rourke, M., (1997a), "Seismic Ground Strain at Sites with Variable Subsurface Conditions," *Computer Methods and Advances in Geomechanics*, (J.X. Yuan, Editor), A.A. Balkema, pp. 2239-2244.

Liu, X. and O'Rourke, M., (1997b), "Behavior of Continuous Pipeline Subject to Transverse PGD," *Journal of Earthquake Engineering and Structural Dynamics*, Vol. 26, pp. 989-1003.

Mabey, M.A., (1992), "Prediction of Displacement Due to Liquefaction Induced Lateral Spreading," Doctoral Dissertation, Department of Civil Engineering, Brigham Young University, Provo, Utah, Technical Report CEG-92-02.

Marek, P.J. and Daniels, J.H., (1971), "Behavior of Continuous Crane Rails," *Journal of the Structural Division*, ASCE, April, Vol. 97, No. ST4, pp. 1081-1095.

Markov, I., Grigoriu, M., and O'Rourke, T., (1994), "An Evaluation of Seismic Serviceability of Water Supply Networks with Application to San Francisco Auxiliary Water Supply System," Technical Report NCEER-94-0001, Multidisciplinary Center for Earthquake Engineering Research, Buffalo, New York.

Mason, J. and O'Rourke, T., (2009), "Tensile Behavior of Steel Pipelines with Welded Slip Joints," *Proceedings of the 2009 TCLEE Conference*, Lifeline Earthquake Engineering in a Multihazard Environment, Oakland, California, pp. 831-841.

Mason, J., O'Rourke, T., and Jones, S., (2009), "Compressive Behavior of Steel Pipelines with Welded Slip Joints," *Proceedings of the 2009 TCLEE Conference*, Lifeline Earthquake Engineering in a Multihazard Environment, Oakland, California, pp. 811-822.

Matsumoto, H., Sasaki, Y., and Kondo, M., (1987), "Coefficient of Subgrade Reaction on Pile in Liquefied Ground," *Proceedings of the Second National Conference on Soil Mechanics and Foundation Engineering*, pp. 827-828 (in Japanese).

McCaffrey, M.A. and O'Rourke, T.D., (1983), "Buried Pipeline Response to Reverse Faulting During the 1971 San Fernando Earthquake," Earthquake Behavior and Safety of Oil and Gas Storage Facilities, Buried Pipelines and Equipment, PVP-77, ASME, New York, New York, June, pp. 151-159.

McLaughlin, P., (2003), "Seismic Response and Behavior of Buried Continuous Piping Systems Containing Elbows," Thesis submitted to Rensselaer in partial fulfillment for Ph.D. degree, 169p.

McLaughlin, P. and O'Rourke, M., (2009), "Strain in Pipe Elbows due to Wave Propagation Hazard," *Proceedings of the 2009 TCLEE Conference, Lifeline Earthquake Engineering in a Multihazard Environment*, Oakland, California, pp. 382-392.

McNorgan, J.D., (1989), "Relieving Seismic Stresses Locked in Gas Pipelines," *Proceedings of the Second U.S.-Japan Workshop on Liquefaction, Large Ground Deformation and Their Effects on Lifelines*, Buffalo, New York, Technical Report NCEER-89-0032, Multidisciplinary Center for Earthquake Engineering Research, Buffalo, New York, pp. 363-369.

Meis, R., Maragakis, E., and Siddharthan, R., (2003), "Behavior of Underground Piping Joints due to Static and Dynamic Loading," Technical Report MCEER-03-006, Multidisciplinary Center for Earthquake Engineering Research.

Merifield, R., White, D., and Randolph, M., (2008), "Analysis of the Undrained Breakout Resistance of Partially Embedded Pipelines," *Geotechnique*, Vol. 58, No. 6, pp. 461-470.

Meyersohn, W.D., (1991), "Analytical and Design Considerations for the Seismic Response of Buried Pipelines," Thesis, Graduate School of Cornell University, January.

Miles, S. and Keefer, D., (2009), "Towards a Comprehensive Areal Model of Earthquake-Induced Landslides," *National Hazards Review*, ASCE, Vol. 10, No. 1, February, pp. 19-28.

Miyajima, M. and Kitaura, M., (1989), "Effects of Liquefaction-Induced Ground Movement on Pipeline," *Proceedings of the Second U.S.-Japan Workshop on Liquefaction, Large Ground Deformation and Their Effects on Lifelines*, Buffalo, New York, Technical Report NCEER-89-0032, Multidisciplinary Center for Earthquake Engineering Research, Buffalo, New York, pp. 386-400.

Miyajima, M., Yoshida, M., and Kitaura, M., (1992), "Small Scale Tests on Countermeasures Against Liquefaction for Pipelines Using Gravel Drain System," *Proceedings of the Fourth Japan-U.S. Workshop on Earthquake Resistant Design of Lifeline Facilities and Countermeasures for Soil Liquefaction*, Honolulu, Hawaii, NCEER-92-0019, Multidisciplinary Center for Earthquake Engineering Research, Buffalo, New York, pp. 381-391.

Mohr, W., (2003), "Strain-Based Design of Pipelines," Report No. 45892 GTH, Department of Interior Minerals Management Service.

Moncarz, P.D., Shyne, J.C., and Derbalian, G.K., (1987), "Failures of 108-inch Steel Pipe Water Main," *Journal of Performance of Construction Facilities*, ASCE, Vol. 1, No. 3, pp. 168-187.

Murff, J., Wagner, D., and Randolph, M., (1989), "Pipe Penetration in Cohesive Soil," *Geotechnique*, Vol. 39, No. 2, pp. 213-229.

National Institute of Building Sciences (NIBS), (1996), "Development of a Standardized Earthquake Loss Estimation Methodology," Vol. II, Risk Management Solutions, Inc., February.

Newmark, N.M., (1965), "Effects of Earthquakes on Dams and Embankments," *Geotechnique*, Vol. 15, No. 2, pp. 139-160.

Newmark, N.M., (1967), "Problems in Wave Propagation in Soil and Rocks," *Proceedings of the International Symposium on Wave Propagation and Dynamic Properties of Earth Materials*, University of New Mexico Press, pp. 7-26.

Newmark, N.M. and Hall, W.J., (1975), "Pipeline Design to Resist Large Fault Displacement," *Proceedings of the 1975 U.S. National Conference on Earthquake Engineering*, Ann Arbor, Michigan, pp. 416-425.

Nishio, N., Ukaji, T., Tsukamoto, K., and Ishita, O., (1983), "Model Experiments on the Behavior of Buried Pipelines During Earthquakes," Earthquake Behavior and Safety of Oil and Gas Storage Facilities, Buried Pipelines and Equipment, PVP-77, ASME, New York, New York, June, pp. 263-272.

Nodine, M., Wright, S., Gilbert, R., and Ward, E., (2006), "Mudflows and Mudslides During Hurricane Ivan," OTC 18328, Offshore Technology Conference, Houston, Texas, May.

Orense, R. and Towhata, I., (1992), "Prediction of Liquefaction-Induced Permanent Ground Displacements: A Three-Dimensional Approach," *Proceedings of the Fourth Japan-U.S. Workshop on Earthquake Resistant Design of Lifeline Facilities and Countermeasures for Soil Liquefaction*, Honolulu, Hawaii, Technical Report NCEER-92-0019, Multidisciplinary Center for Earthquake Engineering Research, Buffalo, New York, pp. 335-349.

O'Rourke, M.J., Bloom, M.C., and Dobry. R., (1982), "Apparent Propagation Velocity of Body Waves," *Earthquake Engineering and Structural Dynamics*, Vol. 10, pp. 283-294.

O'Rourke, M.J., Castro, G., and Hossain, I., (1984), "Horizontal Soil Strain Due to Seismic Waves," *Journal of Geotechnical Engineering*, ASCE, September, Vol. 110, No. 9, pp. 1173-1187.

O'Rourke, M.J. and El Hmadi, K.E., (1988), "Analysis of Continuous Buried Pipelines for Seismic Wave Effects," *Earthquake Engineering and Structural Dynamics*, Vol. 16, pp. 917-929.

O'Rourke, M.J., (1989), "Approximate Analysis Procedures for Permanent Ground Deformation Effects on Buried Pipelines," *Proceedings of the Second U.S.-Japan Workshop on Liquefaction, Large Ground Deformation and Their Effects on Lifelines*, Buffalo, New York, Technical Report NCEER-89-0032, Multidisciplinary Center for Earthquake Engineering Research, Buffalo, New York, pp. 336-347.

O'Rourke, M.J. and Ayala, G., (1990), "Seismic Damage to Pipeline: Case Study," *Journal of Transportation Engineering*, ASCE, March/April, Vol. 116, No. 2, pp. 123-134.

O'Rourke, M.J. and Nordberg, C., (1991), "Analysis Procedures for Buried Pipelines Subject to Longitudinal and Transverse Permanent Ground Deformation," *Proceedings of the Third Japan-U.S. Workshop on Earthquake Resistant Design of Lifeline Facilities and Countermeasures for Soil Liquefaction*, San Francisco, California, Technical Report NCEER-91-0001, Multidisciplinary Center for Earthquake Engineering Research, Buffalo, New York, pp. 439-453.

O'Rourke, M.J. and Nordberg, C., (1992), "Behavior of Buried Pipelines Subject to Permanent Ground Deformation," *Tenth World Conference on Earthquake Engineering*, Madrid, Spain, July 19-24, Vol. 9, pp. 5411-5416.

O'Rourke, M.J. and Ballantyne, D., (1992), "Observations on Water System and Pipeline Performance in the Limon Area of Costa Rica Due to the April 22, 1991 Earthquake," Technical Report NCEER-92-0017, Multidisciplinary Center for Earthquake Engineering Research, Buffalo, New York.

O'Rourke, M.J. and Ayala, G., (1993), "Pipeline Damage Due to Wave Propagation," *Journal of Geotechnical Engineering*, ASCE, September, Vol. 119, No. 9, pp. 1490-1498.

O'Rourke, M.J. and Liu, X., (1994), "Failure Criterion for Buried Pipe Subjected to Longitudinal PGD: Benchmark Case History," *5th U.S.-Japan Workshop on Earthquake Resistant Design for Lifeline Facilities and Countermeasures Against Soil Liquefaction*, Technical Report NCEER-94-0026, Multidisciplinary Center for Earthquake Engineering Research, Buffalo, New York, pp. 639-652.

O'Rourke, M.J., Liu, X.J., and Flores-Berrones, R., (1995), "Steel Pipe Wrinkling Due to Longitudinal Permanent Ground Deformation," *Journal of Transportation Engineering*, September/October, Vol. 121, No. 5, pp. 443-451.

O'Rourke, M.J. and Bouabid, J., (1996), "Analytical Damage Estimates for Concrete Pipelines," *Proceedings of Eleventh World Conference on Earthquake Engineering*, Acapulco, Mexico, June 23-28, No. 346.

O'Rourke, M.J. and Deyoe, E., (2004), "Seismic Damage to Segmented Buried Pipe," *Earthquake Spectra*, Vol. 20, No. 4, pp. 1167-1183.

O'Rourke, M.J., Symans, M., and Masek, J., (2008) "Wave Propagation Effects on Buried Pipe at Treatment Plants," *Earthquake Spectra*, Vol. 24, No. 3, pp. 725-749.

O'Rourke, M.J., (2009), "Analytical Fragility Relations for Buried Segmented Pipe," *Proceedings of 2009 TCLEE Conference, Lifeline Earthquake Engineering in a Multihazard Environment*, ASCE, Oakland, California, pp. 771-780.

O'Rourke, T.D. and Trautmann, C.H., (1980), "Analytical Modeling of Buried Pipeline Response to Permanent Earthquake Displacements," Report No. 80-4, School of Civil Engineering and Environmental Engineering, Cornell University, Ithaca, New York, July.

O'Rourke, T.D. and Trautmann, C.H., (1981), "Earthquake Ground Rupture Effects on Jointed Pipe," *Proceedings of the Second Specialty Conference of the Technical Council on Lifeline Earthquake Engineering*, ASCE, August, pp. 65-80.

O'Rourke, T.D. and Tawfik, M.S., (1983), "Effects of Lateral Spreading on Buried Pipelines During the 1971 San Fernando Earthquake," Earthquake Behavior and Safety of Oil and Gas Storage Facilities, Buried Pipelines and Equipment, PVP-77, ASME, New York, New York, June, pp. 124-132.

O'Rourke, T.D., Grigoriu, M.D., and Khater, M.M., (1985), "A State of the Art Review: Seismic Response of Buried Pipelines," Decade of Progress in Pressure Vessel Technology, (C. Sundararajan, Editor), ASME.

O'Rourke, T.D., (1988), "Critical Aspects of Soil-Pipeline Interaction for Large Ground Deformation," *Proceedings of the First Japan-U.S. Workshop on Liquefaction, Large Ground Deformation and Their Effects on Lifeline Facilities*, Tokyo, Japan, November, pp. 118-126.

O'Rourke, T.D., Gowdy, T.E., Stewart, H.E., and Pease, J.W., (1991), "Lifeline Performance and Ground Deformation in the Marina During 1989 Loma Prieta Earthquake," *Proceedings of the Third Japan-U.S. Workshop on Earthquake Resistant Design of Lifeline Facilities and Countermeasures for Soil Liquefaction*, San Francisco, California, NCEER-91-0001, Multidisciplinary Center for Earthquake Engineering Research, Buffalo, New York, pp. 129-146.

O'Rourke, T.D., Meyersohn, W.D., Shiba, Y., and Chaudhuri, D., (1994), "Evaluation of Pile Response to Liquefaction-Induced Lateral Spread," *Proceedings of the Fifth U.S.-Japan Workshop on Earthquake Resistant Design of Lifeline Facilities and Countermeasures Against Soil Liquefaction*, Snowbird, Utah, Technical Report NCEER-94-0026, Multidisciplinary Center for Earthquake Engineering Research, Buffalo, New York, pp. 457-479.

O'Rourke, T.D. and O'Rourke, M.J., (1995), "Pipeline Response to Permanent Ground Deformation: A Benchmark Case," *Proceedings of the Fourth U.S. Conference on Lifeline Earthquake Engineering*, Technical Council on Lifeline Earthquake Engineering, Monograph No. 6, ASCE, pp. 288-295.

O'Rourke, T.D. and Jeon, S., (1999), "Factors Affecting the Earthquake Damage of Water Distribution Systems," *Proceedings of the Fifth U.S. Conference on Lifeline Earthquake Engineering*, TCLEE Monograph No. 16, ASCE, pp. 379-388.

O'Rourke, T.D. and Turner, J., (2006), "Earthquake Soil – Pipeline Interaction in Partially Saturated Sand," *Proceedings of the Eighth U.S. National Conference of Earthquake Engineering*, EERI, San Francisco, California.

Paolucci, R. and Smerzini, C., (2008), "Earthquake-induced Transient Ground Strains from Dense Seismic Networks," *Earthquake Spectra*, Vol. 24, No. 2, May, pp. 453-470.

Parker, E., Moore, R., Evans, T., and Usher, N., (2008), "Evaluation of Landslide Impact on Deepwater Submarine Pipelines," OTC 19459, Offshore Technology Conference, Houston, Texas, May.

Porter, K.A., Scawthorn, C., Honegger, D.G., O'Rourke, T.D., and Blackburn, F., (1991), "Performance of Water Supply Pipelines in Liquefied Soil," *Proceedings of the Fourth U.S.-Japan Workshop on Earthquake Disaster Prevention for Lifeline Systems*, Los Angeles, California, pp. 3-17.

Prior, J.C., (1935), "Investigation of Bell and Spigot Joints in Cast Iron Water Pipes," Bulletin No. 87, The Engineering Experiment Station, Ohio State University Studies Engineering Series, Vol. IV, No. 1, January.

Ramberg, W. and Osgood, W., (1943), "Description of Stress-Strain Curves by Three Parameters," Technical Note, No. 902, National Advisory Committee for Aeronautics, 28p.

Randolph, M. and White, D., (2008), "Pipelines Embedment in Deep Water: Processes and Quantitative Assessment," Offshore Technology Conference (OTC) 19128.

Roark, R. and Young, W., (1975), "Formulas for Stress and Strain," 5th Edition, McGraw-Hill.

Romero, N., O'Rourke, T., Nozick, L., and Davis, C., (2009), "Los Angeles Water Supply Response to 7-8 M_w Earthquake," *Proceedings of the 2009 TCLEE Conference*, *Lifeline Earthquake Engineering in a Multihazard Environment*, Oakland, California, pp. 1256-1267.

Roth, B.L., O'Rourke, T.D., Dobry, R., and Pierce, C.E., (1990), "Lifeline Performance During the 1979 Imperial Valley Earthquake," *Proceedings of the Third Japan-U.S. Workshop on Earthquake Resistant Design of Lifeline Facilities and Countermeasures for Soil Liquefaction*, San Francisco, California, Technical Report NCEER-91-0001, Multidisciplinary Center for Earthquake Engineering Research, Buffalo, New York, pp. 191-207.

Sakurai, A. and Takahashi, T., (1969), "Dynamic Stress of Underground Pipelines During Earthquakes," *Proceedings of the Fourth World Conference on Earthquake Engineering*, Chilean Association on Seismology and Earthquake Engineering, Santiago, Chile, pp. 811-895.

Sato, K., Hamada, M., and Doi, M., (1994), "An Experimental Study of Effects of Laterally Flowing Ground on In-Ground Structures," *Proceedings of the Fifth U.S.-Japan Workshop on Liquefaction*, Large Ground Deformation and Their Effects on Lifelines, Snowbird, Utah, Technical Report NCEER-94-0026, Multidisciplinary Center for Earthquake Engineering Research, Buffalo, New York, pp. 405-414.

Sato, R. and Shinozuka, M., (1991), "GIS-Based Interactive and Graphic Computer System to Evaluate Seismic Risks on Water Delivery Networks," *Proceedings of the Third U.S. Conference on Lifeline Earthquake Engineering*, Technical Council on Lifeline Earthquake Engineering, Monograph No. 4, ASCE, pp. 651-660.

Schilling, G., (1965), "Buckling Strength of Circular Tubes," *Journal of Structural Division*, ASCE, Vol. 91, No. 5, pp. 325-348.

Schwab, F. and Knopff, L., (1977), "Fast Surface Waves and Free Mode Computations," *Seismology: Surface Waves and Earth Oscillation Methods in Computation, Physics 11*, Academic Press, New York, New York, pp. 87-180.

Shah, H. and Chu, S., (1974), "Seismic Analysis of Underground Structural Elements," *Journal of the Power Division*, ASCE, July, Vol. 100, No. PO1, pp. 53-62.

Shinozuka, M. and Koike, T., (1979), "Estimation of Structural Strains in Underground Lifeline Pipes," Lifeline Earthquake Engineering - Buried Pipelines, Seismic Risk, and Instrumentation, PVP-34, ASME, pp. 31-48.

Siegel, R.A., (1978), STABL User Manual: West Lafayette, Indiana, Purdue University, 104p.

Singhal, A., (1984), "Nonlinear Behavior of Ductile Iron Pipeline Joints," *Journal of Technical Topics in Civil Engineering*, ASCE, Vol. 110, No. 1, pp. 29-37.

Singhal, A. and Benavides, J., (1983), "Axial and Bending Behavior of Pipeline Joints," *Research and Technology Journal*, AWWA, November, pp. 572-578.

Stephens, D.R., Olson, R.J., and Rosenfeld, M.J., (1991), "Pipeline Monitoring – Limit State Criteria," Battelle Memorial Laboratory, AGA NG-18 Report No. 188.

Sun, S. and Shien, L., (1983), "Analysis of Seismic Damage to Buried Pipelines in Tangshan Earthquake," Earthquake Behavior and Safety of Oil and Gas Storage Facilities, Buried Pipelines and Equipment, PVP-77, ASME, New York, New York, June, pp. 365-367.

Suzuki, H., (1988), "Damage to Buried Pipes Caused by Large Ground Displacement," *Proceedings of the First Japan-U.S. Workshop on Liquefaction, Large Ground Deformation and Their Effects on Lifeline Facilities*, Tokyo, Japan, pp. 127-132.

Suzuki, N., Arata, O., and Suzuki, I., (1988), "Parametric Study of Deformation Analysis of Welded Pipeline Subject to Liquefaction-Induced Permanent Ground Displacement," *Proceedings of First Japan-U.S. Workshop on Liquefaction, Large Ground Deformation and Their Effects on Lifeline Facilities*, Tokyo, Japan, pp. 155-162.

Suzuki, N. and Masuda, N., (1991), "Idealization of Permanent Ground Movement and Strain Estimation of Buried Pipes," *Proceedings of the Third Japan-U.S. Workshop on Earthquake Resistant Design of Lifeline Facilities and Countermeasures for Soil Liquefaction*, San Francisco, California, NCEER Report Number 91-0001, Multidisciplinary Center for Earthquake Engineering Research, Buffalo, New York, pp. 455-469.

Takada, S., (1984), "Model Analysis and Experimental Study on Mechanical Behavior of Buried Ductile Iron Pipelines Subjected to Large Ground Deformations," *Proceedings of the Eighth World Conference on Earthquake Engineering*, San Francisco, California, Vol. VII, pp. 255-262.

Takada, S., Tanabe, K., Yamajyo, K., and Katagiri, S., (1987), "Liquefaction Analysis for Buried Pipelines," *Proceedings of the Third International Conference on Soil Dynamics and Earthquake Engineering*.

Takada, S. and Tanabe, K., (1988), "Estimation of Earthquake Induced Settlements for Lifeline Engineering," *Proceedings of the Ninth World Conference Earthquake Engineering*, August, Vol. VII, pp. 109-114.

Takada, S., (1991), Lifeline Earthquake Engineering, (In Japanese), 241p.

Tanabe, K., (1988), "Fundamental Study on Seismic Assessment and Design of Buried Pipelines Subjected to Ground Failure During Earthquake," Doctoral Dissertation, Kobe University, 1988 (in Japanese).

Tawfik, M.S. and O'Rourke, T.D., (1985), "Load-Carrying Capacity of Welded Slip Joints," *Journal of Pressure Vessel Technology*, February, Vol. 107, pp. 37-43.

Tokimatsu, K. and Seed, H.B., (1987), "Evaluation of Settlements in Sands Due to Earthquake Shaking," *Journal of Geotechnical Engineering*, ASCE, August, Vol. 113, No. 8, pp. 861-878.

Towhata, I., Tokida, K., Tamari, Y., Matsumoto, H., and Yamada, K., (1991), "Prediction of Permanent Lateral Displacement of Liquefied Ground by Means of Variational Principle," *Proceedings of the Third Japan-U.S. Workshop on Earthquake Resistant Design of Lifeline Facilities and Countermeasures for Soil Liquefaction*, Technical Report NCEER-91-0001, Multidisciplinary Center for Earthquake Engineering Research, Buffalo, New York, pp. 237-252.

Trautmann, C.H. and O'Rourke, T.D., (1983), Load-Displacement Characteristics of a Buried Pipe Affected by Permanent Earthquake Ground Movements," *Earthquake Behavior and Safety of Oil and Gas Storage Facilities, Buried Pipelines and Equipment*, PVP-77, ASME, New York, June, pp. 254-262.

Trautmann, C.H. and O'Rourke, T.D., (1985), "Lateral Force – Displacement Response of Buried Pipe," *Journal of Geotechnical Engineering*, ASCE, Vol. 111, No. 9, pp. 1077-1092.

Trifunac, M.D. and Lee, V.W. (1996), "Peak Surface Strains during Strong Earthquake Motion," *Soil Dynamics and Earthquake Engineering*, Vol. 15, pp. 311-319.

Trifunac, M., and Todorovska, M., (1997), "Northridge, California Earthquake of 1994: Density of Pipe Breaks and Surface Strain," *Soil Dynamics and Earthquake Engineering*, No. 16, pp. 193-207.

United States Department of Transportation (USDoT), (2011), Research and Innovative Technology Administration, Bureau of Transportation Statistics, http://www.bts.gov/publications/national_transportation_statistics/.

Varnes, D.J., (1978), "Slope Movement Types and Processes," Landslides Analysis and Control, Special Report 176, Transportation Research Board, National Academy of Sciences, Washington, D.C., pp. 11-33.

Verley, R. and Sotberg, T., (1992), "A Soil Resistance Model for Pipelines Placed on Sandy Soils," *Proceedings of the Offshore Mechanics and Arctic Engineering Conference*, Vol. V-A Pipeline Technology, pp. 123-131.

Verley, R. and Lund, K., (1995), "A Soil Resistance Model for Pipelines Placed on Clay Soils," *Proceedings of the Offshore Mechanics and Arctic Engineering Conference*," Copenhagen, Denmark, V, pp. 225-232.

Vitali, L., Bartolini, L., Askeim, D., Reek, R., and Levold, E., (2005), "Hot Pipe JI Project Experimental Test and FE Analyses," *Proceedings of Twenty Fourth International Conference on Offshore Mechanics and Arctic Engineering*, June 2005, Halkidiki, Greece.

Wang, L.R.L. and O'Rourke, M., (1978), "Overview of Buried Pipelines Under Seismic Loading," *Journal of the Technical Councils*, ASCE, November, Vol. 104, No. TC1, pp. 121-130.

Wang, L.R.L., (1979), "Some Aspects of Seismic Resistant Design of Buried Pipelines," Lifeline Earthquake Engineering - Buried Pipelines, Seismic Risk, and Instrumentation, PVP-34, ASME, pp. 117-131.

Wang, L.R.L. and Yeh, Y., (1985), "A Refined Seismic Analysis and Design of Buried Pipeline for Fault Movement," *Journal of Earthquake Engineering and Structural Dynamics*, Vol. 13, pp. 75-96.

Wang, L.R.L., (1994), "Essence of Repair and Rehabilitation of Buried Lifeline Systems," *Proceedings of the Second China-Japan-U.S. Trilateral Symposium on Lifeline Earthquake Engineering*, Xi'an, China, April, pp. 247-254.

Wells, D.L. and Coppersmith, K.J., (1994), "New Empirical Relationships among Magnitude, Rupture Length, Rupture Width, Rupture Area, and Surface Displacement," *Bulletin of the Seismological Society of America*, August, Vol. 84, No. 4, pp. 974-1002.

White, D. and Randolph, M., (2007), "Seabed Characterization and Models for Pipelines-Soil Interaction," *Proceedings of the Seventeenth International Symposium on Offshore and Polar Engineering*, Lisbon, Portugal, July (2007).

Wijewickreme, D., Honegger, D., Mitchell, A., and Fitzell, T., (2005), "Seismic Vulnerability Assessment and Retrofit of a Major Natural Gas Pipeline System: A Case History," *Earthquake Spectra*, Vol. 21, No. 2, pp. 539-567.

Wilson, R.C. and Keefer, D.K., (1983), "Dynamic Analysis of a Slope Failure from the 6 August 1979 Coyote Lake, California Earthquake," *Bulletin of the Seismological Society of America*, Vol. 73, No. 3, pp. 863-877.

Wright, J. and Takada, S., (1978), "Earthquake Relative Motions for Lifelines," *Proceedings of the Fifth Japan Earthquake Engineering Symposium*, Tokyo, Japan.

Yasuda, S., Saito, K., and Suzuki, N., (1987), "Soil Spring Constant on Pipe in Liquefied Ground," *Proceedings of the Nineteenth JSCE Conference on Earthquake Engineering*, pp. 189-192 (in Japanese).

Yasuda, S., Nagase, H., Kiku, H., and Uchida, Y., (1991), "A Simplified Procedure for the Analysis of the Permanent Ground Displacement," *Proceedings of the Third Japan-U.S. Workshop on Earthquake Resistant Design of Lifeline Facilities and Countermeasures for Soil Liquefaction*, San Francisco, California, Technical Report NCEER-91-0001, Multidisciplinary Center for Earthquake Engineering Research, Buffalo, New York, pp. 225-236.

Yeh, G., (1974), "Seismic Analysis of Slender Buried Beams," *Bulletin of the Seismological Society of America*, October, Vol. 64, No. 5, pp. 1551-1562.

Yeh, Y.H. and Wang, L.R.L., (1985), "Combined Effects of Soil Liquefaction and Ground Displacement to Buried Pipelines," *Proceedings of the 1985 Pressure Vessels and Piping Conference - Seismic Performance of Pipelines and Storage Tanks*, PVP-98-4, ASME, pp. 43-52.

Yoshida, T. and Uematsu, M., (1978), "Dynamic Behavior of a Pile in Liquefaction Sand," *Proceedings of the Fifth Japan Earthquake Engineering Symposium*, pp. 657-663 (in Japanese).

Youd, T.L. and Perkins, D.M., (1987), "Mapping of Liquefaction Severity Index," *Journal of Geotechnical Engineering*, ASCE, Vol. 113, No. 11, pp. 1374-1392.

Youd, T.L., Hansen, C., and Bartlett, S., (2002), "Revised Multilinear Regression Equations for Prediction of Lateral Spread Displacement," *Journal of Geotechnical and Geoenvironmental Engineering*, ASCE, Vol. 128, No. 12, pp. 1007-1017.

Youngs, R., Arabasz, W., Anderson, R., Ramelli, A., Ake, J., Slemmons, D., McCalpin, J., Dorser, D., Fridrich, C., Swan, F., Rodgers, A., Yount, J., Anderson, L., Smith, K., Bruhr, R., Knuepter, P., Smith, R., DePolo, C., O'Leary, D., Coppersmith, K., Pezzopane, S., Schwartz, D., Whitney, J., Olig, S., and Toro, G., (2003), "A Methodology for Probabilistic Fault Displacement Hazard Analysis," *Earthquake Spectra*, Vol. 19, No. 1, pp. 191-219.

Zerva, A. and Harada, T., (1997), "Effect of Surface Layer Stochasticity on Seismic Ground Motion Coherence and Strain Estimates," *Soil Dynamics and Earthquake Engineering*, Vol. 16, pp. 445-457.

Zimmerman, T.J., Stephens, M.J., DeGreer, D.D., and Chen Q., (1995), "Compressive Strain Limits for Buried Pipelines," *Proceedings of the 1995 Offshore Mechanics and Arctic Engineering Conference*, ASME, Vol. V, pp. 365-379.

AUTHOR INDEX

A

Abdoun T., 116, 118, 199-201, 214-216, 304
Ake, J., 11-12
Akiyoshi, T., 307
American Lifeline Alliance, 11-12, 15, 20, 28, 31-32, 34, 43, 71-72, 78-80, 82, 95, 109-110, 115-116, 119-122, 221, 225-226, 229, 233, 238, 271, 284-286, 289, 292-293, 296
American Society of Civil Engineers, 71-72, 78-79, 82, 108-110, 114, 119-122, 143, 163, 287, 318, 322
Anderson, L., 11-12
Anderson, R., 11-12
Ando, H., 60-61
Applied Technology Council, 17-18
Arabasz, W., 11-12
Arai, H., 302
Arata, O., 124, 158-159, 161-162, 164, 179-180, 183-184, 186
Ariman, T., 84, 209
Askeim, D., 81
Audibert, J.M.E., 112-113
Ayala, G., 40-41, 99, 249-251, 282-283

B

Bachhuber, J., 196-198
Ballantyne, D.B., 96-97, 295, 307
Bardet, J.P., 27-29, 31-32
Barenberg, M.E., 282
Bartlett, S.F., 27, 29-33
Bartolini, L., 81
Baziar, M.H., 29
Benavides, J., 101
Benjamin, R., 76
Berg, E., 295
Blackburn, F., 292, 305-306
Bloom, M.C., 44-45
Bolton, M., 130
Bouabid, J., 98-100, 272-273, 275-276
Bouckovalas, G., 208, 212-213
Bozorgnia, Y., 42-43
Bradshaw, A., 230
Brockenbrough, R.L.,87-88
Brown, R.W., 132
Bruhr, R., 11-12
Bruton, D., 130-131
Bukovansky, M., 297

C

Cai, J., 185-187
Campbell, K.W., 42-43
Canadian Standards Association, 72, 81
Carr, M., 130-131
Castro, G., 46-48, 50
Chaudhuri, D., 124
Chen, G., 185
Chen Q., 77
Cheng, J., 73, 79, 82
Cheon, J., 328
Cheuk, J., 130-131
Choo, Y., 304
Chow, A.W., 204-208, 211, 213, 298
Chu, S., 257-259, 262-263
Coppersmith, K.J., 11-14
Coyne, M., 328

D

Daniels, J.H., 84
Das, S., 73, 82
Davis, C., 295
DeGreer, D.D., 77
Demars, K.R., 300
DePolo, C., 11-12
Derbalian, G.K., 90, 93

Deyoe, E., 282, 287-289
Dingle, H., 130
Dobry, R., 29, 44-45, 217-218
Doi, M., 125
Dorey, B., 79
Dorser, D., 11-12

E

EDM Services, 281
Eguchi, R.T., 282, 292, 294, 305-306
Eidinger, J.M., 91, 95, 196-198, 292
El Hmadi, K.E., 98, 103, 223, 243-246, 248-249, 270-272, 279-280
Emoto, K., 29, 34-35, 137
Evans, T., 191, 194

F

Fitzell, T., 27, 71-72, 78-79
Flores-Berrones, R., 135, 137, 139-142, 144, 224-225
Ford, D.B., 307, 309
Fridrich, C., 11-12
Fuchida, K., 307
Fujii, Y., 302

G

G&E, 294
Gaudin, C., 130
Gilbert, R., 157, 328
Goodling, E.C., 257-259, 262-263
Gowdy, T.E., 37-38, 97
Green, R.A., 230
Greenwood, J.H., 297
Gresnigt, A.M., 77
Grigoriu, M.D., xii, 109, 294
Guo, P., 111-112

H

Ha, D., 116, 118, 199-201, 214-216, 304
Hall, J.F., 58
Hall, W.J., 71-72, 201-205, 211-212
Hamada, M., 29, 34-35, 125, 137
Hance, J.J., 21-23
Hansen, C., 30-32
Hansen, J.B.,115-116
Harada, T., 57
Harris, L., 76-77
Hasegawa, H., 302
Haskell, N.A., 46
Heubach, W.F., 292
Hobbs, R.E., 84
Hojo, S., 276-278
Honegger, D.G., 15, 24, 27, 34, 37, 71-72, 78-79, 111, 251, 253, 272, 292, 294, 301-302, 305-306
Hossain, I., 46-48, 50
Hou, Z., 185-187, 294
Howard, J.H., 83
Hu, J., 27-29, 31-32

I

Isenberg, J., 293, 307
Ishikawa, M., 158-159, 162-163, 179
Ishita, O., 58-60
Isoyama, R., 29, 34-35, 137, 294-295
Iwamoto, T., 55, 265, 276-278
Iwatate, T., 302

J

Japan Gas Association, 172
Japan Road Association, 125
Jeon, S., 282-284
Jibson, R.W., 18-19
Jones, S., 92, 94

K

Kachadoorian, R., 58
Karamitros, D., 208, 212-213
Katagiri, S., 124, 184
Katayama, T., 294-295
Keefer, D.K., 17-20
Kennedy, J., 295
Kennedy, R.P., 201, 204-208, 211, 213, 298
Khater, M.M., xii, 109
Kiku, H., 29
Kim, J., 230
Kitaura, M., 124, 172-173, 179-180, 302
Knopff, L., 46
Knuepter, P., 11-12
Kobayashi, T., 158-159, 162-163, 179
Koike, T.,240, 242-243, 248-249, 260, 262-263
Kondo, M., 124
Kouretzis, G., 208, 212-213
Krathy, R.G., 100

Kubo, K., 240
Kyriakides, S., 84

L

Lau, B., 292
Lee, B.J., 84, 209
Lee, D., 292
Lee, V.W., 55-57
Levold, E., 81
Liu, X.J., 60, 65-66, 135, 139-142, 144-145, 159, 163-170, 175, 179-181, 185-187, 194, 224-225, 294
Lund, K., 127
Lynch, J.P., 230

M

Mabey, M.A., 29
Mace, N., 27-29, 31-32
Maison, B., 292
Major, G., 297
Maragakis, E., 101
Marek, P.J., 84
Markov, I., 294
Masek, J., 254-256
Mason, J., 89, 92-94
Masuda, N., 32-33, 180, 182, 189
Matsumoto, H., 24, 29, 124
McCaffrey, M.A., 196
McCalpin, J., 11-12
McLaughlin, P., 152, 263-264
McNorgan, J.D., 83
Meis, R., 101
Merifield, R., 132
Meyersohn, W.D., 13, 16-17, 84-85, 124, 241
Michalowski, R.L., 230
Miles, S., 17
Mitchell, A., 27, 71-72, 78-79
Miyajima, M., 124, 172-173, 179-180, 302
Miyamoto, H., 55
Mohr, W., 81, 290
Moncarz, P.D., 90, 93
Moore, R., 191, 194
Murff, J., 132
Murray, D., 73, 79, 82

N

Nagase, H., 29
Nakane, H., 158-159, 162-163, 179-180
National Institute of Building Sciences, 24-27, 294-295
Nazemi, N., 73, 82
Newmark, N.M., 18-19, 29, 50, 71-72, 201-205, 211-212, 240, 243, 249
Nishio, N., 58-60, 66
Nodine, M., 157, 328
Nordberg, C., 134, 136, 226-228
Nozawa, Y., 302
Nozick, L., 295
Nyman, D., 15, 24, 37, 71-72, 111, 301-302
Nyman, K.J., 112-113

O

O'Leary, D., 11-12
O'Rourke, M.J., 41, 44, 46-48, 50, 58, 60, 65-66, 71, 96-99, 101, 103, 116, 118, 134-137, 139-142, 144-145, 158-159, 163-170, 173-175, 179-181, 194, 196-199, 201, 214-216, 223-228, 243-246, 248-251, 254-256, 263-264, 270-272, 275-276, 279-280, 282-283, 287-289, 304
O'Rourke, T.D., xii, 34, 36-38, 71, 86, 88-90, 92-94, 97, 102, 109, 112, 114-118, 120, 124, 137-139, 146, 155, 157, 159-162, 164, 179-180, 182, 196, 199-201, 214-218, 231-233, 238, 270, 282-284, 292, 294-295, 305-306
Offshore Standard OS-F101, 72, 80
Ohtomo, K., 302
Olig, S., 11-12
Olson, R.J., 77
Orense, R., 29
Osgood, W., 69-71, 133, 139-142, 163, 193, 205, 210, 318, 329

P

Palmer, M., 116, 118, 199-201, 214-216
Paolucci, R., 54-57, 288

Parker, E., 191, 194
Pease, J.W., 37-38, 97
Perkins, D.M., 29-30
Pezzopane, S., 11-12
Pierce, C.E., 217-218
Pipeline Research Council International, 15, 71-72, 78-81, 115-116, 119-122
Porter, K.A., 292, 305-306
Pour-Ghaz, M., 230
Prior, J.C., 98, 229

R

Ramberg, W., 69-71, 133, 139-142, 163, 193, 205, 210, 318, 329
Ramelli, A., 11-12
Randolph, M. 127-128, 132
Reek, R., 81
Reneau, R., 295
Richardson, E., 307
Roark, R., 74
Rodgers, A., 11-12
Romero, N., 295
Rosenfeld, M.J., 77
Roth, B.L., 217-218

S

Saito, K., 124
Sakurai, A., 240-241
Salvadori, M.G., 100
Sasaki, Y., 124
Sato, K., 125
Sato, R., 294
Sato, S., 60-61
Scawthorn, C., 292, 305-306
Schilling, G., 74-75
Schwab, F., 46
Schwartz, D., 11-12
Seed, H.B., 37
Shah, H., 257-259, 262-263
Shiba, Y., 124
Shien, L., 96
Shinozuka, M., 240, 242-243, 248-249, 260, 262-263, 294
Shirinashihama, S., 307
Shyne, J.C., 90, 93
Siddharthan, R., 101
Siegel, R.A., 18
Singhal, A., 101, 307
Skene, W., 76
Slemmons, D., 11-12
Smerzini, C., 54-57, 288
Smith, K., 11-12
Smith, R., 11-12
Sotberg, T., 129
Stephens, D.R., 77
Stephens, M.J., 77
Stewart, H.E., 37-38, 97, 116, 118, 199-201, 214-216
Stolle, D., 111-112
Sun, S., 96
Suzuki, H., 156, 221, 229
Suzuki, I., 124, 158-159, 161-162, 164, 179-181, 183-184, 186
Suzuki, N., 32-33, 124, 158-159, 161-164, 179-180, 182-184, 189
Sver, H., 76
Swan, F., 11-12
Symans, M., 116, 118, 199-201, 214-216, 254-256

T

Takada, S., 38, 49, 124, 156, 183-184, 229-230
Takagi, N., 60-61
Takahashi, T., 240-241
Tamari, Y., 24, 29
Tanabe, K., 38, 124, 184
Tawfik, M.S., 36, 88-90, 92, 146, 155, 182
Taylor, C., 293
Tobita, T., 27-29, 31-32
Todorovska, M., 284
Tohma, J., 302
Tokida, K., 24, 29
Tokimatsu, K., 37
Toro, G., 11-12
Towhata, T., 24, 29
Trautmann, C.H., 102, 112, 114-117, 120, 231-233, 238, 270
Trifunac, M.D., 55-57, 284
Tsukamoto, K., 58-60
Tsutsumi, T., 307
Turner, J., 115-116

U

Uchida, Y., 29
Uematsu, M., 124

Ukaji, T., 58-60
US Department of Transportation, xi
Usher, N., 191, 194

V

Varnes, D.J., 16
Verley, R., 127, 129
Vitali, L., 81

W

Wagner, D., 132
Wakai, N., 265
Wang, L.R.L., 58, 184, 207-208, 212-213, 266-267, 279-280, 307
Ward, E., 157, 328
Weiss, W.J., 230
Wells, D.L., 13-14
White, D., 127-128, 130-132
Whitney, J., 11-12
Wijewickreme, D., 27, 71-72, 78-79
Wilkie, S., 73
Williamson, R.A., 204-208, 211, 213, 298
Wilson, R.C., 20
Wright, J., 49
Wright, S., 157, 328
Wrzyszczynski, M., 328
Wu, D., 295

Y

Yamada, K., 24, 29
Yamaji, T., 265
Yamajyo, K., 124, 184
Yamamura, Y., 55, 276-278
Yasuda, S., 29, 34-35, 124, 137
Yeh, G., 52, 240
Yeh, Y.H., 184, 207-208, 212-213
Yew, C.H., 84
Yoshida, M., 302
Yoshida, T., 124
Youd, T.L., 27, 29-33, 37, 301-302
Young, W., 74
Youngs, R., 11-12
Yount, J., 11-12
Yun, H.D., 84

Z

Zerva, A., 57
Zhou, Z., 73
Zimmerman, T.J., 77

Contributors

Dr. Michael J. O'Rourke
Professor
Department of Civil and Environmental Engineering
Rensselaer Polytechnic Institute
Troy, NY 12180-3590
orourm@rpi.edu

Dr. (Jack) X. Liu
President, Principal Consultant
Liu Advanced Engineering, LLC
11211 Katy Freeway, Suite 450
Houston, TX 77079
jack.liu@laengr.com

Monographs and Special Publications

Economic Consequences of Earthquakes: Preparing for the Unexpected, *edited by Barclay G. Jones*

Passive Energy Dissipation Systems for Structural Design and Retrofit, *by M. C. Constantinou, T. T. Soong, and G. F. Dargush*

Engineering and Socioeconomic Impacts of Earthquakes: An Analysis of Electricity Lifeline Disruptions in the New Madrid Area, *edited by M. Shinozuka, A. Rose, and R. T. Eguchi*

Response of Buried Pipelines Subject to Earthquake Effects, *by M.J. O'Rourke and (Jack) X. Liu*

MCEER
EARTHQUAKE ENGINEERING TO EXTREME EVENTS
University at Buffalo, The State University of New York
133A Ketter Hall ▪ Buffalo, New York 14260-4300
Phone: (716) 645-3391 ▪ Fax: (716) 645-3399
Email: *mceer@buffalo.edu* ▪ Web: *http://mceer.buffalo.edu*
University at Buffalo *The State University of New York*

ISBN 978-0-9656682-4-8
9 780965 668248 >